Sea Ice Climate Change Initiative: Phase 2

D4.1 Product Validation & Intercomparison Report (PVIR)

Doc Ref: SICCI-PVIR-SIC

Version: 1.1

Date: 23 July 2018

Consortium Members

ESA UNCLASSIFIED - For Official Use

Change Record

Issue	Date	Reason for Change	Author
PVIR_P2 1.0.D	10 January 2017	First draft of PVIR_P2_v1.0	Stefan Kern
	January 26 2017	Added SIC0 results	Stefan Kern
	February 06 2017	Added SIC1 results	Stefan Kern
	February 08 2017	Completed scientific content; added input from Henriette	Stefan Kern, Henriette Skourup
PVIR-SIC v1.1 version01	January 10 2018	Cut PVIR_P2 into two parts. This document is the SIC part	Stefan Kern
PVIR-SIC v1.1 v01 shared with met.no	January 23 2018	Included all results obtained at ICDC except the results of the correlation analysis	Stefan Kern with analysis contributions of: Louisa Bell, Maybritt Meyer, Luise Zimmermann, Leif T. Pedersen, Roberto Saldo
PVIR-SIC v1.1 v01 shared with CGI	January 30 2018	Completed the report with the correlation analysis. What is missing: Thin ice analysis and the summary as well as a revision of the reference list	Stefan Kern with analysis contributions of: Louisa Bell, Maybritt Meyer, Luise Zimmermann, Leif T. Pedersen, Roberto Saldo
PVIR-SIC v1.1 v02	February 13 2018	Revised reference list Summary included Outlook included	Stefan Kern with analysis contributions of: Louisa Bell, Maybritt Meyer, Luise Zimmermann, Leif T. Pedersen, Roberto Saldo
PVIR-SIC v1.1 v03	July 08 2018	Some refinement in section about correlation analysis and outlook, added one reference	Stefan Kern
PVIR-SIC v1.1	July 23 2018	Issued for Milestone #6 (KO+42)	Stefan Kern

Authorship

Role	Name	Signature
Written by:	Stefan Kern	
Checked by:	Gary Timms	
Approved by:	Stein Sandven	
Authorised by:	Pascal Lecomte	

Distribution

Organisation	Names	Contact Details
ESA	Pascal Lecomte, Anna Maria	Pascal.Lecomte@esa.int; Anna.Maria.Trofaier@esa.int
NERSC	Stein Sandven, Kirill Khvorostovsky	Stein.Sandven@nersc.no; kirill.khvorostovsky@nersc.no
CGI	Gary Timms, Sabrina Mbajon, Clive Farquhar	gary.timms@cgi.com; sabrina.mbajon.njiche@cgi.com; clive.farquhar@cgi.com
MET Norway	Thomas Lavergne, Atle Sørensen	t.lavergne@met.no; atlems@met.no
DMI	Rasmus Tonboe	rtt@dmi.dk
DTU	Roberto Saldo, Henriette Skourup, Leif Toudal Pedersen	rs@space.dtu.dk; hsk@space.dtu.dk; ltp@space.dtu.dk
FMI	Marko Mäkynen, Eero Rinne	marko.makynen@fmi.fi; eero.rinne@fmi.fi;
University of Hamburg	Stefan Kern, Lars Kaleschke, Xiangshan Tian-Kunze	stefan.kern@zmaw.de; lars.kaleschke@uni-hamburg.de; xiangshan.tian-kunze@uni-hamburg.de
University of Bremen	Georg Heygster	heygster@uni-bremen.de
MPI-M	Dirk Notz, Louisa Bell	dirk.notz@mpimet.mpg.de; louisa.bell@mpimet.mpg.de
Ifremer	Fanny Ardhuin	Fanny.Ardhuin@ifremer.fr
AWI	Marcel Nicolaus, Stefan Hendricks, Thomas Hollands	marcel.nicolaus@awi.de; stefan.hendricks@awi.de; thomas.hollands@awi.de

Table of Contents

List of Figures

ESA UNCLASSIFIED - For Official Use

ESA UNCLASSIFIED - For Official Use

ESA UNCLASSIFIED - For Official Use

ESA UNCLASSIFIED - For Official Use

ESA UNCLASSIFIED - For Official Use

ESA UNCLASSIFIED - For Official Use

ESA UNCLASSIFIED - For Official Use

ESA UNCLASSIFIED - For Official Use

ESA UNCLASSIFIED - For Official Use

List of Tables

ESA UNCLASSIFIED - For Official Use

ESA UNCLASSIFIED - For Official Use

ESA UNCLASSIFIED - For Official Use

ESA UNCLASSIFIED - For Official Use

Table 4-4: Error (= SICCI-2 SIC minus reference SIC), error standard deviation (Error SDEV), retrieval standard error (RSE) and total standard error (TSE) for the comparison with Landsat-8 SIC, and with ship-based observations from ASPeCt for the Southern Hemisphere; "Wi" and "Su" denotes winter (May-Oct.) and summer (Dec.-Feb.), respectively. For Landsat, RSE and TSE are the average of pack ice conditions during summer and winter (in contrast to Table 4-3 Landsat-8 images are partly from summer and winter). For ASPeCt Wi and ASPeCT Su RSE and TSE are the average of the open water and pack ice values of the respective season. Highlighted in *bold italic* are those "Error" and "Error SDEV" values where RSE > |Error| and RSE > Error SDEV. Highlighted in bold only are those "Error" values where RSE < |Error| but TSE > |Error|. "Error SDEV" values in *italic* are < TSE. 249

1   Introduction

1.1   Purpose and Scope

This document informs about the results of the validation and inter-comparison of the SICCI project Phase 2 sea ice concentration (SIC, released in December 2016, updated in October 2017) data sets.

1.2   Document Structure

After this introduction and the list of references, the document describes the Sea Ice Concentration validation and inter-comparison efforts.

1.3   Document Status

This is issue 1.1 released to ESA as part of the project's contractual deliverable set.

1.4   Applicable Documents

The following table lists the Applicable Documents that have a direct impact on the contents of this document.

Acronym	Title	Reference	Issue
AD-1	Sea Ice ECV Project Management Plan	ESA-CCI_SICCI_PMP_D6.1_v1.1	1.3

Table 1-1: Applicable Documents

1.5   Reference Documents

Acronym	Title	Reference	Issue
RD-01	Algorithm Theoretical Basis Document (ATBDv1)	Pedersen, L. T., et al.	v2.2, Sep. 2017
RD-02	Product Validation Plan (PVP)	Laxon, S., and L. T. Pedersen, SICCI-PVP-05-12	v1.1, Sep. 2012
RD-03	Data Access Requirement Document (DARD)	Kern, S., SICCI-P2-DARD-08-15	v2.0, Sep. 2015
RD-04	D3.4 Product User Guide (PUG)	Sørensen, A., and T. Lavergne, SICCI-PUG-P2-17-09	V1.1, Sep. 2017
RD-05	Product Validation and Intercomparison Report for SICCI 1	Kern, S., et al., ESA-CCI-SICCI-PVIR	V1.1, Feb. 2015

Acronym	Title	Reference	Issue
RD-06	Round Robin Data Package for SICCI 2 SIC	Pedersen, L.T., et al.	v2.1 Aug. 2017
RD-07	Revised Landsat-5 Thematic Mapper Radiometric Calibration	Chander, G., B. L. Markham, and J. A. Barsi, IEEE Geoscience and Remote Sensing Letters, 4(3), 490-494, 2007	n.a.
RD-08	Summary of current radiometric calibration coefficients for Landsat MSS, TM, ETM+, and EO-1 ALI sensors	Chander, G., B. L. Markham, and D. L. Helder, Remote Sensing of Environment, 113, 893-903, 2009	n.a.
RD-09	Removal of Atmospheric Effects from AVHRR albedos	Koepke, P., Journal of Applied Meteorology, 28, 1341-1348, 1989	n.a.
RD-10	Comparison of Landsat TM-derived and ground-based albedos of Haut Glacier d'Arolla, Switzerland	Knap, W. H., B. W. Brock, J. Oerlemans, and I. C. Willis, International Journal of Remote Sensing, 20(17), 3293-3310, 1999	n.a.
RD-11	Surface Albedo of the Antarctic sea ice zone	Brandt, R. E., S. G. Warren, A. P. Worby, and T. C. Grenfell, Journal of Climate, 18, 3606-3622, 2005	n.a.
RD-12	Melt ponds on Arctic sea ice determined from MODIS satellite data using an artificial neural network	Rösel, A., L. Kaleschke, and G. Birnbaum, The Cryosphere, 6, 431-445, doi:10.5194/tc-6-431-2012, 2012	n.a.
RD-13	On the estimation of melt pond fraction on the Arctic sea ice with ENVISAT WSM images	Mäkynen, M., S. Kern, A. Rösel, and L.T. Pedersen, IEEE Transactions on Geoscience and Remote Sensing, 52(11), doi:10.1109/TGRS.2014.2311476, 2014	n.a.

Acronym	Title	Reference	Issue
RD-14	The impact of melt ponds on summertime microwave brightness temperatures and sea-ice concentrations	Kern, S., A. Rösel, L. T. Pedersen, N. Ivanova, R. Saldo, and R. T. Tonboe, The Cryosphere, 10, doi:10.5194/tc-10-1-2016	n.a.
RD-15	Studies of the Antarctic sea ice edge and sea ice extent from satellite and ship observations	Worby, A. P. and J. C. Comiso, Remote Sensing of Environment, 92, 98–111, doi:10.1016/j.rse.2004.05.007, 2004	n.a.
RD-16	Antarctic summer sea ice concentration and extent: comparison of ODEN 2006 ship observations, satellite passive microwave and NIC sea ice charts	Ozsoy-Cicek, B., H. Xie, S. F. Ackley, and K. Ye, The Cryosphere, 3, 1-9, 2009	n.a.
RD-17	Comparison of SSM/I and AMSR-E sea ice concentrations with ASPeCt ship observations around Antarctica	Beitsch, A., S. Kern, and L. Kaleschke, IEEE Transaction on Geoscience and Remote Sensing, 53(4), 10.1109/TGRS.2014.2351497, 2015	n.a.
RD-18	Thickness distribution of Antarctic sea ice	Worby, A. P., C. A. Geiger, M. J. Paget, M. L. VanWoert, S. F. Ackley, and T. L. DeLiberty, Journal of Geophysical Research, 113(C5), C05S92, doi:10.1029/2007JC004254, 2008.	n.a.
RD-19	The Expedition of the Research Vessel Polarstern to the Antarctic in 2013 (ANT-XXIX/6)	Lemke, P., Reports on Polar and Marine Research, 679, 154pp, https://doi.org/10.2312/BzPM_0679_2014, 2014	n.a.
RD-20	The Expedition of the Research Vessel Polarstern to the Antarctic in 2013 (ANT-XXIX/7)	Meyer, B., and L. Auerswald, Reports on Polar and Marine Research, 674, 130pp, https://doi.org/10.2312/BzPM_0674_2014, 2014	n.a.

Acronym	Title	Reference	Issue
RD-21	The Expedition PS82 of the Research Vessel POLARSTERN to the southern Weddell Sea in 2013/2014	Knust, R., and M. Schröder, Reports on Polar and Marine Research, 680, 155pp, https://doi.org/10.2312/BzPM_0680_2014, 2014	n.a.
RD-22	The Expedition PS89 of the Research Vessel POLARSTERN to the Weddell Sea in 2014/2015	Boebel, O., Reports on Polar and Marine Research, 689, 151pp, https://doi.org/10.2312/BzPM_0689_2015, 2015	n.a.
RD-23	The Expedition PS96 of the Research Vessel POLARSTERN to the southern Weddell Sea in 2015/2016	Schröder, M., Reports on Polar and Marine Research, 700, 142 pp, https://doi.org/10.2312/BzPM_0700_2016, 2016	n.a.
RD-24	The Expedition ARKTIS-XIX/1 a, b and XIX/2 of the Research Vessel Polarstern in 2003	Schauer, U., and G. Kattner, Reports on Polar and Marine Research, 481, 194pp, https://doi.org/10.2312/BzPM_0481_2004, 2004	n.a.
RD-25	The Expeditions ARKTIS-XX/1 and ARKTIS-XX/2 of the Research Vessel Polarstern in 2004	Budéus, G., and P. Lemke, Reports on Polar and Marine Research, 544, 242pp, https://doi.org/10.2312/BzPM_0544_2007, 2007	n.a.
RD-26	Scientific cruise report of the Arctic Expedition ARK-XX/3 of RV Polarstern in 2004: Fram Strait, Yermak Plateau and East Greenland Continental Margin	Stein, R., Reports on Polar and Marine Research, 517, 188pp, https://doi.org/10.2312/BzPM_0517_2005, 2005	n.a.
RD-27	The Expedition ARKTIS-XXII/2 of the Research Vessel Polarstern in 2007	Schauer, U., Reports on Polar and Marine Research, 579, 264pp, https://doi.org/10.2312/BzPM_0579_2008, 2008	n.a.

Acronym	Title	Reference	Issue
RD-28	The Expedition of the Research Vessel Polarstern to the Arctic in 2011 (ARK-XXVI/3 - TransArc)	Schauer, U., Reports on Polar and Marine Research, 649, 205pp, https://doi.org/10.2312/BzPM_0649_2012, 2012	n.a.
RD-29	The Expedition of the Research Vessel Polarstern to the Arctic in 2012 (ARK-XXVII/3)	Boetius, A., Reports on Polar and Marine Research, 663, 166pp, https://doi.org/10.2312/BzPM_0663_2013, 2013	n.a.
RD-30	The Expedition PS86 of the Research Vessel POLARSTERN to the Arctic Ocean in 2014	Boetius, A., Reports on Polar and Marine Research, 685, 133pp, https://doi.org/10.2312/BzPM_0685_2015, 2015	n.a.
RD-31	The Expedition PS92 of the Research Vessel POLARSTERN to the Arctic Ocean in 2015	Peeken, I., Reports on Polar and Marine Research, 694, 153pp, https://doi.org/10.2312/BzPM_0694_2016, 2016	n.a.
RD-32	IceWatch: Standardizing and expanding Arctic ship-based sea-ice observations	Hutchings, J., N. Hughes, A. Orlich, S. MacFarlane, A., Cowan, L. Farmer, and K. Faber, White Paper, College of Earth Ocean and Atmospheric Sciences, Oregon State University	n.a.
RD-33	2006 Ice Watch Joint Ocean Ice Study (JOIS) Sea Ice Observation Program, 1.00	Hutchings, J., and A. Orlich, Arctic Data archive System (ADS), Japan, https://ads.nipr.ac.jp/dataset/A20140623-014, 2011	n.a.
RD-34	2007 Ice Watch Joint Ocean Ice Study (JOIS) Sea Ice Observation Program, 1.00	Hutchings, J., and A. Orlich, Arctic Data archive System (ADS), Japan, https://ads.nipr.ac.jp/dataset/A20140623-008, 2011	n.a.

Acronym	Title	Reference	Issue
RD-35	2008 Ice Watch Joint Ocean Ice Study (JOIS) Sea Ice Observation Program, 1.00	Hutchings, J., and A. Orlich, Arctic Data archive System (ADS), Japan, https://ads.nipr.ac.jp/dataset/A20140623-012, 2011	n.a.
RD-36	2009 Ice Watch Joint Ocean Ice Study (JOIS) Sea Ice Observation Program, 1.00	Hutchings, J., and A. Orlich, Arctic Data archive System (ADS), Japan, https://ads.nipr.ac.jp/dataset/A20140623-006, 2011	n.a.
RD-37	2010 Ice Watch Joint Ocean Ice Study (JOIS) Sea Ice Observation Program, 1.00	Hutchings, J., and A. Orlich, Arctic Data archive System (ADS), Japan, https://ads.nipr.ac.jp/dataset/A20140623-013, 2011	n.a.
RD-38	Sea Ice Ship Based Underway Standard Sea Ice Observation Reports Healy Cruises HLY-07-01 and HLY-07-02	Staup, R., M. Prevenas, and K. E. Frey, https://www.eol.ucar.edu/projects/best/, 2007	n.a.
RD-39	Sea Ice Ship Based Underway Standard Sea Ice Observation Reports, for Healy Cruises HLY-08-01 and HLY-08-02	Gradinger, R., B. Bluhm, K. Iken, and K. Frey (UAF), https://www.eol.ucar.edu/projects/best/, 2008	n.a.
RD-40	Sea Ice Ship Based Underway Standard Sea Ice Observation Reports, Healy Cruises HLY-09-01 and HLY-09-02	Gradinger, R., K. Iken, H. Chenelot, B. McConnell, M. Reedy, and J. Weems, https://www.eol.ucar.edu/projects/best/, 2009	n.a.
RD-41	Sea Ice Ship Based Underway Standard Sea Ice Observation Reports Polar Sea Cruise PSEA-10-01	Gradinger, R., M. Schuster, and J. Weems, https://www.eol.ucar.edu/projects/best/, 2010	n.a.

Acronym	Title	Reference	Issue
RD-42	HLY12-01 Marine Mammal Watch	Moore, S. E., and J. M. Grebmeier, doi:10.5065/D6028PM0 (https://arcticdata.io/metacat/metacat/doi:10.5065/D6028PM0/default), 2012	n.a.
RD-43	HLY13-01 Marine Mammal Watch	Moore, S. E., and J. M. Grebmeier, doi:10.5065/D6V98643 (https://arcticdata.io/metacat/metacat/doi:10.5065/D6V98643/default), 2013	n.a.
RD-44	SWL14 Marine Mammal Watch	Moore S. E., J. M. Grebmeier, and S. Vagle, doi:10.5065/D6KS6PMR (https://arcticdata.io/metacat/metacat/doi:10.5065/D6KS6PMR/default), 2015	n.a.
RD-45	Underway Sea Ice Observations during SUBICE 2014	Polashenski, C., doi:10.18739/A2KW8F (https://arcticdata.io/metacat/metacat/doi:10.18739/A2KW8F/default), 2016	n.a.
RD-46	Independent uncertainty estimates for coefficient based sea surface temperature retrieval from the along-track scanning radiometer instruments	Bulgin, C.E., O. Embury, G. Corlett, and C. J. Merchant, Remote Sensing of Environment, 178, 213-222, 2016	n.a.
RD-47	Uncertainty propagation in observational references to climate model scales	Bellprat, O., F. Massonnet, S. Siegert, C. Prodhomme, D. Macias-Gómez, V. Guemas, F. Doblas-Reyes, Remote Sensing of Environment, 203, 101-108, https://doi.org/10.1016/j.rse.2017.06.034 , 2017	n.a.

Table 1-2: Reference Documents

ESA UNCLASSIFIED - For Official Use

1.6   Acronyms and Abbreviations

Acronym	Meaning
AMSR-E	Advanced Microwave Scanning Radiometer aboard EOS
AO	Announcement of Opportunity
ASCII	American Standard Code for Information Interchange
ASIRAS	Airborne Synthetic Aperture and Interferometric Radar Altimeter System
ATBD	Algorithm Theoretical Basis Document
CM-SAF	Climate Monitoring Satellite Application Facility
DMSP	Defence Meteorological Satellite Program
DWD	Deutscher Wetterdienst
EASE2	Equal-Area Scalable Earth Grid 2
ECV	Essential Climate Variable
Envisat	Environmental Satellite
ERS	European Remote Sensing satellite
ESA	European Space Agency
EUMETSAT	European Organisation for the Exploitation of Meteorological Satellites
FB	Freeboard
FCDR	Fundamental Climate Data Record
FOC	Free of Charge
FOV	Field-of-View
FTP	File Transfer Protocol
GB	GigaByte
GCOM	Global Change Observation Mission
H	Horizontal polarization
H+V	Horizontal and vertical polarization
L1B	Level 1b
MB	MegaByte
MODIS	Moderate Resolution Imaging Spectroradiometer
MSS	Mean Sea Surface
n.a.	Not applicable
NetCDF	Network Common Data Format
NSIDC	National Snow and Ice Data Center
OCOG	Offset Centre of Gravity
OIB	Operation Ice Bridge
OSI-SAF	Ocean and Sea Ice Satellite Application Facility
OW	Open Water
PI	Principal Investigator
PMW	Passive Microwave
POES	Polar Operational Environmental Satellite
PRF	Pulse Repetition Frequency
RA	Radar Altimeter

ESA UNCLASSIFIED - For Official Use

Acronym	Meaning
RADAR	Radio Detection and Ranging
SAR	Synthetic Aperture Radar
SGDR	Sensor Geophysical Data Record
SIC	Sea Ice Concentration
SIRAL	SAR/Interferometric Radar Altimeter
SIT	Sea Ice Thickness
SSM/I	Special Sensor Microwave / Imager
SSM/IS	Special Sensor Microwave / Imager+Sounder
TB	TeraByte
t.b.d.	To be determined
TM	Thematic Mapper
ULS	Upward Looking Sonar
URL	Uniform Resource Locator
V	Vertical polarization
WGS84	World Geodetic System revision -84

Table 1-3: Acronyms

2   Preface

The algorithms used to obtain the products are described in the Algorithm Theoretical Basis Document (ATDB) [RD-01]. The Product Validation Plan (PVP) [RD-02] reveals the steps and strategies that ought to be used for the validation. The sources for the data to be used are compiled in the Data Access Requirement Document (DARD) [RD-03]. The products are described in the netCDF file attributes and in the Product User Guide (PUG) did not yet exist [RD-04].

The validation and inter-comparison was carried out using the SIC product v2.0 and v2.1 downloaded from met.no. SICCI-2 SIC products are available for both hemispheres year-round for the time periods: 06/2002-09/2011 (AMSR-E) and 07/2012-04/2017 (AMSR2); note that actually the last day with data is May 15 2017.

We note that passages of this report, where data input and methodologies did not change with respect to the SICCI phase 1 project are 1-to-1 copies of the respective report (PVIR) delivered in the context of the SICCI-1 project [RD-05].

3   Sea Ice Concentration

Validation of the SICCI Phase 2 SIC product was carried out for the v2.0 and v2.1 product based on AMSR-E and AMSR2 data.

In contrast to SICCI Phase 1, validation of the product based on SSM/I and SMMR data is not part of the SICCI 2 WP4000 activities.

Note further that in contrast to SICCI Phase 1 three different products are evaluated [RD-05], namely **SICCIHF**, the high frequency algorithm using the channels 18.7V, 89.0V, 89.0H (H = horizontal, V = vertical polarization, the number is the frequency in GHz), **SICCILF**(or SICCI-25km), the low frequency algorithm using the channels 18.7V, 36.5V, 36.5H (similar to SICCI 1), and **SICCIVLF**(or SICCI-50km), the very low frequency algorithm using the channels 6V, 36.5V, 36.5H. Given the different footprint sizes of the channels used the grid resolution of the three products is **12.5 km**, **25 km** and **50 km**, respectively. Henceforth we will refer to the three different products also via their grid resolution, i.e. name them 12.5 km product, 25 km product and 50 km product.

Elements of the validation were:

- A health check of the SIC products in collaboration with met.no to mitigate errors in the product prior to its final release

- Inter-comparisons of the SIC product with:

    - independent SIC data at 0% and 100%

    - high-resolution optical satellite imagery

    - 8-day melt-pond cover fractions

    - visual ship-based ASPeCt and ASSIST sea-ice observations

- Investigation of amount and distribution of SIC < 0% and > 100%

- Investigation of the SIC uncertainties

- Correlation length scales of SIC and SIC uncertainties

ESA UNCLASSIFIED - For Official Use

3.1   SIC prototype product health check

The health check (first item in the list) was done in cooperation with WP3000 and can be seen as an optimization of the SICCI 2 products rather than their evaluation. We do not report about the results of this check in detail therefore.

It was checked whether data files contain all the necessary information and whether these can be read easily with standard programs such as IDL, Matlab, Python, and others and whether results can be displayed with standard imaging software such as Ferret, ncview, IDL, and others.

Animated loops of maps of the SIC and the uncertainty parameters were run to search for inconsistencies in the data sets. Very few were found and were corrected in the code to be incorporated into the final release of the SICCI 2 SIC products.

3.2 Sea Ice Concentration Evaluation: 0% and 100%

Similar to SICCI Phase 1, the evaluation of the SIC products focused on the evaluation of the products at 0% and 100% sea-ice concentration. For these sea-ice concentration values well validated independent data exist.

For 0% sea-ice concentration we used the entire data set generated from ice charts for the Round Robin Exercise (RRE) of phase 2. It comprises a number of locations where according to the ice charts the daily sea-ice concentration was 0% with high confidence [RD-06].

For 100% sea-ice concentration locations were used where analysis of collocated Envisat ASAR and Sentinel-1A SAR ice drift estimates provided convergent sea-ice conditions with a little or no change in sea-ice area in predefined grid cells. During freezing conditions this provides a very valuable data set of SIC = 100% because leads, which might still form under convergent sea-ice motion in the 100 km x 100 km large areas used to derive this independent data set, will freeze over. During melting conditions such leads generally do not freeze over; hence the SIC = 100% data set is of less good quality during summer months and is not used in the evaluation.

This SIC = 100% data set was also generated for the RRE [RD-06] of phase 2 but can be entirely used in WP4000.

The evaluation will be carried out for the fully filtered product (see [RD-04]) and for the product which includes off-range SIC, i.e. values above 100% and below 0% to take into account the variability of retrieved SIC values around these two threshold concentrations due to noise in the used brightness temperatures.

We exclude data where SIC values are indicated to coincide with too high air temperature. We further excluce data where the land-spillover correction of the brightness temperature turned out to be not sufficient requiring post-processing in form of filtering of the SIC product.

3.2.1 Open water SIC evaluation (0%)

In this subsection we show the results of the evaluation of the SICCI 2 SIC products at 0% sea-ice concentration, i.e., how well the product identifies completely ice free areas.

For this purpose, the unfiltered SIC product is used. Using the filtered SIC product does not result in a meaningful statement because i) the filtering – namely the weather filter – sets SIC values to 0% sharp in open water areas, and ii) the variability of the SIC values around 0% caused by the variability of the used brightness temperatures around the open water tie point is suppressed. This variability of both the brightness temperatures and the retrieved SIC is, however, a measure of the quality of the correction of the weather influence by the radiative transfer modeling applied and the suitability of the tie points used. Therefore in order to make a quantitative statement about the quality of the SICCI 2 SIC products one needs to evaluate the unfiltered SIC.

We obtained the retrieved SIC at those locations which have been defined as open water for the SIC RRDP2 data set. These are fixed locations close to the southern (Northern Hemisphere) and northern (Southern Hemisphere)

of the climatological sea-ice extent spread zonally. Different locations have been chosen in the RRDP2 for summer and winter in order to account for the seasonal variation of the sea-ice extent. It is five locations in the Northern Hemisphere and five (winter) and four (summer) locations in the Southern Hemisphere [RD-06].

We considered retrieved SIC of months January / February, i.e. Northern Hemisphere winter and Southern Hemisphere summer, and August / September, i.e. Northern Hemisphere summer and Southern Hemisphere winter for the entire AMSR-E/AMSR2 period. The co-location to the RRDP2 open water locations is done via finding the grid cell which center coordinate (given in the SICCI 2 SIC products) has minimum distance to that location. This was done separately for SICCI products with the 50 km, 25 km, and 12.5 km grid resolution. No averaging was done for the finer resolved SIC data to match the coarsest resolution of 50 km x 50 km.

In addition to the retrieved SIC we also obtained the retrieval uncertainty and the total uncertainty at these locations. While these are shown here for completeness these are discussed in the respective section 3.7.1

We note that at these locations the filtered SICCI 2 SIC is 0%.
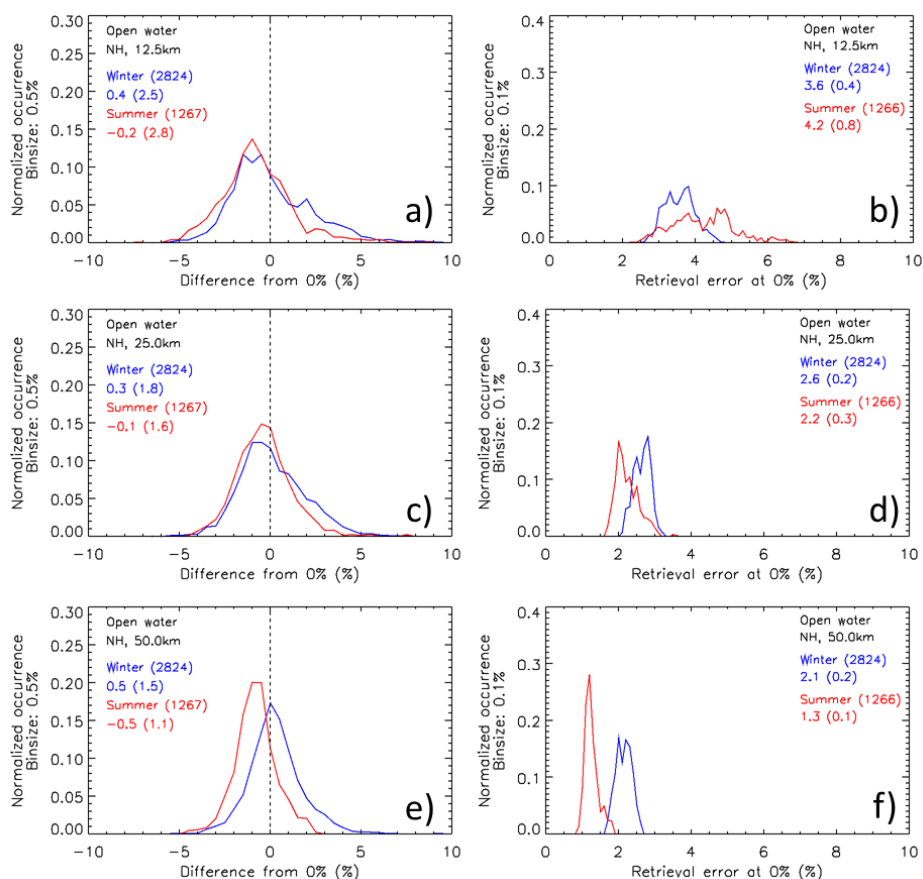
Figure 3-1: Distribution of the difference 0% minus SICCI 2 SIC (= SIC error) at the RRDP 2 open water locations in the Northern Hemisphere (left hand side) together with the distribution of the SIC retrieval uncertainty at these locations (right hand side). Winter (Jan./Feb.) and summer (Aug./ Sep.) values are denoted in blue and red, respectively. Grid resolution decreases from 12.5 km (a,b) through 25 km (c,d) to 50 km (e,f).

The distributions of the difference 0% minus SICCI 2 SIC (= SIC error), shown in Figure 3-1 for the Northern Hemisphere for winter (blue) and summer (red) for the 12.5 km (a), 25 km (c) and 50 km (e) product reveal modal values between 0 and -1%. The modal SIC error agrees between winter and summer for the 12.5 km and 25 km products while the 50 km product the modal SIC error is -1% in summer compared to 0% in winter. Note the binsize of 0.5%. Not unexpectely the distributions are quite narrow for the 50 km product and comparably wide for the 12.5 km product. The mean errors, can be considered accuracy or bias, and their standard deviations, i.e. the precision, are summarized in Table 3-1. The mean error is smallest in summer and for the 25 km product. Best precision (smallest standard deviation) is obtained for summer for the 50 km product. The degradation in precision increases with resolution refinement and/or utilization of higher frequencies.

Table 3-1: Mean difference of Northern Hemisphere open water location 0% SIC minus SICCI 2 SIC (mean SIC error or bias) followed in parentheses by the SIC standard deviation (precision) for seasons winter and summer for the grid resolutions given. All quantities – except N – are given in percent. Highlighted in bold font are the results for the 25 km product.

season	12.5 km	**25 km**	50 km	N
winter	0.4 (2.5)	**0.3 (1.8)**	0.5 (1.5)	2824
summer	-0.2 (2.8)	**-0.1 (1.6)**	-0.5 (1.1)	1266

The distributions of the difference 0% minus SICCI-2 SIC (= SIC error) shown in Figure 3-2 for the Southern Hemisphere for winter (blue) and summer (red) for the 12.5 km (a), 25 km (c) and 50 km (e) products reveal modal values between 0.5 and -0.5%. The modal SIC error agrees between winter and summer for the 12.5 km and 25 km products while for the 50 km product the modal SIC error is -0.5% in summer compared to 0.5% in winter. Note the binsize of 0.5%. The distributions are narrower for the 50 km than the 12.5 km product. The mean errors (also accuracy or bias) and the respective standard deviations, i.e. the precision, are summarized in Table 3-2. The smallest mean bias of -0.0% is found for summer for the 12.5 km product; during summer also the highest mean bias is found: -0.4% (50 km product). In winter the bias is 0.1% for all three products. Best precision (smallest standard deviation) is obtained for summer for the 50 km product. The degradation in precision increases with resolution refinement and/or utilization of higher frequencies but is more pronounced between the 25 km and 12.5 km products than between the 50 km and 25 km products.
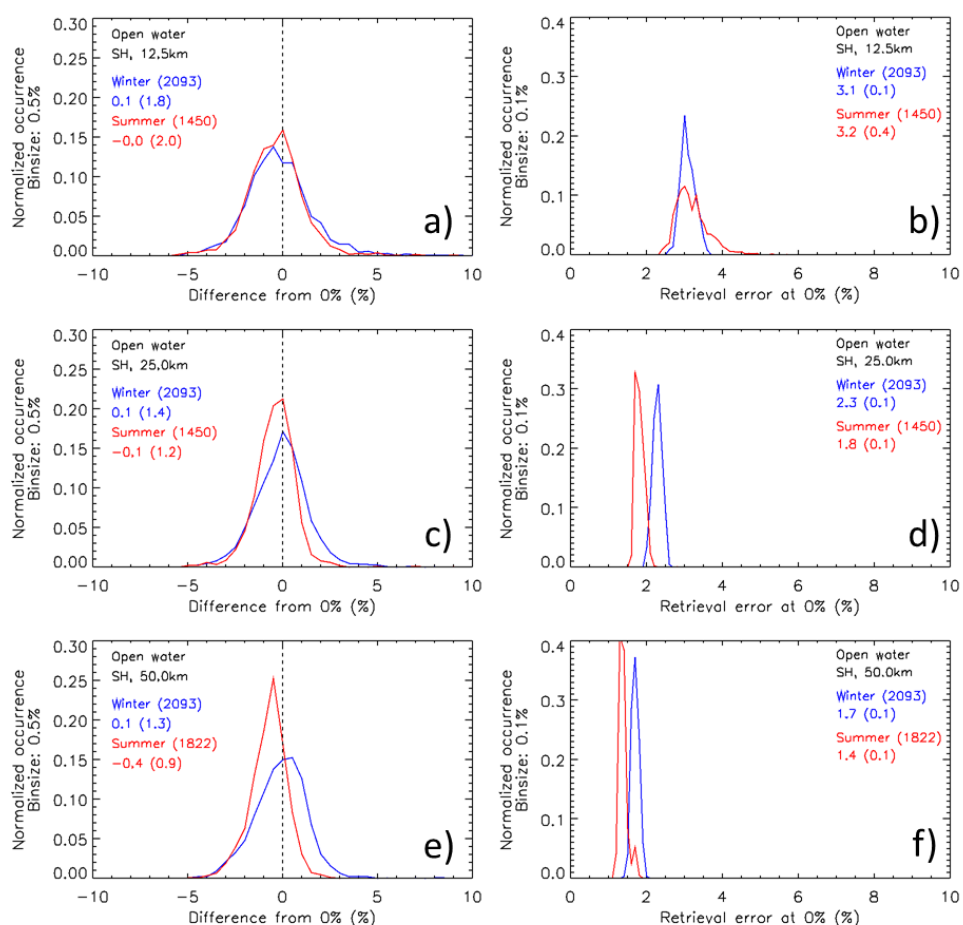
Figure 3-2: Distribution of the difference 0% minus SICCI 2 SIC (= SIC error) at the RRDP 2 open water locations in the Southern Hemisphere (left hand side) together with the distribution of the SIC retrieval uncertainty at these locations (right hand side). Winter (Aug./Sep.) and summer (Jan./ Feb.) values are denoted in blue and red, respectively. Grid resolution decreases from 12.5 km (a,b) through 25 km (c,d) to 50 km (e,f).

Table 3-2: Mean difference of Southern Hemisphere open water location 0% SIC minus SICCI 2 SIC (mean SIC error or bias) followed in parentheses by the SIC standard deviation (precision) for seasons winter and summer for the grid resolutions given. All quantities – except N – are given in percent. Highlighted in bold font are the results for the 25 km product. The second number given in the second row of column N is for 50 km grid resolution; here one of the open water locations was outside the valid area for the 12.5 km and 25 km products but inside for the 50 km product.

season	12.5 km	**25 km**	50 km	N
winter	0.1 (1.8)	**0.1 (1.4)**	0.1 (1.3)	2093
summer	-0.0 (2.0)	**-0.1 (1.2)**	-0.4 (0.9)	1450 / 1822

3.2.2 *Pack ice SIC evaluation (100%)*

In this subsection we show the results of the validation of the SICCI 2 SIC products at 100% sea-ice concentration, i.e., how well the product identifies completely ice covered areas.

For this purpose, the unfiltered SIC product is used. Using the filtered SIC product does not result in a meaningful statement because the variability of the SIC values around 100% caused by the variability of the used brightness temperatures around the sea ice tie point is suppressed. This variability of both the brightness temperatures and the retrieved SIC is, however, a measure of the suitability of the tie points used. Therefore in order to make a quantitative statement about the quality of the SICCI 2 SIC product one needs to evaluate the unfiltered SIC.

We obtained the retrieved SIC at those locations for which the RRDP2 indicates 100% sea-ice concentation estimated via analysis of consecutive, overlapping pairs of completely ice-covered Envisat ASAR or Sentinel-1 SAR imagery. Ice motion derived from such image pairs indicating convergence ensures an ice concentration of or very close to 100% (see [RD-06]), particularly during freezing conditions when eventually remaining small open water areas can be expected to freeze over quickly. During summer and/or non-freezing conditions the assumption that residual open water areas freeze over quickly does not hold and the accuracy of the RRDP2 100% sea-ice concentration data set can expected to be worse compared to winter. Because of this we carried out this evaluation only for data from freezing season months, i.e. Nov. through Mar. for the Northern Hemisphere and May through Sep. for the Southern Hemisphere. We restrict the analysis further to data where the control variable "area change" in the RRDP-2 SIC data set is between 0.985 and 0.996 to ensure high quality SIC estimates. Note that we used a new version of the RRDP2 with improved and additional data compared to the version utilized for issue 1.0 of this PVIR.

Even though the limitation to freezing season might be a sufficient criterion to avoid biases in the RRDP-2 SIC data set we carried out the evaluation also for a further limited RRDP-2 SIC data set by using only data with ERA-Interim 2m air temperatures below -5°C or -10°C.

The co-location to the locations of the RRDP2 100% sea-ice concentration is done via finding the grid cell which center coordinate (given in the SICCI 2 SIC products) has minimum distance to the RRDP2 location. This was done separately for the 50 km, 25 km, and 12.5 km SICCI 2 products. No averaging was done for the finer resolved SIC data to match the coarsest SICCI 2 SIC product resolution of 50 km x 50 km or the even coarser resolution of the RRDP2 data.

In addition to the retrieved SIC we also obtained the retrieval uncertainty and the total uncertainty at the locations of RRDP2 100% sea-ice concentration. These are discussed, however, in the respective section 3.7.2.

The following results only look at the entire combined AMSR-E – AMSR2 period without differentiating between AMSR-E and AMSR2, or between years or between seasons.
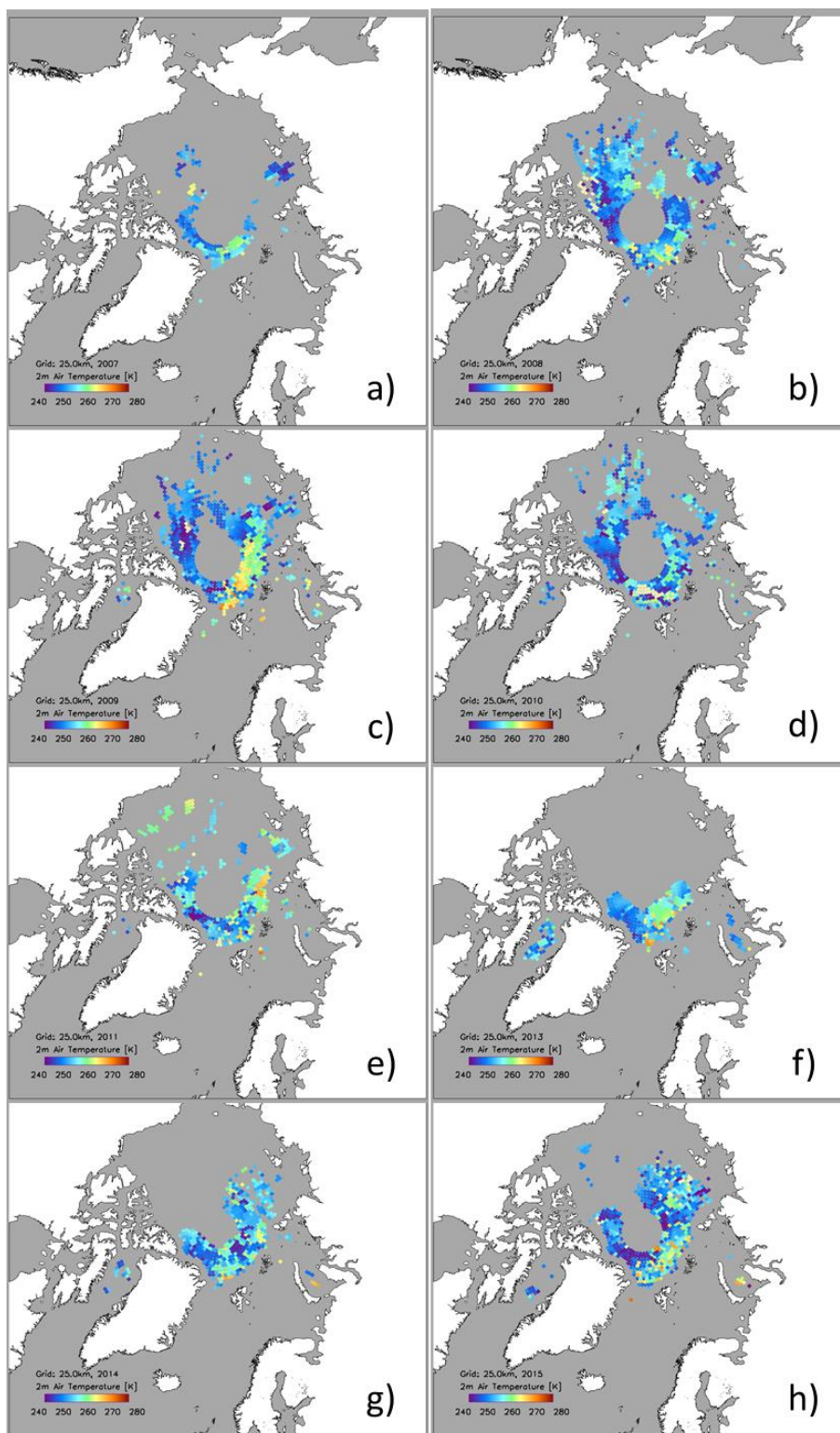
Figure 3-3: Distribution of the co-located data pairs for AMSR-E years 2007 through 2011 (images a) through e)) and for AMSR2 years 2013 through 2015 (images f) through h)) for the Northern Hemisphere. Shown is the ERA-Interim 2m air temperature of the respective inter months taken from the RRDP2 data set at the co-located SICCI-2 grid cells.
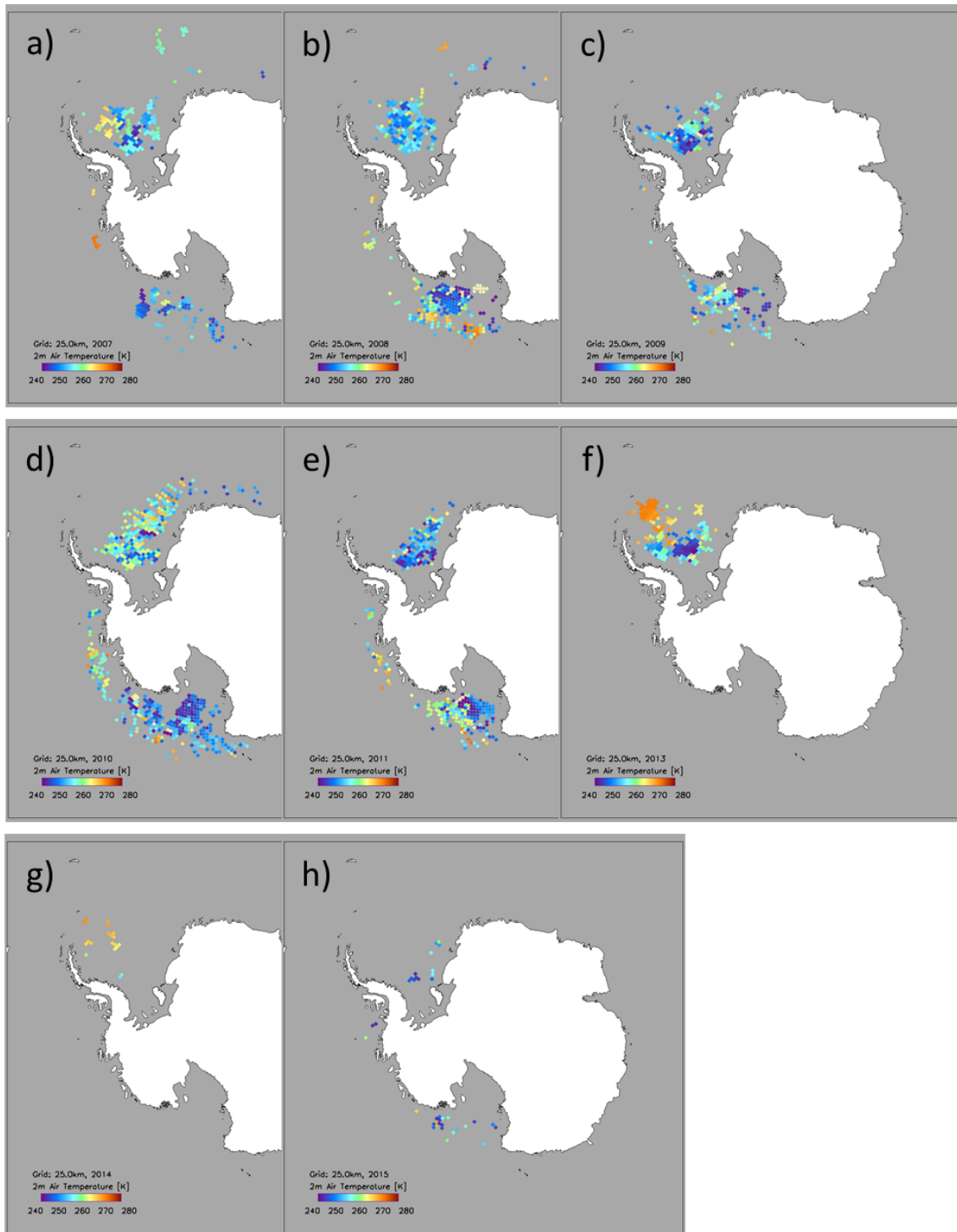
Figure 3-4: Distribution of the co-located data pairs for AMSR-E years 2007 through 2011 (images a) through e)) and for AMSR2 years 2013 through 2015 (images f) through h)) for the Southern Hemisphere. Shown is the ERA-Interim 2m air temperature of the respective inter months taken from the RRDP2 data set at the co-located SICCI-2 grid cells.

Figure 3-3 and Figure 3-4 illustrate the spatial distribution of co-located SICCI-2 SIC – RRDP2 data points in the Northern and Southern

ESA UNCLASSIFIED - For Official Use

Hemisphere, respectively. Shown is the ERA-Interim 2m air temperature at all co-located grid cells during the respective winter; the temperature filters mentiond above have not been applied. It is evident that the majority of the evaluation data is from the Arctic Ocean and we have more data from the Eurasian side than from the western side. In the Southern Hemisphere we have most data in the Weddell and Ross Seas with considerably less data after 2013 than before 2012.
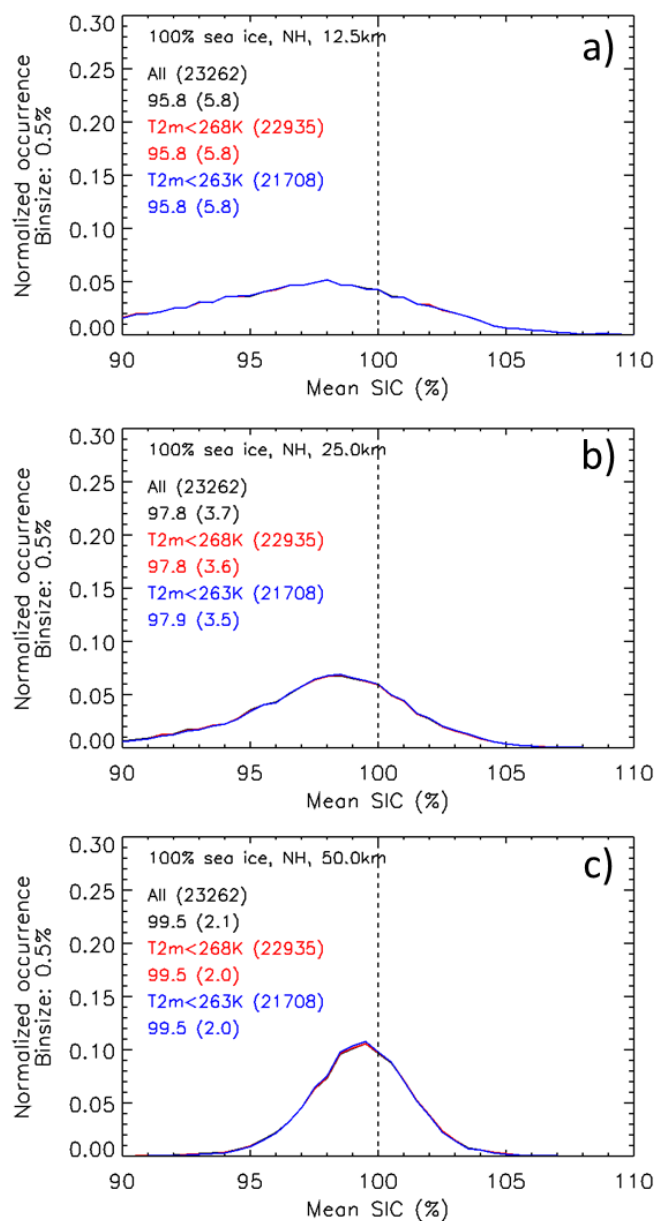
Figure 3-5: Histograms of all SICCI 2 sea-ice concentrations at locations with RRDP2 SIC = 100% using all RRDP2 data (black) and excluding those data with ECMWF 2m air temperatures above -5°C (red) or above -10°C (blue) for the 12.5 km (a), 25 km (b), and 50 km (c) product of the Northern Hemisphere. The overall mean SIC is given in percent together with one standard deviation (in parentheses) for every case; i.e. 50 km, all data: 99.5% (2.1%). The number of valid SIC data pairs is given as well (e.g. 23262 when considering all RRDP2 data).

The distributions of the co-located SICCI 2 sea-ice concentration of the Northern Hemisphere reveal modal values of 99.5%, 98.5% and 98.0% for the 50 km, 25 km and 12.5 km product, respectively (Figure 3-5 a) to c), which suggests an overall negative bias of around 1%. Mean values of the co-located SICCI 2 sea-ice concentration are considerably smaller, suggesting an overall negative bias (or SIC error) between 0.5% (50 km product) and 4% (12.5 km product). The distribution is close to Gaussian and also quite narrow for the 50 km product and non-Gaussian and much wider for the other two products. The overall mean co-located SICCI 2 sea-ice concentrations at RRDP2 SIC=100% locations are summarized together with their standard deviations in Table 3-3. Confining the RRDP2 SIC = 100% data to freezing conditions by using the above-mentioned air temperature thresholds does not change the results by more than 1/10 of a percent in the Northern Hemisphere.

Table 3-3: Northern Hemisphere SICCI 2 mean SIC at RRDP2 SIC=100% locations computed for the entire AMSR-E – AMSR2 time series for the three products. Values in parentheses are one standard deviation of the mean. All quantities – except N – are given in percent. Highlighted in bold font are the results for the 25 km product.

	12.5 km	**25 km**	50 km	N
all	95.8 (5.9)	**97.8 (3.7)**	99.5 (2.1)	23255
T2m < -10°C	95.8 (5.9)	**97.9 (3.6)**	99.5 (2.0)	21701
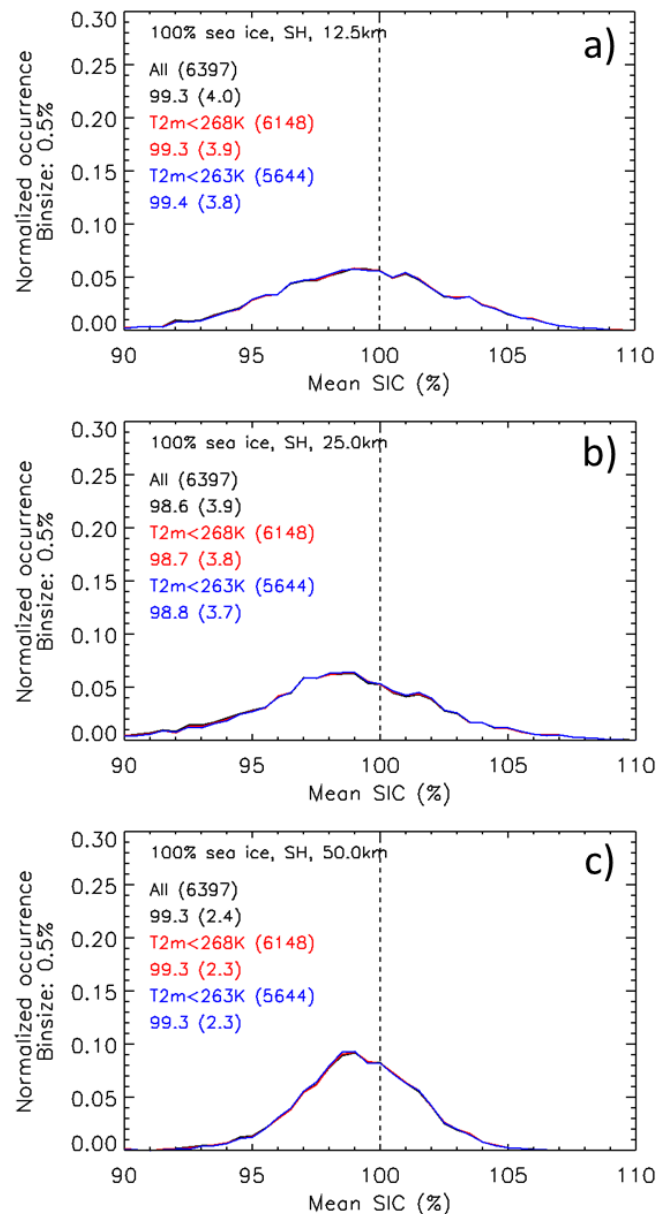
Figure 3-6: Histograms of all SICCI 2 sea-ice concentrations at locations with RRDP2 SIC = 100% using all RRDP2 data (black) and excluding those data with ECMWF 2m air temperatures above -5°C (red) or above -10°C (blue) for the 12.5 km (a), 25 km (b), and 50 km (c) product of the Southern Hemisphere. The overall mean SIC is given in percent together with one standard deviation (in parentheses) for every case; i.e. 50 km, all data: 99.3% (2.4%). The number of valid SIC data pairs is given as well (e.g. 6397 when considering all RRDP2 data).

The distributions of the co-located SICCI 2 sea-ice concentration reveal modal values between 99.0%, 98.5% and 99.5% for the 50 km, 25 km and 12.5 km product of the Southern Ocean, respectively (Figure 3-6 a) to c), which suggests an overall negative bias of around 1%. Mean values of the co-located SICCI 2 sea-ice concentration are similar to the modal values (see Table 3-4). The distribution is close to Gaussian for all three products,

quite narrow for the 50 km product and considerably wider for the other two products. The overall mean co-located SICCI 2 sea-ice concentrations at RRDP2 SIC=100% locations is summarized together with their standard deviations in Table 3-4.

Table 3-4: Southern Hemisphere SICCI 2 mean SIC at RRDP2 SIC=100% locations computed for the entire AMSR-E – AMSR2 time series for the three products. Values in parentheses are one standard deviation of the mean. All quantities – except N – are given in percent. Highlighted in bold font are the results for the 25 km product.

	12.5 km	**25 km**	50 km	N
all	99.3 (4.0)	**98.6 (4.0)**	99.3 (2.4)	6369
T2m < -10°C	99.4 (3.8)	**98.9 (3.8)**	99.4 (2.3)	5619

Overall, SICCI 2 sea-ice concentrations have an overall smaller mean error, i.e. better accuracy, in the Southern Hemisphere (Table 3-4) compared to the Northern Hemisphere (Table 3-3). This applies to all products but specifically to the 12.5 km product for which the overall error is ~4% in the Northern Hemisphere and ~1% in the Southern Hemisphere. Also the overall standard deviation is smaller, i.e. the precision better, for the Southern Hemisphere compared to the Northern Hemisphere.

Confining the comparison to non-melting conditions, i.e. 2m air temperatures below -10°C does not change the results by more than 3/10 of a percent; it leads to a reduction of the standard deviation by 0.2% for the 12.5 km and 25 km products.

3.2.3   *A note on the grid resolution*

The SIC evaluation results described above are based on the three SICCI 2 SIC CDRs at their native resolution. In order to investigate whether the same evaluation would result in substantially different results when doing it at the coarsest grid resolution , i.e. 50 km, we repeated the evaluation of the two CDRs with the finer grid resolution, i.e. 12.5 km (SICCIHF) and 25.0 km (SICCILF) averaged to a coarser grid.

One obvious way to do this would be to block-average the finer resolved CDRs onto the grid with 50 km grid resolution. This would, however, change the center coordinate of the grid cells co-located with the validation data grid cells. Therefore, in order to benefit from the more precise co-location at the two finer resolved CDRs we averaged the SIC over grid cells adjacent to the co-located grid cell at 25 km and 12.5 km grid resolution as illustrated in Figure 3-7. At least three of these grid cells need to have valid values to be used for the evaluation.
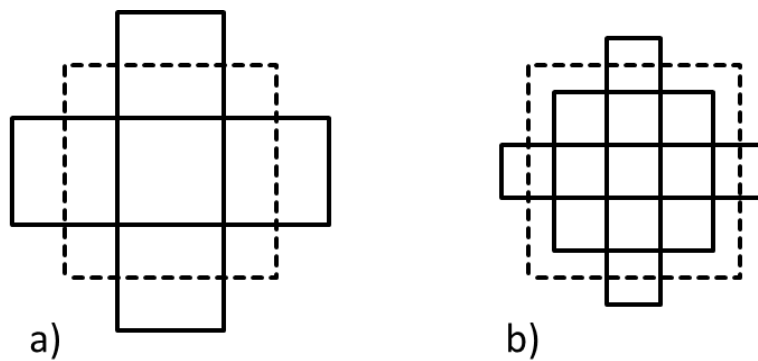
Figure 3-7: Illustration of grid cells used for the 25 km product (a) and the 12.5 km product (b) to approximate the area covered by the 50 km product (dashed square) and compute ~50km averages of the SIC and its retrieval error.

It turns out that this does not change the results substantially. For open water (SIC = 0%), the precision (bias) does not change by more than 0.1% in both hemispheres. The accuracy deteriorates by 0.1% to 0.2% in the Northern Hemisphere and improves by 0.1% to 0.2% in the Southern Hemisphere. The retrieval uncertainties do not change. For sea ice (SIC = 100%), the precision (bias) does not change by more than 0.1% in both hemispheres – if it changes at all. The accuracy improves by 0.1% to 0.2%. The retrieval uncertainties do not change.

3.3   Sea Ice Concentration evaluation with optical data

Visible imagery from Landsat-TM / ETM / OLI offers a unique source of fine spatial resolution (30 m) imagery for sea-ice concentration (SIC) validation.

Data were ordered in GeoTIFF format from https://earthexplorer.usgs.gov. for Landsat 5 TM, Landsat 7 ETM, and Landsat 8 OLI for years 2002 through 2015. Images of months March/April/May for the Northern Hemisphere and for months October through March for the Southern Hemisphere were selected and order; images / months with melt ponds were not used. At the moment of writing this report 387 images have been acquired of which 138 are from Landsat 5, 27 from Landsat 7 and 222 from Landsat 8. Images are mostly from close to the coasts around the Arctic Ocean, e.g. the Greenland, Barents, and Kara Seas, the Bering Strait area, the southern Beaufort Sea, the Labrador Sea and the Hudson Bay, and around the Antarctic continent.

Analysis of the images is the same as described in the PVIR of SICCI phase 1 [RD-05]. In brief, images of channels 2, 3, and 4 are preprocessed and the top of atmosphere (TOA) reflectance is computed following Chander et al. [RD-07; RD-08]. The solar zenith angle and other parameters required for this computation is either included in the Landsat data files or is taken from [RD-07; RD-08] and the Landsat 8 user guide [Landsat Project Science Team, 2016]. To convert the TOA reflectances to surface reflectances or surface albedo we followed the approaches of Koepke [RD-09] and Knap et al. [RD-10] which assume that the TOA reflectance (or planetary reflectance) equals the TOA albedo (or planetary albedo) and which assume that the TOA albedo ρ_{TOA} is related to the surface albedo $\rho_{surface}$ via the simple linear relationship:

$$\rho_{TOA} = a + b\rho_{surface}$$

The coefficients a and b are a function of the atmospheric conditions, the solar zenith angle, and the wavelength. We follow Koepke [RD-09] and read the values for a and b from his figure 1 and figure 2. We use figure 1 for Landsat channels 2 and 3 (that figure is for AVHRR channel 1) and we use figure 2 for Landsat channel 4 (that figure is for AVHRR channel 2). For aerosol optical depth we used 0.05, for ozone content we used 0.24 cm NTP, and for water vapor content we used 0.5 g/cm². Subsequently, the TOA albedo is converted into a surface albedo for channels 2, 3, and 4. These surface albedo values are then averaged into an estimate of the broadband shortwave albedo (see Brandt et al. [RD-11]) using the bandwidths of the channels as weights. The change in bandwidths between Landsat 5, 7 and 8 was taken into account.

Next the surface albedo maps are classified into open water, thin ice and thick ice. All pixels with an albedo of, on average (*) < 0.06 are associated to the open water class; all pixels with an albedo of, on average (*) > 0.4 are associated to the class thick ice and all remaining pixels are associated to the class thin ice. The value of 0.4 was chosen based on Brandt et al. [RD-11] who found the albedo to be around 0.33 for bare thin ice of less than 30 cm thickness and to be around 0.42 for thin ice (5 - 10 cm) with a thin (< 3 cm) snow cover.

The used three class distribution is motivated by the fact that it has been shown that the sea ice concentration retrieved with the SICCI algorithm could be substantially reduced over thin ice. Therefore, in addition to using

the Landsat images just for a high-resolution ice-water discrimination we also use them to derive the fraction of thin ice assuming that this could help to discuss potential discrepancies between the Landsat ice concentration and the SICCI ice concentration. Before the comparison to the SICCI 2 sea-ice concentration product the surface type maps are projected onto the same EASE-V2 grid; the high resolution of 30 m is preserved.

For the inter-comparison we first select a sub-region in the SICCI-2 SIC map by using the corner coordinates of the Landsat image. Subsequently, we find the Landsat pixels which ar co-located with the center coordinate of every SICCI-2 grid cell with a valid SIC within that sub-region. For each such Landsat pixel, we then define a box around it which has the dimension of the respective SICCI-2 SIC grid cell; this is 12.5 km x 12.5 km for SICCI-HF, 25.0 km x 25.0 km for SICCI-LF, and 50.0 km x 50.0 km for SICCI-VLF. For this grid box we compute the Landsat SIC by summing over all pixels which are classified as ice; we get the total SIC when summing over thin and thick ice and the thick ice SIC when summing over the thick ice pixels only.

(*) The albedo values given here have to be considered average values. The varying illumination conditions (varying sun zenith angles) and the varying validity of the coefficients used to convert TOA reflectance to surface reflectance (see above), which depends on the actual weather conditions, cause that we cannot use a fixed albedo threshold value to reliably discriminate between open water and thin ice and also between thin an thick ice. The values used may change from image to image; hence the classification is a time-consuming supervised one. Typical values for the open water – thin ice albedo threshold vary between 0.03 and 0.08; those for the thin ice – thick ice albedo threshold vary between 0.4 and 0.5.

Sensitivity Analysis

In order to estimate how the obtained sea-ice concentration may depend on the choice of the albedo thresholds for the open water – thin ice discrimination and the thin ice – thick ice discrimination we repeated the classification into the three surface types with various thresholds. If the main thresholds chosen are 0.06 and 0.45, respectively, then we classify the image also with the combinations 0.03/0.35; 0.03/0.55; 0.09/0.35; 0.09/0.55. That is, we vary the open water – thin ice threshold by ± 0.03 and the thin ice – thick ice threshold by ± 0.1. The results of this sensitivity analysis are summarized in Table 3-5. We use 15 Landsat images from the Southern Hemisphere and 12 images from the Northern Hemisphere. All these images were from Landsat-8 OLI. While the images of the Northern Hemisphere were all from the winter / spring season (April and May) the images of the Southern Hemisphere were mostly images from summer season, i.e., December through February. Only four images were from November and March and hence count to the winter / spring season.

Table 3-5 illustrates i) Variation of the albedo threshold for the water-to-ice discrimination by ± 0.03 results in a variation of the overall mean SIC derived for the co-located SICCI-2 algorithm grid cells of ~ 1%. The value obtained for the few Southern Hemisphere winter cases is ~ 2%; ii) SICCI-VLF (50 km) and SICCI-LF (25 km) provide similar values; iii) When taking all data into account results of the Northern and Southern Hemisphere are similar; iv) Variation of the albedo threshold for the thin ice-to-thick ice discrimination by ± 0.1 results in a variation of the respective SIC by ~ 2% for the Northern and by ~4% for the Southern Hemisphere.

Table 3-5: Summary of the mean values and their standard deviations of the mean SIC range around and the mean SIC difference with respect to the SIC derived from the classified Landsat-8 OLI images with the selected albedo thresholds for the water-to-ice and thin ice-to-thick ice transition that have been obtained by varying these thresholds as explained in the text. Values are shown separately for the Northern (left) and Southern (right) Hemisphere and for the water-to-ice (top) and the thin ice-to-thick ice (bottom) transition for products SICCI-VLF (50 km) and SICCI-LF (25 km). All values are given in %. See text for meaning of "winter" and "summer". Values in parentheses denote the numbers of Landsat images used. No values are given for the Southern Hemisphere for the thin ice-to-thick ice transition for "winter+summer" because during summer no thin ice is present.

Hemisphere		Northern		Southern			
Season		winter (12)		winter (4)		winter+summer (15)	
Transition	Product	50 km	25 km	50 km	25 km	50 km	25 km
water to ice	range	2.0±2.4	2.0±2.4	3.5±1.6	3.4±2.0	2.2±1.5	2.4±1.5
	difference	1.0±1.4	1.0±1.4	1.8±1.0	1.7±1.1	1.1±0.9	1.1±0.9
thin ice to thick ice	range	3.5±1.4	3.8±1.6	7.4±6.6	7.3±5.9	--	--
	difference	1.8±1.0	1.9±1.1	3.7±3.4	3.7±3.1	--	--

Even though the values obtained for the few winter cases for the Southern Hemisphere are about double of those obtained for the Northern Hemisphere and for the Southern Hemisphere during summer for, both, the water-to-ice transition, we suggest that we can issue an accuracy of 1% for the Landsat SIC. This high accuracy can be explained with a relatively straightforward possibility to discriminate between open water and thin ice in the Landsat imagery when using a supervised classification as is done in our case.

For the transition thin ice-to-thick ice and hence for the computed thick ice SIC from Landsat the accuracy is worse; the results of the Northern Hemisphere suggest an accuracy of 2%. Given the fact that even with a supervised classification it is still much more subjective where one puts this threshold and that even a thin snow cover and/or a dense coverage with frostflowers can easily increase the albedo considerably above the "typical" threshold taken, we suggest to issue an accuracy of 3% for the average thick ice SIC from Landsat when averaged over an entire image.

Note that we only carried out this sensitivity study for SICCI-VLF and SICCI-LF; since results are relatively similar we skipped to also carry out the investigation for SICCI-HF.

Northern Hemisphere

In this section we present the results obtained for the Northern Hemisphere. These rely on all available Landsat-5 TM (2003-1011) and Landsat-7 ETM (2003) images as well as on Landsat-8 OLI images (2013-2015). Table 3-6 illustrates the number of images per month.

Table 3-6: Number N of Landsat images per month used for the Northern Hemisphere.

Month	March	April	May
N	19	147	43
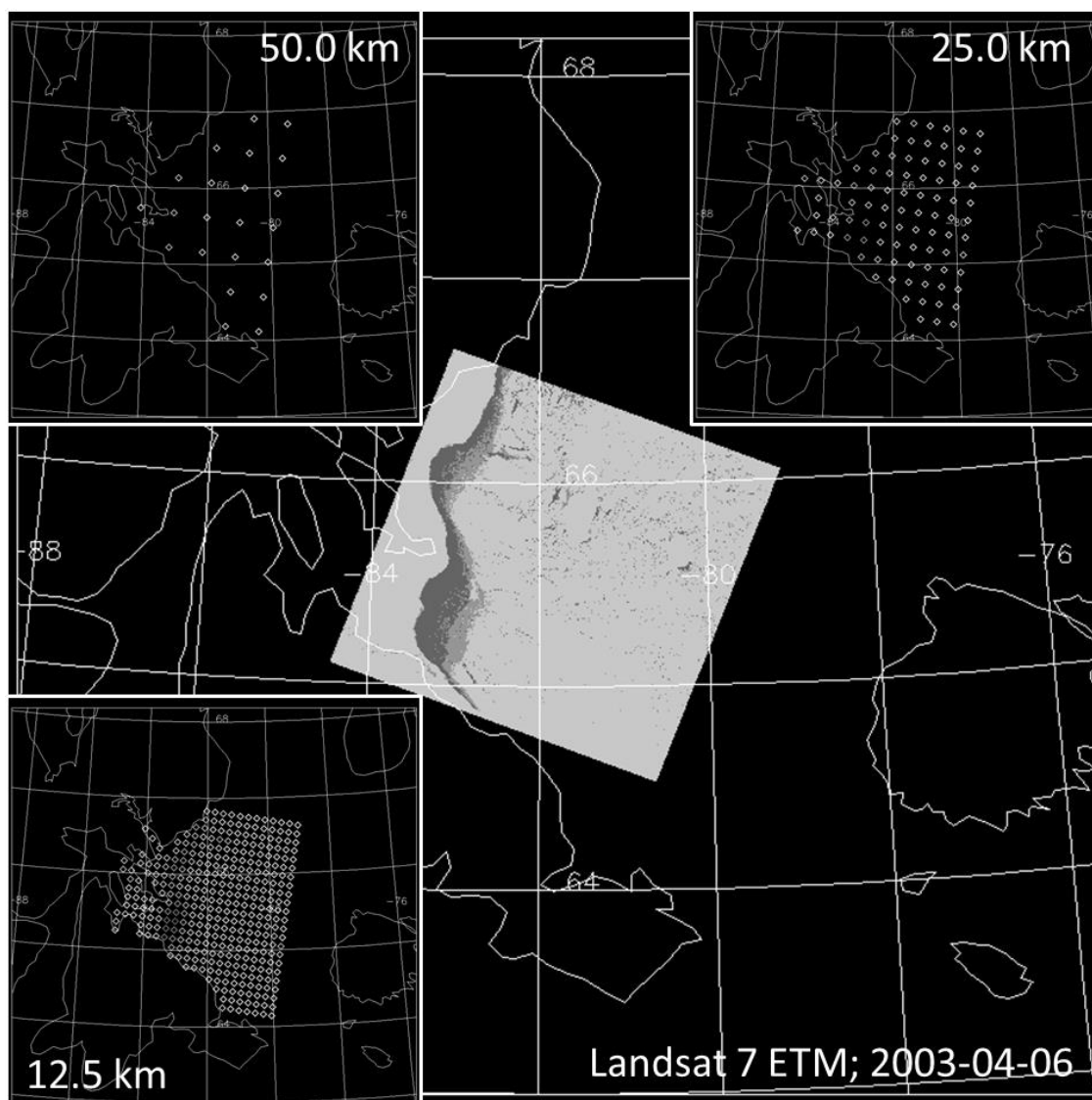
Figure 3-8: A classified Landsat-7 ETM image of April 6, 2003, north of Hudson Bay, Northern Hemisphere, with the corresponding maps of the center coordinates of the three SICCI-2 algorithms denoted by their grid resolution. Colors dark grey, medium grey and light grey in the classified Landsat image denote open water, thin ice and thick ice, respectively. The color coding in the co-located SICCI-2 maps is the sea-ice concentration (compare Figure 3-9).

The example of a Landsat image and the co-located SICCI-2 SIC maps shown in Figure 3-8 (and similar figures further down) illustrate how the two data sets are located relative to each other, and how few or how many grid cells are co-located with the Landsat image depending on the SICCI-2 SIC product grid resolution. Clearly, the 12.5 km product shows the best agreement with the high-resolution classified Landsat image. Note that the geographic orientation of the Landsat image differs from the SICCI-2 data. The choosen scene is in an area north of the Hudson Bay with a coverage of close pack ice in the eastern half of the image, some fast ice in its western parts and a well developed polynya in the lee of the coast / fast ice border

which – according toe Landsat contains a fairly large area of open water and also some thin ice.
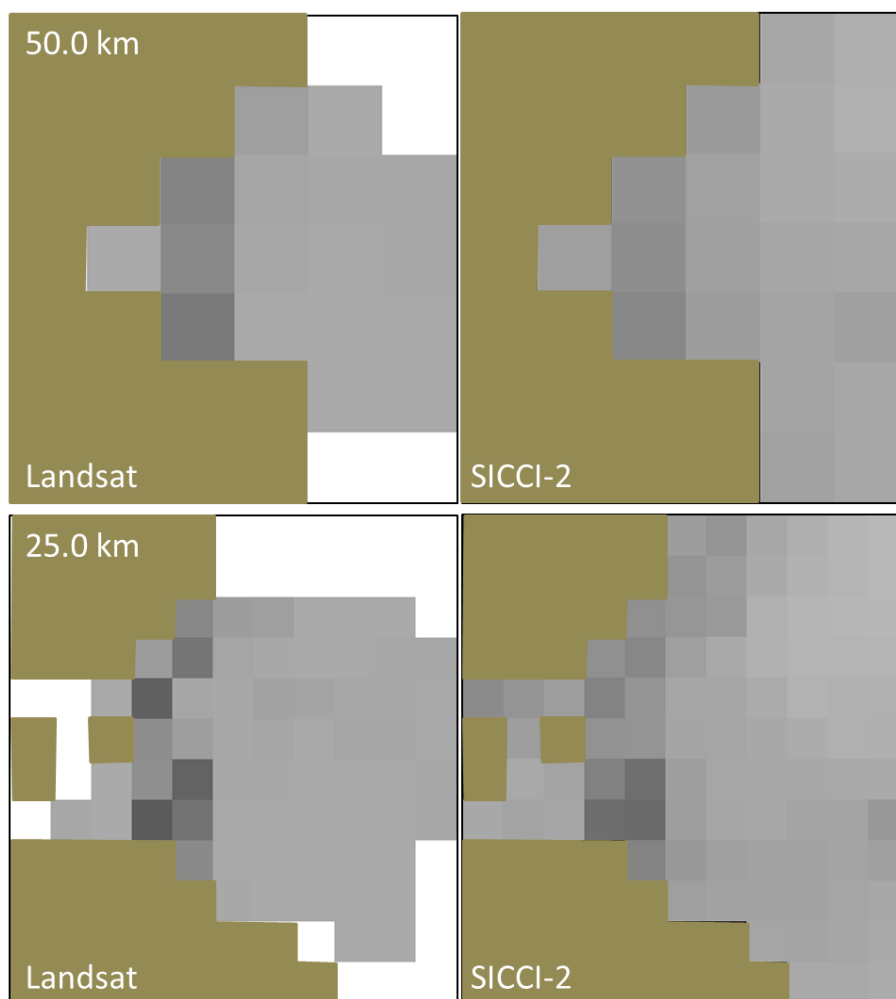
Figure 3-9: Inter-comparison of Landsat SIC (left) and SICCI-2 SIC (right) for SICCI-VLF (50.0 km) and SICCI-LF (25.0 km) for the example shown in Figure 3.3.1. Grid cells colored in olive denote land as given in the SICCI-2 product. White grid cells in the Landsat SIC maps denote no data. Brightest grey (black) grid cells in the Landsat maps denote SIC = 100% (SIC = 0%). Grid cells being brighter in the SICCI-2 maps denote SIC > 100%.

We find a relative good correspondence between Landsat SIC and SICCI-2 SIC data in Figure 3-9. The polynya shown in the left part of the classified Landsat image (Figure 3-8) is clearly visible in the Landsat SIC maps at all grid resolutions. Also all SICCI-2 SIC maps reveal a few to some grid cells with reduced SIC. None of the SICCI-2 maps provide an as low SIC as the Landsat SIC maps. We find more SIC variability in the pack ice east of the polynya in the SICCI-2 SIC maps than in the Landsat SIC maps. At 12.5 km grid resolution, we also observe a substantially sharper gradient in the Landsat SIC compared to the SICCI-2 SIC map.

The mean SIC computed for the maps in Figure 3-9 reveal that SICCI-HF SIC is about 2% larger than SICCI-LF and SICCI-VLF SIC which agree within 0.5% (Table 3-7). Interestingly, the mean Landsat SIC is largest when computed at 50.0 km grid resolution (94.9%) and smallest when computed

at 12.5 km grid resolution (93.8%). The same applies when using only the pixels classified as thick ice. We find that the Landsat SIC when limited to thick ice, LS thick SIC, is smaller by 5% to 6% than the regular Landsat SIC, which is based on all pixels classified as ice.
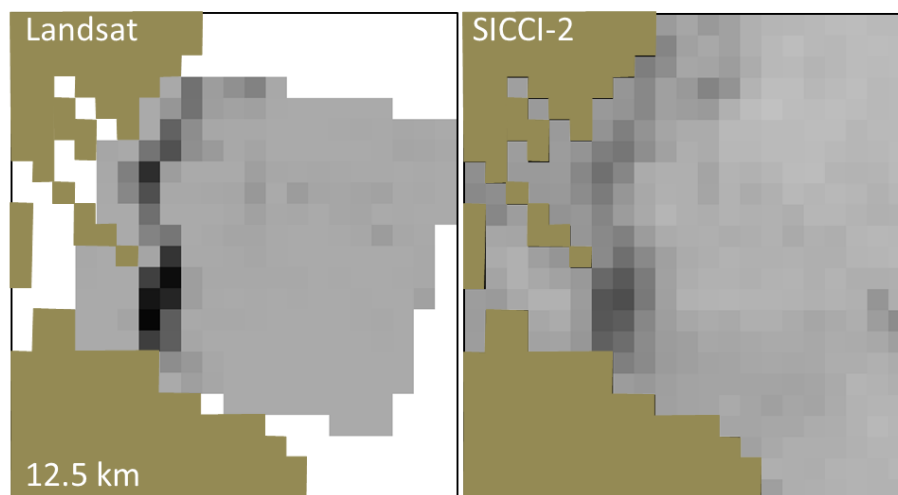
Figure 3-9 continued for SICCI-2 SIC of SICCI-HF (12.5 km).

Table 3-7: Summary of the results from Figure 3-9 (from top to bottom): mean sea-ice concentration (SIC) and its standard deviation (SIC SDEV); mean sea-ice concentration total error (SICCI only); number of grid cells with the respective grid resolution; SICCI-2 SIC (SICCI) minus Landsat SIC (LS); SICCI-2 SIC (SICCI) minus Landsat SIC limited to class thick ice only (LS thick). All quantities except N are given in %. Values were calculated only from those grid cells where both data sets have valid values.

	SICCI-VLF (50.0 km)			SICCI-LF (25.0 km)			SICCI-HF (12.5 km)		
	SICCI	LS	LS thick	SICCI	LS	LS thick	SICCI	LS	LS thick
SIC	93.8	94.9	89.5	94.1	94.5	88.8	96.4	93.8	87.7
SIC SDEV	6.1	9.0	14.6	9.8	11.0	17.2	12.3	16.3	22.7
SIC total error	11.1			13.3			12.5		
N	17			63			233		
SICCI minus LS		-1.1	+4.3		-0.4	+5.3		+2.6	+8.7

The difference SICCI-2 SIC minus LS SIC is smallest for SICCI-LF (-0.4%) and largest (and of different sign) for SICCI-HF (+2.6). The difference SICCI minus LS thick SIC is smallest for SICCI-VLF (+4.3%) and largest for SICCI-HF (+8.7%). We find, therefore, that the difference SICCI-2 SIC minus LS thick SIC is not smaller than SICCI-2 SIC minus LS SIC, which is kind of counter-intuitive. We would have expected that because of the notable thin ice fraction in this sample Landsat scene, the underestimation of the LS SIC by SICCI-2 SIC would be larger and that by using LS thick SIC this underestimation is reduced. This could be caused by a biased Landsat SIC value. A more detailed, grid cell-by-grid cell investigation is required for better understanding.
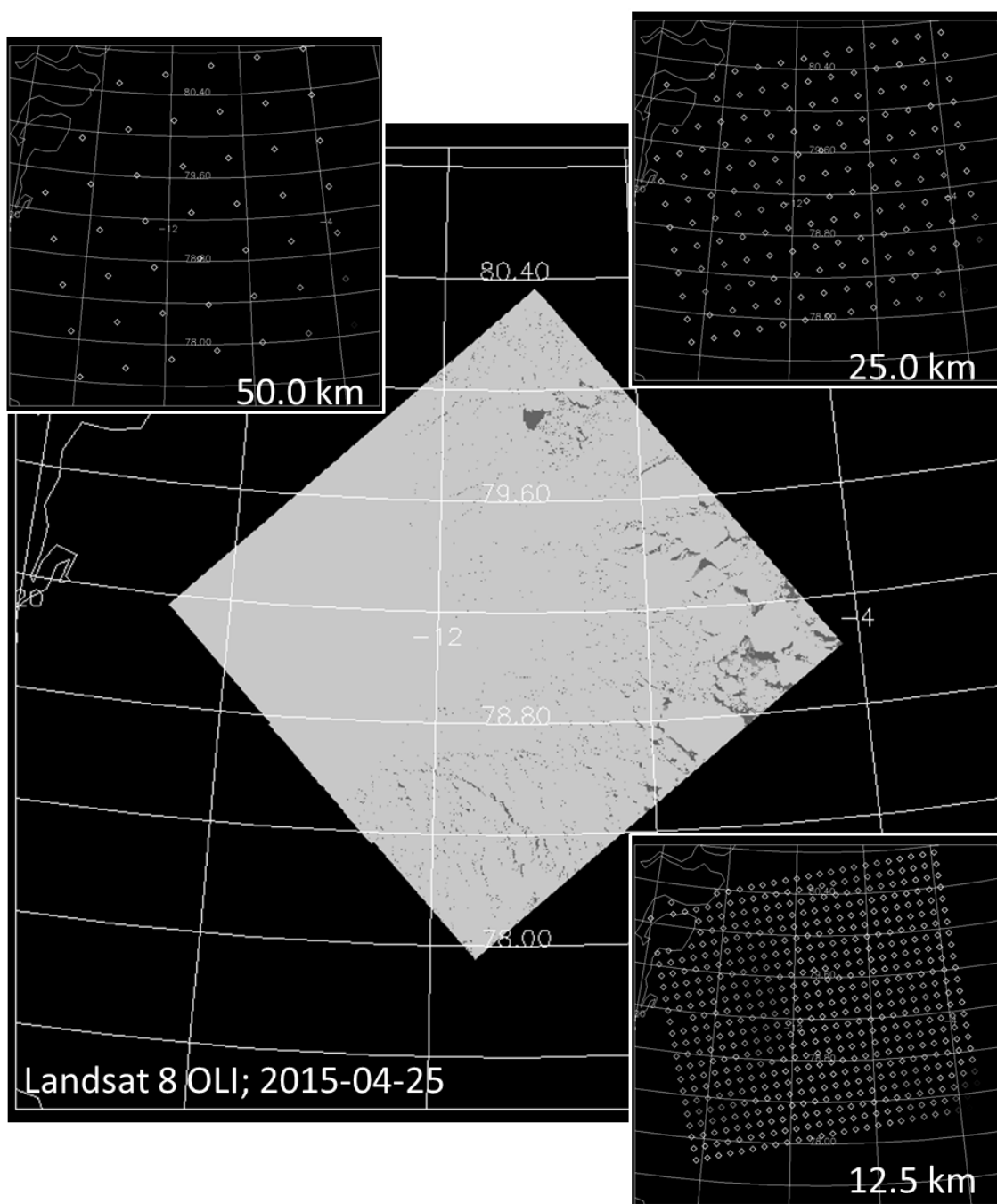
Figure 3-10: A classified Landsat-8 OLI image of April 25, 2015, east of Greenland close to the Fram Strait at 79°N, Northern Hemisphere, with the corresponding maps of the center coordinates of the three SICCI-2 algorithms denoted by their grid resolution. Colors dark grey, medium grey and light grey in the classified Landsat image denote open water, thin ice and thick ice, respectively. The color coding in the co-located SICCI-2 maps is the sea-ice concentration (compare Figure 3-11).

The example shown in Figure 3-10 represents a very close sea-ice cover in the West and a close sea-ice cover with few smaller leads and some openings in the East; several larger floes can be identified there.
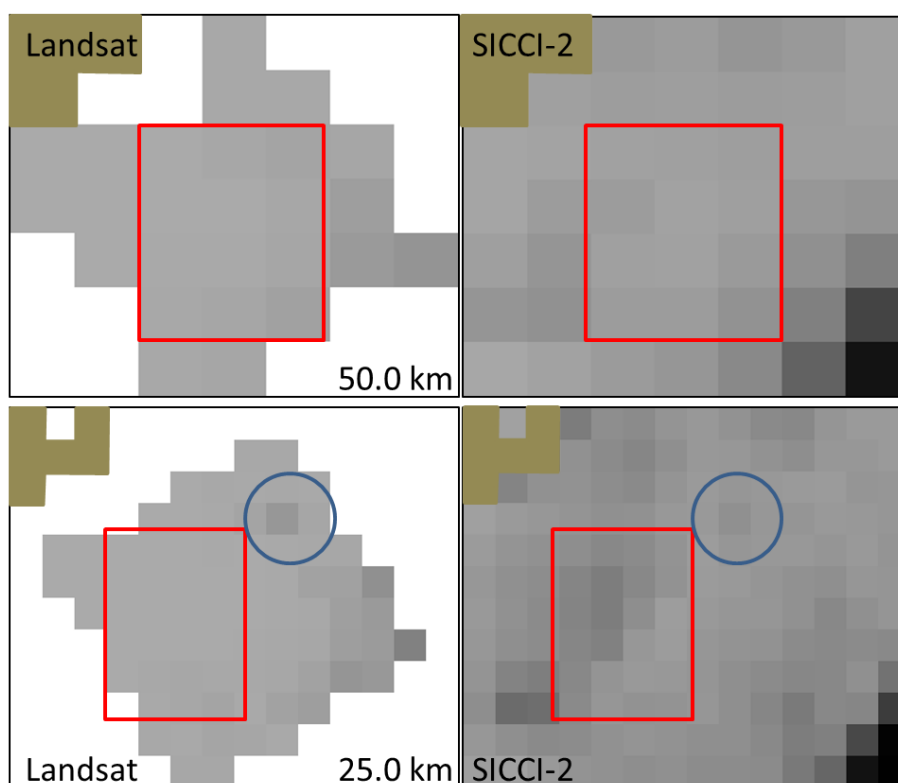
Figure 3-11: Inter-comparison of Landsat SIC (left) and SICCI-2 SIC (right) for SICCI-VLF (50.0 km) and SICCI-LF (25.0 km) for the example shown in Figure 3.3.4. Grid cells colored in olive denote land as given in the SICCI-2 product. White grid cells in the Landsat SIC maps denote no data. Brightest grey (black) grid cells in the Landsat maps denote SIC = 100% (SIC = 0%). Grid cells being brighter in the SICCI-2 maps denote SIC > 100%. For blue circle and red box see text.

The corresponding sea-ice concentration maps reveal substantial differences between the algorithm / products. At 50 km grid resolution both SIC data sets are quite similar and reveal almost no details – which is not surprising at that grid resolution (Figure 3-11, top). The red box focusing on the same areas in both images mostly confirms this view. At 25 km grid resolution a large part of the Landsat SIC maps is at SIC = 100%; only towards the east and in the region marked by the blue circle Landsat SIC drops below 100%.
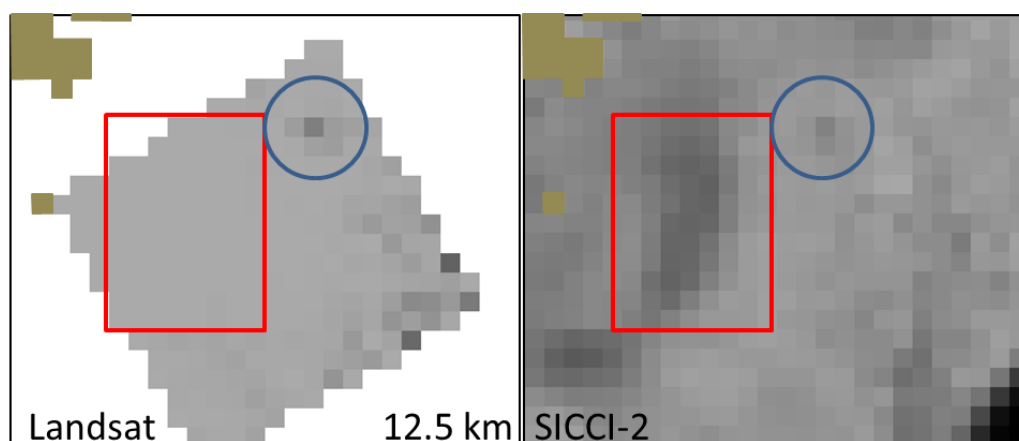
Figure 3-11 continued for SICCI-2 SIC of SICCI-HF (12.5 km).

One can identify the reduced SIC at this location also in the SICCI-LF SIC map (Figure 3-11 bottom) albeit with a higher SIC value. More interestingly is that within the red box variation in SICCI-LF SIC is much higher than variation in Landsat SIC – which is actually almost constant throughout that red box. Since the Landsat SIC is close to 100% in the red box, this variation in SICCI-LF SIC points towards an under-estimation of Landsat Sic by SICCI-LF. This is even more pronounced for SICCI-HF (Figure 3-11 continued). We find an elongated, north-south extending area of reduced SIC values in the red box in SICCI-HF but no indication of it in the Landsat SIC map. Both data sets do agree, however, in the location of the SIC drop in the blue circle.

Table 3-8: Summary of the results from Figure 3-11 (from top to bottom): mean sea-ice concentration (SIC) and its standard deviation (SIC SDEV); mean sea-ice concentration total error (SICCI only); number of grid cells with the respective grid resolution; SICCI-2 SIC (SICCI) minus Landsat SIC (LS); SICCI-2 SIC (SICCI) minus Landsat SIC limited to class thick ice only (LS thick). All quantities except N are given in %. Values were calculated only from those grid cells where both data sets have valid values.

	SICCI-VLF (50.0 km)			SICCI-LF (25.0 km)			SICCI-HF (12.5 km)		
	SICCI	LS	LS thick	SICCI	LS	LS thick	SICCI	LS	LS thick
SIC	91.4	97.7	96.2	85.1	97.6	96.1	83.3	97.8	96.3
SIC SDEV	4.6	3.2	4.6	4.2	4.1	5.6	9.1	5.0	6.7
SIC total error	12.8			9.4			13.0		
N	26			76			265		
SICCI minus LS		-6.3	-4.8		-12.5	-11.0		-14.5	-13.0

Table 3-8 reveals that for this example SICCI-2 SIC is underestimating Landsat SIC by ~6% (SICCI-VLF), ~12% (SICCI-LF) and ~15% (SICCI-HF). This under-estimation is not notably reduced (only by 1.5%) when using Landsat pixels with thick sea ice (LS thick SIC). In contrast, in the previous example this number was 5% to 6% (Table 3-7). The reason for this is the lower fraction of leads and openings in the sea-ice cover. We hypothesize

that the algorithm dependent increase in the observed under-estimation could be related to snow property changes to which the low-frequency channels used in SICCI-VLF are rather insensitive while the high-frequency channels (37 GHz and 89 GHz) are considerably more sensitive.

Figure 3-12 illustrates another example of that kind. The image used is located just north of the Canadadian Arctic Archipelago; actually it is north of the Prince Gustav Adolf Sea. The classified Landsat image shows a very close sea ice cover with only a few leads and possibly only ~0.5% of open water. The SIC map from SICCI-VLF is in line with that view. SICCI-LF already seems to provide some variation in the SIC which is not visible in the Landsat image and SIC values seem to be a bit lower than from SICCI-VLF. SICCI-HF, finally, offers substantially lower SIC values and also provides a lot of spatial variation in the SIC which is not in place in the Landsat image. Average over all co-located grid cells we obtain a Landsat SIC of 99.6% ± 1.2% at 12.5 km grid resolution and of 99.4% ± 1.1% (or 0.8%) at the other two resolutions. We obtain a SICCI-2 SIC of 96.4% ± 1.9% for SICCI-VLF and 95.8% ± 2.8% for SICCI-LF. Hence these two products can be termed to agree reasonably well with the Landsat SIC – particularly when taking into account that the thick sea-ice only Landsat SIC value is ~ 98.0%. We obtain an average SICCI-2 SIC value of 75.0% ± 6.1% for SICCI-HF. This is an under-estimation of more than 20%.
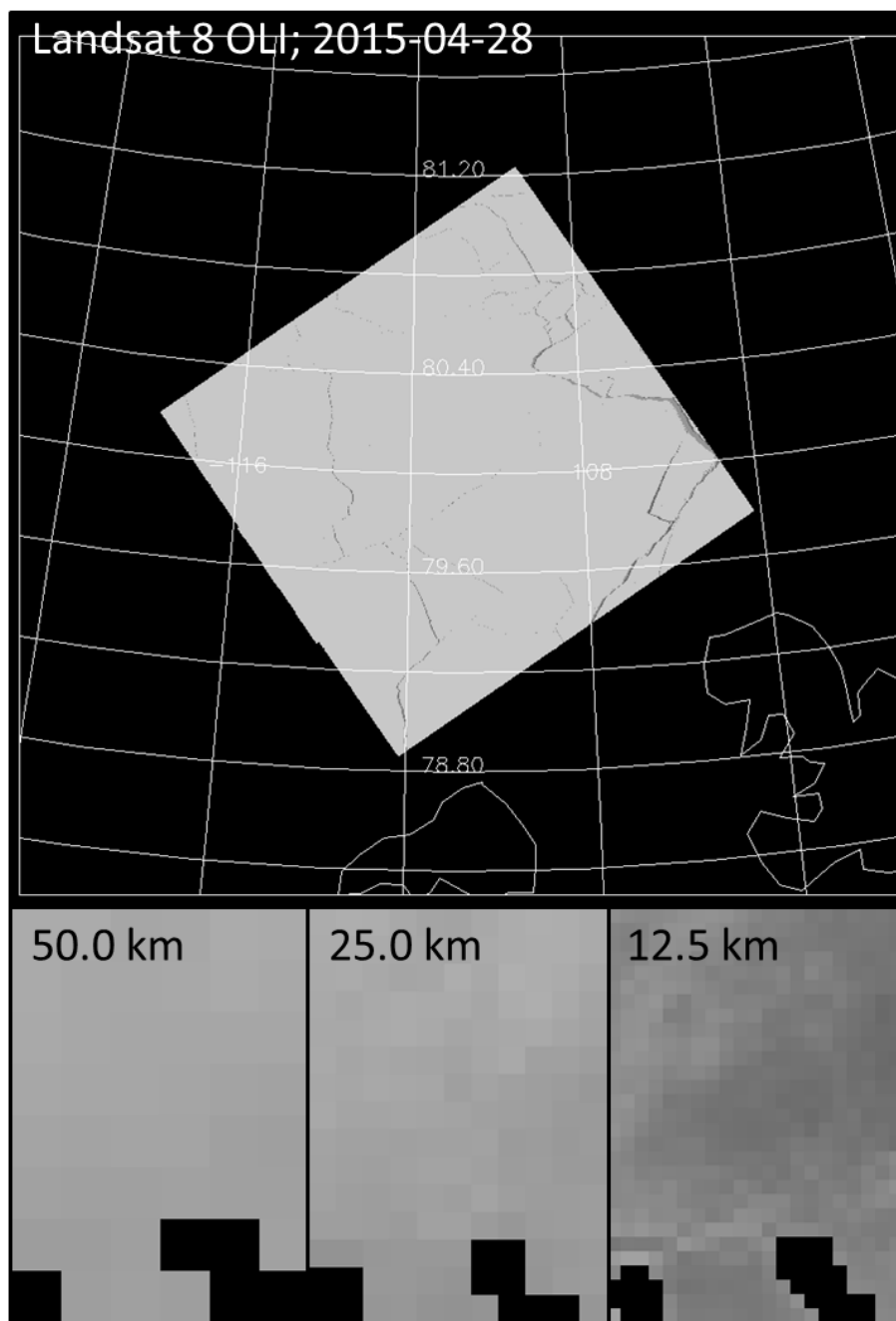
Figure 3-12: Classified Landsat-8 OLI image north of the Canadian Arctic Archipelago from April 28 2015 (top) with the co-located SICCI-2 SIC maps (bottom) for, from left to right, SICCI-LVF (50.0 km), SICCI-LF (25.0 km) and SICCI-HF (12.5 km). Colors in the Landsat image are like in Figure 3-8; colors in the SIC maps are like in Error! Reference source not found. **instead of that land is denoted black.**

In Figure 3-13 to Figure 3-15 and Table 3-9 and Table 3-10 we give the overview about the results of the inter-comparison between SICCI-2 SIC and Landsat SIC based on Landsat-5 TM images.
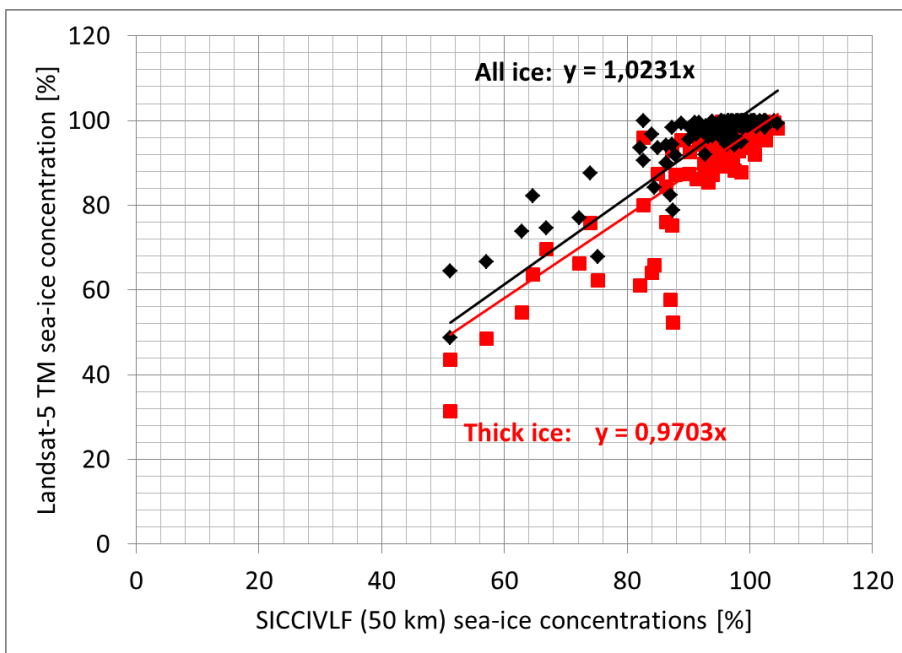
Figure 3-13: Summary scatterplot of Landsat SIC versus SICCI-VLF (50.0 km) SIC for the Northern Hemisphere for Landsat-5 TM images between 2003 and 2011. Data pairs, regression lines and equations with Landsat SIC are given in black, those with Landsat only thick ice SIC are given in red.
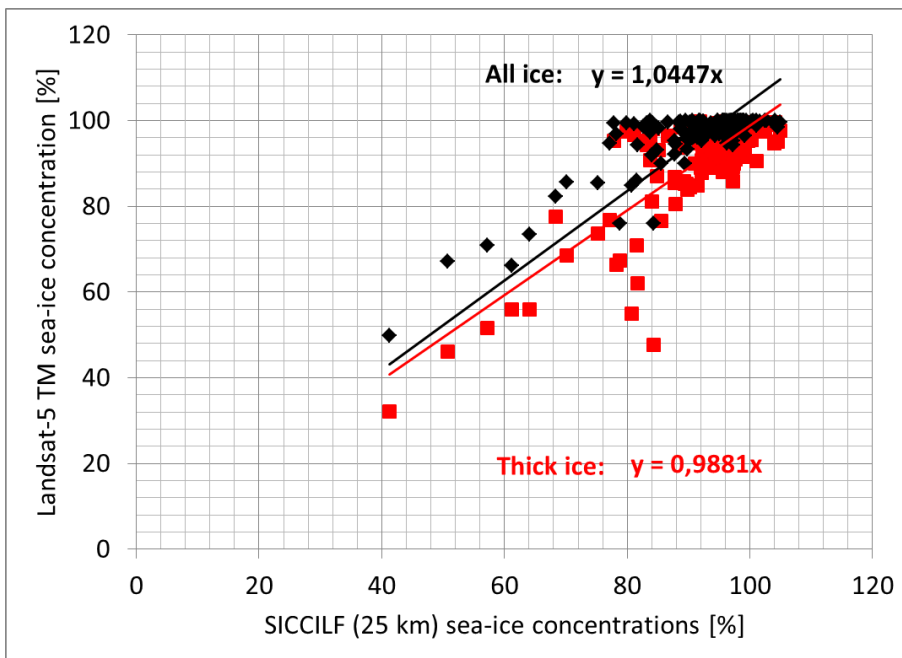
Figure 3-14: As Figure 3-13 but for SICCI-LF (25.0 km).

ESA UNCLASSIFIED - For Official Use
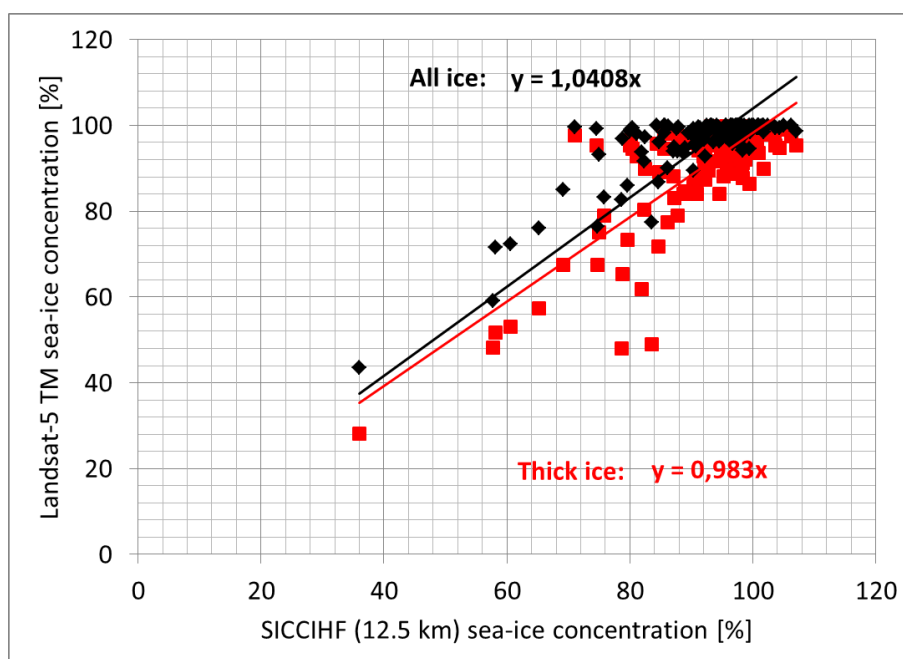
Figure 3-15: As Figure 3-13 but for SICCI-HF (12.5 km).

Table 3-9: Summary of results for the SIC for Landsat-5 TM (Figure 3-13 to Figure 3-15) for 134 images (from top to bottom): mean SIC and mean SIC standard deviation (SIC SDEV) for SICCI-2 (SICCI), Landsat (LS) and Landsat only thick ice (LS thick); mean sea-ice concentration total error (SICCI only); modal SIC values. All quantities are given in %.

	SICCI-VLF (50.0 km)			SICCI-LF (25.0 km)			SICCI-HF (12.5 km)		
	SICCI	LS	LS thick	SICCI	LS	LS thick	SICCI	LS	LS thick
SIC	93.8	96.2	90.8	91.6	96.2	90.5	91.8	96.1	90.3
SIC SDEV	6.9	8.4	11.8	8.6	9.0	13.1	9.4	10.1	14.7
SIC total error	9.1			9.8			10.3		
SIC mode	96.6	99.9	94.3	97.7	99.9	98.5	98.4	99.9	95.3

Table 3-10: Summary of results for the SIC differences for Landsat-5 TM (Figure 3-13 to Figure 3-15) for 134 images (from top to bottom): mean difference SICCI-2 SIC minus Landsat SIC (SICD) and its standard deviation (SICD SDEV) for Landsat (LS) and Landsat only thick ice (LS thick); modal SIC difference (SICD mode). All quantities are given in %. Smallest differences appear bold.

	SICCI-VLF (50.0 km)		SICCI-LF (25.0 km)		SICCI-HF (12.5 km)	
	LS	LS thick	LS	LS thick	LS	LS thick
SICD	**-2.4**	+3.0	-4.6	**+1.1**	-4.3	+1.5
SICD SDEV	4.3	6.2	5.7	7.2	6.3	8.0
SICD mode	**-1.4**	**-0.3**	-4.3	+3.7	-3.5	+2.1

We find a relatively good agreement between Landsat SIC and SICCI-2 SIC for these, in total, 134 Landsat images. Most of the data pairs tend to cluster close to SIC = 100%. We find that SICCI-2 values range between ~80% and ~105% for Landsat SIC > 95%. We observe that this range is smaller for SICCI-VLF (Figure 3-13) than for SICCI-LF (Figure 3-14) and SICCI-HF (Figure 3-15). Only few clear-sky Landsat images covered the sea-ice edge and/or the marginal ice zone and therefore we only have few data points at lower SIC values. Still, these align nicely along regression lines forced through (0,0) given together with the data pairs in each figure. The slopes of the regression lines are all quite close to one and range between 1.023 and 1.045 for Landsat SIC and between 0.970 and 0.988 when excluding thin ice (Landsat thick SIC). The slopes suggest that the agreement between Landsat SIC and SICCI-2 SIC improves for SICCI-LF and SICCI-HF when using Landsat thick SIC (red symbols and lines); the slopes are closer to one.

Table 3-9 summarizes the results as absolute values while Table 3-10 summarizes the differences. We find that SICCI-VLF has the smallest difference SICCI-2 SIC minus Landsat SIC: -2.4%, while SICCI-LF has the largest one: -4.6%; SICCI-HF is similar to SICCI-LF. We find further that when excluding thin ice, i.e. LS thick, then the smallest difference SICCI-2 minus Landsat thick ice SIC is obtained for SICCI-LF: +1.1%, while the largest difference is obtained for SICCI-VLF: +3.0%; again SICCI-HF provides a result similar to SICCI-LF. If we look at the mode of the difference SICCI-2 SIC minus Landsat SIC, then in both cases, LS and LS thick, SICCI-VLF provides the smallest values: -1.4% and -0.3%, respectively. Respective values are notably larger for the other two algorithms (Table 3-10). The tables confirm our view from the figures. These are the results for Landsat-5.

Table 3-11: Summary of results for the SIC for Landsat-7 ETM for 12 images (from top to bottom): mean SIC and mean SIC standard deviation (SIC SDEV) for SICCI-2 (SICCI), Landsat (LS) and Landsat only thick ice (LS thick); mean sea-ice concentration total error (SICCI only). All quantities are given in %.

	SICCI-VLF (50.0 km)			SICCI-LF (25.0 km)			SICCI-HF (12.5 km)		
	SICCI	LS	LS thick	SICCI	LS	LS thick	SICCI	LS	LS thick
SIC	94.1	96.8	92.5	95.4	96.5	91.9	97.1	96.7	92.1
SIC SDEV	7.8	5.8	8.4	8.8	8.5	11.8	9.0	9.9	13.5
SIC total error	8.8			8.7			9.3		

Table 3-12: Summary of results for the SIC differences for Landsat-7 ETM for 12 images (from top to bottom): mean difference SICCI-2 SIC minus Landsat SIC (SICD) and its standard deviation (SICD SDEV) for Landsat (LS) and Landsat only thick ice (LS thick); modal SIC difference (SICD mode). All quantities are given in %. Smallest differencess appear bold.

	SICCI-VLF (50.0 km)		SICCI-LF (25.0 km)		SICCI-HF (12.5 km)	
	LS	LS thick	LS	LS thick	LS	LS thick
SICD	-2.7	**+1.7**	-1.1	+3.5	**+0.4**	+5.0
SICD SDEV	5.9	4.6	4.8	4.6	6.0	5.9

Results obtained from the inter-comparison with LS and LS thick using Landsat-7 ETM images shown in Table 3-11 (absolute values) and Table 3-12 (SIC differences) are slightly different from those obtained for Landsat-5. The difference SICCI-2 SIC minus Landsat SIC is largest for SICCI-VLF: -2.7% and smallest for SICCI-HF: +0.4% with SICCI-LF being right between the other two. This is how it is supposed to be. Limiting the Landsat SIC to the thick ice pixels (LS thick) provides the smallest difference for SICCI-VLF: +1.7% and the largest one for SICCI-HF: +5.0%. Note, however, that these numbers are based on only 12 Landsat images.

The results from the inter-comparison with Landsat SIC based on Landsat-8 OLI images shown in Figure 3-16 through Figure 3-18 and Table 3-13 and 3.3.10 confirm the results obtained for Landsat-5 with regard to regression line slopes.
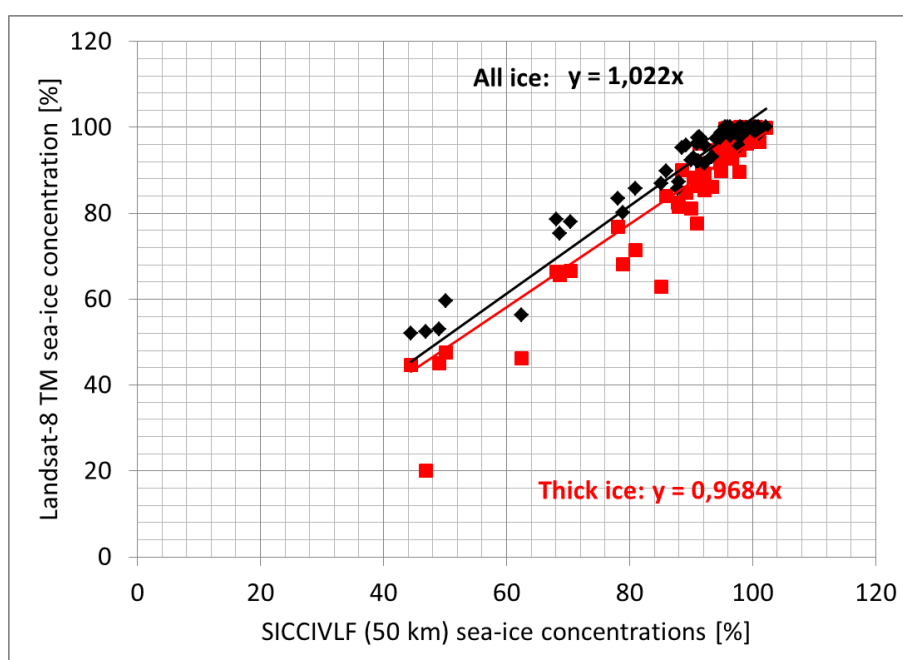
Figure 3-16: Summary scatterplot of Landsat SIC versus SICCI-VLF (50.0 km) SIC for the Northern Hemisphere for Landsat-8 OLI images between 2013 and 2015. Data pairs, regression lines and equations with Landsat SIC are given in black, those with Landsat only thick ice SIC are given in red.

For SICCI-VLF, the slope of the linear regression between Landsat SIC and SICCI-2 SIC is closer to one when not limiting the investigation to thick ice Landsat pixels (Figure 3-16): 1.022 versus 0.968. In contrast, for SICCI-LF and SICCI-HF the respective slope is closer to one when only using the thick ice Landsat pixels: 1.036 versus 0.980 (Figure 3-17) and 1.042 versus 0.985 (Figure 3-18), respectively.

For SICCI-HF we observe a substantially larger spread of SICCI-2 SIC for Landsat SIC > 95%: ~62% to ~115% (Figure 3-18) - as can be expected already from the examples shown in Figure 3-11 and Figure 3-12. This spread is much smaller for SICCI-LF (Figure 3-17) and particularly SICCI-VLF (Figure 3-16). It is also obvious that for SICCI-VLF, when using all Landsat SIC data the data pairs are located closer to the regression line than when excluding thin ice.
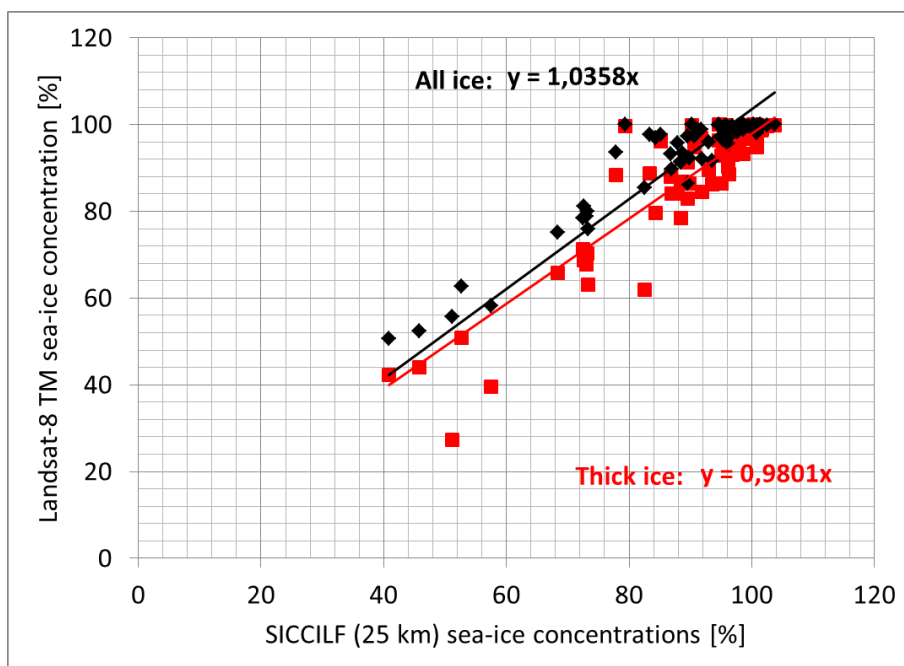
Figure 3-17: As Figure 3-16 but for SICCI-LF (25.0 km).
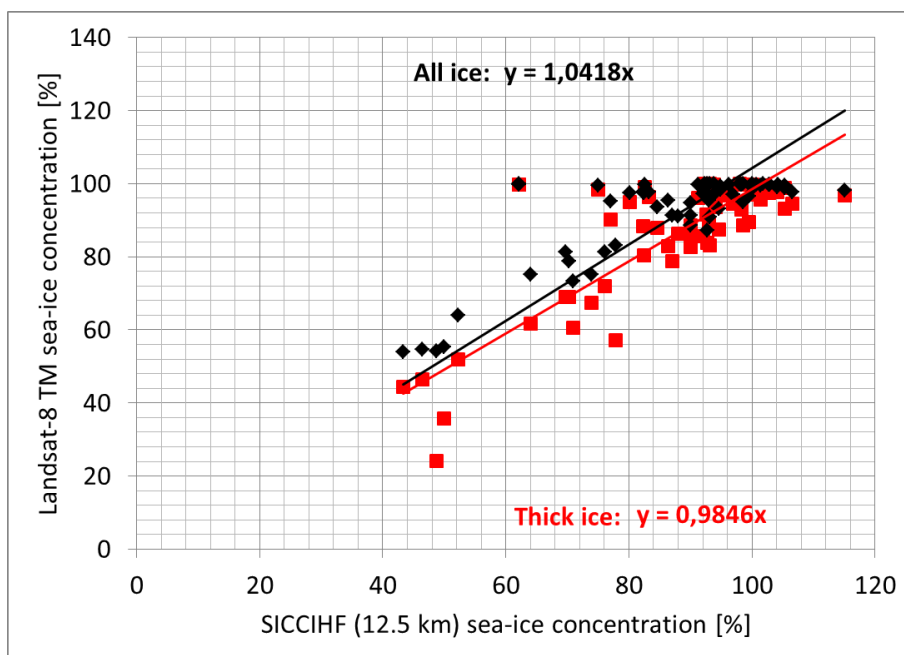
Figure 3-18: As Figure 3-16 but for SICCI-HF (12.5 km).

Table 3-13: Summary of results for the SIC for Landsat-8 OLI (Figure 3-16 to Figure 3-18) for 63 images (from top to bottom): mean SIC and mean SIC standard deviation (SIC SDEV) for SICCI-2 (SICCI), Landsat (LS) and Landsat only thick ice (LS thick); mean sea-ice concentration total error (SICCI only); modal SIC values. All quantities are given in %.

	SICCI-VLF (50.0 km)			SICCI-LF (25.0 km)			SICCI-HF (12.5 km)		
	SICCI	LS	LS thick	SICCI	LS	LS thick	SICCI	LS	LS thick
SIC	89.9	92.2	86.7	88.4	92.0	86.4	87.1	92.0	86.2
SIC SDEV	12.0	13.6	15.0	13.4	15.0	16.8	13.8	16.1	18.2
SIC total error	11.4			11.4			12.0		
SIC mode	100.3	100.0	99.8	96.8	100.0	99.8	90.1	99.8	99.8

Table 3-14: Summary of results for the SIC differences for Landsat-8 OLI (Figure 3-16 to Figure 3-18) for 63 images (from top to bottom): mean difference SICCI-2 SIC minus Landsat SIC (SICD) and its standard deviation (SICD SDEV) for Landsat (LS) and Landsat only thick ice (LS thick); modal SIC difference (SICD mode). All quantities are given in %. Smallest difference values are given in bold font.

	SICCI-VLF (50.0 km)		SICCI-LF (25.0 km)		SICCI-HF (12.5 km)	
	LS	LS thick	LS	LS thick	LS	LS thick
SICD	**-2.3**	+3.3	-3.7	+2.0	-4.9	**+0.9**
SICD SDEV	3.2	5.5	4.9	6.6	9.3	10.8
SICD mode	**+1.0**	**+1.5**	-2.9	+1.9	-5.3	+5.3

SICCI-HF provides the smallest overall mean SIC value: ~87% compared to ~90% for SICCI-VLF (Table 3-13) – which still seems surprisingly close to each other in the light of Figure 3-11 and Figure 3-12, where SICCI-HF is shown to under-estimate Landsat SIC considerably, but which is reasonable when taking into account the spread in SIC at high Landsat SIC mentioned above in the context of Figure 3-18.

The overall mean difference SICCI-2 SIC minus Landsat SIC is smallest for SICCI-VLF: -2.3% and largest for SICCI-HF: -4.9% while SICCI-LF is between the two (Table 3-14); under-estimation of Landsat SIC is largest for the high resolution, high-frequency algorithm. When excluding thin ice, i.e. using LS thick, the picture reverses: SICCI-VLF has the largest difference and over-estimates LS thick SIC by 3.3%, SICCI-HF has the smallest difference and over-estimates LS thick SIC by 0.9%, and SICCI-LF is between the two (Table 3-14). If we look at the mode of the difference SICCI-2 SIC minus Landsat SIC, then in both cases, LS and LS thick, SICCI-VLF provides the smallest values: +1.0% and +1.5%, respectively. Respective values are larger for the other two algorithms, especially for SICCI-HF (Table 3-14).

For a concluding statement we suggest to keep out the results obtained for the few Landsat-7 ETM images. For both, Landsat-5 and Landsat-8, we find that the overall mean difference SICCI-2 SIC minus Landsat SIC is smallest for SICCI-VLF. It is around -2%, suggesting a slight under-estimation. This under-estimation is a bit larger for the other two algorithms: -3% to -5%. Limiting the inter-comparison to thick ice Landsat pixels result in a reduction of the overall mean Landsat SIC by ~5%. This has to be understood in the sense that the average area fraction of thick ice in the Landsat equivalent of the co-located SICCI-2 SIC grid cells is ~5% smaller than the average area fraction of thin plus thick ice. Or, in other words, the average thin ice area

fraction is 5%. When we compare the SICCI-2 SIC to the Landsat thick ice SIC we can expect and actually observe a change in the difference SICCI-2 SIC minus Landsat SIC which corresponds to this 5% change: SICCI-VLF over-estimates Landsat SIC by ~3% while the other two algorithms over-estimate Landsat SIC by 0% to 2%.

Our interpretation of this result is as follows: SICCI-VLF uses a frequency combination which is most sensitive to thin ice, followed by SICCI-LF and then SICCI-HF. For SICCI-HF the smallest sensitivity to the presence of thin ice can be expected. For a considerable thin ice fraction we can expect that SICCI-VLF under-estimates Landsat SIC *more* than SICCI-LF and SICCI-HF. The fact that this is not the case suggests that *other reasons than thin ice* are responsible for the observed under-estimation – as for instance snow or sea-ice property changes causing a reduction in surface emissivity at the higher frequencies (see Figure 3-11 and Figure 3-12).

We note that it is completely fine, that SICCI-VLF (and the other two algorithms) over-estimates Landsat SIC when limited to the thick ice pixels only, because the SIC retrieved by the SICCI-2 algorithms over the sea-ice area fraction excluded from the Landsat data is not zero. It is just reduced by a certain amount which is a function of the thin sea-ice thickness and which is the smaller the thicker the thin sea ice is. We therefore find that SICCI-VLF SIC possibly agrees better with Landsat SIC than SICCI-LF and SICCI-HF do and take the results of this comparison as a hint that SICCI-LF and particularly SICCI-HF in fact under-estimate Landsat SIC during months March through May in the Northern Hemisphere – at least for the subset of Landsat images used. If we assume that SICCI-HF is not sensitive to the presence of thin ice at all, then this under-estimation amounts ~4.5%.

Southern Hemisphere

In this section we present the results obtained for the Southern Hemisphere. These rely exclusively on Landsat-8 OLI images (2013-2015). In contrast to the results from the Northern Hemisphere the Landsat images are mostly from the spring / summer season (see Table 3-15).

Table 3-15: Number N of Landsat images per month used for the Southern Hemisphere.

Month	October	November	December	March	April
N	27	31	37	5	2

Figure 3-19 shows a classified sample Landsat-8 OLI image together with the co-located SICCI-2 SIC product grid orientations and locations from the southwestern Weddell Sea. The Landsat image is dominated by the Ronne-Filcher Ice Shelf polynya off the Ronne-Filcher Ice Shelf visible in the classified Landsat scene by a band with some open water along the ice shelf, followed by a broad band of thin ice before in quite some distance to the ice shelf thick ice kicks in. The bright grey signatures at the southern and western edges of the scene denote the ice shelf and/or also landfast sea ice cover. The coloring of the diamonds in the maps already suggests reduced SIC values in the polynya area.
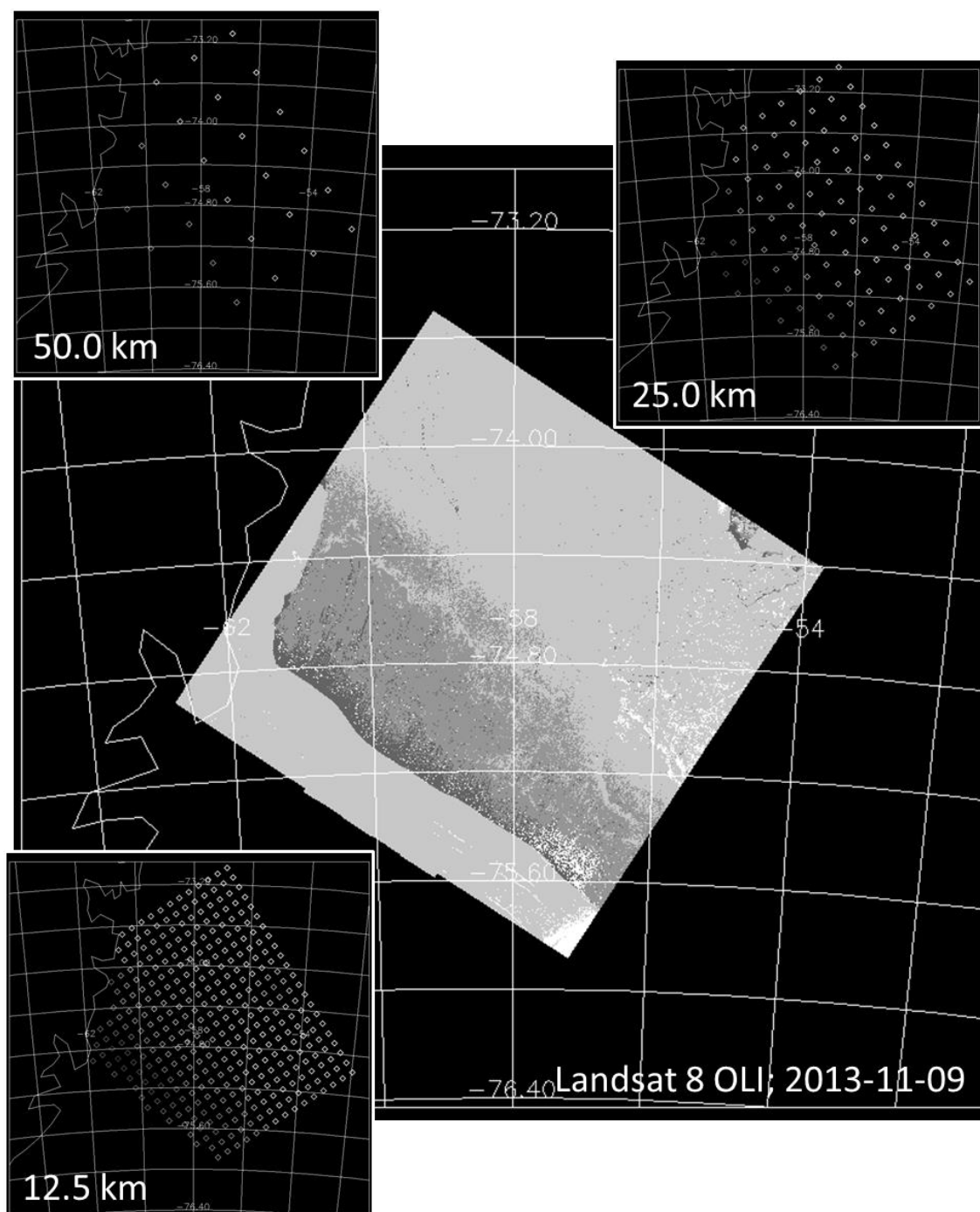
Figure 3-19: A classified Landsat-8 OLI image of November 9, 2013, southwestern Weddell Sea, Southern Hemisphere, with the corresponding maps of the center coordinates of the three SICCI-2 algorithms denoted by their grid resolution. Colors dark grey, medium grey and light grey in the classified Landsat image denote open water, thin ice and thick ice, respectively. The color coding in the co-located SICCI-2 maps is the sea-ice concentration (compare Figure 3-20).
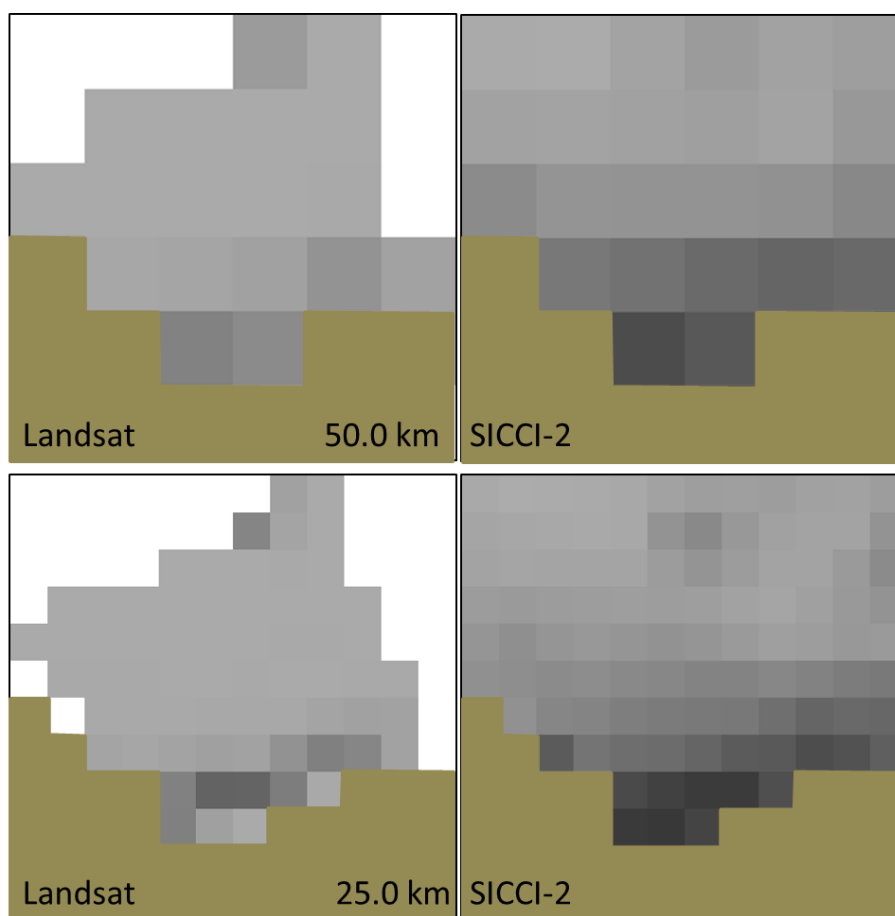
Figure 3-20: Inter-comparison of Landsat SIC (left) and SICCI-2 SIC (right) for SICCI-VLF (50.0 km) and SICCI-LF (25.0 km) for the example shown in Figure 3-19. Grid cells colored in olive denote land as given in the SICCI-2 product. White grid cells in the Landsat SIC maps denote no data. Brightest grey (black) grid cells in the Landsat maps denote SIC = 100% (SIC = 0%). Grid cells being brighter in the SICCI-2 maps denote SIC > 100%. Black denotes SIC = 0%.

In all three SIC products, the presence and location of the Ronne-Filchner Ice Shelf polynya can be clearly seen by means of an area of reduced SIC in the bottom half of the map stretching along the coast line. We note two things. First, SICCI-2 SIC tends to be lower than the Landsat SIC for SICCI-VLF and SICCI-LF not only in the "core" of the polynya but also further off the ice shelf border / coast line. For SICCI-HF, SIC values are as low as Landsat SIC. While there is a sharp SIC gradient in the Landsat SIC (Figure 3-20, bottom and continued), the transition in the SIC away from the ice shelf / coast line is more smooth for the SICCI-2 SIC data – particularly for SICCI-HF. It also seems as if SICCI-2 SIC hardly reaches to the high sea-ice concentration values visible in most Landsat SIC grid cells. Secondly, there seems to be a mismatch between the land mask used for the SICCI-2 SIC products and the actual border of the Ronne-Filcher Ice Shelf – which can be clearly seen in the Landsat SIC map as a 1-2 grid-cells wide region of SIC = 100% just south of the polynya (Figure 3-20 continued). This suggests that the land mask used is off by 1-2 grid cells, i.e. 12.5 km to 25.0 km. This mismatch area is not excluded from the inter-comparison between SICCI-2 SIC and Landsat SIC in Table 3-16. None such mismatch areas are excluded

from the inter-comparison in general, i.e. are included in the results shown in Table 3-18 and Table 3-19. For the example shown in Figure 3-20 and Table 3-16 this results in an under-estimation of Landsat SIC by SICCI-2 SIC by between ~17% (SICCI-VLF) and ~22% (SICCI-HF). But it is clearly evident from Figure 3-20 that even when excluding that region all three algorithms are under-estimating Landsat SIC. It seems to be justified to assume as well that this under-estimation is largest for SICCI-HF and smallest for SICCI-VLF. Limiting the inter-comparison to Landsat thick ice pixels brings SICCI-2 and Landsat SIC into an agreement similar to what is observed for the Northern Hemisphere (see Table 3-10 and Table 3-14).
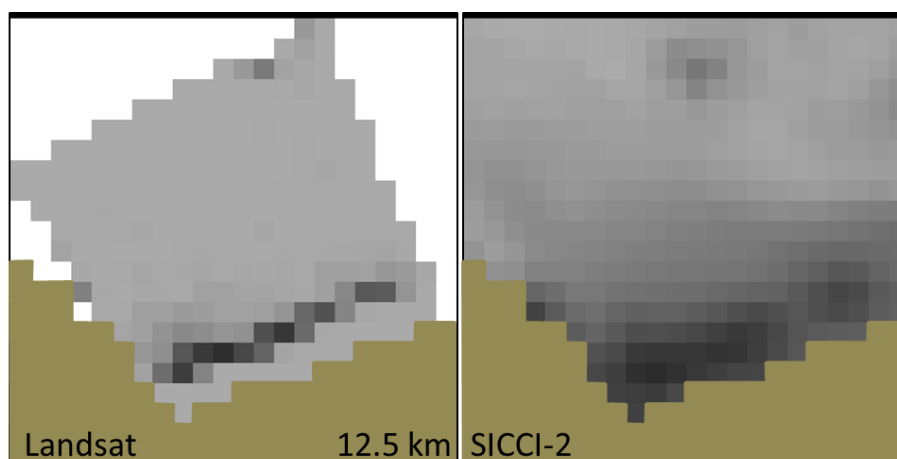
Figure 3-20 continued for SICCI-HF (12.5 km)

Table 3-16: Summary of the results from Figure 3-20 (from top to bottom): mean sea-ice concentration (SIC) and its standard deviation (SIC SDEV); mean sea-ice concentration total error (SICCI only); number of grid cells with the respective grid resolution; SICCI-2 SIC (SICCI) minus Landsat SIC (LS); SICCI-2 SIC (SICCI) minus Landsat SIC limited to class thick ice only (LS thick). All quantities except N are given in %. Values were calculated only from those grid cells where both data sets have valid values.

	SICCI-VLF (50.0 km)			SICCI-LF (25.0 km)			SICCI-HF (12.5 km)		
	SICCI	LS	LS thick	SICCI	LS	LS thick	SICCI	LS	LS thick
SIC	78.4	95.5	74.7	75.0	95.2	72.8	72.6	95.0	72.1
SIC SDEV	16.6	7.1	29.7	19.0	9.6	35.6	19.6	12.8	38.0
SIC total error	24.5			19.8			13.3		
N	18			65			245		
SICCI minus LS		-17.1	+3.7		-20.2	+2.2		-22.4	+0.5

ESA UNCLASSIFIED - For Official Use
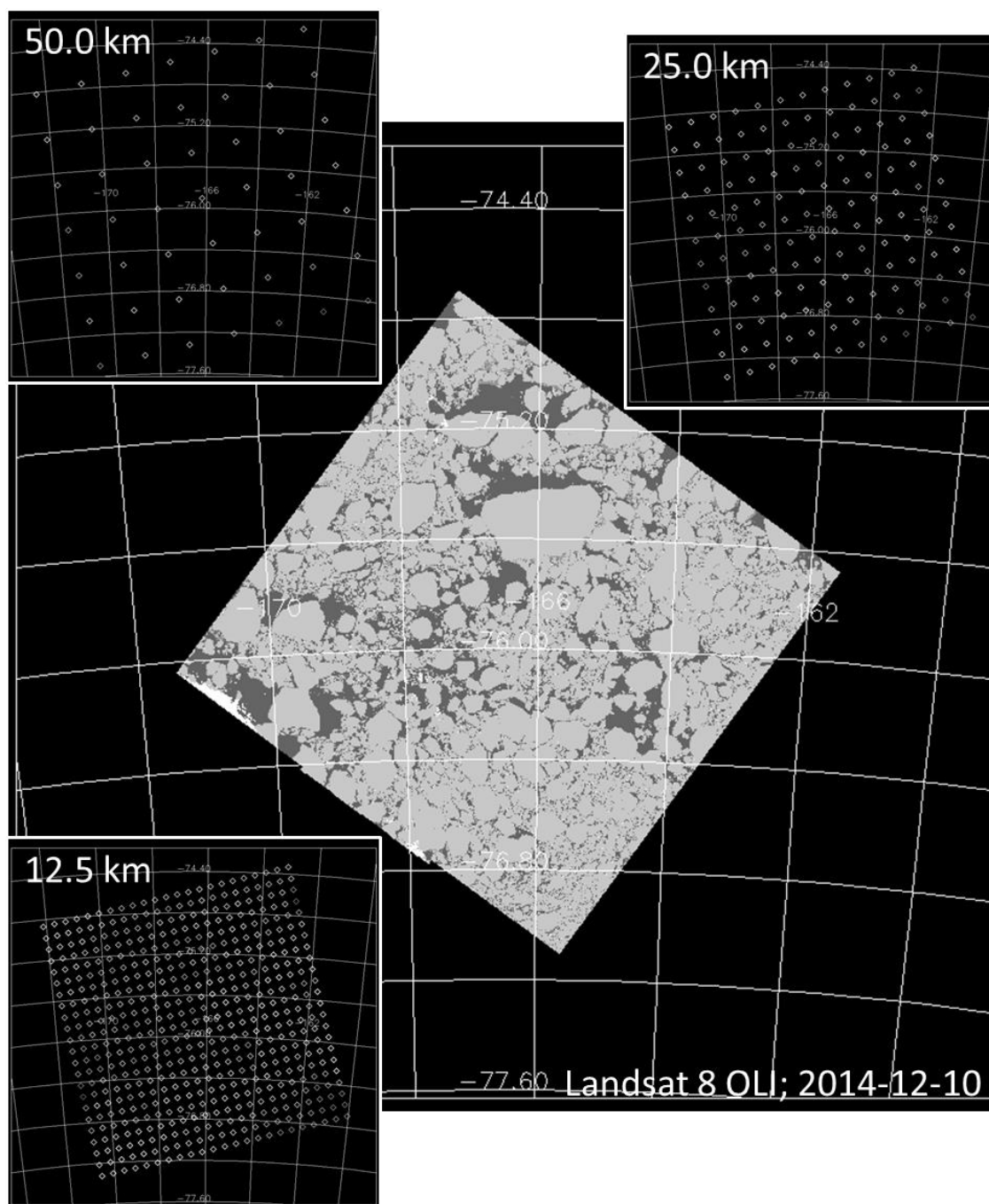
Figure 3-21: A classified Landsat-8 OLI image of December 10, 2014, Ross Sea, Southern Hemisphere, with the corresponding maps of the center coordinates of the three SICCI-2 algorithms denoted by their grid resolution. Colors dark grey, medium grey and light grey in the classified Landsat image denote open water, thin ice and thick ice, respectively. The color coding in the co-located SICCI-2 maps is the sea-ice concentration (compare Figure 3-22). White patches in the Landsat image denote cloudy areas excluded from the analysis.

The example shown in Figure 3-21 is from December 10, i.e. during early summer, from the Ross Sea. Classes thick ice and open water dominate the

classified Landsat image; in fact the thin ice fraction is still ~5% (see Table 3-17). The sea-ice cover is open to close with a considerable open water fraction between the floes. Certaintly there is almost no new ice formation – in contrast to Figure 3-19.
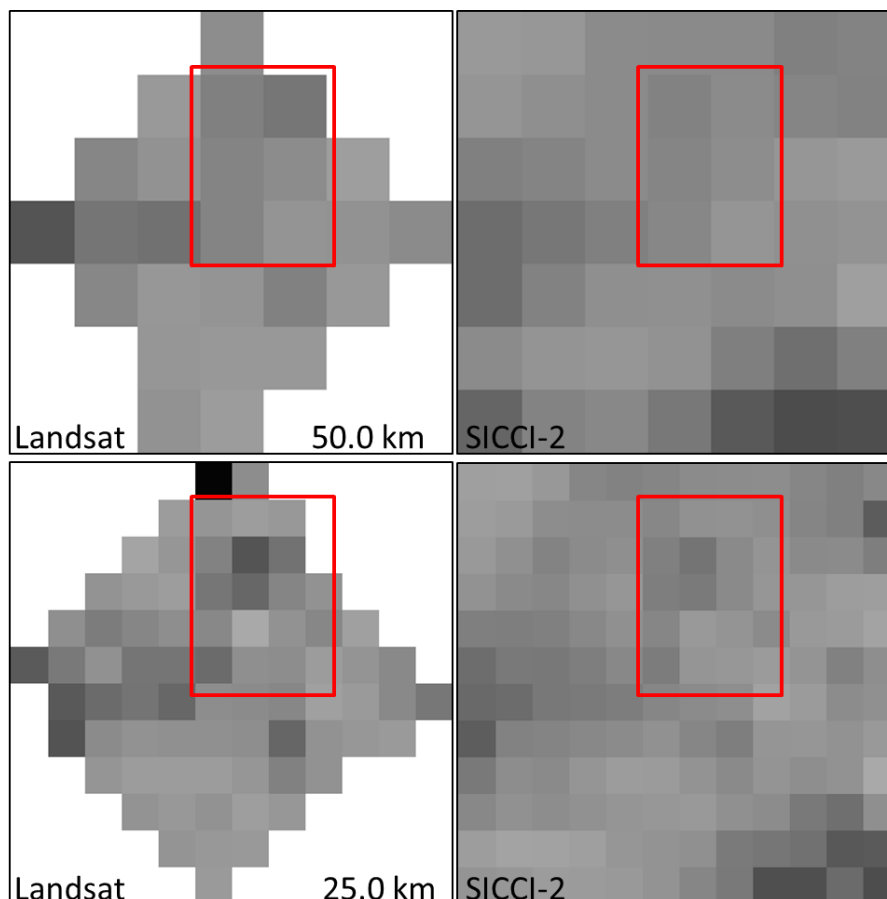
Figure 3-22: Inter-comparison of Landsat SIC (left) and SICCI-2 SIC (right) for SICCI-VLF (50.0 km) and SICCI-LF (25.0 km) for the example shown in Figure 3-21. White grid cells in the Landsat SIC maps denote no data. Brightest grey (black) grid cells in the Landsat maps denote SIC = 100% (SIC = 0%). Grid cells being brighter in the SICCI-2 maps denote SIC > 100%. Black denotes SIC = 0%. See text for the red boxes.

In the pairs of SIC maps shown in Figure 3-22 it is very difficult to find matching grid cells. There are certain patterns which seem to be the same in both SIC maps – like those highlighted by the red boxes. These patterns seem to be more clear in the Landsat SIC map than in the SICCI-2 SIC map and also have a larger range in SIC values occurring within, e.g., the red box. This is particularly evident for SICCI-HF (Figure 3-22 continued). Still, the grid resolution of the SICCI-HF product is sufficiently fine to resolve SIC gradients as associated with the vast ice floe at 75.6°S / 166°W (Figure 3-21) and the surrounding open water areas. But while the Landsat SIC indeed go down ~0% in one grid cell north of this vast ice floe SICCI-HF SIC values tend to stay at ~50%. On that ice floe itself SICCI-HF is ~ 100%, though. The other two products are far away from resolving these small-scale SIC variations and even the Landsat SIC maps produced at the respective grid resolutions 25.0 km and 50.0 km (Figure 3-22, left) do only

give a relatively poor representation of the actual SIC variations. However, the "counting" of 30 m x 30 m pixels preserves these variations still much better than the corresponding SICCI-2 SIC products.
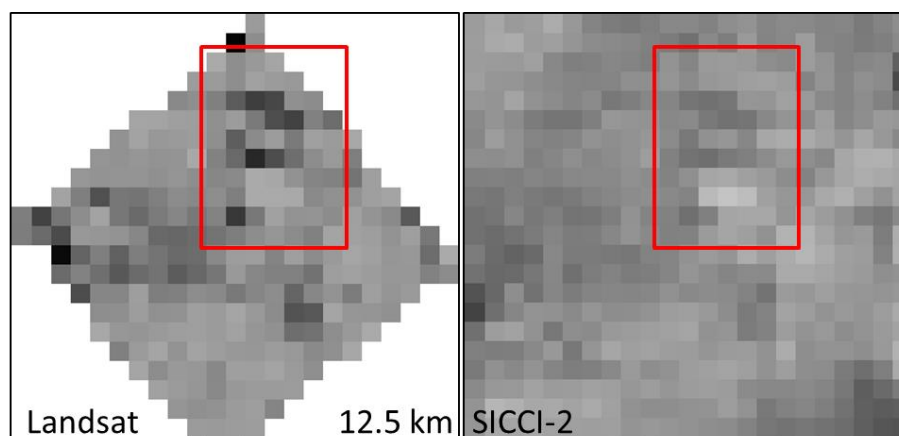
Figure 3-22 continued for SICCI-HF (12.5 km).

Table 3-17: Summary of the results from Figure 3-22 (from top to bottom): mean SIC (SIC) and its standard deviation (SIC SDEV); mean SIC total error (SICCI only); number of grid cells with the respective grid resolution; SICCI-2 SIC (SICCI) minus Landsat SIC (LS); SICCI-2 SIC (SICCI) minus Landsat SIC excluding thin ice (LS thick). All quantities except N are given in %. Values were calculated only from those grid cells where both data sets have valid values.

	SICCI-VLF (50.0 km)			SICCI-LF (25.0 km)			SICCI-HF (12.5 km)		
	SICCI	LS	LS thick	SICCI	LS	LS thick	SICCI	LS	LS thick
SIC	80.3	81.4	76.6	81.8	80.2	75.4	84.0	81.1	76.5
SIC SDEV	5.9	9.8	9.4	6.8	14.7	14.1	9.9	15.4	15.5
SIC total error	17.3			15.4			18.9		
N	26			75			270		
SICCI minus LS		-1.1	+3.7		+1.6	+6.4		+2.9	+7.5

Table 3-17 illustrates that overall SICCI-VLF SIC is closest to the Landsat SIC, under-estimating it by ~ 1%, while SICCI-HF over-estimates Landsat SIC by ~3% - which agrees with the impression of Figure 3-22 continued. According to these results the thin ice fraction in the classified Landsat image is ~5%. We note that at this time of the year it could also well be the case, that what the classification sees as thin ice is in fact a coverage of brash ice / sub-pixel size melting ice floes which altogether result in an albedo typical for thin ice but might actually be composed of sea ice substantially thicker than the anticipated 0.2 m limit associated with the albedo threshold of 0.4 for snow-free thin ice. This needs to be kept in mind for the interpretation of Figure 3-23 through Figure 3-25 and Table 3-18 and Table 3-19.

The scatterplots Landsat SIC versus SICCI-2 SIC shown in Figure 3-23 through Figure 3-25 are similar in terms of the obtained linear regression line slopes, the clustering of points close to 100% and/or along the regression line as well as the larger spread at Landsat SIC > 95% for SICCI-HF.
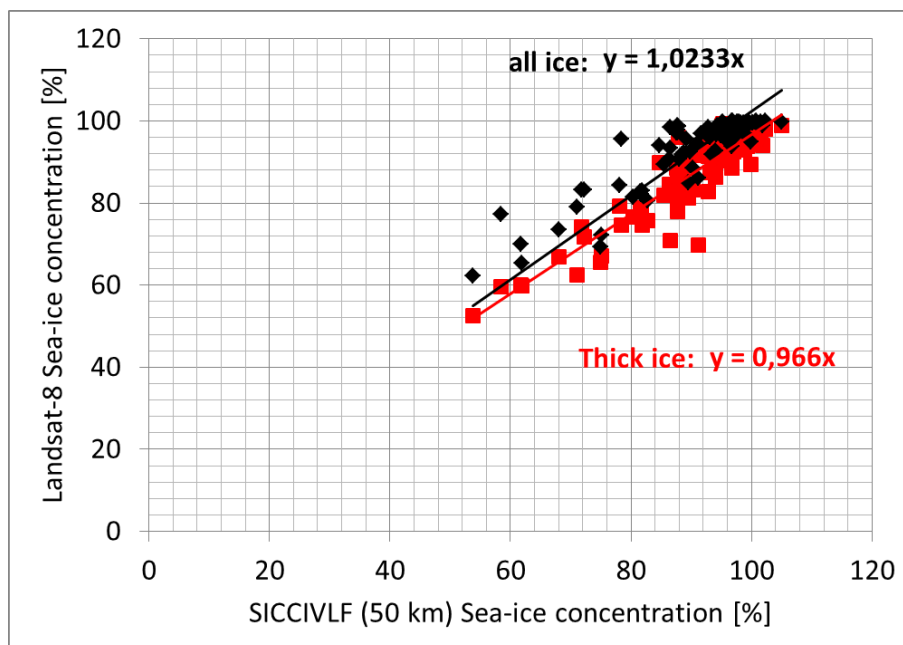
Figure 3-23: Summary scatterplot of Landsat SIC versus SICCI-VLF (50.0 km) SIC for the Southern Hemisphere for Landsat-8 OLI images between 2013 and 2015. Data pairs, regression lines and equations with Landsat SIC are given in black, those with Landsat only thick ice SIC are given in red.
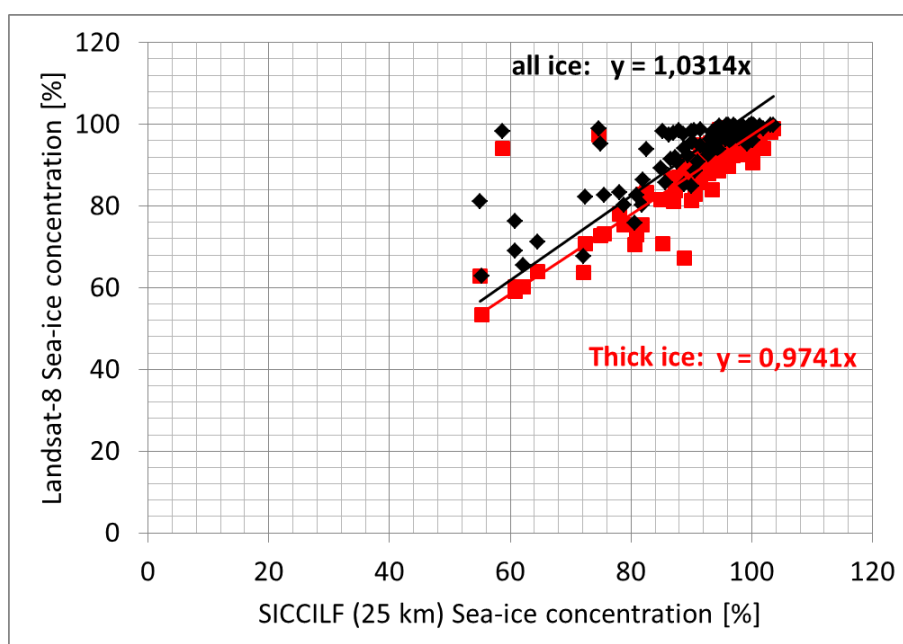
Figure 3-24: As Figure 3-23 but for SICCI-LF (25.0 km).

In contrast to the Northern Hemisphere, there is no clear message from the slopes regarding excluding or including thin ice into the inter-comparison. For SICCI-LF, slopes are both close to one: 1.031 versus 0.974. For SICCI-VLF and SICCI-HF, respectively, slopes including thin ice: 1.023 and 1.021, are closer to one than slopes excluding thin ice: 0.966 and 0.964.
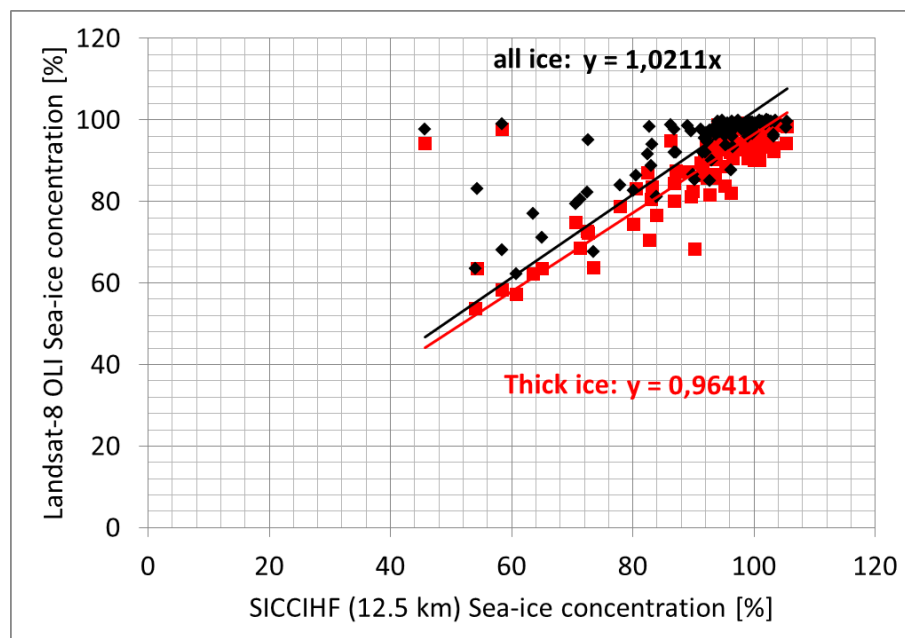
Figure 3-25: As Figure 3-23 but for SICCI-HF (12.5 km).

Table 3-18: Summary of results for the SIC for Landsat-8 OLI (Figure 3-23 to Figure 3-25) for 102 images (from top to bottom): mean SIC and mean SIC standard deviation (SIC SDEV) for SICCI-2 (SICCI), Landsat (LS) and Landsat only thick ice (LS thick); mean SIC total error (SICCI only); modal SIC values. All quantities are given in %.

	SICCI-VLF (50.0 km)			SICCI-LF (25.0 km)			SICCI-HF (12.5 km)		
	SICCI	LS	LS thick	SICCI	LS	LS thick	SICCI	LS	LS thick
SIC	91.4	93.8	88.3	90.5	93.8	88.3	91.1	93.9	88.3
SIC SDEV	9.6	10.2	10.6	10.5	10.9	13.4	10.7	11.9	14.8
SIC total error	12.5			11.1			10.1		
SIC mode	96.1	99.4	92.1	96.4	99.7	92.5	99.7	99.6	94.1

Table 3-19: Summary of results for the SIC differences for Landsat-8 OLI (Figure 3-23 to Figure 3-25) for 102 images (from top to bottom): mean difference SICCI-2 SIC minus Landsat SIC (SICD) and its standard deviation (SICD SDEV) for Landsat (LS) and Landsat only thick ice (LS thick); modal SIC difference (SICD mode). All quantities are given in %. Smallest difference values are given in bold font.

	SICCI-VLF (50.0 km)		SICCI-LF (25.0 km)		SICCI-HF (12.5 km)	
	LS	LS thick	LS	LS thick	LS	LS thick
SICD	**-2.4**	+3.1	-3.4	**+2.2**	-2.8	+2.7

ESA UNCLASSIFIED - For Official Use

SICD SDEV	4.4	4.1	6.4	5.9	8.5	8.2
SICD mode	**-1.3**	**+2.8**	-3.7	+2.2	+2.9	+3.5

Table 3-18 and Table 3-19 provide results which are similar to those obtained for the Northern Hemisphere. SICCI-VLF underestimates Landsat SIC by ~2% while SICCI-LF and SICCI-HF provide a slightly (!) larger under-estimation. The difference between the three algorithms is smaller than in the Northern Hemisphere, though. On average, the thin-ice fraction in the Landsat images is between 5% and 6% - again. Accordingly, when excluding the thin ice from the inter-comparison between SICCI-2 SIC and Landsat SIC, the difference in SIC values changes sign and, correspondingly, all SICCI-2 algorithms over-estimate Landsat thick ice SIC by 2% to 3%.

Summary

By comparing the SIC derived from ~300 30 m pixel resolution classified Landsat optical imagery from both the Northern and the Southern Hemisphere, Landsat SIC, with SICCI-2 SIC data we find

- SICCI-VLF (50.0 km) under-estimates Landsat SIC on average by 2%

- SICCI-LF (25.0 km) and SICCI-HF (12.5 km) under-estimate Landsat SIC on average by 3%-5% in the Northern Hemisphere and by ~3% in the Southern Hemisphere.

- The thin-ice fraction observed in the classified Landsat images is on average 5% to 6%.

- The higher average under-estimation of Landsat SIC by SICCI-LF and SICCI-HF compared to SICCI-VLF in the Northern Hemisphere cannot be explained with a higher sensitivity to thin ice. Instead we hypothesize based on our results that surface emissivity changes caused by changes in snow and/or thick sea ice physical properties are responsible for this observation.

- A logical next step, the inter-comparison of SICCI-2 and Landsat SIC on a grid cell-by-grid cell basis, is under preparation but not content of this report.

3.4   SICCI SIC versus MODIS melt pond fraction & sea ice concentration

Here we present the results of the inter-comparison between the SICCI-2 SIC products of the Arctic Ocean and the 8-day MODIS melt-pond fraction and summer sea-ice concentration data set available from WDCC and ICDC via: http://icdc.cen.uni-hamburg.de/daten/cryosphere/arctic-meltponds.html (DOI:10.1594/WDCC/MODIS__Arctic__MPF_V02). Note that we use the bias-corrected V02 of this product. The ICDC MODIS data product is based on 8-day composite reflectances and has hence 8-day temporal resolution. The time period covered each year is year day 129 (first day of first 8-day period) until year day 249 (first day of last 8-day period) for years 2000 to 2012. The grid resolution of the used MODIS product is 12.5 km by 12.5 km. Only data are used which have less than 10% cloud coverage. For details of the melt pond fraction and MODIS SIC retrieval algorithm see Rösel et al. [RD-12]. For details regarding the above-mentioned bias correction see [RD-13] and Kern et al. [RD-14].

The comparison is carried out for year 2003 through 2011; for these years the AMSR-E SICCI-2 SIC products cover the full melting season from May through August. The comparison is carried out for all three SICCI-2 products.

Co-location between SICCI-2 and MODIS grid cells is done by computing the distance between grid-cell centers after the grid coordinates of the respective projections have been converted into Cartesian coordinates in kilometers with reference at the North Pole and finding the grid cell with the minimum distance. All data are taken at their native grid resolutions. This means that for the SICCI-2 12.5 km product it is likely that every match-up between MODIS MPF data and SICCI-2 data is unique because of the similar grid resolutions. For the SICCI-2 25.0 km and 50.0 km there is an increasing probability that different MODIS MPF grid cells are co-located with the same SICCI-2 SIC grid cell. Based on our experience with the evaluation of the SICCI-2 products with the RRDP-2 evaluation data, where we tested whether block-averaging of finer-resolution data would change the results – which was not the case – we decided to carry out the co-location and hence the entire analysis without any gridding of MODIS MPF data to coarser grids.

SICCI-2 SIC data are averaged over the 8-day period represented by the MODIS MPF product, i.e. for the MODIS MPF product of year day 129 we use SICCI-2 data from year days 129 through 136. Only those SICCI-2 SIC data are used where the flags provided with the product indicate no bias due to too high temperatures and/or by land contamination of the radiometric signal (land-spillover). A minimum of three valid SICCI-2 SIC data is required to compute an average SICCI-2 SIC value.

In addition to the minimum cloud cover criterion we also only used MPF data where the ratio between MPF and MPF standard deviation is larger than one.

Further, in order to evaluate the SICCI-2 SIC during the summer period, we also took the MODIS SIC from the data set and, in addition, computed the MODIS net ice-surface fraction (ISF) (see also [RD-14])

The comparison contains the following elements of which only a selection is presented in this report: 1) maps of the MPF distribution in the native product, 2) maps of the SICCI-2 SIC indicating areas of SIC > 100% without and with superposed grid-cell mean MPF information, 3) maps of the

ESA UNCLASSIFIED - For Official Use

difference SICCI-2 SIC minus MODIS SIC and SICCI-2 SIC minus MODIS ISF; 4) histograms of the MPF, MODIS SIC, MODIS ISF and SICCI-2 SIC, 5) 2-dimensional scatterplots of SICCI-2 SIC versus MODIS SIC or versus MODIS ISF together with a linear regression and correlation analysis.
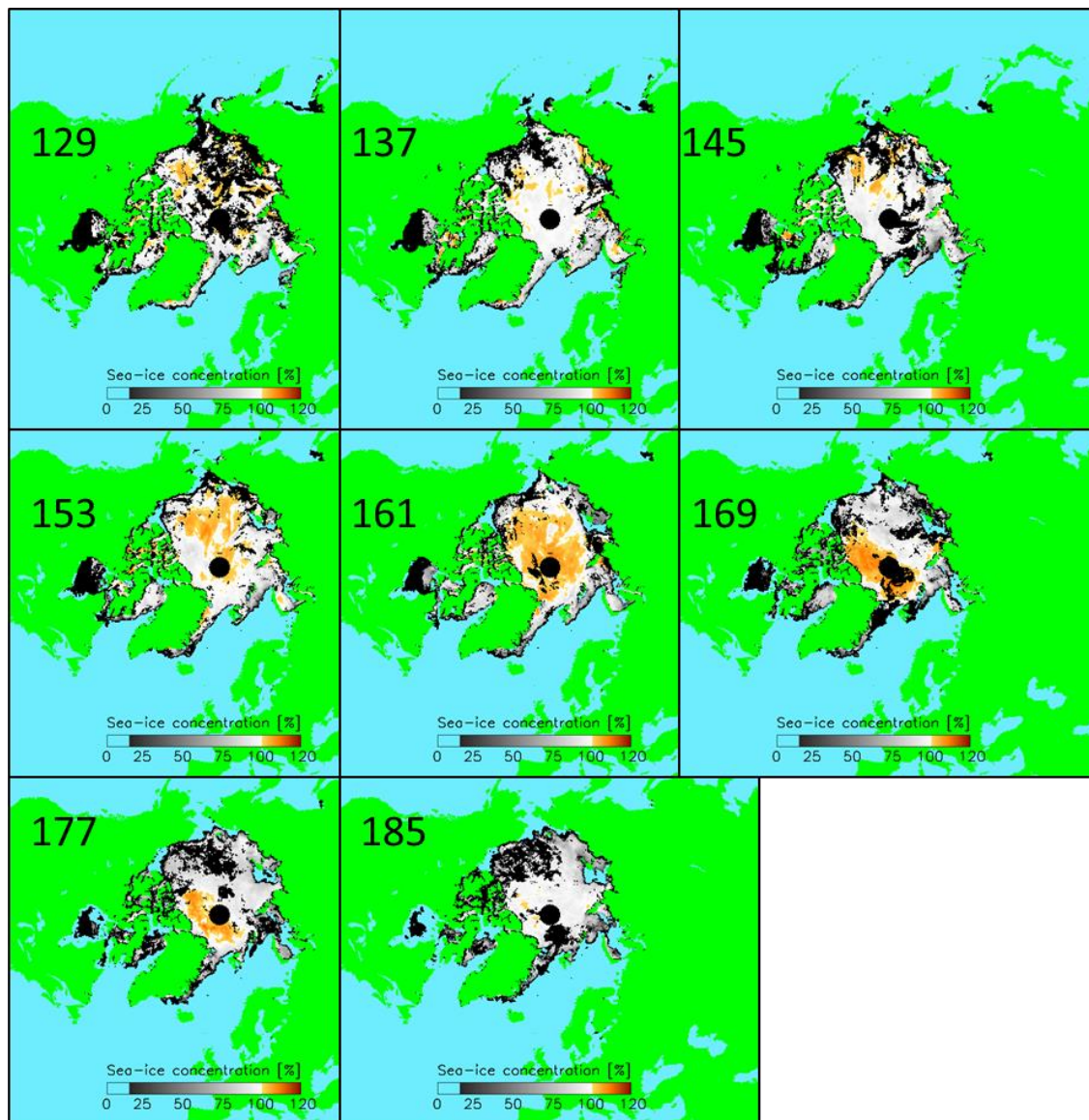
Figure 3-26: Sample set of SICCI-2 SIC maps (SICCI-LF, 25.0 km) collocated with MODIS MPF/SIC information for 8-day periods yearday 129 through 185 (~ 2nd week of May through 1st week of July) for the year 2005. Black areas denote the observation hole at the pole and data discarded from the MODIS data (too many clouds, too small MPF-to-MPF standard deviation ratio). SIC are cut off at 20%.

We start in Figure 3-26 and Figure 3-27 with an illustration of the summer-time SIC distribution in the Arctic Ocean after co-location with the MODIS MPF/ISF/SIC data. The reasoning behind this is twofold. On the one hand we want to illustrate the size, location and variability of areas without valid MODIS data (denoted as black patches in these two figures). We find that unfortunately quite large areas cannot be used for our inter-comparison –

ESA UNCLASSIFIED - For Official Use

basically because of too many clouds but also due to a too high variation of MPF values contributing to the grid-cell mean MPF value used here. Up to 20% of the entire area might be discarded from our analysis because of this. However, we find that these patches vary over space with time so that we still believe that the MPF data set gives a viable representation of the summertime MODIS based MPF / ISF / SIC.
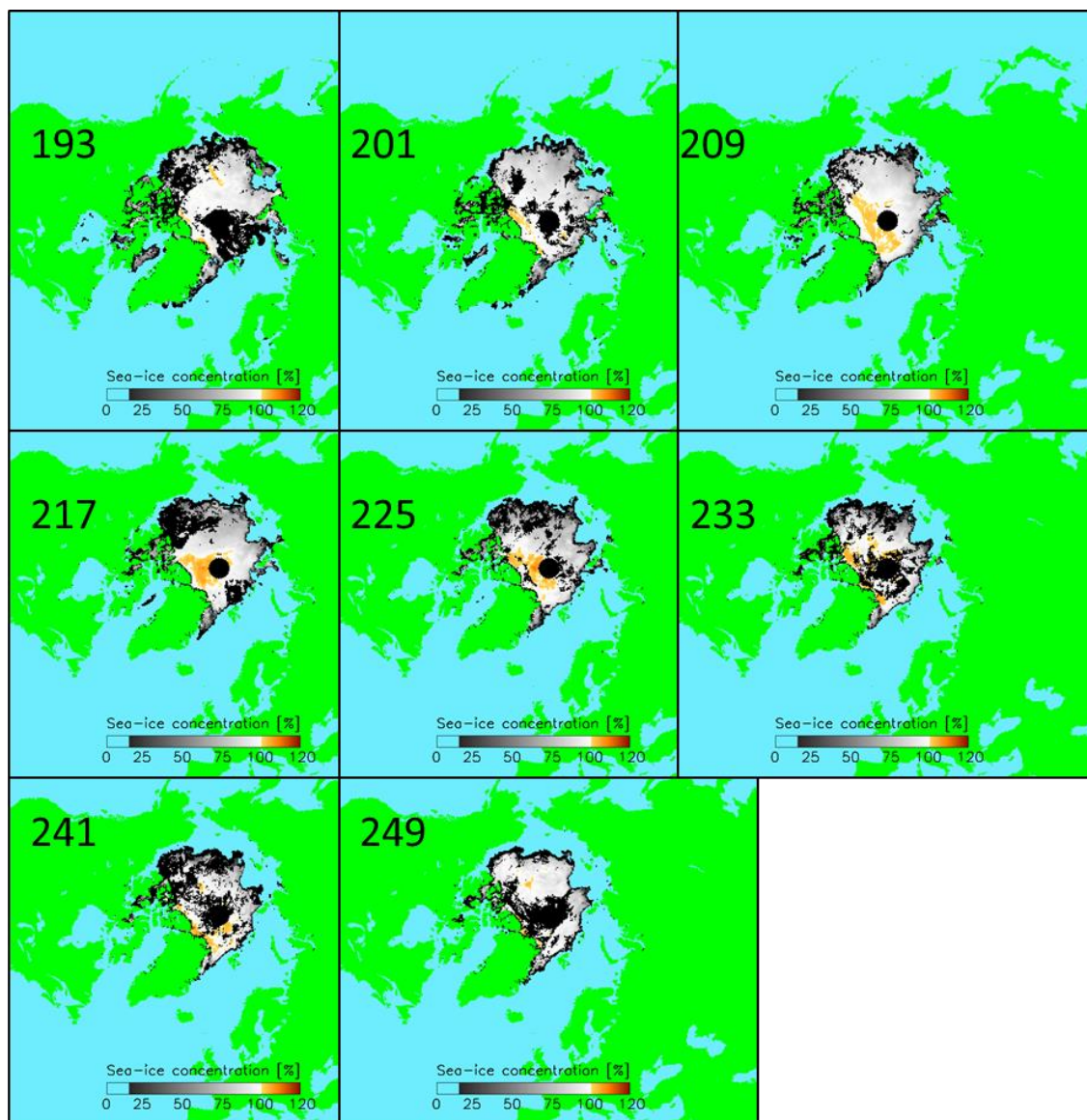
Figure 3-26 continued for 8-day periods of yearday 193 through 249, e.g. 2nd week of July through 2nd week of September of the year 2005.

On the other hand these figures illustrate how SIC > 100% distribute across the Arctic Ocean and how this distribution changes with time intra- as well as inter-annually. In 2005 there is a massive occurrence of SIC > 100% starting at yearday 153 (1st week of June) and lasting until yearday 177 (last week of June) (Figure 3-26). While the coverage with SIC > 100% is pan-Arctic for yearday 153 and 161 it tends to be limited to the MYI area north of Greenland and the Canadian Arctic Archipelago (CAA) for yearday 169 and 177. In contrast, in 2008 (Figure 3-27) we cannot observe such a

massive occurrence of SIC > 100%; instead patches with SIC > 100% occur here and there already starting at yearday 129 (2nd week of May) and lasting unti yearday 185 (1st week of July). But also after the peak melting period in July / August differences in SIC > 100% area distribution occur. In 2005 there are notable areas with SIC > 100% from yearday 209 (last week of July until yearday 241 (last week of August) (Figure 3-26). In contrast, in 2008, only for the 8-day period starting at yearday 249 we find a patch of SIC > 100% of notable size north of Greenland (Figure 3-27).
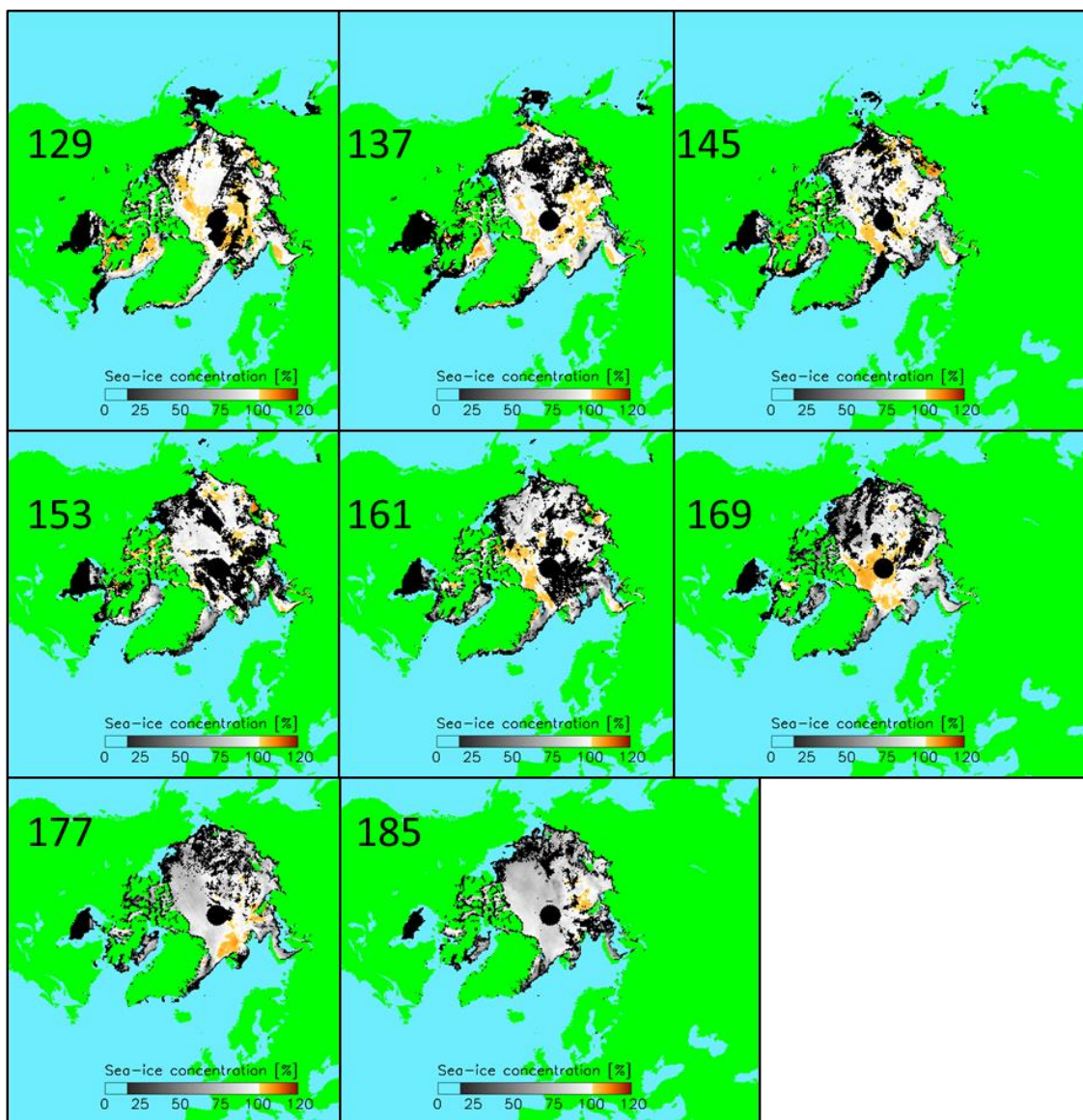
Figure 3-27: As Figure 3-26 but for the year 2008.
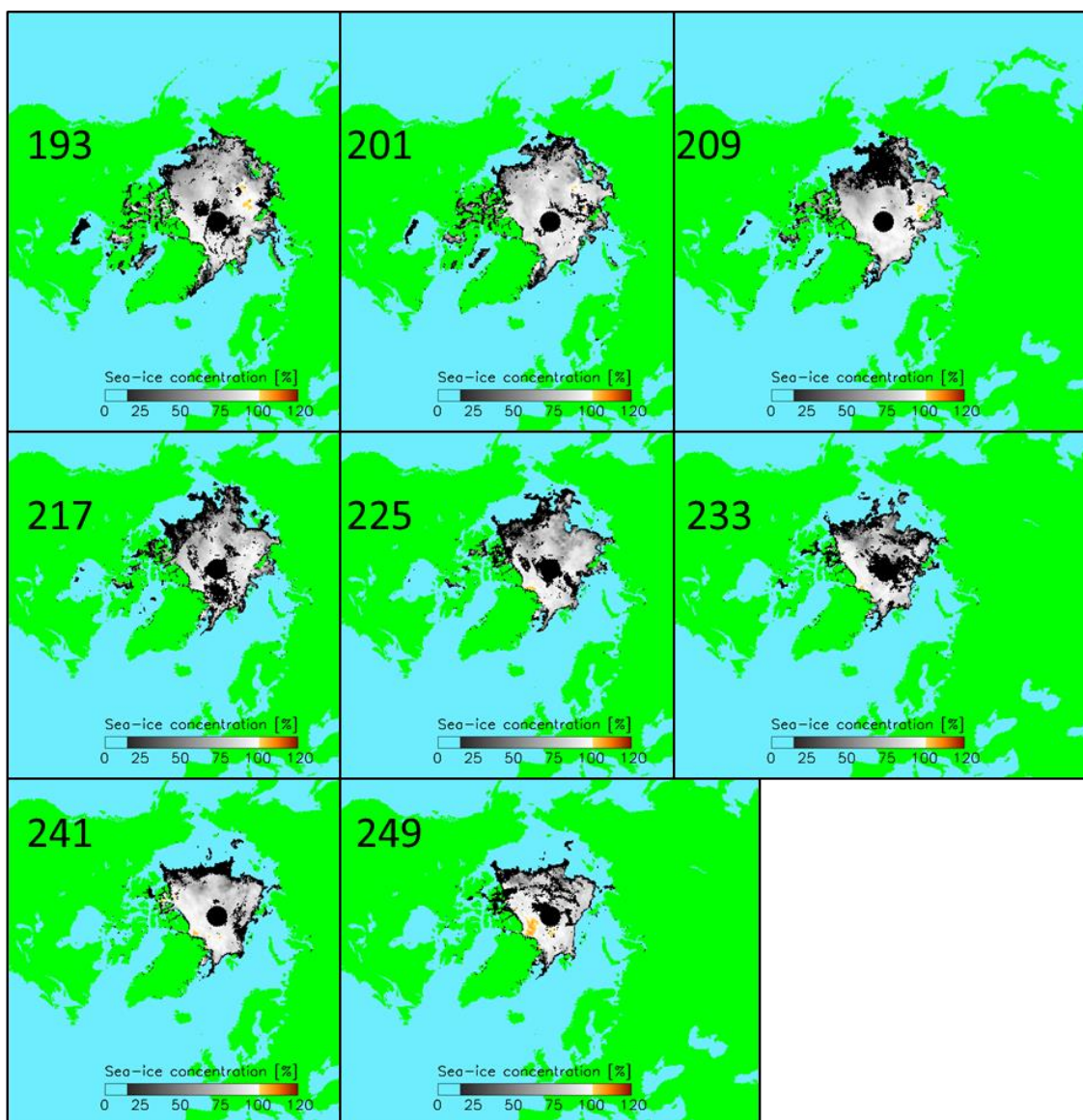
Figure 3-27 continued for 8-day periods of yearday 193 through 249, e.g. 2nd week of July through 2nd week of September of the year 2008.

Next is to take a look at the MODIS MPF data. This is done via Figure 3-28 and Figure 3-29. With Figure 3-28 we aim to show an example of MODIS MPF together with SICCI-2 SIC side by side - also to illustrate how areas of SIC > 100% may behave in the MODIS MPF product. Figure 3-28 illustrates nicely, that the majority of the areas with SICCI-2 SIC > 100% (see images at the left for the absolute SIC values) are also exhibiting a non-zero MPF – often already above 5% or even above 10% as in some areas on yearday 153 and 161.

In Figure 3-29 we illustrate one full seasonal cycle of the development of the MPF distribution for the year 2005 in form of histograms. At the beginning of the melt season the MPF is – as excpected – low; until including the 8-day period starting at yearday 153 (1st week of June) hardly any grid cells exhibit MPF > 20%. Commence of melt-pond formation can be

set to yearday 145 (last week of May) when the MPF distribution peaks at 5%. Over the first half of June until yearday 169 melting progresses.
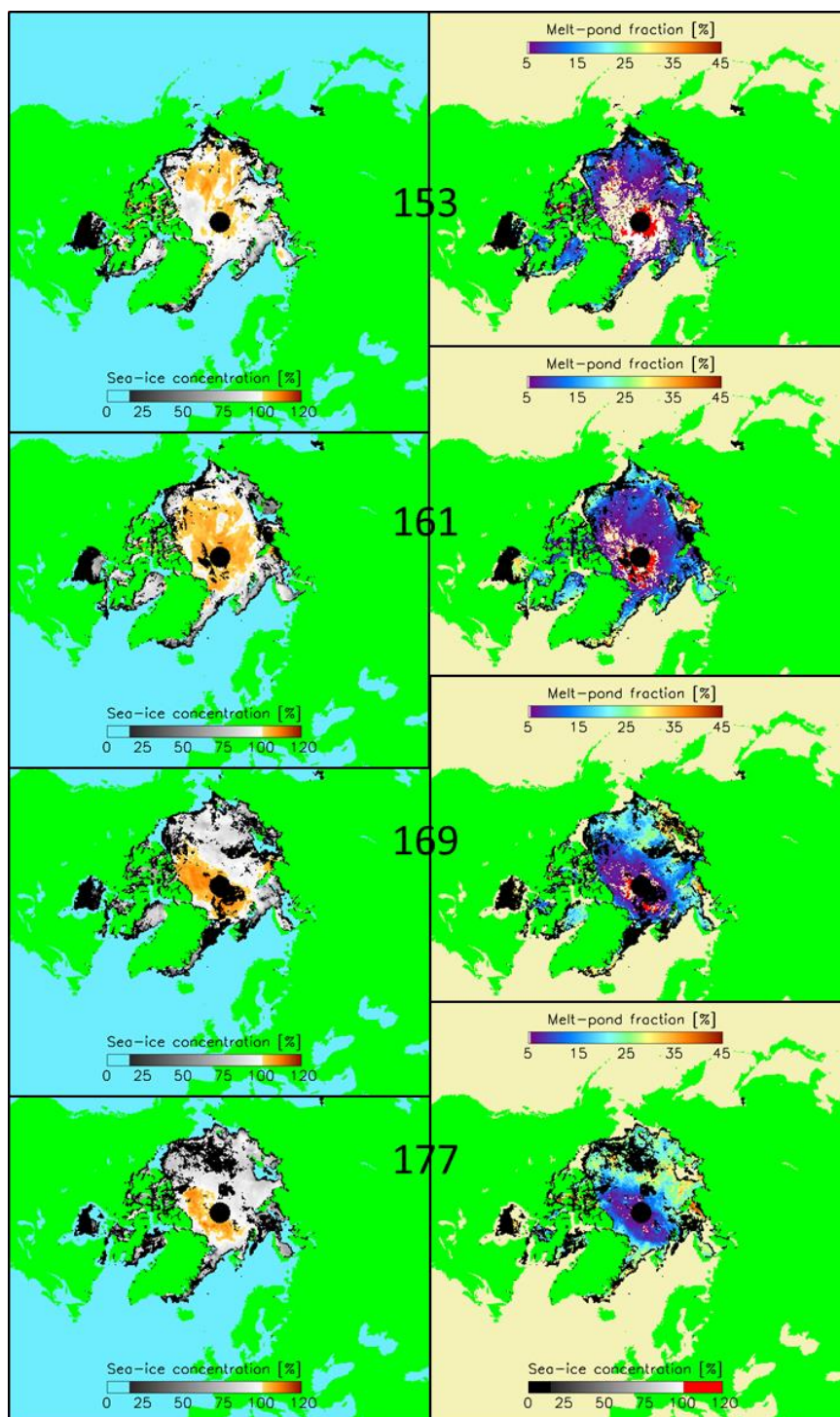
Figure 3-28: Illustration of, on the left hand side, SICCI-2 SIC (SICCI-LF, 25.0 km) for 2005 for those 8-day periods which showed substantial areas of SIC > 100% (see Figure 3-26) and, on the right hand side, co-located MODIS MPF (grid-cell mean) for the same periods. Here SIC > 100% is simply denoted in red; black areas denote discarded grid cells (see Figure 3-26); note that MPF < 5% is displayed in the same color as the open water areas.
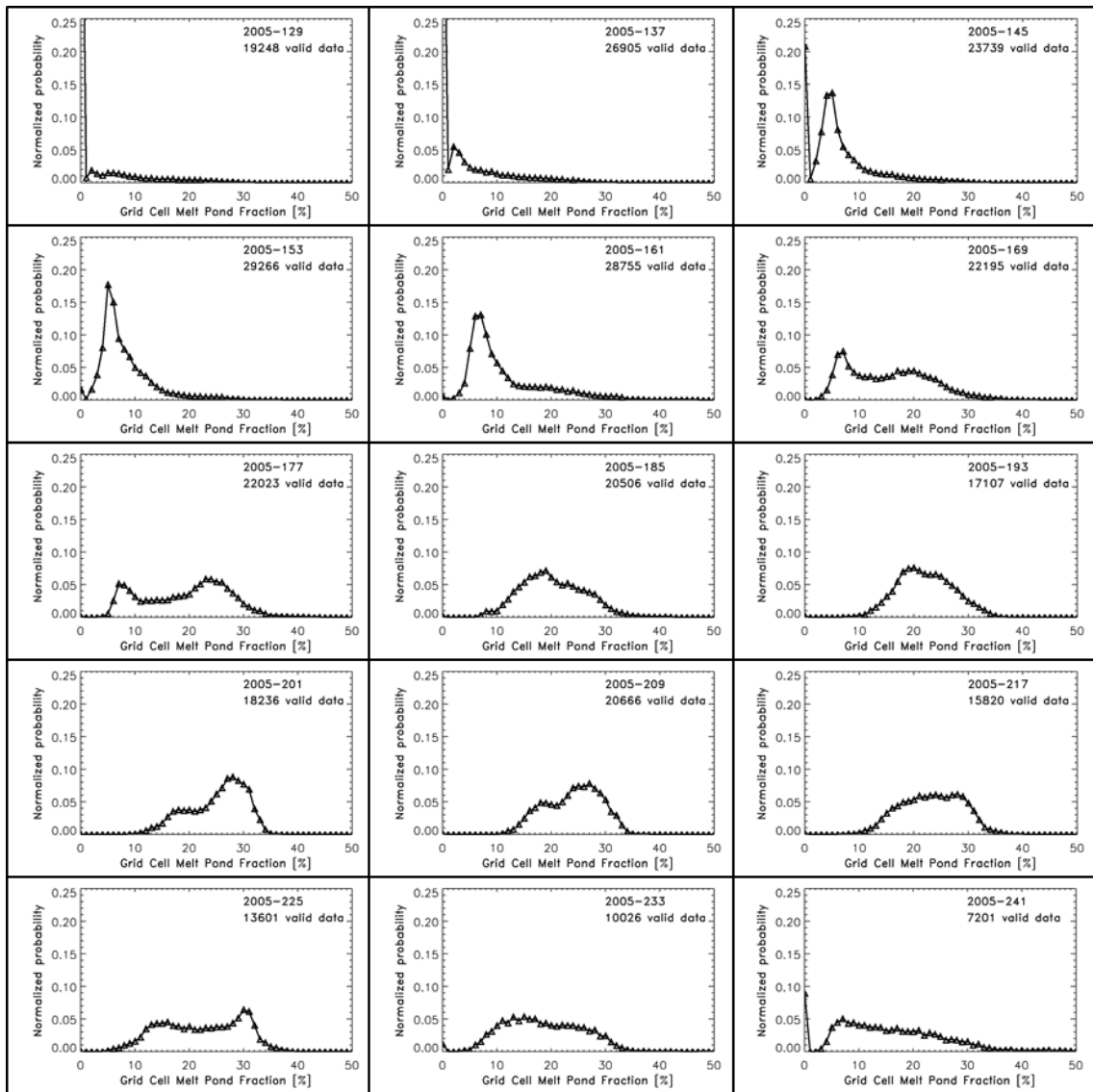
Figure 3-29: One seasonal cycle of the MODIS MPF distribution for 8-day periods of yearday 129 (2nd week of May) through 241 (last week of August / 1st week of September) for the year 2005. Binsize is 1%. Histograms are normalized such that the sum of all probabilities displayed equal one.

At yearday 169 a secondary mode occurs at MPF ~20% and the fraction of grid cells without melt ponds is zero. The secondary mode become the primary mode at yearday 177 when it peaks at MPF = 24%. At least five percent of the grid cells have a melt-pond fraction > 30% now. The further development of the histograms suggests that melt continues until the 8-day period of yearday 217 (1st / 2nd week of August). This period marks the end of four 8-day periods lasting peak melting phase with no grid cells having MPF < 10% and modal MPF values between 20% and almost 30%. Close to 20% of all grid cells exhibits a MPF > 30%. During the remainder of August melt continued for some parts of the area (modal MPF = 30% for yearday 225) but freeze-up commenced as well as illustrated by an increasing number of grid cells with a MPF < 10% or even 0% (after yearday 233).

While in 2005 MPF values hardly exceed 35% in 2007, for instance, 15 percent of the grid cells with valid MPF values had an MPF > 35% for the 8-day periods at yearday 161 and also at yearday 233; even MPF > 40% occurred in 2007. The transition between yearday 169 and yearday 177 or 185 marks the onset of wide-spread melt-pond formation and MPF increase, illustrated by a jump of the modal MPF value from 5% to 10% to 20% to 25% in all years considered but 2007.
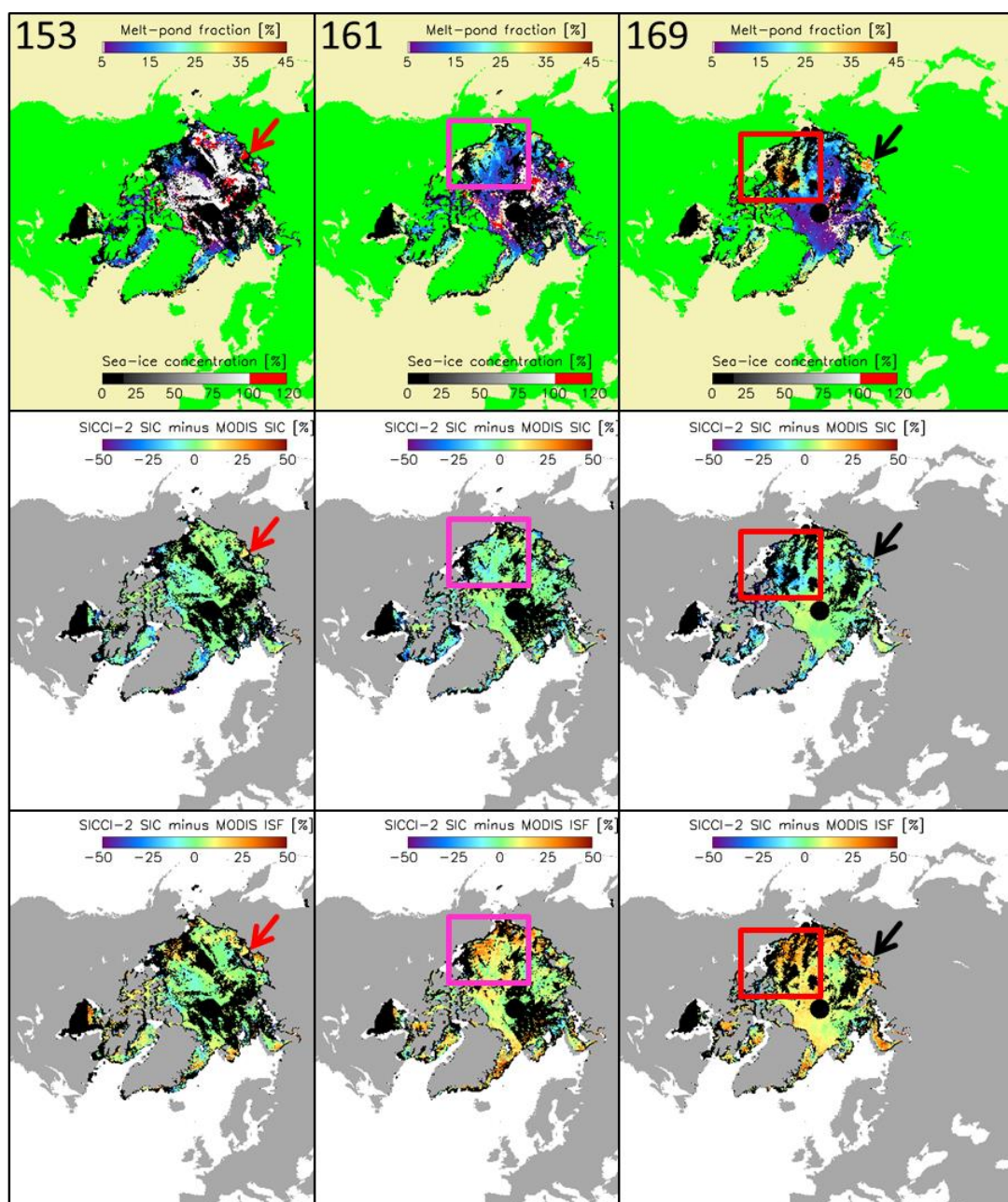
Figure 3-30: Top: MODIS MPF superposed onto SICCI-2 SIC (SICCI-LF, 25.0 km) (see Figure 3-28), middle: SICCI-2 SIC minus MODIS SIC, bottom: SICCI-2 SIC minus MODIS ISF, for yeardays 153, 161, and 169 of the year 2008. Black areas denote the observation hole at the pole and grid cells discarded from the analysis due to too many clouds, too few valid SICCI-2 SIC data, or a too low MPF to MPF-standard deviation ratio. See Figure 3-31 for the corresponding scatterplots. See the text for the boxes and arrows.

Starting with Figure 3-30 (see previous page) we illustrate the spatiotemporal development of i) the MPF co-located with the SICCI-2 SIC of SICCI-LF (25.0 km), ii) the difference SICCI-2 SIC minus MODIS SIC, iii) the difference SICCI-2 SIC minus MODIS ISF, and iv) the distributions of SICCI-2 SIC versus MODIS SIC, SICCI-2 SIC versus MODIS ISF, and SICCI-2 SIC versus MODIS MPF in form of 2-D histogram scatterplots.

At the beginning of June 2008 (yearday 153 in Figure 3-30) the MPF is still < 10% over most of the Arctic Ocean and only the peripheral seas, e.g. the Greenland Sea and the Baffin Bay, exhibit areas of elevated MPF values. Both differences, i.e. SICCI-2 SIC minus MODIS SIC (middle) and SICCI-2 SIC minus MODIS ISF (bottom) fall into the range -5% … +5%; differences with the ISF seem to be slightly more on the positive side, though. The red arrow points to an area in the East Siberian Sea, where SICCI-2 SIC > 100% (actually at least 105% according to the respective map in Figure 3-27), which results in differences of ~ +10%, i.e., SICCI-2 overestimates MODIS SIC and ISF by about 10%.

About a week later (yearday 161 in Figure 3-30) melt-pond formation in the Beaufort Sea has led to widespread MPF > 20%, peaking at ~ 30% (see magenta box). In this region SICCI-2 SIC minus MODIS SIC still stays in the range -5% … +5% (middle) while SICCI-2 SIC minus MODIS ISF is around +15% for a notable fraction of the region, peaking at ~ 25% (bottom).

Again about a week later (yearday 169 in Figure 3-30) the region with MPF > 20% has expanded north- and eastward and peak values are > 35% (red box). Another region located in the Laptev Sea (black arrow) also exhibit an MPF > 30%. In these regions the difference SICCI-2 SIC minus MODIS SIC is negative, falling approximately into the range -20% … -10%, i.e. SICCI-2 SIC is smaller than MODIS SIC. In the same regions the difference SICCI-2 SIC minus MODIS ISF is positive, falling into the range +10% … +25%, i.e. SICCI-2 is larger than MODIS ISF. We note that in the region north of Greenland, where the MPF is between 5% and 10%, the difference SICCI-2 SIC minus MODIS SIC is slightly positive (0% … 10%) as is the difference SICCI-2 minus MODIS ISF (5% … 15%). We observe a pan-Arctic increase in the difference SICCI-2 SIC minus MODIS MPF from yearday 153 to yearday 169. At the same time the value range of the difference SICCI-2 SIC minus MODIS SIC stays more or less the same and only the spatial distribution changes notably.

The corresponding scatterplots (Figure 3-31) illustrate these findings from a different viewpoint. We observe that indeed at yearday 153 the majority of the obtained MPF values are < 15%. Note that the transition from cyan to green marks ~10 cases of the respective data pair. Melt progresses with time resulting in a considerable number of cases with MPF ~ 30% at yearday 169; these coincide with a SICCI-2 SIC of 70%. The distribution of data points with > ~10 cases suggests a linear decrease of SICCI-2 SIC with increasing MPF. This linear relationship can be found as well in the images of the bottom row of Figure 3-31. Here we can see that from yearday 153 to yearday 169 the data points become increasingly better organized in an elongated point cloud which is located above the 1-to-1 line with a slope < 1. This indicates an increasing difference SICCI-2 SIC minus MODIS ISF with decreasing ISF or, in other words: the smaller MODIS ISF gets the more does SICCI-2 SIC over-estimate it (see the red line). At this time of the year it is fair to assume that a change in ISF over time is primarily coupled to a change in MPF and not so much to a change in sea-ice area fraction (including melt ponds) by sea ice melt. In the middle row of Figure 3-31 we can observe a less elongated point cloud developing which

actually suggests a slope > 1. This indicates an under-estimation of MODIS SIC by SICCI-2 SIC. We find, for instance, that SICCI-2 SIC is ~80% when MODIS SIC is ~90%.
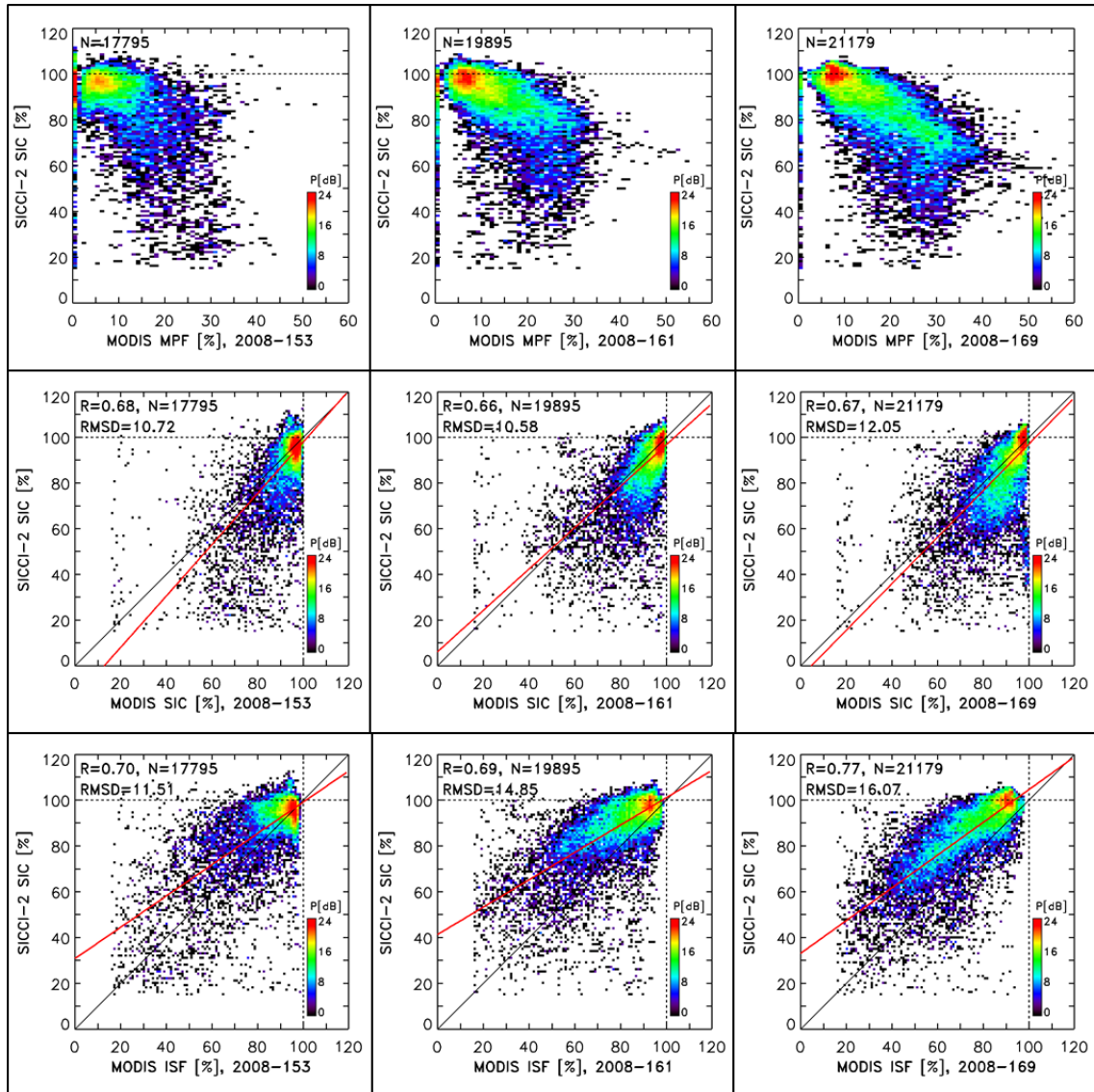
Figure 3-31: Scatterplots SICCI-2 SIC versus, top: MODIS MPF, middle: MODIS SIC, and bottom: MODIS ISF in form of a 2-dimensional histogram with logarithmic scaling, for the data shown in Figure 3.4.5 as maps. Binsizes are 1% for both axes. The transition to orange to red (from cyan to green) marks that the number of respective data pairs exceeds 100 (10). Given at the top are the total number of valid data pairs N (all images), the linear correlation coefficient R (MODIS SIC and MODIS ISF only), and the root mean squared difference RMSD in percent (MODIS SIC and MODIS ISF only). The solid black line in the middle and bottom row of images denotes the 1-to-1 line. The red line denotes the linear regression computed from all data pairs.
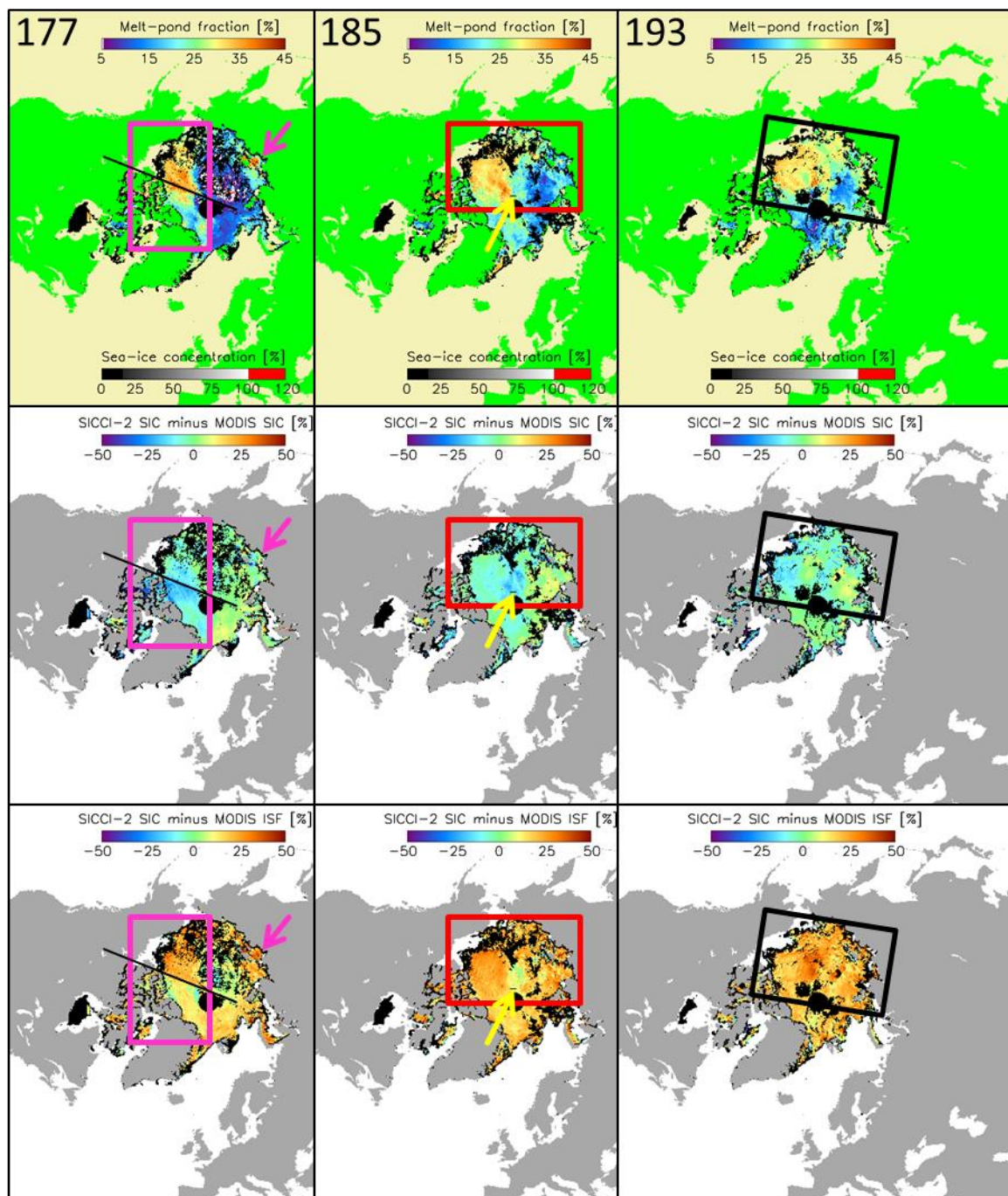
Figure 3-32: As Figure 3-30 but using data for 8-day periods starting at yearday 177, 185, and 193.

Melting peaks from end of June towards mid July and regions with MPF < 10% vanish in 2008 at yearday 185 and 193 when most of the Arctic Ocean sea ice exhibits MPF > 20% peaking at ~ 35% (Figure 3-32, top row). We can see a relatively clear difference in the regional MPF distribution with higher values in the western Arctic than in the eastern Arctic – except for the small region in the Laptev Sea denoted by the magenta arrow at yearday 177 (compare black arrow in Figure 3-30, yearday 169). This regional MPF distribution can be observed in the difference SICCI-2 SIC

minus MODIS SIC (middle row) as well. Those regions with a comparably high MPF (magenta box, left side of red and black boxes) coincide typically with a difference SICCI-2 SIC minus MODIS SIC on the negative side, falling into the range -25% … -5%. Those regions with a comparably low MPF (~ outside magenta box, right side of red and black boxes) coincide typically with a difference SICCI-2 SIC minus MODIS SIC on the positive side, falling into the range 0% … +15%. The difference SICCI-2 SIC minus MODIS ISF (bottom row) has a less clear association of low and high MPF values. This difference is with few exceptions positive, generally ranging between +10% and +30%.

The yellow arrows point to a feature, where the MPF is ~25%, i.e., smaller than to the East but larger than to the West. But the difference SICCI-2 SIC minus MODIS SIC is the most negative in the red box: ~ -20%, and the difference SICCI-2 SIC minus MODIS ISF is surprisingly close to zero: between +5% and +10%, compared to the West and the East where this difference is ~ +25%. This deserves a closer examination and discussion.
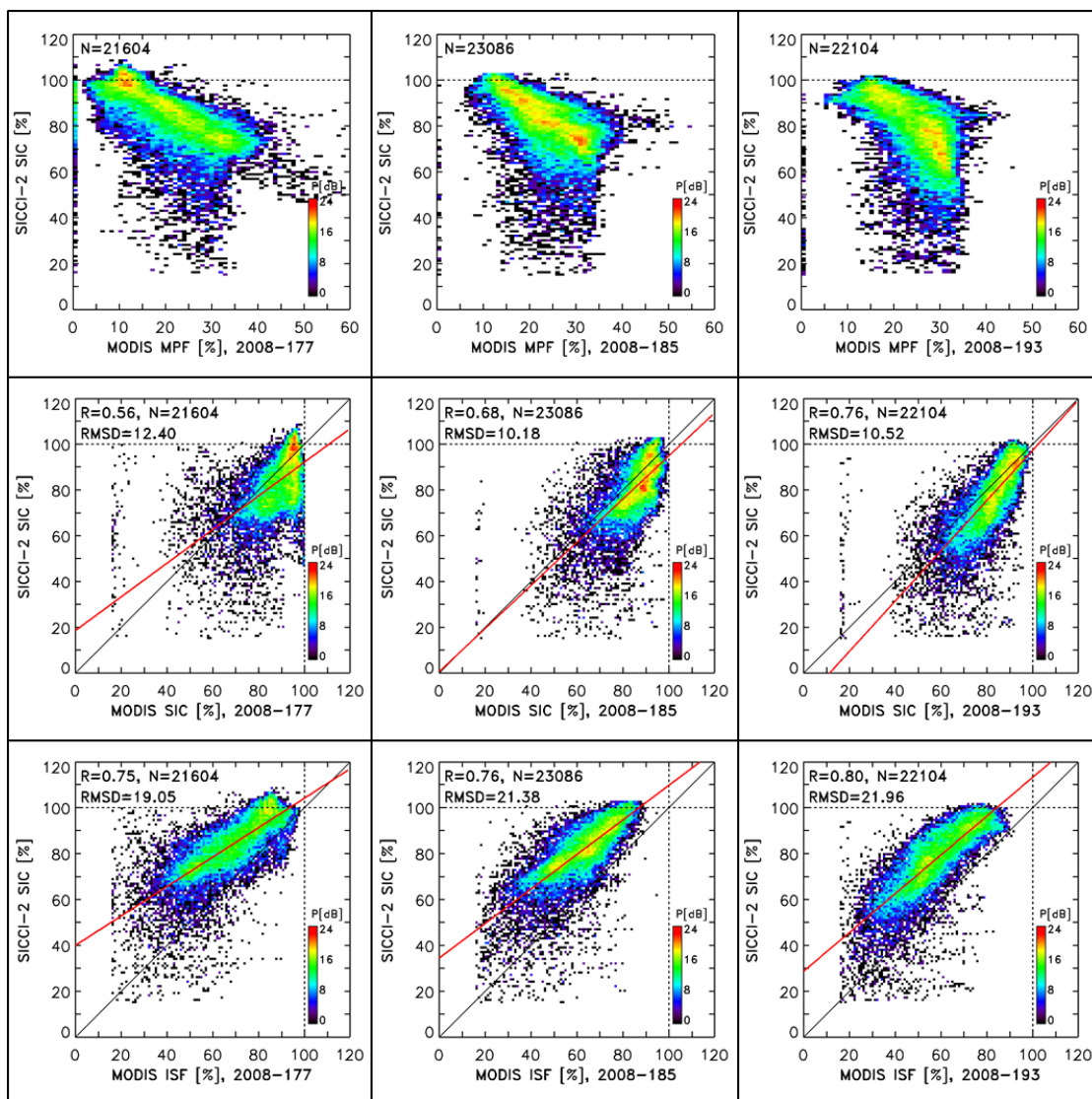
Figure 3-33: As Figure 3-31 but using data for 8-day periods starting at yearday 177, 185, and 193 (see Figure 3-32 for the corresponding maps).

The thin black lines crossing the magenta boxes at yearday 177 (Figure 3-32) also point to a remarkable, to be discussed feature. In the top row, this line roughly separates a region with MPF > 35% from a region with MPF < ~25%. The separation is not perfect, though. The same line, however, separates very clearly a region with comparably small differences SICCI-2 SIC minus MODIS SIC West of it from larger differences East of it and a region with comparably large differences SICCI-2 SIC minus MODIS ISF West of it from smaller differences East of it. If we assume a close-to-100% sea-ice cover in this region, then the spatial distribution of the MPF and of the difference SICCI-2 SIC minus MODIS ISF agree well with each other. The distribution of SICCI-2 SIC minus MODIS SIC in this area, however, requires a closer examination and discussion.

The scatterplots of SICCI-2 SIC versus MODIS MPF (Figure 3-33, top row) nicely illustrate the temporal development of the MPF distribution. Compared to Figure 3-31, yearday 169, the distribution has further expanded towards even larger MPF values; now we observe a number of cases with MPF ~ 40% at SICCI-2 SIC ~ 70%. The linear relationship mentioned in the context of Figure 3-31 is even better visible here in Figure 3-33, yearday 177. The most notable further development illustrated by the scatterplots in the top row is the shift of the center of the distribution from SICCI-2 SIC ~ 100% / MPF ~ 10% (yearday 177) to SICCI-2 SIC ~ 70% / MPF ~ 30% (yearday 193). Melting is at its peak. Almost no grid cells exhibit MPF < 5%. The change in the shape of the point cloud from yearday 177 to 193 can possibly explained by the superposition of the (first) drainage phase over first-year ice, which usually causes a decrease in MPF, and the onset of melt-pond formation on multiyear ice.

The scatterplots of SICCI-2 SIC versus MODIS SIC (Figure 3-33, middle row) basically show three issues. First, we find that the fraction of SICCI-2 SIC > 100%, which made a considerable fraction of the shown cases (compare Figure 3-31, middle row, yearday 161 and 169), is reduced now and hardly any cases are observed at yearday 193. Second, we find a substantial number of cases where MODIS SIC > 90% but SICCI-2 SIC takes values as low as 70% (yearday 177); there is a considerable degree of under-estimation of MODIS SIC by SICCI-2 SIC. Third, from yearday 177 to yearday 193 SIC data pairs become organized in an elongated point cloud suggesting a slope slightly larger than 1 with less under-estimation of MODIS SIC by SICCI-2 SIC than at yearday 169 (Figure 3-31).

The scatterplots of SICCI-2 SIC versus MODIS ISF (Figure 3-33, bottom row) show: i) the overwhelming fraction of the data pairs is located above the 1-to-1 line; ii) the data pairs are organized nicely in an elongated point cloud which slope is < 1; iii) the slope increases from yearday 177 to 193 becoming more and more parallel to the 1-to-1 line (see red lines in Figure 3-33, bottom row). The average over-estimation of MODIS ISF by SICCI-2 SIC is 15% to 20%. Figure 3-33, yearday 193, shows two "centers of action" where the probability is highest (yellow color). At the top one we find SICCI-2 SIC ~90% versus MODIS ISF ~75%; at the bottom one we find SICCI-2 SIC ~75% versus MODIS ISF ~55%. Note that for this case we also have the highest correlation between the two data sets for the cases shown in this report for 2008: 0.80.

For the yearday 201 through 217 shown in Figure 3-34 and Figure 3-35 it can be assumed that the sea-ice area fraction including the melt-pond fraction on top, or in other words, the sub-surface sea-ice area fraction, begins to deviate more and more from 100%. This has to be taken into account in the interpretation of the difference maps in Figure 3.4.9. The

maps of the MPF distribution (Figure 3-34, top row) illustrate that, at least in 2008, the MPF was not increasing anymore generally at this time of the melting season and that overall MPF stayed above 10-15% peaking close to 35%.
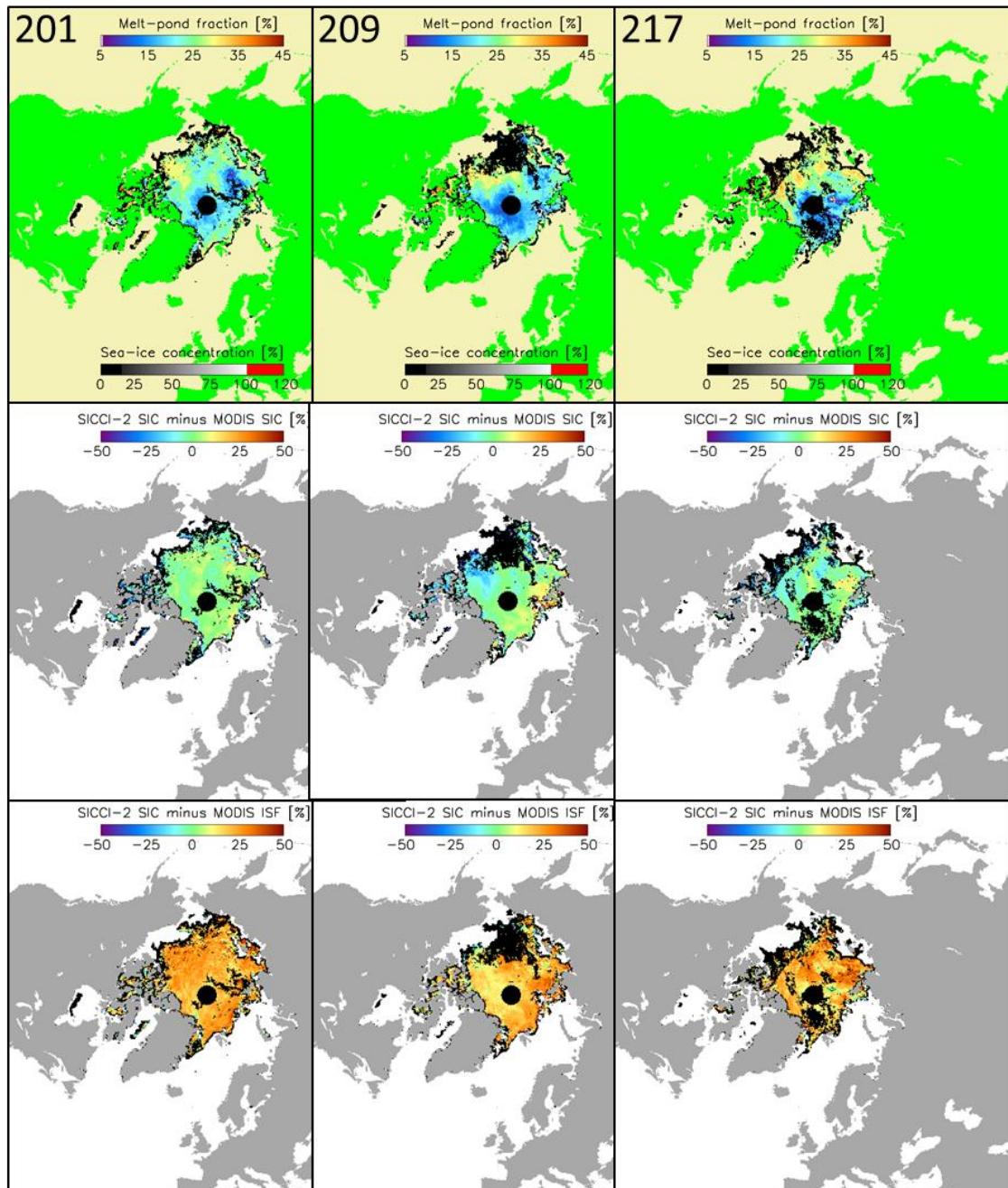
Figure 3-34: As Figure 3-30 but using data for 8-day periods starting at yearday 201, 209, and 217.

The difference SICCI-2 SIC minus MODIS SIC becomes more and more patchy; it is generally more on the positive side (0% to +10%) at yearday 201 but shows a larger range with no dominance of negative or positive values at yearday 209 and 217: -20% to +15% (Figure 3-34, middle row).

ESA UNCLASSIFIED - For Official Use

The difference SICCI-2 SIC minus MODIS ISF stays at a high level and ranges with a few local exceptions between +15% and +35% (Figure 3-34, bottom row). In contrast to the previous periods (Figure 3-30 and Figure 3-32) it is less closely associated with the MPF distribution. This can be seen, e.g., for yearday 201 and 209, when pattern of low and high values in the MPF distribution cannot be found in a respective variation in the difference SICCI-2 SIC minus MODIS ISF. We hypothesize that this is because at this time of the year the ISF is not anymore dominated by the ISF alone but the change in the sub-surface sea-ice area fraction also influences its value.
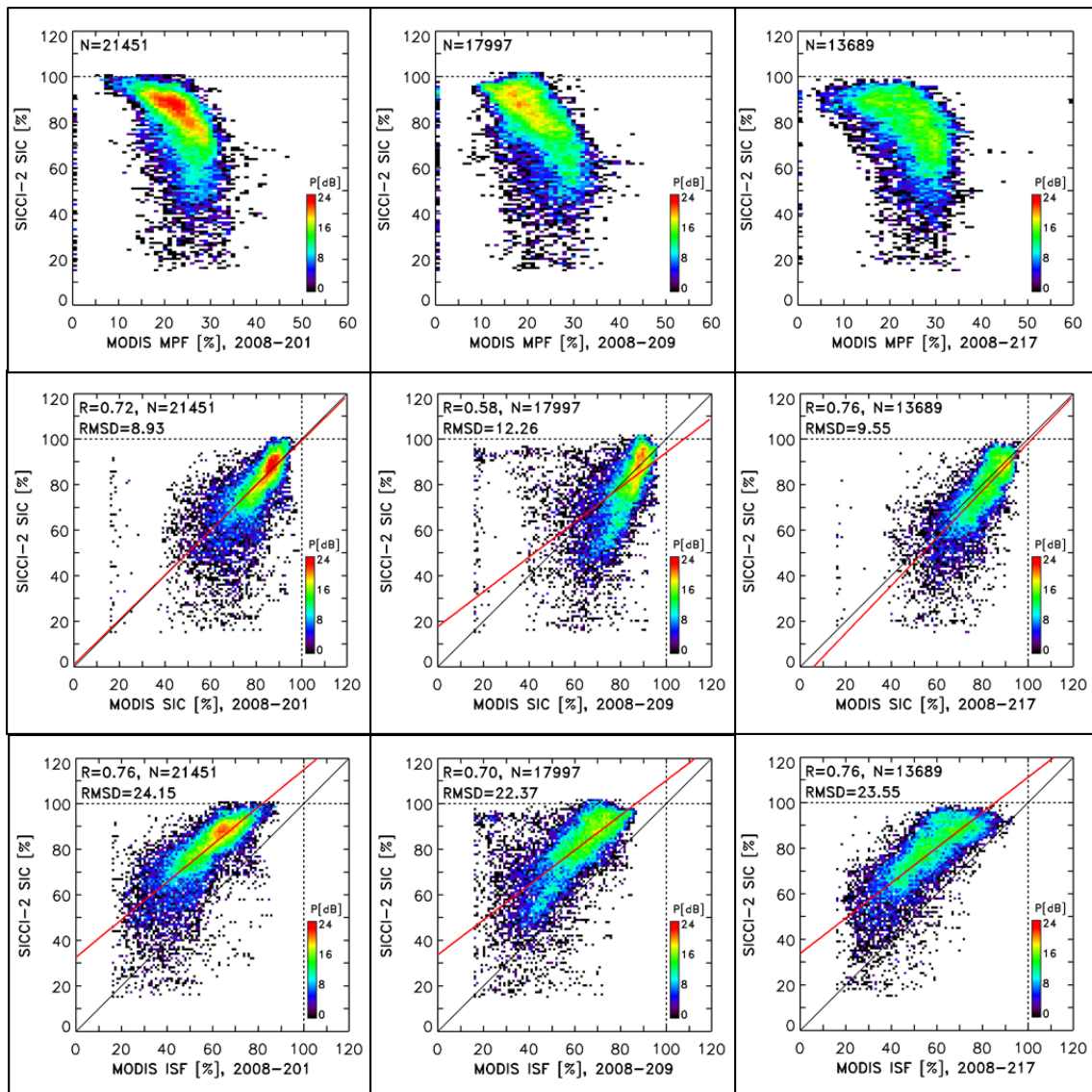
Figure 3-35: As Figure 3-31 but using data for 8-day periods starting at yearday 201, 209, and 217 (see Figure 3-34 for the corresponding maps).

With regard to the MPF the scatterplots (Figure 3-35, top row) confirm that MPF values stayed at a maximum between 30% and 35%. At yearday 201 there is a very well defined "center of action" marked by yellowish-orange-red grid cells falling into a MPF range of ~15% to ~30%. In the following this center vanishes and the scatterplot contains less and less data points – possibly because of complete melt of some sea ice. At this time of the year this possibly removes first-year ice with a comparably large MPF, while the

thicker multiyear ice remains; the increase of its MPF with time certainty has an increasing influence on the distribution of points in these scatterplots.

In the scatterplots of SICCI-2 SIC versus MODIS SIC (Figure 3-35, middle row) we can observe that the distribution gets closer to the 1-to-1 line from yearday 193 (Figure 3-33) to yearday 201. But then again we find a notable under-estimation of MODIS SIC by SICCI-2 SIC indicated by an elongated point cloud below the 1-to-1 line suggesting a slope > 1 before at yearday 217 the point cloud switches back close to the 1-to-1 line; unfortunately for yearday 209, the linear regression line (red line) does not agree with the visual impression of the scatterplot.

The scatterplots of SICCI-2 SIC versus MODIS ISF (Figure 3-35, bottom row) are remarkable similar to the one at yearday 193 (Figure 3-33, bottom row); not much has changed and the general statement that SICCI-2 SIC over-estimates MODIS ISF by between 15% and 20% holds.
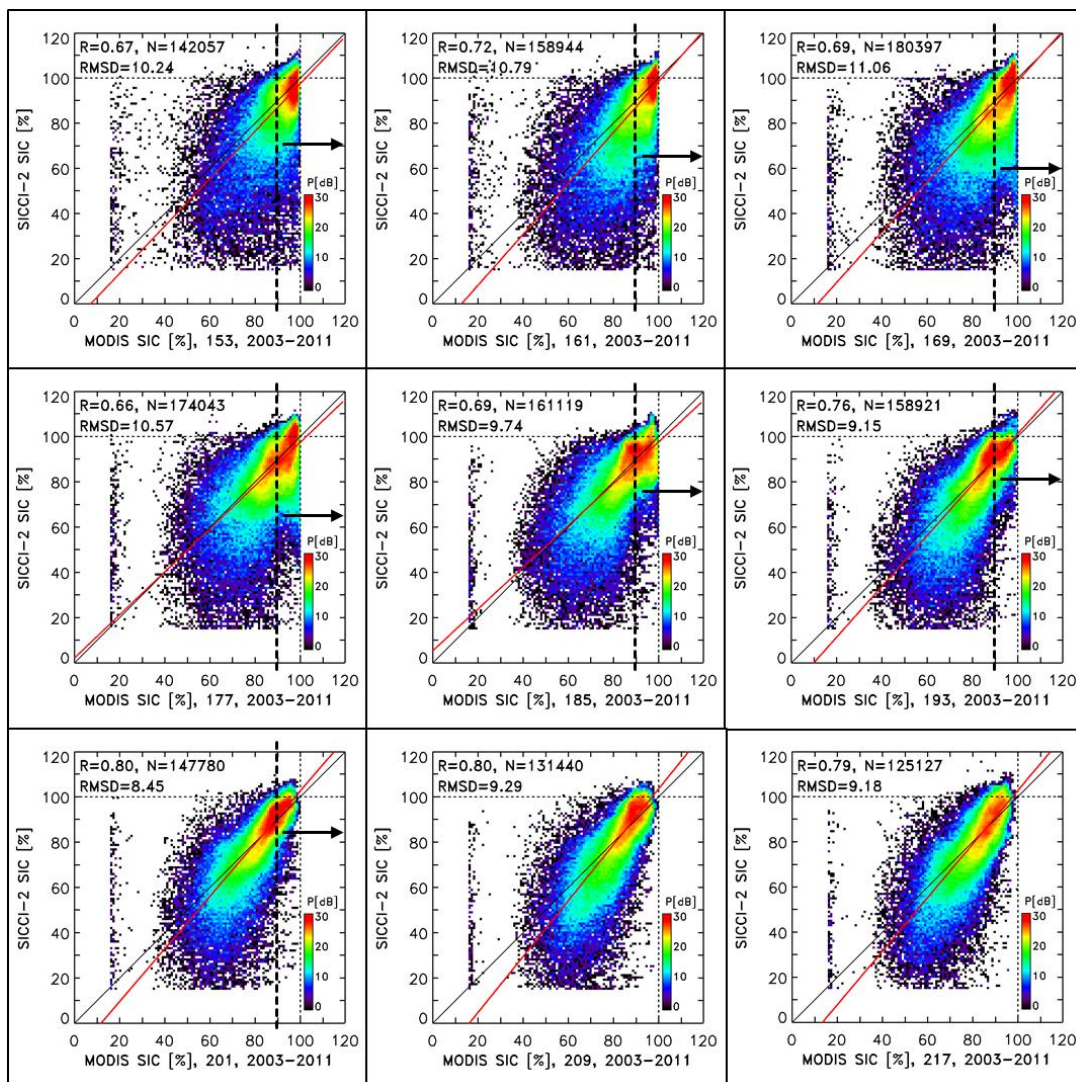
Figure 3-36: Scatterplots of SICCI-2 SIC versus MODIS SIC as 2-dimensional histograms for periods starting at yearday 153 through 217 taking into account data of the entire investigation period from 2003 through 2011. Note the logarithmic scaling of the color scale; the transition blue-cyan (green-yellow) marks 10 (100) cases of the respective data pair.

Figure 3-30 through Figure 3-35 showed results from one year (2008) but in fact the inter-comparison covered data from the years 2003 through 2011. In Figure 3-36 and Figure 3-37 we illustrate that the statements made from the scatterplots between SICCI-2 SIC and MODIS SIC and MODIS ISF for 2008 basically hold as well for the entire period.

For MODIS SIC this is basically the finding that SICCI-2 SIC under-estimates MODIS SIC – as indicated by a slope < 1 suggested by the elongated point cloud formed by the SIC data pairs (Figure 3-36) – at least for a substantial fraction of the SICCI-2 SIC data. However, there is a considerable portion of SICCI-2 SIC data for which SICCI-2 SIC actually over-estimates MODIS SIC. This is predominantly the case for the higher SIC values and seems to be associated more with those periods with a notable region covered by SICCI-2 SIC > 100%.
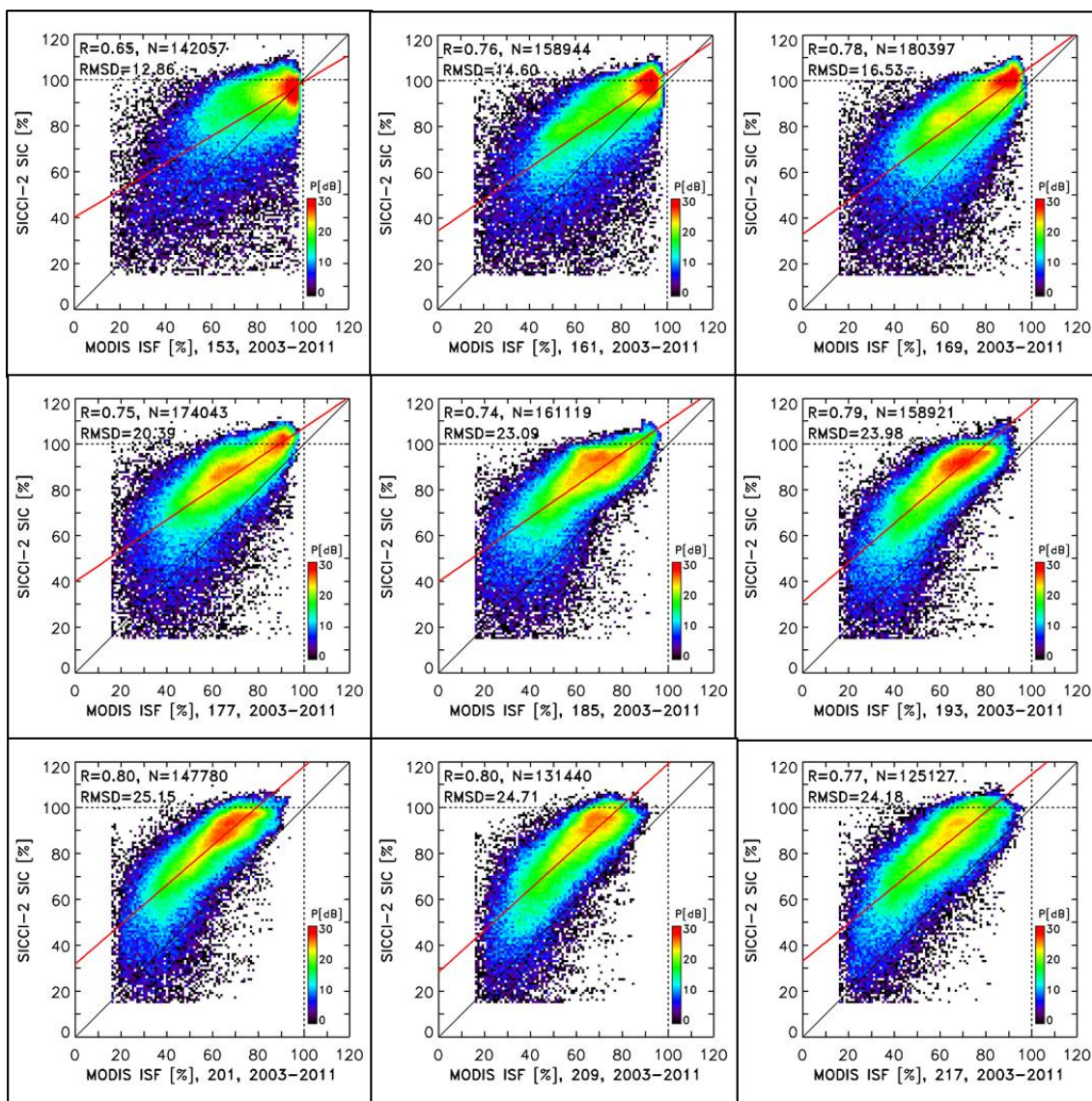
Figure 3-37: Scatterplots of SICCI-2 SIC versus MODIS ISF as 2-dimensional histograms for periods starting at yearday 153 through 217 taking into account data of the entire investigation period from 2003 through 2011. Note the logarithmic scaling of the color scale; the transition blue-cyan (green-yellow) marks 10 (100) cases of the respective data pair.

ESA UNCLASSIFIED - For Official Use

In Figure 3-36 we can also follow the potential maximum mean under-estimation of MODIS SIC by SICCI-2 SIC for high MODIS SIC, i.e. > 90%. While the dashed black lines in Figure 3-36 denote MODIS SIC = 90%, the arrows denote the approximate position where the number of observed data pairs at the respective location in the histogram, i.e. at MODIS SIC > 90%, drops below ~ 10 (blue-cyan transition). We find this drop to occur at SICCI-2 SIC values of 70%, 65%, and 60% in the top row, i.e. yearday 153 through 169; that is prior to peak melt but already at a time where MPF may reach 30 or even 40% locally. Subsequently, the drop is located at increasingly higher SICCI-2 SIC values: 65%, 76%, 81%, and 84% for yearday 177 through 201.

Figure 3-37 illustrates nicely, that MODIS ISF is over-estimated by SICCI-2 SIC on average by between 15% and 20% during and after peak melt, i.e. in July. This does not mean that there are no cases where SICCI-2 SIC and MODIS ISF do agree with each other. But these are clearly the minority of the data. In June, before wide-spread commence of melt-pond formation, SICCI-2 SIC and MODIS ISF agree with each other at the high values, i.e. > 90%. However, the smaller the ISF gets the larger is, on average, its over-estimation by SICCI-2 SIC. It can be anticipated that this is primarily driven by the melt-pond fraction.

In Figure 3-38 and Figure 3-39 we summarize the findings in a pan-Arctic fashion using data from the entire period 2003 through 2011. When doing so we find that i) on average SICCI-2 SIC is over-estimating MODIS ISF for every 8-day period used; ii) this over-estimation is small (< 5%) in May, increases to ~20% during June, and remains at that level through July and most of August; iii) the multi-annual pan-Arctic mean SICCI-2 SIC decreases from ~94% in mid May to ~80% end of August while the respective MODIS ISF decreases from ~90% in mid May to ~60% end of August (Figure 3-38, a).

We find further that the multi-annual pan-Arctic mean MPF agrees within 3% with the difference SICCI-2 SIC minus MODIS ISF (Figure 3-38, a).

Finally, we find that the over-estimation of MODIS ISF by SICCI-2 SIC depends on the MPF (not surprizing). This is illustrated by a rather small difference between SICCI-2 SIC (red symbols) and MODIS ISF (blue symbols) when using only cases with MPF of the range 0% … 10% (Figure 3-38 b) which increases substantially when using cases with MPF of the range 20% … 30% or 30% … 40% (Figure 3-38 d,e)). The difference SICCI-2 SIC minus MODIS ISF seems to be a good approximation of the MPF (see Figure 3-38 a). In images b) to e) of Figure 3-38 we find that this difference falls out of the MPF range used but not by more than 5% for MPF < 20%. For MPF > 20%, however, we find that the difference SICCI-2 SIC minus MODIS ISF is smaller than the MPF by up to 8% during June (Figure 3-38 d) and by between 5% and 10% during May/June/July (Figure 3-37 e). The cause of it requires further examination and discussion.
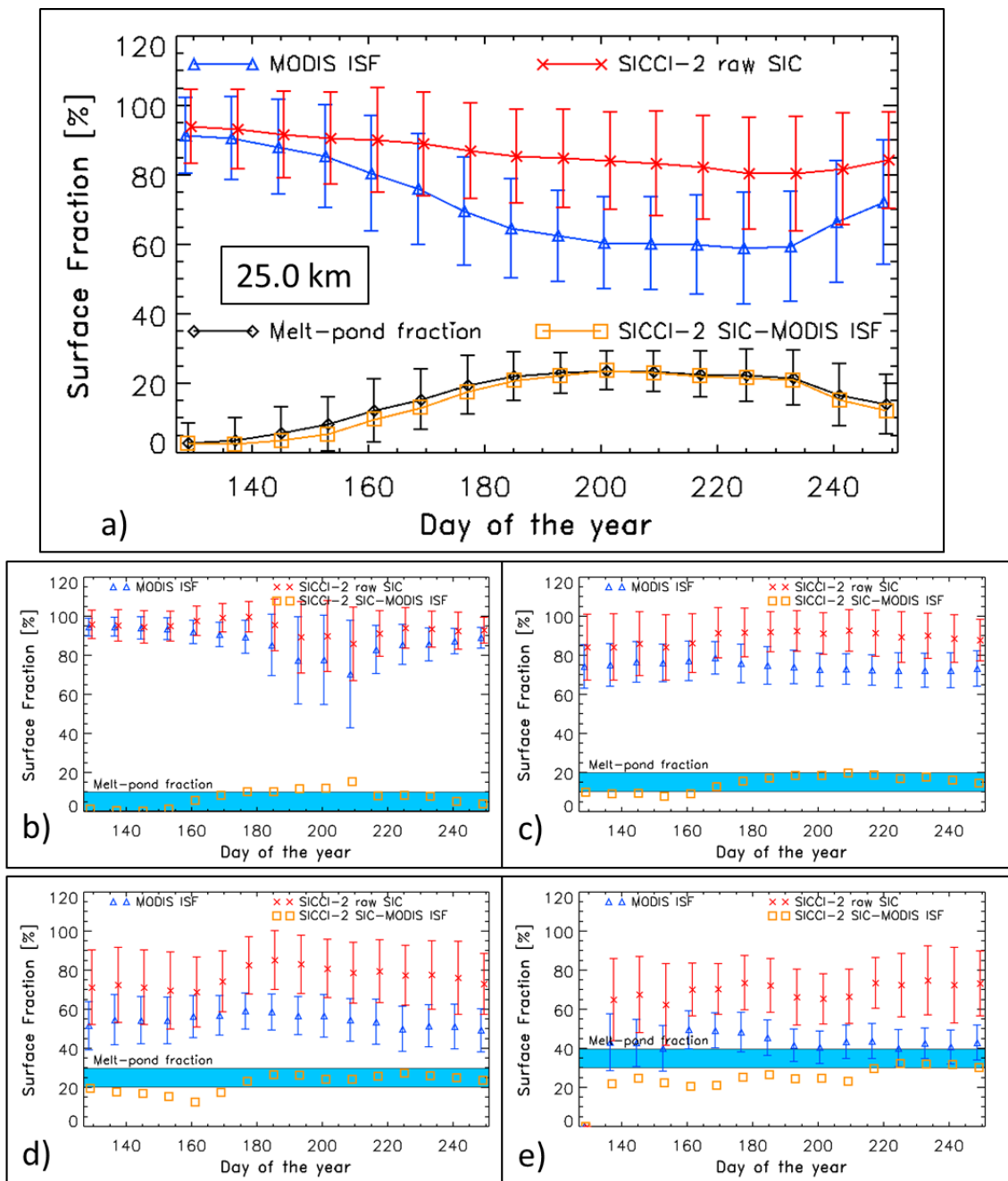
Figure 3-38: Summary of the comparison between MODIS SIC and ISF and SICCI-2 SIC based on SICCI-LF (25.0 km). Image a) Time series of the pan-Arctic mean SICCI-2 SIC (red), MODIS ISF (blue), MODIS MPF (black) and difference SICCI-2 SIC minus MODIS ISF (orange). Image b) to e) Time series of the same parameters as in image a) except that MODIS MPF is used to constrain the data of the time series shown to certain MPF ranges. These ranges are 0%-10%, 10%-20%, 20%-30% and 30%-40% and are illustrated in every image by the horizontal cyan bar. All vertical bars denote plus/minus one standard deviation of the mean.
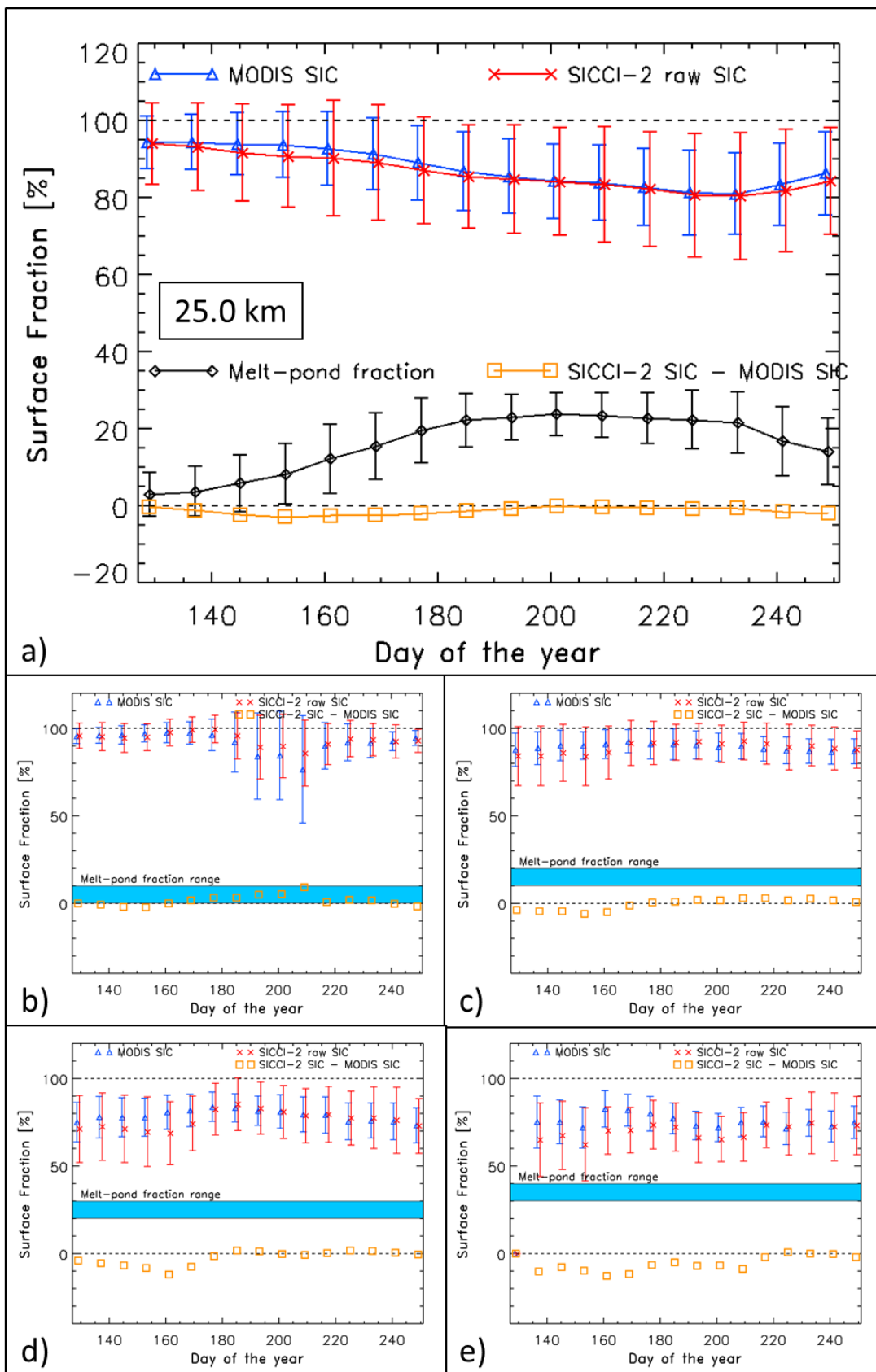
Figure 3-39: As Figure 3-38 except that instead of MODIS ISF we use MODIS SIC.

Multi-annual pan-Arctic mean values of the SICCI-2 SIC agree quite close to the respective MODIS SIC values as illustrated in Figure 3-39 a). The difference between both average values is < 5% for all 8-day periods. We break down this analysis again to the same MPF ranges as described in the previous paragraph in the context of Figure 3-38. In that case we observe elevated positive differences (up to 10%) during July for MPF 0% … 10% (Figure 3-39 b), elevated negative differences (up to -13%) during June for MPF 20% … 30% (Figure 3-39 d) and differences around -10% for May/June/July for MPF 30% … 40% (Figure 3-39 d). During June, when the sea-ice cover is still quite compact with close-to-100% sea-ice area fraction, these differences can most likely attributed to an under-estimation of SICCI-2 SIC caused by an increasing melt-pond fraction (see Figure 3-39 a) because it is most pronounced for cases with MPF > 20%. The fact that these differences do not increase further during July/August could be related to a change in the radiometric surface properties of the sea ice, counterbalancing the impact the melt ponds have on the brightness temperatures used to compute the SIC – as hypothesized e.g. in Kern et al. ([RD-14]).

In Figure 3-40 and Figure 3-41 we show the results obtained using the coarse resolution product of SICCI-VLF (50.0 km). For the results with the multi-annual pan-Arctic mean ISF the direct comparison of Figure 3-38 and Figure 3-40 reveal only minor differences. The performances of SICCI-LF and SICCI-VLF are similar in this global view. The most notable differences occur in image e) where for May through July the difference SICCI-2 SIC minus MODIS ISF seems to be smaller for SICCI-VLF than for SICCI-LF by a few percent for some of the 8-day periods. This would mean that for cases with high MPF (30% - 40%) SICCI-VLF provides lower SIC values which are slightly closer to the physically more meaningful ISF than SICCI-LF. This is confirmed by Figure 3-41 d) and e) for May/early June and May through July, respectively, by values of the difference SICCI-2 SIC minus MODIS SIC being slightly more negative for SICCI-VLF than for SICCI-LF (compare Figure 3-39 d) and e)).

In Figure 3-42 and Figure 3-43 we show the results obtained using the fine resolution product of SICCI-HF (12.5 km). For the results with the multi-annual pan-Arctic mean ISF the direct comparison of Figure 3-38 and Figure 3-42 reveal only minor differences. The performances of SICCI-LF and SICCI-HF are similar in this global view. We note that the tendency of SICCI-HF to provide SIC > 100% in May and particularly in June (see Figure 3-97) results in multi-annual pan-Arctic mean SIC values of ≥ 100% for low MPF (0% - 10%) during June Figure 3-42 b), Day of year 160-180); during this period mean SIC values reach but do not exceed 100% for the other two algorithms (image b) of Figure 3-38 and Figure 3-40). Differences between SICCI-HF SIC and MODIS-SIC as illustrated in Figure 3-43 are very similar to those for SICCI-LF (Figure 3-39).

Table 3-20 through Table 3-22 summarize the results from Figure 3-38 through Figure 3-43. These tables confirm that the performance of all three products is similar. Overall differences between SICCI-2 SIC and MODIS SIC are < 2%; when breaking down these differences to MPF ranges then SICCI-2 SIC tends to over-estimate MODIS SIC by ~ 2% for low MPF and to underestimate MODIS SIC by ~5% for high MPF. The already discussed over-estimation of MODIS-ISF by SICCI-2 SIC is of the same order of magnitude as the MPF for MPF < ~20% but becomes smaller than the MPF for MPF > ~20%; it is ~10% less for MPF ~ 35%. This indicates that at least for high MPF the algorithms correctly identify a certain fraction of melt ponds as open water.
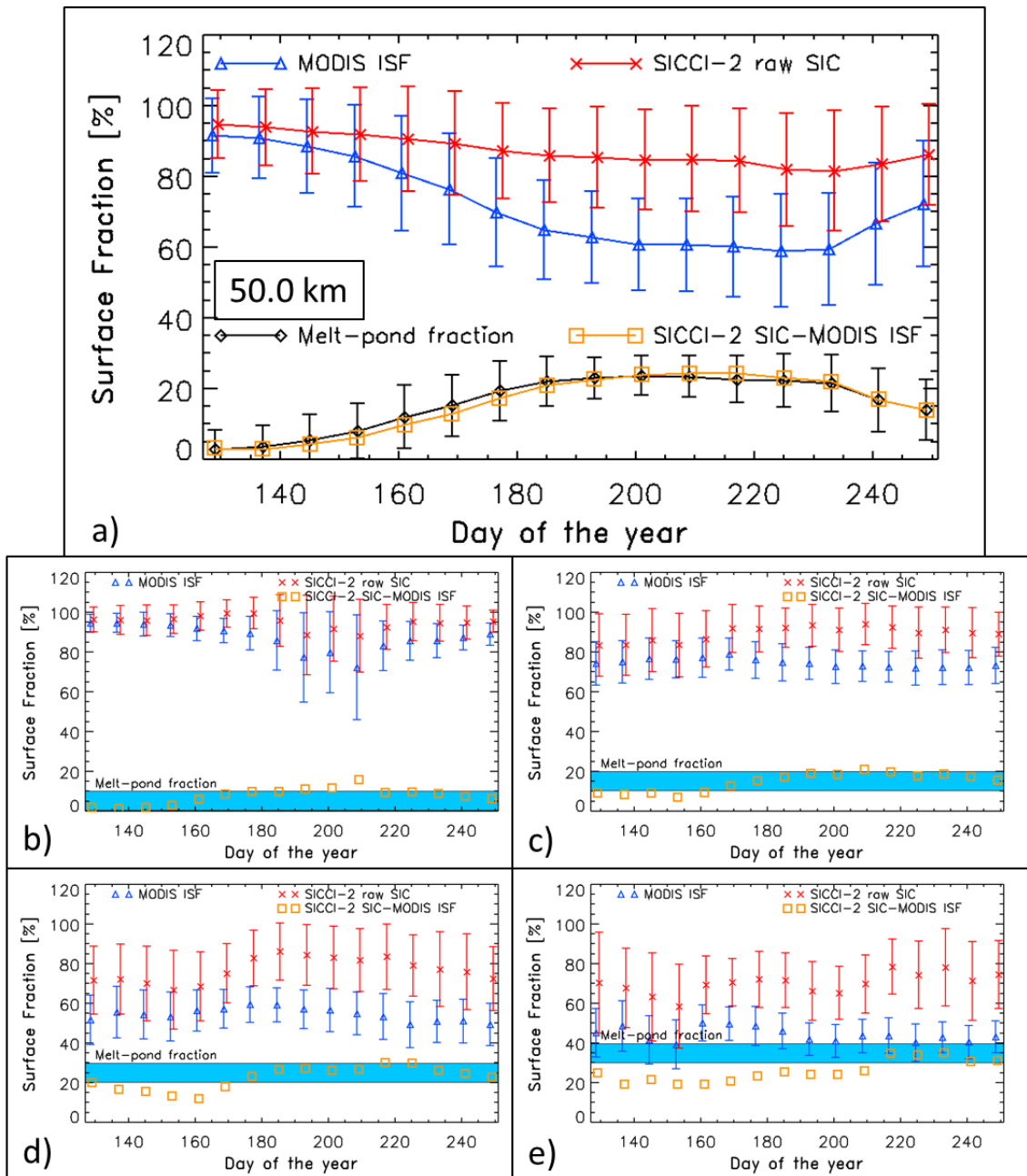
Figure 3-40: As Figure 3-38 but using data from the SICCI-2 SICCI-VLF (50.0 km) product.
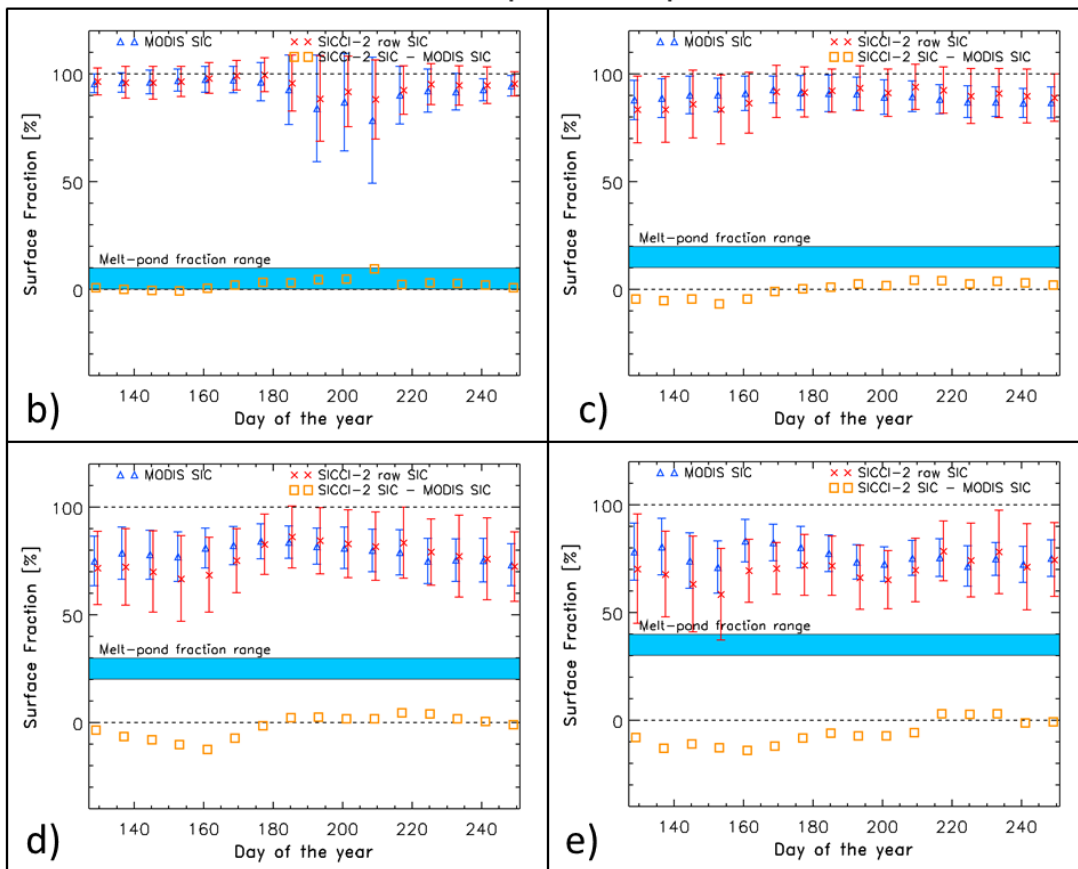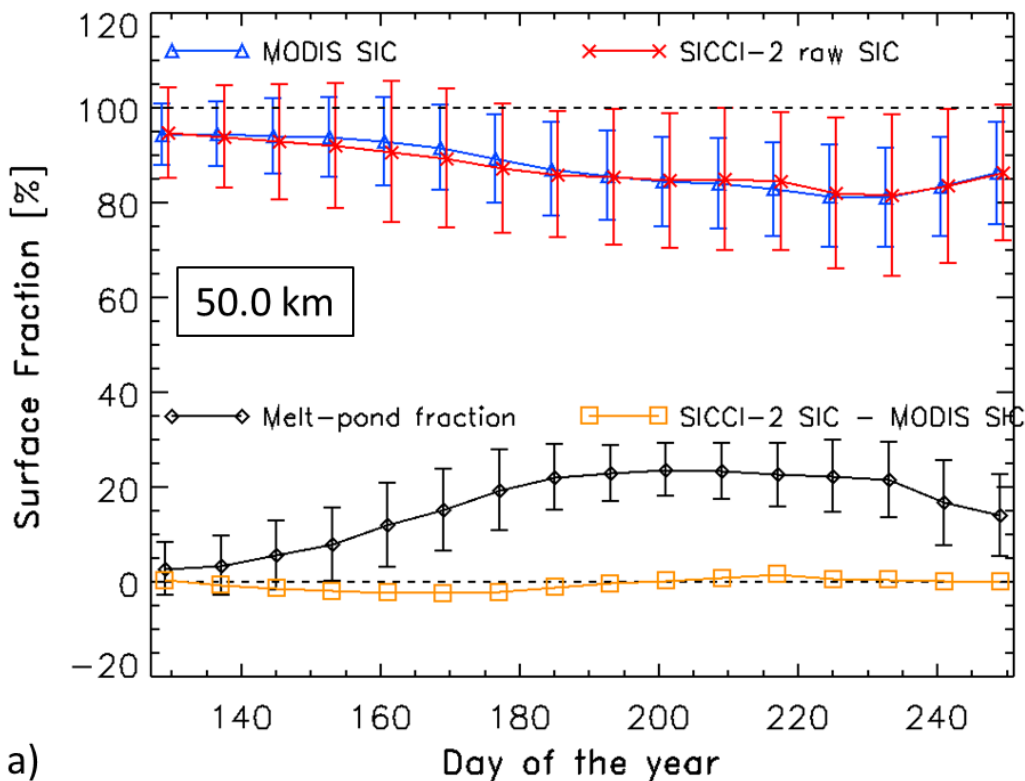
Figure 3-41: As Figure 3-39 but using data from the SICCI-2 SICCI-VLF (50.0 km) product.
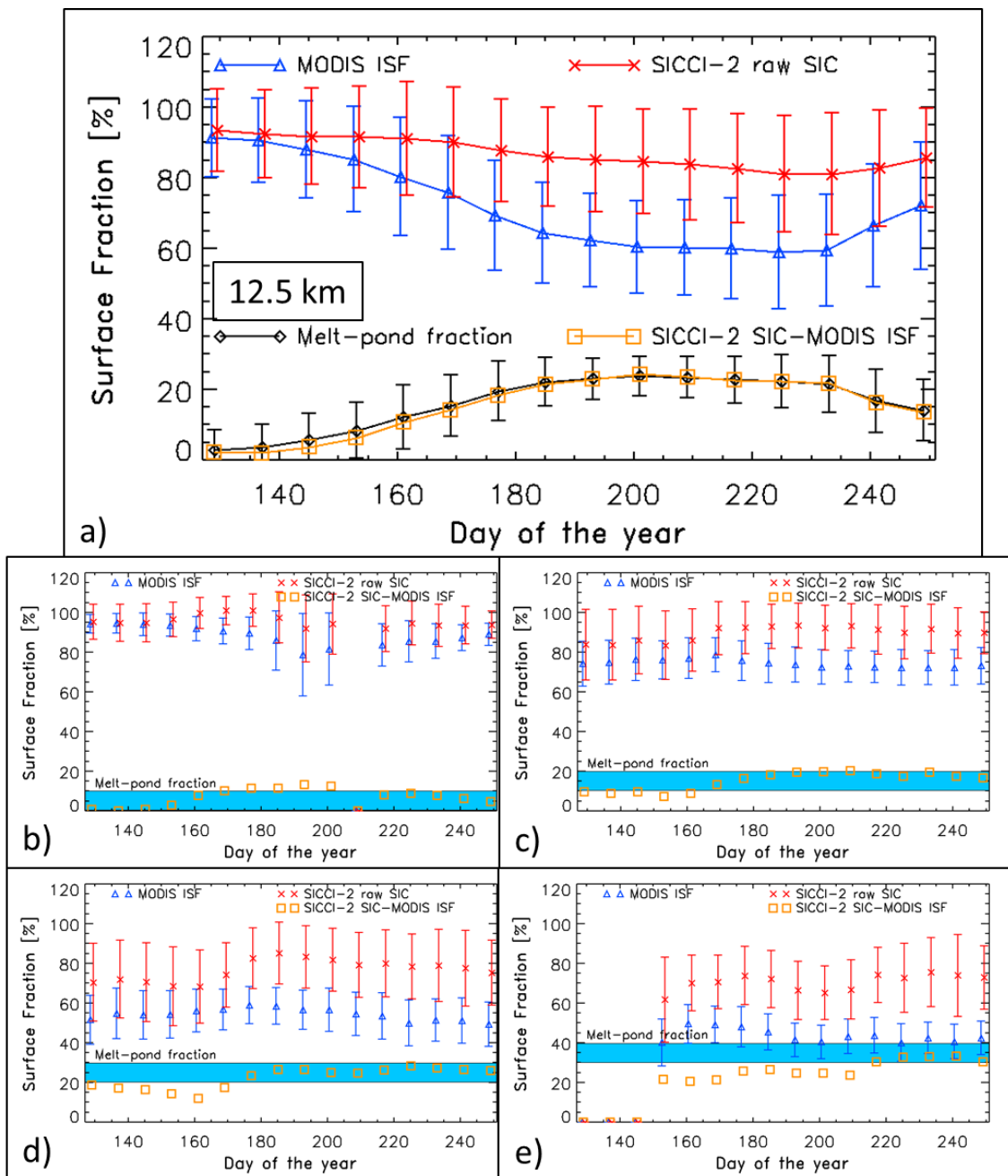
Figure 3-42: As Figure 3-38 but using data from the SICCI-2 SICCI-HF (12.5 km) product.
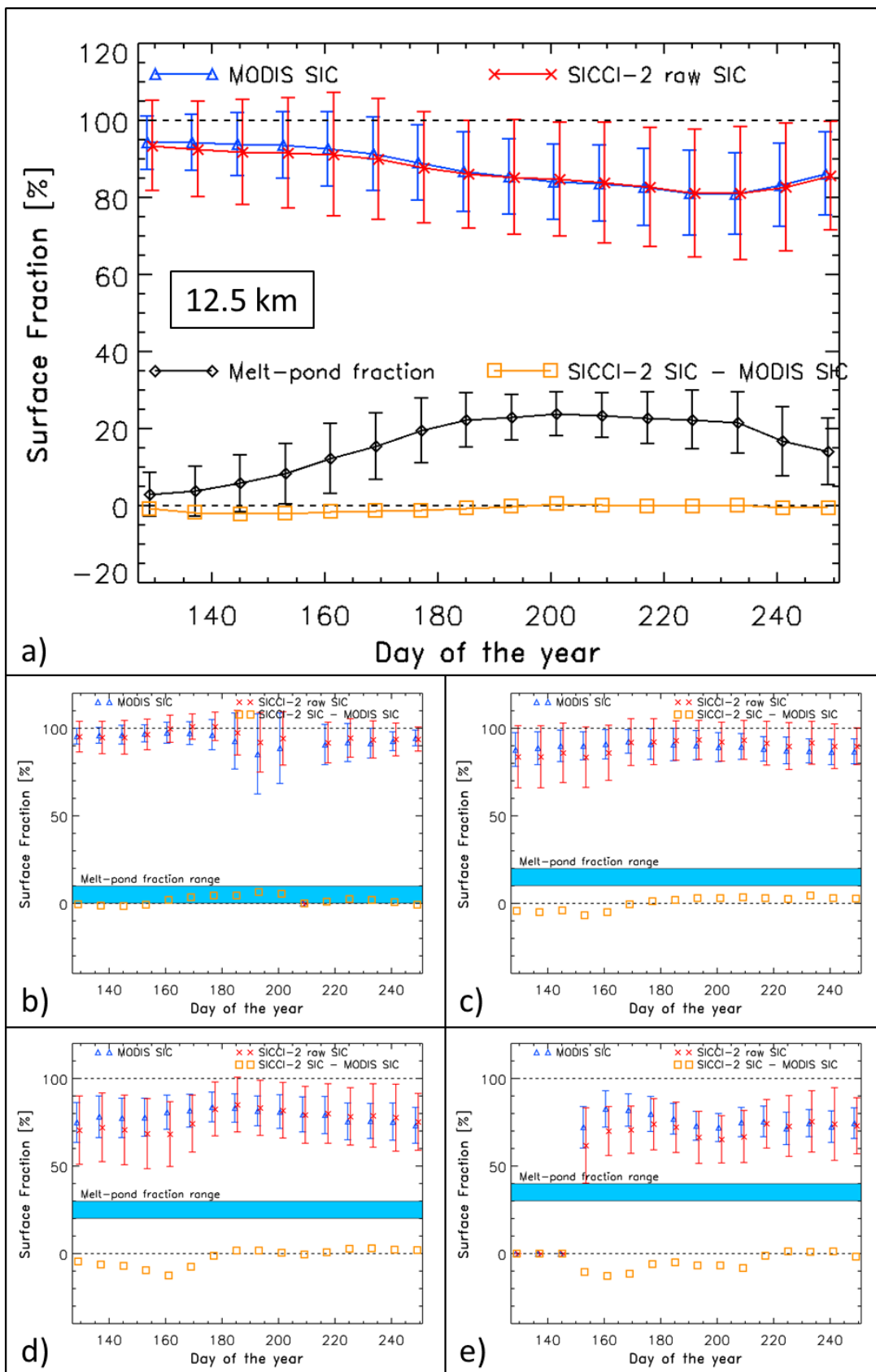
Figure 3-43: As Figure 3-39 but using data from the SICCI-2 SICCI-HF (12.5 km) product.

Table 3-20: Overall mean difference SICCI-2 SIC minus MODIS ISF and its standard deviation for the entire Arctic for 2003-2011 for the four MODIS MPF ranges given in the left column.

SICCI-2 SIC minus MODIS ISF	SICCI-HF	SICCI-LF	SICCI-VLF
MPF 0% - 10%	7.2% ± 4.3%	7.0% ± 4.4%	7.8% ± 4.0%
MPF 10% - 20%	15.2% ± 4.5%	14.6% ± 4.4%	14.9% ± 4.5%
MPF 20% - 30%	22.4% ± 5.2%	22.0% ± 4.5%	22.6% ± 5.6%
MPF 30% - 40%	26.9% ± 4.5%	26.1% ± 4.0%	26.0% ± 5.5%

Table 3-21: Overall mean difference SICCI-2 SIC minus MODIS SIC and its standard deviation for the entire Arctic for 2003-2011 for the four MODIS MPF ranges given in the left column.

SICCI-2 SIC minus MODIS SIC	SICCI-HF	SICCI-LF	SICCI-VLF
MPF 0% - 10%	2.0% ± 2.5%	1.7% ± 3.0%	2.5% ± 2.4%
MPF 10% - 20%	0.3% ± 3.7%	-0.3% ± 3.1%	0.0% ± 3.7%
MPF 20% - 30%	-2.0% ± 4.8%	-2.4% ± 4.2%	-1.9% ± 5.2%
MPF 30% - 40%	-5.0% ± 4.7%	-5.8% ± 4.2%	-6.0% ± 5.7%

Table 3-22: Overall mean difference SICCI-2 SIC minus MODIS SIC and its standard deviation for the entire Arctic for 2003-2011. Unfiltered SIC is the one used in this section (see also Table 3-21); "Filtered SIC" is the product where SIC < 0% and > 100% are set to 0% and 100%, respectively.

SICCI-2 SIC minus MODIS SIC	SICCI-HF	SICCI-LF	SICCI-VLF
Unfiltered SIC	-1.3% ± 1.2%	-1.7% ± 1.1%	-0.7% ± 1.4%
Filtered SIC	-0.7% ± 0.8%	-1.4% ± 0.9%	-0.5% ± 1.2%

Daily melt-pond cover fraction

From the ESA-SICCI project phase-1 a tailored daily melt-pond fraction data set exists which is based on daily MODIS data and which was used for inter-comparison of SICCI-1 SIC data. This product spans over the months June through August of the year 2009, has daily temporal resolution, and has the same characteristics and parameters as the 8-daily MODIS MPF and SIC data set used above. We carried out an investigation using also this data set which is illustrated in terms of its content in Figure 3-44 and Figure 3-45.
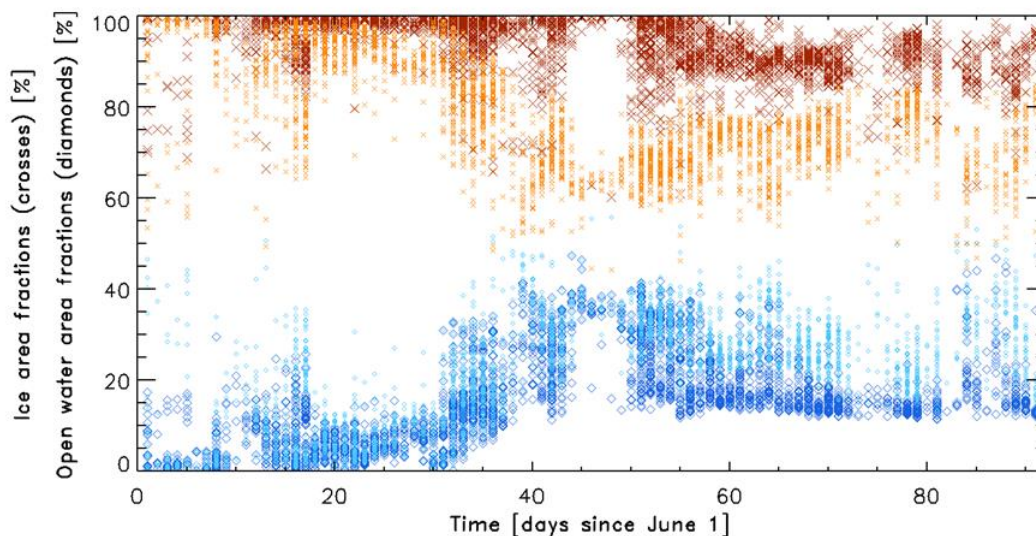
Figure 3-44: Time series of the sea-ice area fractions (crosses) and open water area fractions (diamonds) of the daily MODIS MPF and SIC data set. Large crosses denote the MODIS SIC, small crosses denote the MODIS ISF. Large diamonds denote the MODIS MPF, small diamonds denote the total open water fraction, i.e. the water of leads and openings between the ice floes and the water on top of the sea ice, the melt ponds.
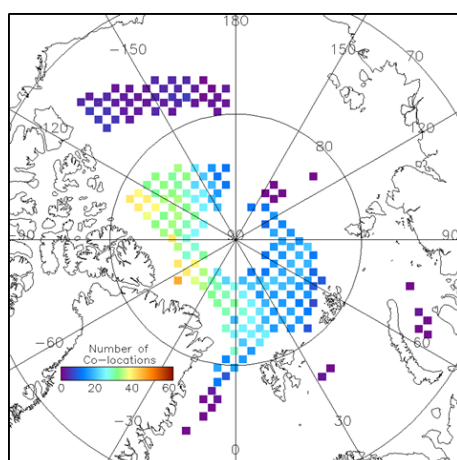
Figure 3-45: Distribution of the daily MODIS MPF/SIC/ISF data set together with the number of co-located SICCI-2 SIC grid cells. For the comparison shown in the next figures, the locations in the Kara Sea, Barents Sea and Greenland Sea south of 80°N have been excluded.
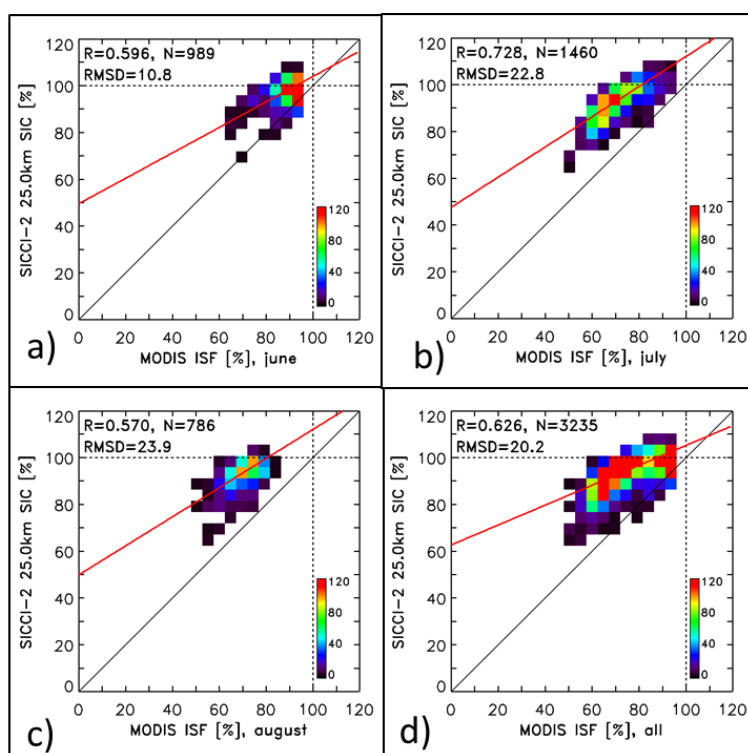
Figure 3-46: SICCI-2 SICCI-LF (25.0 km) SIC versus MODIS ISF for, from a) to c): June, July, and August, and for the entire period (d). Binsize is 5%. Black line is the 1-to-1 line. Red line is the linear regression through the data pairs. The number of data pairs, the root-mean-squared difference (RMSD) and the linear correlation coefficient R are given in every image's upper left corner.

Figure 3-46 a) is of the same type as Figure 3-31, bottom row, and shows a similar distribution of data pairs with a similar location and slope of the regression line for the comparison shown in Figure 3-31, bottom row, which is also for June. For July (Figure 3-46 b) we find a very clear indication that SICCI-LF SIC over-estimates MODIS ISF by an increasing amount the smaller the ISF gets. This over-estimation is ~15% for ISF = ~90% and ~20% for ISF = ~60% (compare Figure 3-33, yearday 185 and 193, and Figure 3-35, yearday 201). The same degree of over-estimation also holds for August (Figure 3-46 c). Note that this daily MODIS data set is far more sparsely distributed over the Arctic Ocean. It should therefore not be expected that the distribution of data pairs is exactly the same as for the 8-daily product. The overall view – which is illustrated in Figure 3-46 d) – confirms the picture: MODIS ISF is over-estimated by SICCI-LF the more the smaller the ISF gets.

Figure 3-47 shows a similar set of scatterplots as Figure 3-46 except that this time MODIS SIC is shown instead of MODIS ISF. Without going into detail also this set of scatterplots resembles similar characteristics as the respective scatterplots obtained for the 8-daily MODIS product shown in the middle row of Figure 3-31, Figure 3-33, and Figure 3-35. We observe a great deal of over-estimation of MODIS SIC at particularly high sea-ice area fractions but also a substantial amount of under-estimation – without a clear preference of either of these.
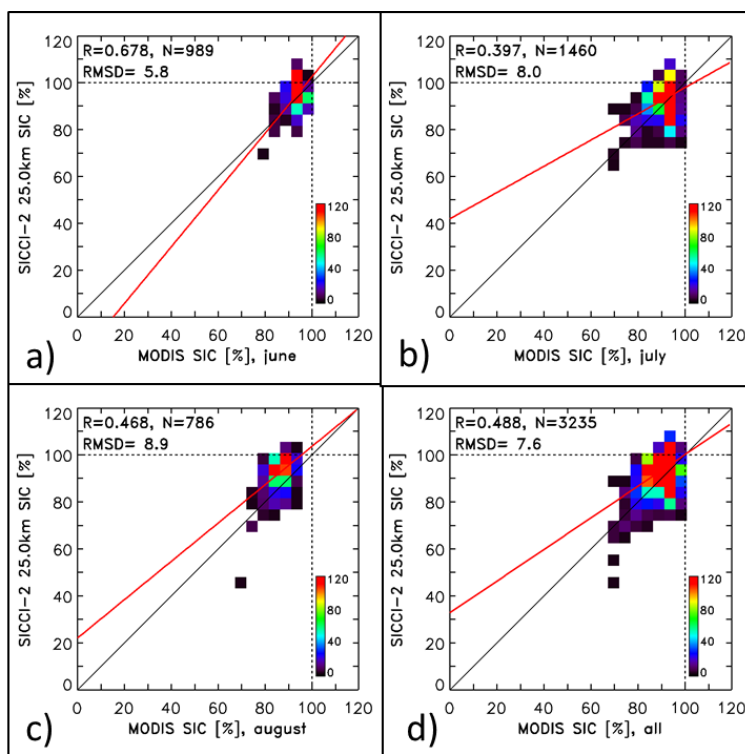
Figure 3-47: As Figure 3-46 but using MODIS SIC instead of MODIS ISF.
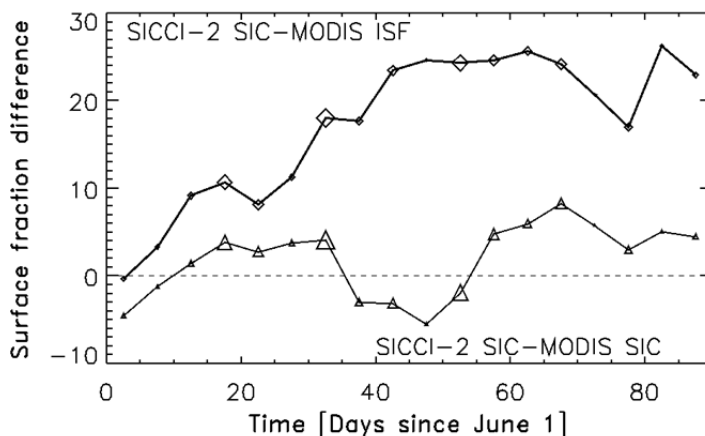
Figure 3-48: Time-series of the 5-day mean difference SICCI-2 (SICCI-LF, 25.0 km) SIC minus MODIS SIC (triangles) and the 5-day mean difference SICCI-LF SIC minus MODIS ISF (diamonds). Symbols are scales linearly with the number of valid data pairs used to compute the mean values.

Also with the daily MODIS SIC/ISF data set we observe a relatively small difference between SICCI-2 and MODIS SIC, varying basically in the range -5% … +5%. Similarly to results discussed above SICCI-2 over-estimates MODIS ISF and this over-estimation seems to increase with MPF because the difference SICCI-2 SIC minus MODIS ISF is close to zero beginning of June, increases during June to ~18% and further until peak melt in July to ~ 25% and tends to stay at that level and/or decrease by a few percent by

the end of August. This agrees well with the findings illustrated in, e.g., Figure 3-38 a) and Figure 3-29 as well as in Table 3-21.

3.5   SICCI SIC versus ASPeCt and IceWatch/ASSIST ship-based sea-ice observations

Visual ship-based observations provide a good measure of the sea-ice conditions and have been used for inter-comparison studies and SIC evaluation in the Antarctic [e.g. RD-15; RD-16, RD-17] but are also available for the Arctic.

According to the ASPeCt protocol http://www.aspect.aq ship-based observations of the sea ice conditions shall be carried out every hour, at least every second hour, during daylight conditions while the ship is traversing the sea ice. Observations shall be carried out from the ship's bridge within an area of about 1 kilometer around the ship and shall report ice conditions as follows: total ice concentration, type of openings, concentration, thickness, ridge fraction and height, snow depth and type of up to three ice types (see also [RD-18]).
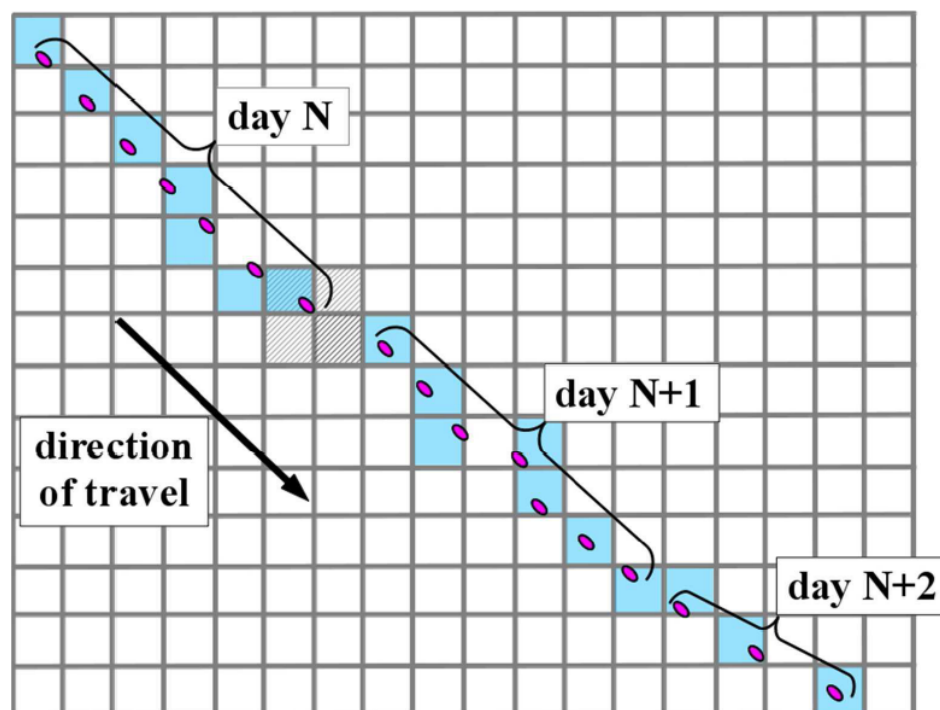
Figure 3-49: Illustration of the co-location of satellite measurements (blue and shaded boxes) and ASPeCt ship-based observations (purple dots).

As described in Beitsch et al. [RD-17] the difference in the spatio-temporal statistics between the satellite observations and the ship-based observations could be mitigated by inter-comparing both data sets on the basis of daily averages of the along-track sea-ice concentration [RD-17]. Ship-based observations of one day are co-located to grid cell centers of the contemporary daily average sea-ice concentrations. The co-located data are then averaged over each day. Cases with less than three contemporary observations per day are discarded.

We have been updating the ASPeCt ship-based sea-ice observations data base from SICCI phase 1 for the Antarctic, focusing solely on the period during which AMSR-E and AMSR2 data are available. The data used stem only partly from the original ASPeCt data base (see above) because that one ends in 2005. Since then ASPeCt data have been collected at ICDC from various sources, compiled partly in Beitsch et al. [RD-17], have been provided by AWI personnel, e.g. Sandra Schwegmann, Marcel Nicolaus, by ACE-CRC, e.g. Jan Lieser and Petra Heil (personal communication, 2016, ACE-CRC, Hobart Tasmania), by Steve Ackley (personal communication, 2015, University of San Antonio, Texas, U.S.) or which have been obtained via the PANGAEA data portal. Table 3-23 summarizes cruise and/or ship name together with its period and source [RD-17 through RD-23].

Table 3-23: List of cruises into Antarctic waters from which ASPeCt ship-based sea-ice observations are used. Highlighted in yellow are cruises which have not yet been included into the harmonized data file.

Cruise name	Ship	First day	Last day	Source
GLOBEC-2002	Laurence M. Gold	2002-08-01	2002-09-12	ASPeCt
McMurdo Supp.	Nathaniel B. Palmer	2002-12-17	2002-12-31	ASPeCt
ANT XX/2	Polarstern	2002-12-04	2003-01-03	ASPeCt
ANSLOPE-2003	Nathaniel B. Palmer	2003-03-01	2003-04-02	ASPeCt
ARISE	Aurora Australis	2003-09-23	2003-10-23	ASPeCt
ANSLOPE-2004	Nathaniel B. Palmer	2004-02-23	2004-04-02	ASPeCt
n.n.	Aurora Australis	2004-10-16	2004-11-07	ASPeCt
ISPOL	Polarstern	2004-11-13	2005-01-05	ASPeCt
ANT XXII/3	Polarstern	2005-02-12	2005-03-25	ASPeCt
Maudness	Nathaniel B. Palmer	2005-07-30	2005-09-07	ASPeCt
WWOS	Polarstern	2006-09-05	2006-10-21	Beitsch et al.
McMurdo Supp.	Oden	2006-12-19	2006-12-26	Beitsch et al.
SIMBA	??	2007-09-24	2007-10-27	Beitsch et al.
SIPEX-I	Aurora Australis	2007-09-09	2007-10-11	ACE-CRC / AAD
McMurdo Supp.	Oden	2007-12-05	2008-01-03	Beitsch et al.
n.n.	Aurora Australis	2008-10-19	2008-11-14	ACE-CRC / AAD
McMurdo Supp	Oden	2008-12-10	2009-01-09	Beitsch et al.
n.n.	Nathaniel B. Palmer	2009-01-11	2009-02-16	Beitsch et al.
n.n.	Aurora Australis	2009-11-08	2009-11-27	ACE-CRC / AAD

n.n.	Aurora Australis	2010-11-01	2010-11-23	ACE-CRC / AAD
IceBell	Nathaniel B. Palmer	2010-11-11	2011-01-09	S. Ackley
n.n.	Oden	2010-12-15	2011-01-09	S. Ackley
SIPEX-II	Aurora Australis	2012-09-22	2012-11-11	ACE-CRC / AAD
AWECS	Polarstern	2013-06-17	2013-08-08	AWI
ANT XXIX/7	Polarstern	2013-08-28	2013-10-06	AWI
ANT XXIX/9	Polarstern	2013-12-28	2014-21-02	AWI
ANT XXX/2	Polarstern	2014-12-14	2015-01-18	AWI
ANT XXXI/2	Polarstern	2015-12-13	2016-02-08	AWI
n.n.	Aurora Australis	2016-11-04	2016-11-23	ACE-CRC

In addition to the Antarctic, we also followed up with recent advances with respect to report Arctic sea-ice conditions from aboard ships cruising through the sea ice. A decent collection of Arctic ship-based sea-ice observations collected under the IceWatch/ASSIST (Arctic Ship-based Sea-Ice Standardization) initiative and can be found under the web-based portal icewatch.gina.alaska.edu from which the majority of the data used herein for the Arctic has been taken. Additional sources for ship-based sea-ice observations are PANGAEA (for Polarstern cruises before IceWatch/ASSIST), the Arctic Data Center of the NSF: https://arcticdata.io/catalog/#data, and the data archive of the Bering Sea Ecosystem Study (BEST): https://www.eol.ucar.edu/projects/best/ice.shtml (see [RD-24] through [RD-45]).

Table 3-24: List of cruises into Arctic waters from which IceWatch or other ship-based sea-ice observations are used. Highlighted in yellow are cruises which have not yet been included into the harmonized data file.

Cruise	Ship	First day	Last day	Source
SBI	Healy	2002-05-08	2002-06-14	BEST
ARK XIX/1	Polarstern	2003-03-06	2003-04-21	PANGAEA
SBI	Healy	2004-05-17	2004-06-21	BEST
ARK XX/2	Polarstern	2004-07-24	2004-08-18	PANGAEA
ARK XX/3	Polarstern	2004-09-07	2004-09-23	PANGAEA
JOIS2006	Louis S. Laurent	2006-08-07	2006-09-12	IceWatch
BEST	Healy	2007-04-14	2007-06-10	BEST
JOIS2007	Louis S. Laurent	2007-07-29	2007-08-27	IceWatch

ARK XXII/2	Polarstern	2007-08-01	2007-09-24	PANGAEA
BEST	Healy	2008-03-14	2008-05-04	BEST
JOIS2008	Louis S. Laurent	2008-07-27	2008-08-20	IceWatch
BEST	Healy	2009-01-13	2009-05-09	BEST
JOIS2009	Louis S. Laurent	2009-09-20	2009-10-13	IceWatch
BEST	Polar Sea	2010-03-10	2010-04-05	BEST
JOIS2010	Louis S. Laurent	2010-09-21	2010-10-13	IceWatch
JOIS2011	Louis S. Laurent	2011-07-14	2011-08-14	IceWatch
ARK XXVI/3	Polarstern	2011-08-09	2011-09-19	PANGAEA
n.n.	Healy	2011-11-14	2011-12-12	C. Ashjian
JOIS2012	Louis S. Laurent	2012-08-08	2012-08-29	IceWatch
BeringStrait	Healy	2012-08-11	2012-08-24	BEST
FramStrait	Lance	2012-08-20	2012-09-10	IceWatch
FramStrait	Oden	2012-09-12	2012-09-23	IceWatch
ARK XXVII/3	Polarstern	2012-08-06	2012-10-02	IceWatch
BeringStrait	Healy	2013-07-29	2013-08-14	BEST
JOIS2013	Louis S. Laurence	2013-08-04	2013-08-31	IceWatch
FramStrait	Lance	2013-08-13	2013-09-11	IceWatch
FramStrait	Oden	2013-08-21	2013-08-31	IceWatch
FramStrait	Lance	2014-02-21	2014-02-28	IceWatch
SUBICE	Healy	2014-05-15	2014-06-20	NSF
ARK XXVIII/3	Polarstern	2014-07-10	2014-07-31	IceWatch
BeringStrait	Laurier	2014-07-11	2014-07-23	BEST
FramStrait	Lance	2014-08-25	2014-09-11	IceWatch
JOIS2014	Louis S. Laurence	2014-09-22	2014-10-15	IceWatch
N-ICE	Lance	2015-01-12	2015-03-26	IceWatch
N-ICE	Lance	2015-04-11	2015-06-22	IceWatch
ARK XXIX/1	Polarstern	2015-05-27	2015-06-24	IceWatch

n.n.	50LetPobedy	2015-08-03	2015-08-17	IceWatch
n.n.	Healy	2015-08-18	2015-09-07	IceWatch
FramStrait	Lance	2015-08-25	2015-09-09	IceWatch
JOIS2015	Louis S. Laurent	2015-09-22	2015-10-15	IceWatch
Arctic	Sikuliaq	2015-10-05	2015-11-04	IceWatch
Arctic	50LetPobedy	2016-07-17	2016-08-08	IceWatch
FramStrait	Lance	2016-08-26	2016-09-11	IceWatch

Note that AMSR-E and AMSR2 SIC data will not be investigated separately. Our investigation will focus on the unfiltered versions of all three SICCI 2 sea-ice concentration products.

Evaluation is done at the native grid resolution of the products. Finer resolved SIC data of SICCI-HF (12.5 km grid resolution) and SICCI-LF (25.0 km grid resolution) are not degraded to the grid resolution of the coarsest resolved product SICCI-VLF (50.0 km grid resolution).

Available for the investigation are 7012 and 8280 ship-based sea-ice observations in the Southern and Northern Hemisphere, respectively.

In the following, we show the results separately for the Northern and Southern Hemisphere. We begin with a map showing the distribution of the observations which is followed by the results obtained for all three products for all data. Subsequently, we illustrate how SICCI-2 SIC and ship-based observations (SHIP SIC) compare for summer and winter months. For that we define summer (winter) in the Northern Hemisphere using months May through September (October through April); we define summer (winter) in the Southern Hemisphere using months November through March (April through October).

The comparison is carried via computation of the difference, the root mean square difference (RMSD), and a linear correlation / regression analysis.

Northern Hemisphere
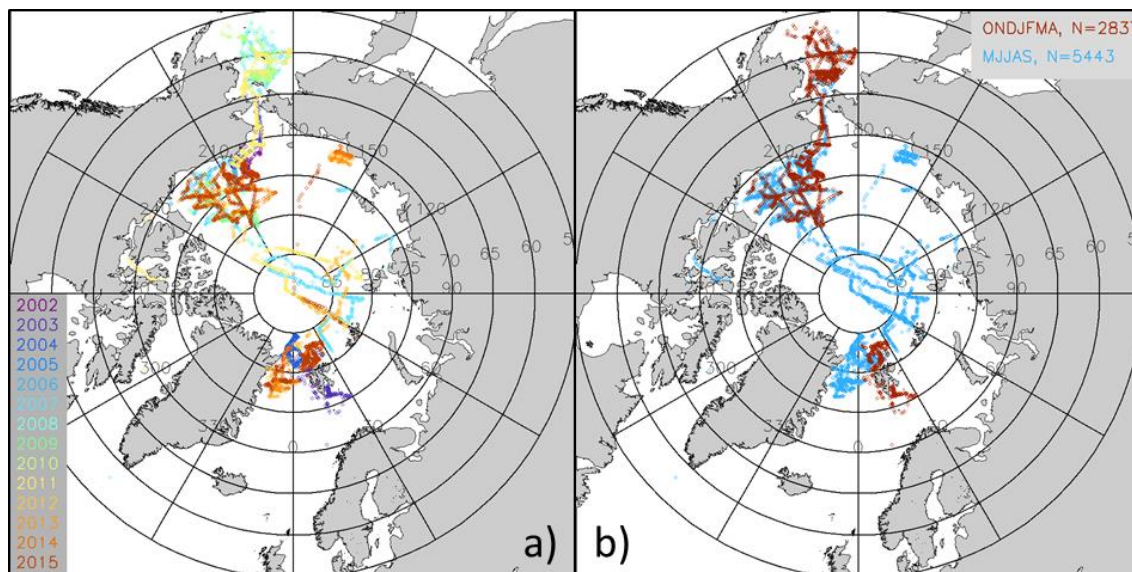
Figure 3-50: Illustration of the distribution of ship-based sea-ice observations in the Northern Hemisphere. Ship tracks are split by year (a) and by season (b). Note that for positions visited repeatedly the last year shows up in image a).

In the Northern Hemisphere ship-observations concentrate on three regions (Figure 3-50): the Beaufort / Chukchi Sea, the Bering Sea, and the Fram Strait region. Few transects cross the Arctic Ocean. Few observations are located in the Laptev and East Siberian Seas. The distribution between summer and winter (Figure 3-50 b) clearly demonstrates that 2/3 of the observations were collected during the five summer months.
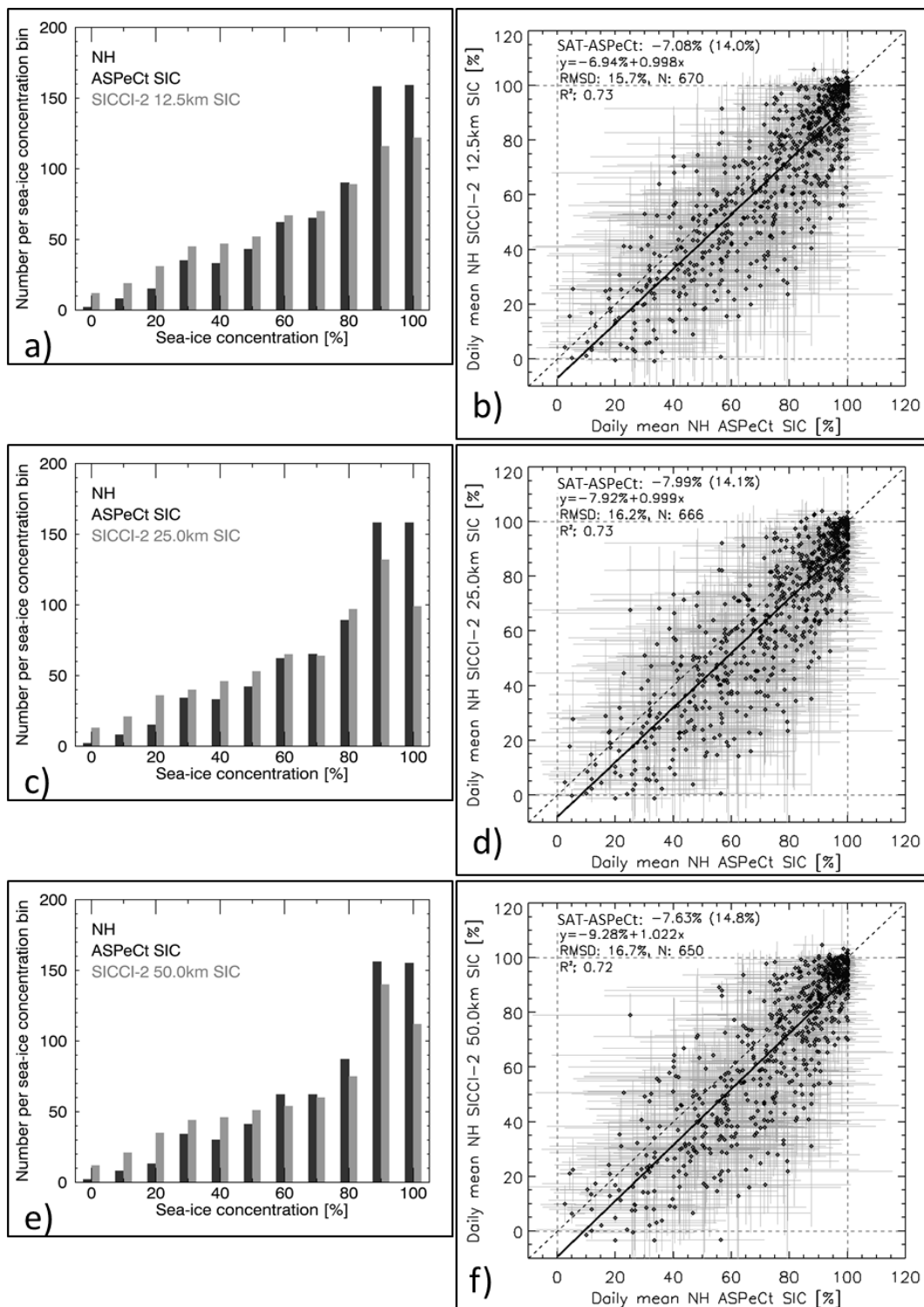
Figure 3-51: Histograms (left) and scatterplots (right) of co-located daily mean ASPeCt and SICCI-2 SIC using all data for, from top to bottom, SICCI-HF (12.5 km), SICCI-LF (25.0km) and SICCI-VLF (50.0km) for the Northern Hemisphere. Bars in scatterplots denote ± 1 standard deviation. "SAT-ASPeCt" is the mean difference SICCI-2 minus ASPeCt SIC together with its standard deviation in parentheses. Also given are the equation of the linear regression, RMSD, number of days with valid data pairs N and the squared linear correlation coefficient R².

Figure 3-51 illustrates how well SICCI-2 SIC data agree with ship-based observations of the SIC (ASPeCt SIC). In the scatterplots (images b, d, and f) the overall mean difference is -7.1%, -8.0% and -7.6% for SICCI-HF, SICCI-LV and SICCI-VLF, respectively, with a similar standard deviation of 14% to 15% for all three algorithms. This negative difference is also reflected by a negative intercept of the linear regression of about -7%, -8% and -9%, respectively. The slope of the linear regression is almost 1 for SICCI-HF and SICCI-LF and slightly larger for SICCI-VLF. Squared linear correlation coefficients take values of 0.72 and 0.73. The root mean square difference RMSD is a bit larger than the standard deviation of the SIC difference and is smallest for SICCI-HF and largest for SICCI-VLF accordingly. Overall the scatterplots suggest a good agreement. We note that we have ~660 days with valid daily mean SIC data pairs.

In the histograms (images a, c, and e), where SIC were binned to: SIC < 5%, 5% ≤ SIC < 15%, 15% ≤ SIC < 25%, … 85% ≤ SIC < 95%, 95% ≤ SIC, a few more details become apparent. In the following, we term these bins 0&%, 10%, 20%, …, 90%, 100%. Note that the accuracy of a single ASPeCt ship-based SIC observations is ~10%. The daily mean ASPeCt SIC observations used here might have a better accuracy given the fact that we average over about 8280 / ~660, i.e. about 12 observations per day. This reduces the accuracy values according to 10% / SQRT(12) = ~ 3% which is possibly a bit too small since subsequent ASPeCt observations might not be independent of each other. We suggest working with an accuracy of 5% therefore. Keeping this in mind the binning into 10% is justified.

All histograms have in common that the largest fraction of observations occupies bins 90% and 100% while the smallest fraction is observed for bins 0%, 10% and 20%. ASPeCt SIC of bins 90% and 100% are observed equally often. SICCI-2 SIC is dominating in bin 90% for SICCI-LF (Figure 3-51 c) and SICCI-VLF (Figure 3-51 e) while most SICCI-HF SIC values fall into bin 100% (Figure 3-51 a). Note that we use the un-filtered SICCI-2 SIC so that a fair amount of SIC values falls below 15% or even 0% and some SIC values exceed 100%. SICCI-2 SIC < 0% are binned into the first bin (SIC < 5%) and SICCI-2 SIC > 100% are binned into the last bin (95% ≤ SIC). All histograms show the same pattern: SICCI-2 SIC has a smaller probability than ASPeCt SIC for higher sea-ice concentrations while the probability of SIC values to fall into low SIC bins is higher for ASPeCt SIC than for SICCI-2 SIC.

For SICCI-HF (12.5 km) (Figure 3-51 a) the probability for bins 90% and 100% is substantially larger for ASPeCt than SICCI-2 SIC; there are about 40 more cases with ASPeCt SIC observations in both bins. Best agreement is number of cases is achieved for bins 60% to 80%; for all other bins with SIC < 60% SICCI-2 SIC has larger probability (by ~ 10 cases) than ASPeCt SIC. For SICCI-LF (25.0km) (Figure 3-51 c) we find the by far largest difference in probabilities for bin 100%: ASPeCt SIC: 159 cases versus SICCI-2 SIC: 99 cases. Also bin 90% is populated more by ASPeCt than SICCI-2 SIC: ~30 cases difference. We find best agreement for bins 60% and 70%. For SICCI-VLF (50.0km) (Figure 3-51 e) we find the same distribution at bins 100% and 90% like for SICCI-LF (Figure 3-51 c) albeit with a considerable smaller difference in the probabilities. Best agreement is observed for bin 70%. Bins 60% and higher are populated more by ASPeCt SIC while bins 50% and lower are populated more by SICCI-2 SIC.

Note that the histograms do not allow to quantify under- or overestimation of the SIC.
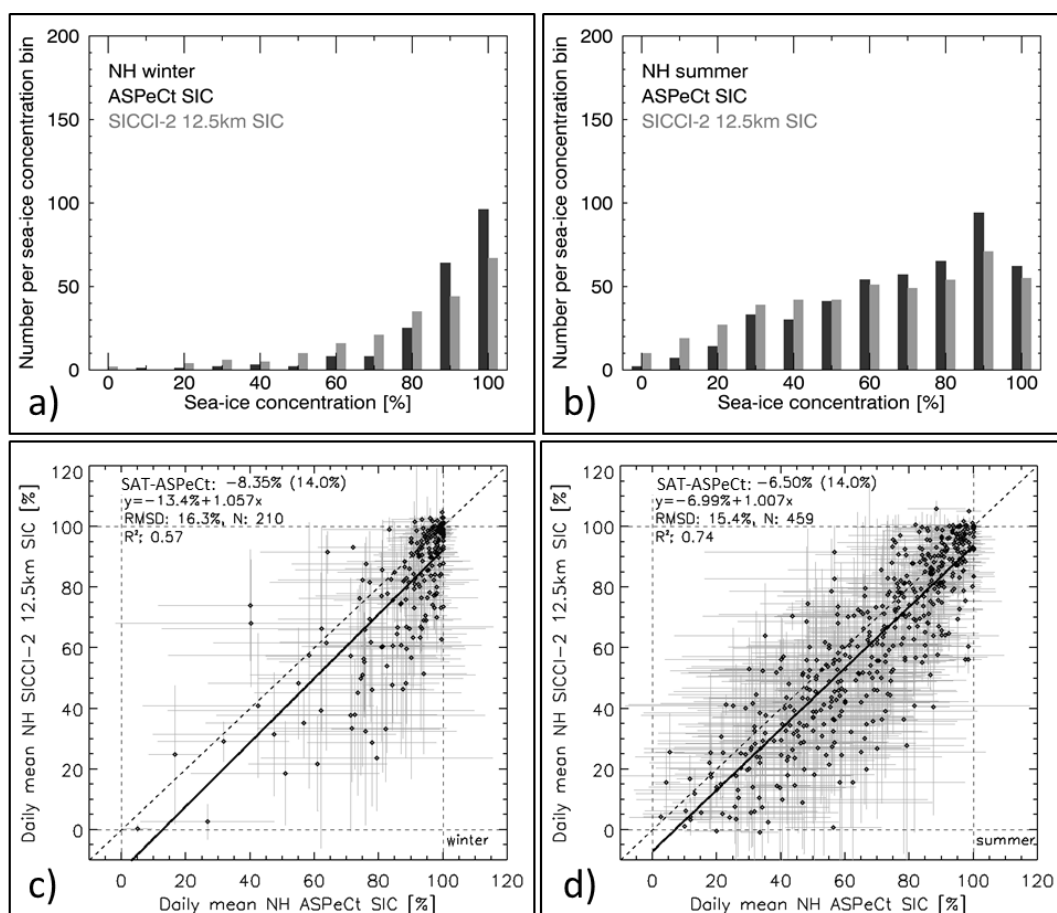
Figure 3-52: As Figure 3-51 but separately for winter (left) and summer (right) for SICCI-HF (12.5km).

In Figure 3-52, Figure 3-53 and Figure 3-54 we split the results shown in Figure 3-51 into winter and summer for SICCI-HF, SICCI-VF, and SICCI-VLF, respectively. These three figures reveal that the good overall agreement shown in Figure 3-51 is merely based on observations from summer (see also Figure 3-51 b). This is not unexpected given the fact that low and medium SIC values, typical for summer conditions, are rarely found during winter.

Common to all three algorithms is that the agreement between ASPeCt SIC and SICCI-2 SIC is better during summer than during winter. This is illustrated by the difference SICCI-2 minus ASPeCt SIC, which is more negative for winter than for summer with summer values being -6.5%, -7.5% and -7.5% for SICCI-HF, SICCI-LF and SICCI-VLF, respectively. Squared correlations are higher during summer. Intercepts of the linear regression are smaller, i.e. closer to zero, and slopes are closer to one during summer.

During winter, about ~20 and ~30 cases less cases with SIC values in bins 90% and 100% are counted for SICCI-HF (Figure 3-52 a,c) than for ASPeCt SIC. Bin 100% is clearly the most populated one in both, ASPeCt SIC and SICCI-HF SIC. Starting at bin 80%, however, the number of SICCI-HF exceeds the number of ASPeCt SIC by between five to ten cases. During summer, SICCI-HF and ASPeCt SIC (Figure 3-52 b, d) agree upon bin 90% as the most populated one even though the probability for SICCI-HF is

considerably smaller than for ASPeCt SIC: ~25 cases. The number of SICCI-HF cases exceeds (falls below) the one of ASPeCt SIC cases for all bins with SIC = 60% or larger (SIC = 40% or smaller). Bin 50% has the best agreement.
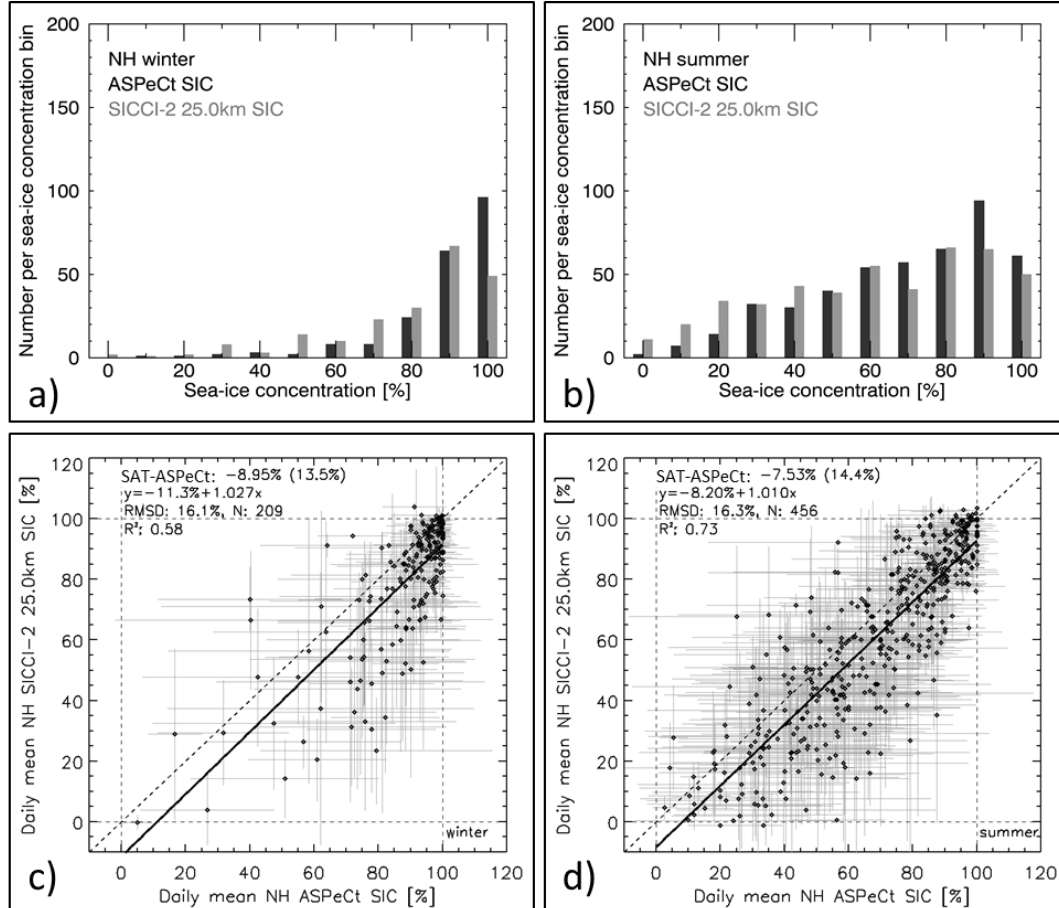
Figure 3-53: As Figure 3-52 but for SICCI-LF (25.0km).

During winter, almost twice as many ASPeCt SIC (97) than SICCI-LF SIC (49) observations fall into bin 100% (Figure 3-53 a). For bin 90%, both data sets differ only by three cases: 63 and 66; accordingly the most populated bin is 100% for ASPeCt SIC but 90% for SICCI-LF SIC. Population of the other bins is small. During summer (Figure 3-53 b), the distribution is similar to that of SICCI-HF (Figure 3-52 b) in terms of bin 90% as most populated bin, with ~25 cases more ASPeCt SIC than SICCI-LF in this bin, and particularly large differences in the number of cases (ASPeCt SIC < SICCI-LF) for bins 20% (20 cases) and 40% (~12 cases) (compare also Figure 3-52 b). We note good agreement with only one to two cases difference for bins 30%, 50%, 60% and 80%.
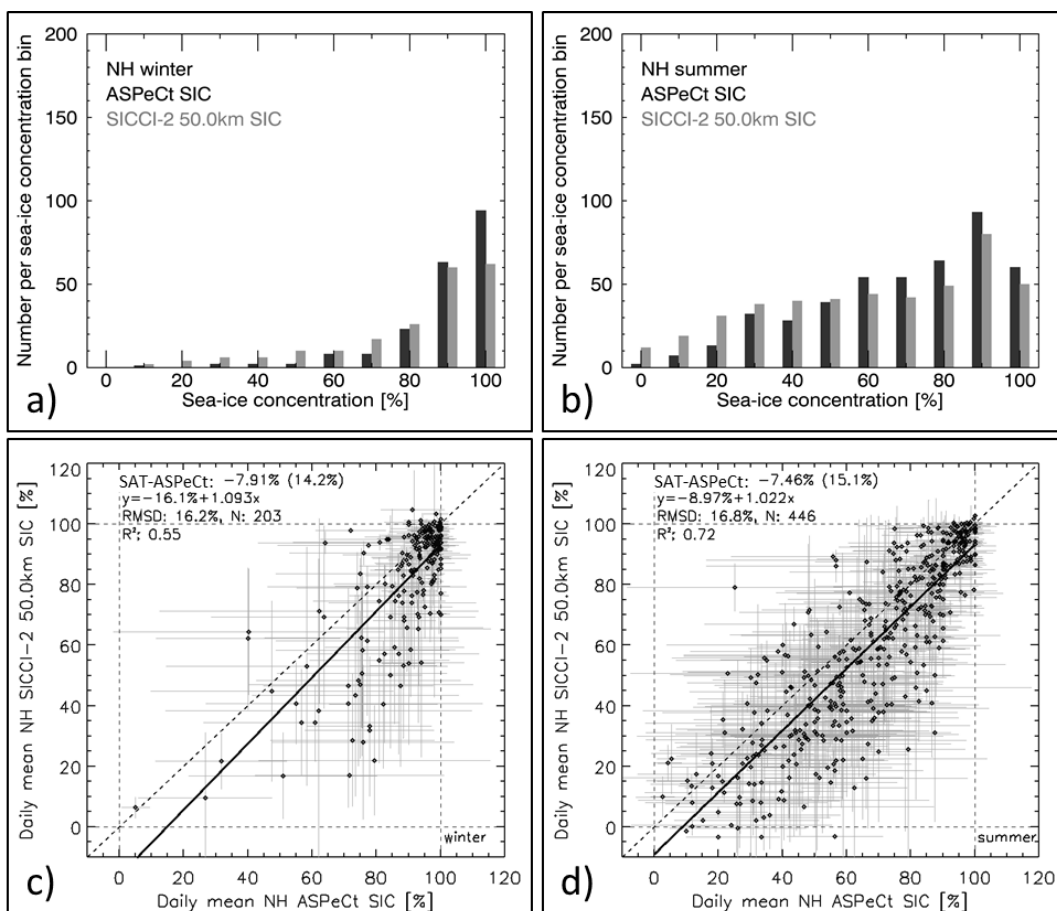
Figure 3-54: As Figure 3-52 but for SICCI-VLF (50.0km).

During winter, SICCI-VLF (Figure 3-54) SIC populate bins 90% and 100% almost equally resulting in ~ 35 but < 5 less cases than ASPeCt SIC for bin 100% and bin 90%, respectively (Figure 3-54 a); agreement at bins 90% and 80% is equally good. During summer (Figure 3-54 b), SICCI-VLF agrees best with the ASPeCt view that bin 90% is the most populated one. In contrast to the other two algorithms (Figure 3-52 and Figure 3-53) but in agreement with the all-year results (Figure 3-51 e), we find about 10-15 less SICCI-VLF cases than ASPeCt SIC in all bins with SIC 60% or larger. Best agreement is achieved for bin 50%.

During summer ASPeCt observations also include data about the melt-pond fraction on sea ice. We extracted this information and computed the net ice surface fraction ISF, i.e. the fraction of ice which is actually at the surface (and not inundated under a melt pond) and therefore is the fraction of the summer-time sea-ice cover a passive microwave satellite sensor is able to detect; note that the penetration depth of microwaves into liquid water is a few millimeters.

Because single ASPeCt observations carried out during one day occasionally recorded a "-9", meaning that no proper estimate of the melt-pond fraction could be carried out despite a SIC estimate exists, daily mean ASPeCt SIC and daily mean SICCI-2 SIC values needed to be recomputed taking only those ASPeCt observations with a valid melt-pond fraction record into account. By subtracting the total ASPeCt melt-pond fraction *MPF*, computed from the melt-pond fractions on the single three ice types observed (if a valid observation exists) via

$$MPF = (SIC1 \times MPF1 + SIC2 \times MPF2 + SIC3 \times MPF3) / SIC$$

Where *SIC* is the total ASPeCt sea-ice concentration, from *SIC*, we obtain the ASPeCt ice-surface fraction *ISF*

$$ISF = SIC - MPF \times SIC$$

Where *MPF* is scaled to range between 0.0 and 1.0.
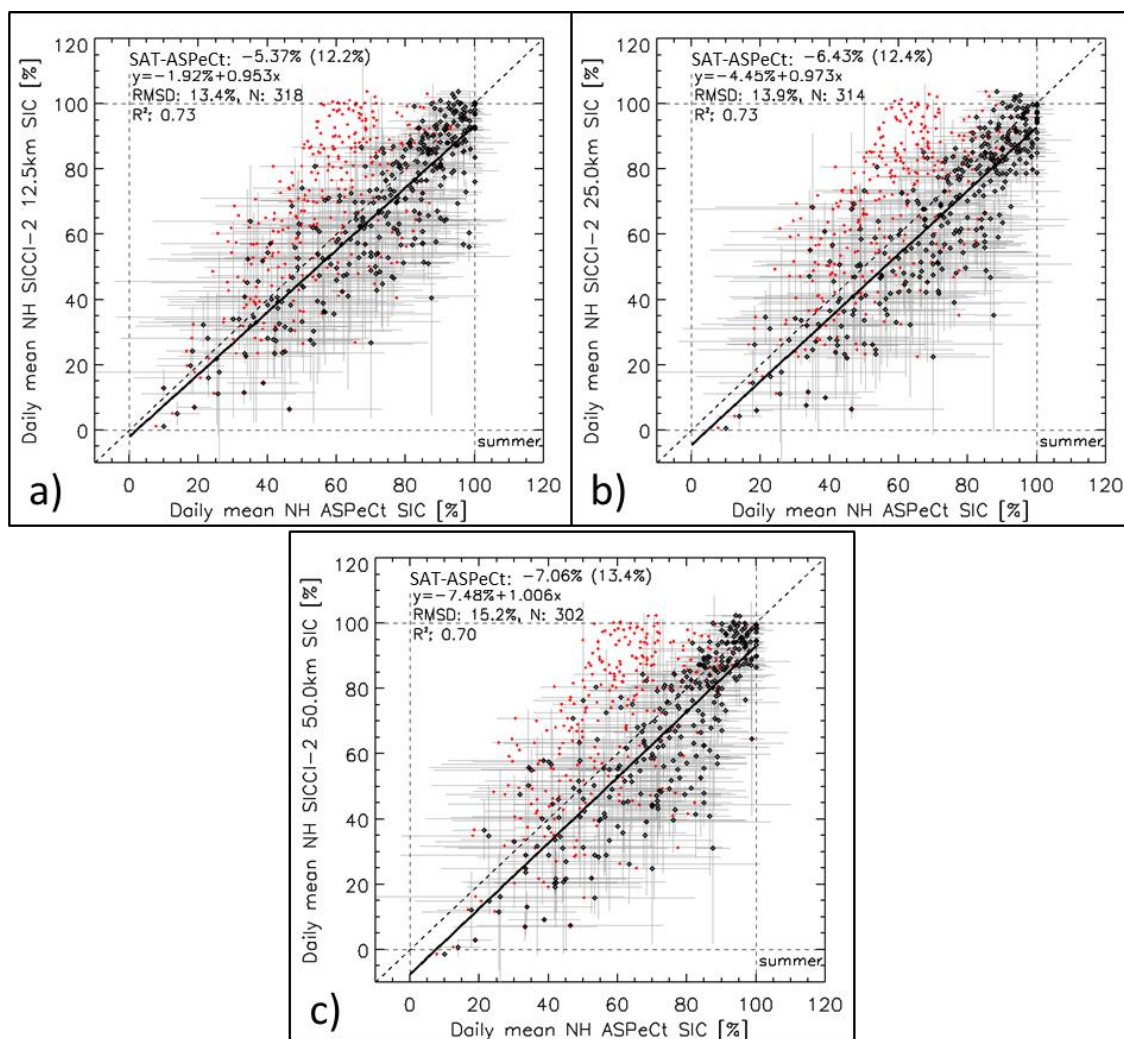
Figure 3-55: Repetition of image d) of Figure 3-52 through Figure 3-54 with a reduced data set (see text for explanation) superposed in red with data pairs of daily mean NH SICCI-2 SIC versus daily mean ASPeCt net ice surface fraction (ISF).

With this reduced data set (compare values of N between Figure 3-55 and image d) of Figure 3-52 to Figure 3-54) the scatterplots between ASPeCt SIC and SICCI-2 SIC (black symbols and regression) are similar to those shown in Figure 3-52 to Figure 3-54, image d). The red symbols denoting the scatterplot between ASPeCt ISF and SICCI-2 SIC are found to align not as good along the 1-to-1 line (black dashed line) as the black symbols do. ASPeCt ISF values are mostly smaller than the corresponding (i.e. at the same SICCI-2 SIC) ASPeCt SIC – as expected. Particularly for SICCI-2 SIC > ~ 80% red symbols are located above the 1-to-1 line by about 30%. In other words, the majority of the SICCI-2 SIC around ~ 90% tends to coincide with ASPeCt ISF values around ~ 60%. This would suggest an overestimation of the ice surface fraction by 30% in this sea-ice concentration range which seems to reduce for smaller sea-ice concentration values.

One needs to keep in mind that the scatter among the data points is truly large but there are a substantial number of red data points which fall out of

ESA UNCLASSIFIED - For Official Use

the range given by the grey bars of SIC standard deviation. We therefore think that despite the uncertainties inherent in the ASPeCt observations of both SIC and MPF there is some value in the illustration given in Figure 3-55. We note that this observation is valid for all three algorithms.
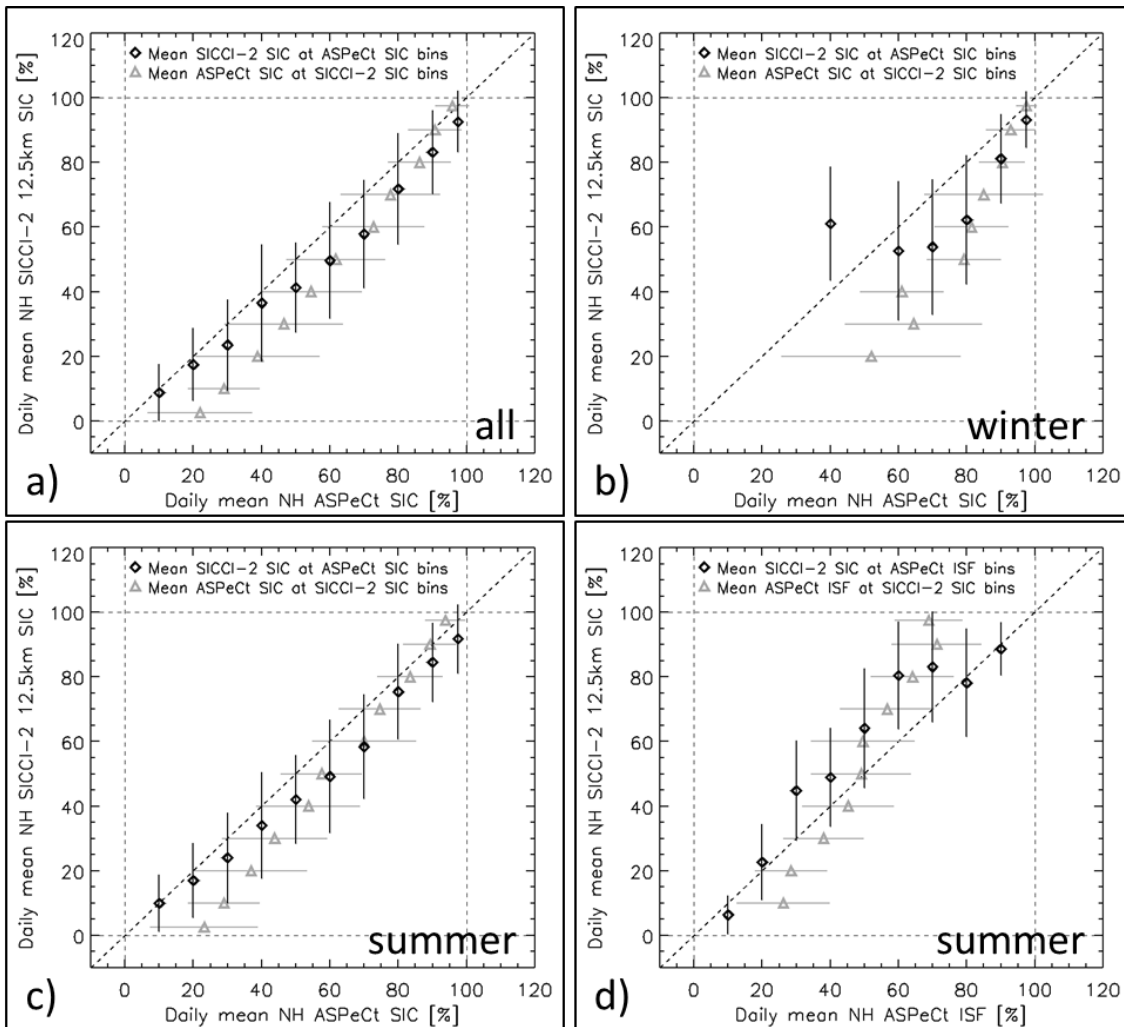
Figure 3-56: Images a) to c): Mean SICCI-2 (here: SICCI-HF, 12.5 km resolution) SIC plus/minus one standard deviation (vertical bars) computed for each ASPeCt SIC bin used in the histograms in Figure 3-52 (black symbols) and mean ASPeCt SIC plus/minus one standard deviation (horizontal bars) computed for SICCI-2 SIC bins of the same bin widths (grey symbols) for the Northern Hemisphere. Image d): as image c) but using the ASPeCt ice surface fraction (ISF) instead of SIC.

We finalize these investigations by showing plots of the mean SICCI-2 SIC computed from all SIC values falling into the same bins used for the histograms shown in Figure 3-52 to Figure 3-54. This way we aim to illustrate whether SICCI-2 SIC matches ASPeCt SIC particularly good or bad in the respective bin and also illustrate the SICCI-2 SIC variation by showing the corresponding standard deviation of the mean. For completeness – since ASPeCt SIC is not necessarily the truth – we also reverse this investigation and compute the mean ASPeCt SIC for the same bins as used above. These mean values are shown together with the corresponding standard deviation in the background of the Figure 3-56 to

Figure 3-58. We show these comparisons using all valid data pairs, the summer pairs, and the winter pairs, and in addition, repeat the computation for the ASPeCt ISF (image d) in Figure 3-56 to Figure 3-58) to illustrate the mismatch between SIC and ISF in a more easy to quantify way. Mean values are not computed in case less than three observations fall into the respective bin.
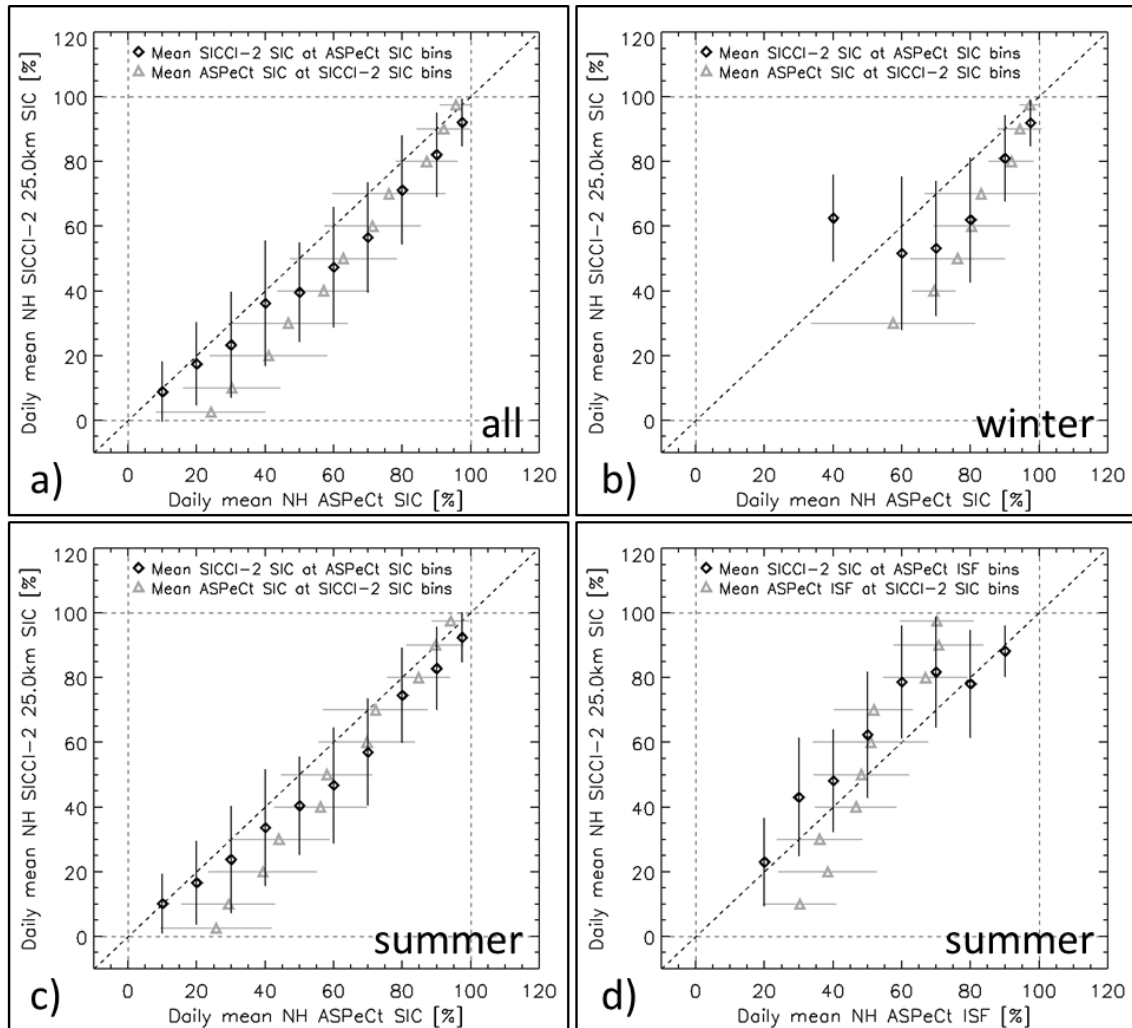
Figure 3-57: As Figure 3-56, using SICCI-2 SIC of SICCI-LF (25.0 km).

As expected, Figure 3-56 to Figure 3-58, which can be regarded as a condensed version of the scatterplots shown in Figure 3-51 (b,d,f) and Figure 3-52 to Figure 3-54 (b,d), show similar results for the tree algorithms for the respective season. The under-estimation of SICCI-2 SIC relative to ASPeCt SIC ranges between 0% and 20% and depends on the sea-ice concentration. It is between 10% and 15% for a SIC range between ~30% and ~80%; differences are smaller below and above this range. Interestingly, during winter, only for 90% and higher SIC values, differences between SICCI-2 and ASPeCt SIC are < 10%. For lower SIC bins the differences take values of ~20%.

In the light of the Figure 3-56 to Figure 3-58, image d) we need to revise the statement given above about SICCI-2 SIC overestimating ASPeCt ISF by 20 to 30%. These images here indicate that the differences between SIC

and ISF depend on ISF. For low ISF, i.e. < ~25%, and high ISF, i.e. >
~75%, SICCI-2 SIC and ASPeCt ISF tend to agree within 5%. For the
intermediate SIC range, however, ASPeCt ISF is overestimated by SICCI-2
SIC by 10% to 20%.
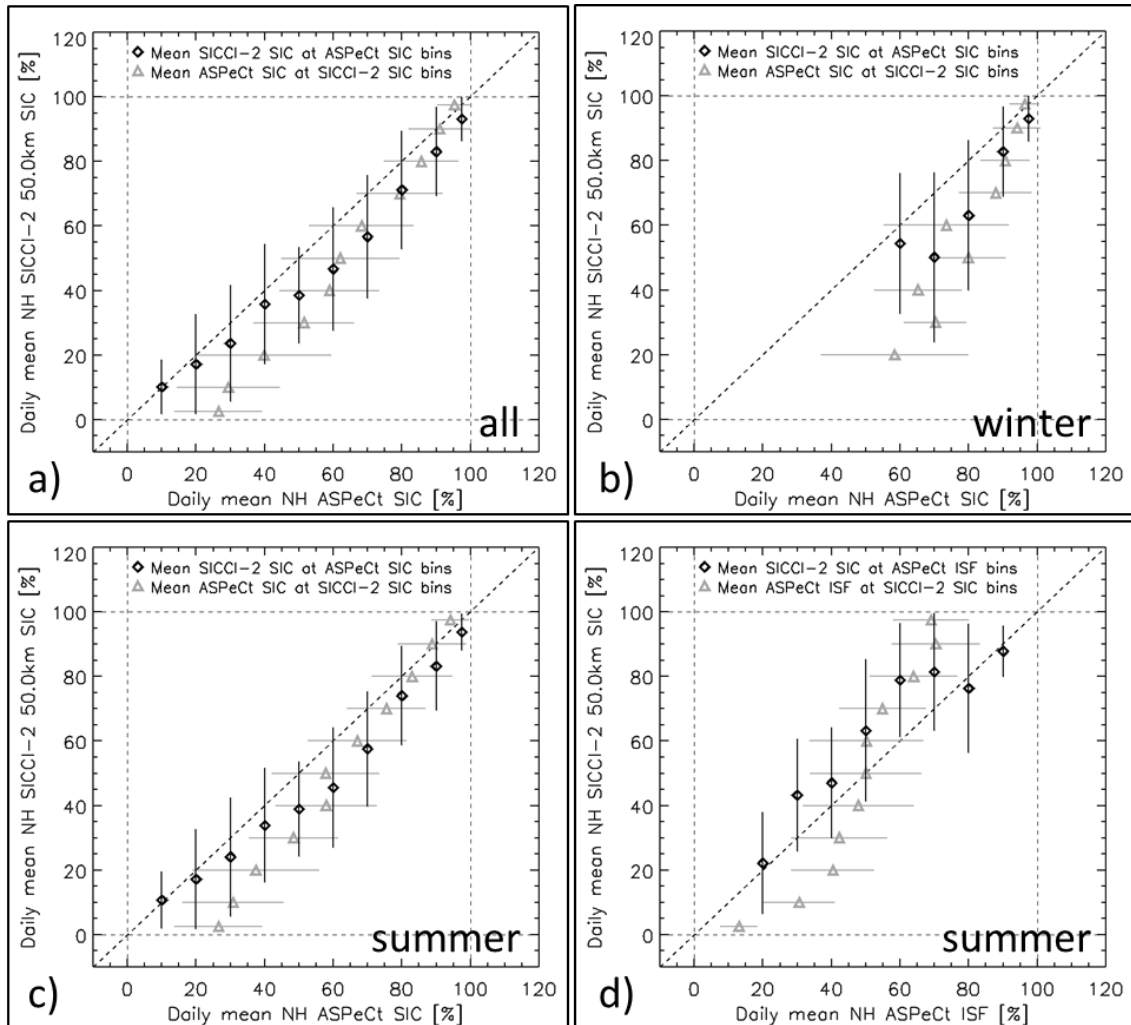
Figure 3-58: As Figure 3-56, using SICCI-2 SIC of SICCI-VLF (50.0 km).

For the reversed comparison, i.e. computing mean ASPeCt SIC (and ISF) for
SICCI-2 SIC bins, we find that the results mostly agree well. We find that
the mean ASPeCt SIC for SICCI-2 bins is situated close to the mean SICCI-2
SIC for ASPeCt SIC bins – predominantly for SIC > ~ 50% when considering
the entire year and summer and for SIC > ~ 80% for winter. For SIC <
50% the deviation between the two mean SIC values increases, and we find
considerable higher mean ASPeCt SIC for SICCI-2 SIC bins up to 40% (see
e.g. image c) in Figure 3-56 to Figure 3-58). For ASPeCt ISF the deviations
are more variable and partly also larger. While the mean ASPeCt ISF tends
to be larger than SICCI-2 SIC for SICCI-2 SIC bins up to 40-50% SIC the
reverse applies to SIC > 50%, when mean ASPeCt ISF takes values
between ~50% and ~70% for SICCI-2 bins 50% trough 100%, which
corresponds to a larger overestimation of ASPeCt ISF by SICCI-2 SIC than
reported above; so we come back to values of up to 30%.

Southern Hemisphere
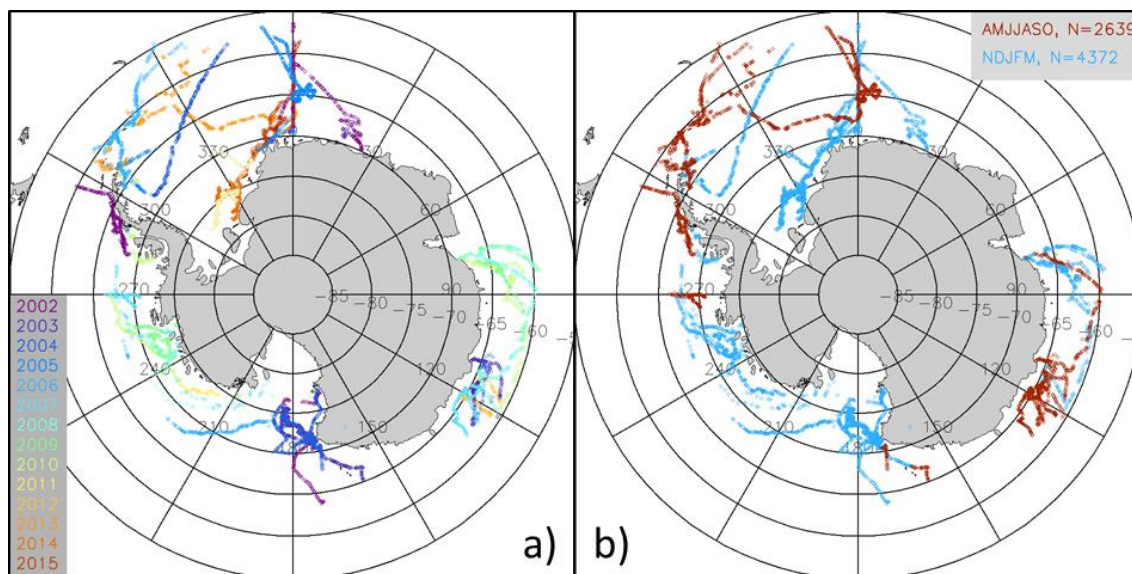
Figure 3-59: As Figure 3-50 but for the Southern Hemisphere.

In the Southern Hemisphere available ASPeCt sea-ice observations concentrate on the Weddell Sea: basically between 60W and 10E, on an area in the Eastern Antarctic: between 75E and 130E, and on some parts of the Ross Sea and the Amundsen-Bellingshausen Sea (Figure 3-59). Observations are distributed more sporadically over the years (Figure 3-59 a). For instance, we have no observations of the western Ross Sea after 2006. Except in the Weddell Sea, we have no observations during recent (after 2012) years. The split between winter and summer observations is less pronounced than for the Northern Hemisphere (Figure 3-59 b).

Figure 3-60 illustrates how well SICCI-2 SIC data agree with ship-based observations of the SIC (ASPeCt SIC). In the scatterplots (images b, d, and f) the overall mean difference is close to zero: -0.8%, -2.5% and -1.1% for SICCI-HF, SICCI-LV and SICCI-VLF, respectively, with a similar standard deviation of 13% to 14% for all three algorithms. These small overall differences are also reflected by regression lines with intercept close to zero: -2.8%, -3.0% and -0.2%, respectively, and slope close to 1: 1.027, 1.007, and 0.988; actually for SICCI-VLF the regression line almost coincides to the line of 1-to-1 agreement. Squared linear correlation coefficients are a bit higher than in the Northern Hemisphere (compare to Figure 3-51 and Table 3-25): 0.76, 0.74 and 0.71 for SICCI-HF, SICCI-LV and SICCI-VLF, respectively. The root mean square difference RMSD matches the standard deviation of the SIC difference for SICCI-HF and SICCI-VLF and exceeds the one for SICCI-LF by 0.2%. Overall the scatterplots suggest a good agreement albeit the substantial scatter of the data points. Agreement seems to better for SIC > ~50%. We note that we have ~520 days with valid daily mean SIC data pairs.
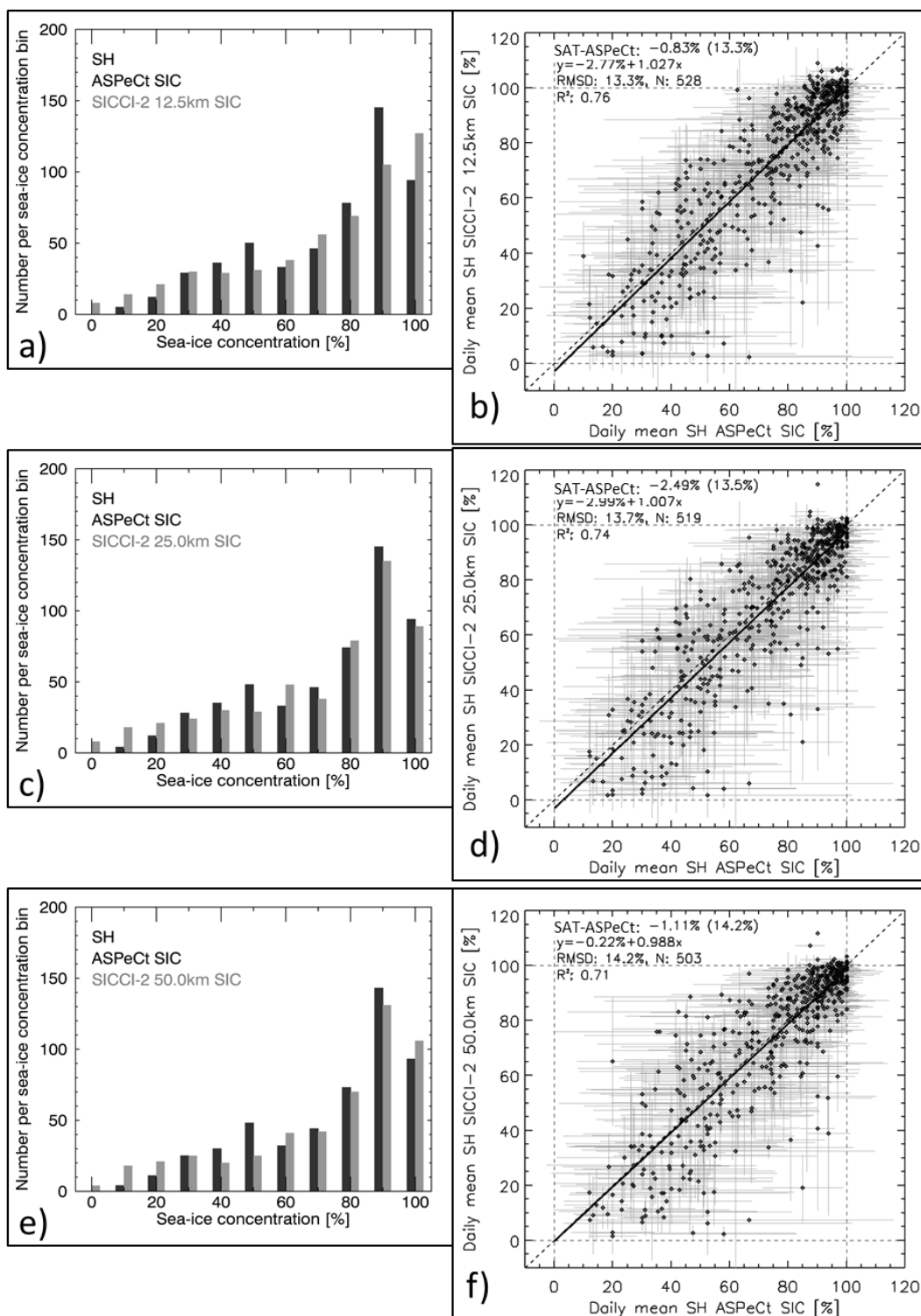
Figure 3-60: Histograms (left) and scatterplots (right) of co-located daily mean ASPeCt and SICCI-2 SIC using all data for, from top to bottom, SICCI-HF (12.5 km), SICCI-LF (25.0km) and SICCI-VLF (50.0km) for the Southern Hemisphere. Bars in scatterplots denote ± 1 standard deviation. "SAT-ASPeCt" is the mean difference SICCI-2 minus ASPeCt SIC together with its standard deviation in parentheses. Also given are the equation of the linear regression, RMSD, number of days with valid data pairs N and the squared linear correlation coefficient R².

All histograms in Figure 3-60 have in common that the largest fraction of observations falls into bins 90% and 100% while the smallest fraction falls into bins 0%, 10% and 20%. In contrast to the Northern Hemisphere, ASPeCt SIC clearly dominates bin 90%; of the ~ 250 cases of ASPeCt SIC in bins 90% and 100% there are ~150 in bin 90% and ~100 in bin 100%. This distribution is most closely followed by SICCI-2 SIC of the SICCI-LF (25.0km) algorithm (Figure 3-60 c). In contrast but actually in agreement with the Northern Hemisphere (compare Figure 3-51 a) most SICCI-HF SIC values fall into bin 100% (Figure 3-60 a), which means the largest discrepancy among the three algorithms exists at these two bins.

Except in the two high sea-ice concentration bins all histograms show more or less the same pattern: a fairly similar number of cases, differences are less than ten, from ASPeCt SIC and SICCI-2 SIC falling into most SIC bins. One exception is bin 50% which is populated considerably less by all SICCI-2 algorithms compared to ASPeCt SIC. Another exception is given by bins 10% and 20%, which are populated notably more by SICCI-2 SIC, particularly of SICCI-LF, than by ASPeCt SIC.
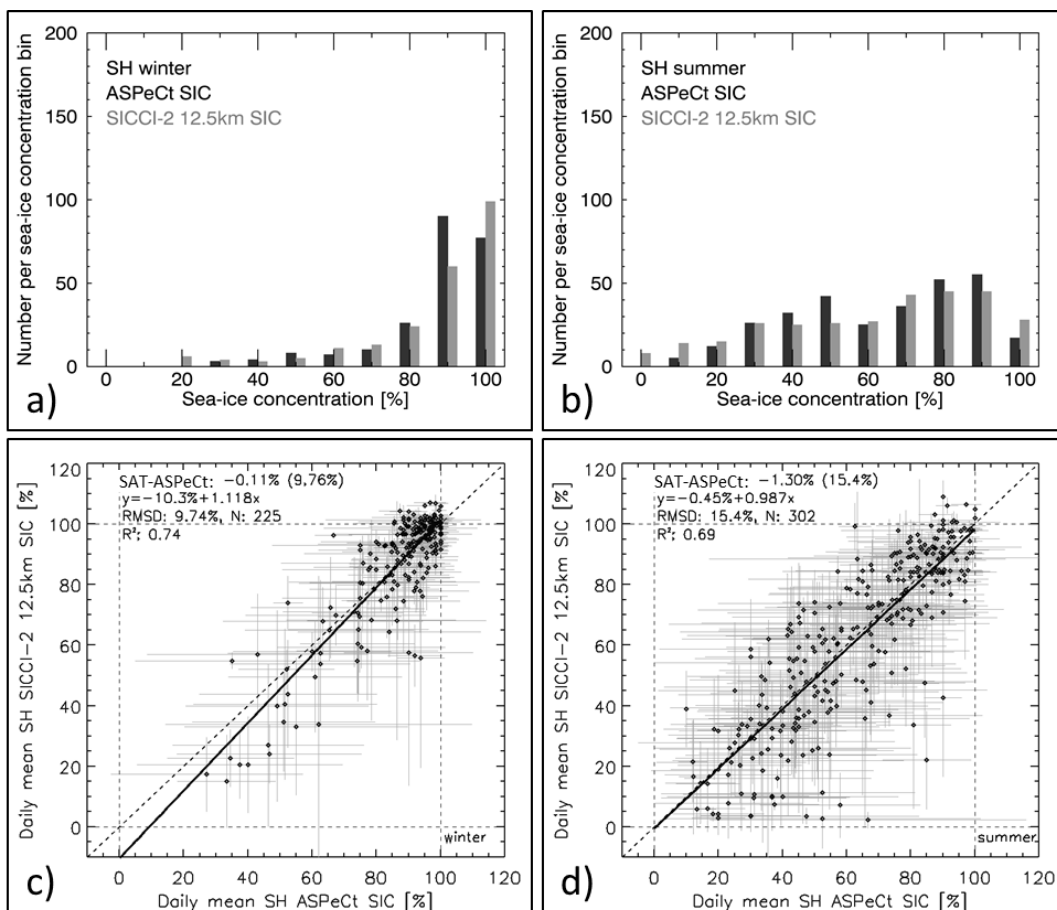
Figure 3-61: As Figure 3-60 but separately for winter (left) and summer (right) for SICCI-HF.

In Figure 3-61 through Figure 3-63 we illustrate how the data pairs split between winter and summer (compare Figure 3-59 b). For winter, i.e. their left side, these figures clearly demonstrate that SIC is concentrated almost completely to values SIC > 80%: of the 225 available data pairs ~ 190 fall into bins 80% or higher. The mean SIC difference is again smallest for

SICCI-HF followed by SICCI-VLF and SICCI-LF: -0.1%, -1.3%, and -1.7%, respectively. Standard deviations of these differences and RMSD values are 9% to 10% with the smallest value 9.2% and 9.3% observed for SICCI-LF. Thanks to more SIC data pairs at low sea-ice concentrations falling below the 1-to-1 line than above it, all three linear regressions have a negative intercept and slope > 1, but still relatively close to one. Best SICCI-2 algorithm is again SICCI-LF. This is supported by the respective histograms (image a) in Figure 3-61 through Figure 3-63). It is interesting to see that the difference in probabilities between SICCI-2 SIC and ASPeCt SIC for bins 80% and higher is similar for SICCI-HF and SICCI-VLF: A higher probability of SICCI-2 SIC for bin 100% and lower probability for bins 80% and 90% when compared to ASPeCt SIC; this differs for SICCI-LF which shows less cases than ASPeCt SIC in bins 90% and 100% but more cases in bin 80%.
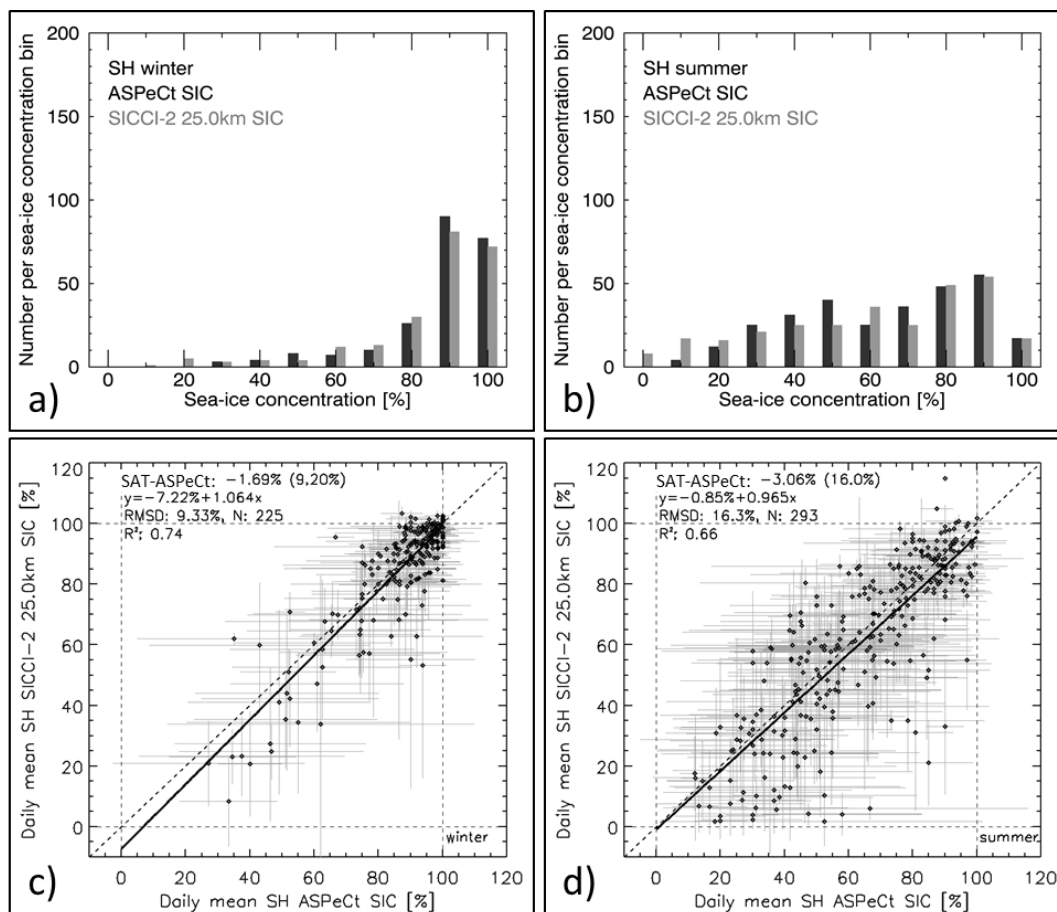
Figure 3-62: As Figure 3-60 but separately for winter (left) and summer (right) for SICCI-LF.

For summer, i.e. their right side, Figure 3-61 through Figure 3-63 show values falling into the entire SIC range; bins 90%, 80%, and 50% have the highest numbers of ASPeCt SIC observations, closely followed by bins 70% and 40%. The algorithms differ in their agreement with ASPeCt SIC for SIC probability in these five bins.

Apart from these differences in the histograms the statistics written in the scatterplots for summer are again relatively similar. The mean difference is -1.3%, -3.1% and -0.9% for SICCI-HF, -LF, and –VLF, respectively. The standard deviations of these differences and the RMSD values are

considerably larger than during winter: between 15.4% and 16.6%. Linear regressions for summer are closer to the 1-to-1 line that for winter. Intercepts are -0.5%, -0.9%, and 1.7% for SICCI-HF, -LF, and −VLF, respectively, and corresponding slopes are 0.987, 0.965, and 0.959. This suggests best agreement for SICCI-HF during the summer months. This is also supported by the squared linear correlation coefficients of 0.69, 0.66 and 0.63, respectively.
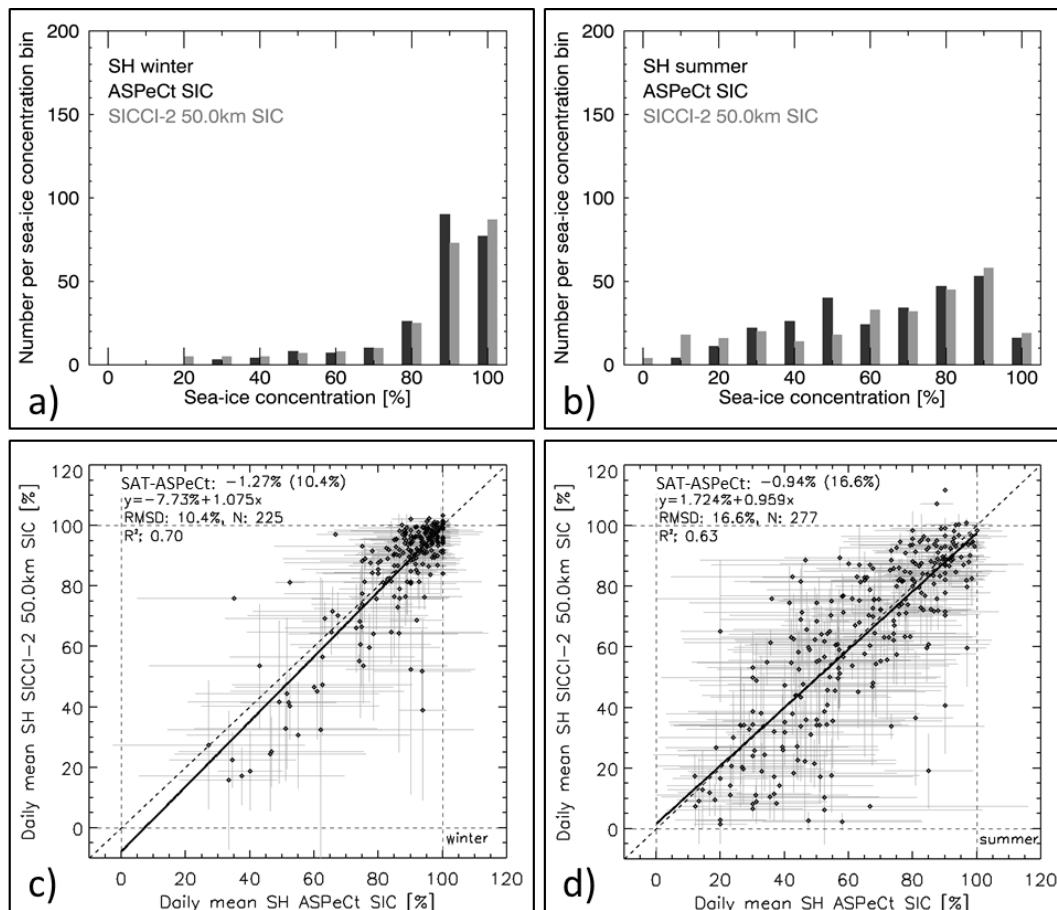
Figure 3-63: As Figure 3-60 but separately for winter (left) and summer (right) for SICCI-VLF.

The scatterplots indicate a few cases where ASPeCt SIC values are substantially larger than SICCI-2 SIC. In Figure 3-61 d), for instance, there is a group of four values with ASPeCt SIC > 80% where SICCI-2 SIC is between 20% and 50%, and there is another group of five values with ASPeCt SIC > 45% where SICCI-2 SIC is between 2% and 10%. This is in line with the observation mentioned already in the context of the scatterplots shown in Figure 3-60, that SICCI-2 SIC tend to be too low compared to ASPeCt SIC particularly for lower sea-ice concentrations. One possible explanation could be limited visibility during the ASPeCt observations while the ship was following a band of close(r) sea ice than in the surrounding area. This is unlikely since ships tend to follow leads and openings in the ice cover. Another possible explanation is that the surface of the sea ice encountered was wet, i.e. covered with slush or snow being soaked wet from the action of sea water spilling over the ice floe, or that the sea ice was in a such advanced state of melt that it was hardly afloat at the

sea surface. This would cause the algorithms to underestimate the actual sea-ice concentration. Evidence of this has been reported in the literature, e.g. [RD-15, RD-16].

Similar to the investigation in the Northern Hemisphere we close the investigation in the Southern Hemisphere with scatterplots of the mean SICCI-2 SIC computed for all ASPeCt SIC bins given, for all algorithms together with the standard deviation of the mean in Figure 3-64 through Figure 3-66. We also illustrate the mean ASPeCt SIC computed for the same SICCI-2 SIC bins. When considering the entire year (images a) and summer (images c) mean SICCI-2 SIC and ASPeCt SIC of the used SIC bins agree within 5% for almost all bins. During winter the agreement is a bit worse but still differences are below 10%. The reversed view, i.e. computing mean ASPeCt SIC for SICCI-2 bins reveals convincing agreement for almost the entire SIC range; only – like in the Northern Hemisphere – for very low SIC, i.e. < ~ 40% mean ASPeCt SIC and SICCI-2 bin have larger discrepancies with ASPeCt SIC exceeding SICCI-2 SIC.
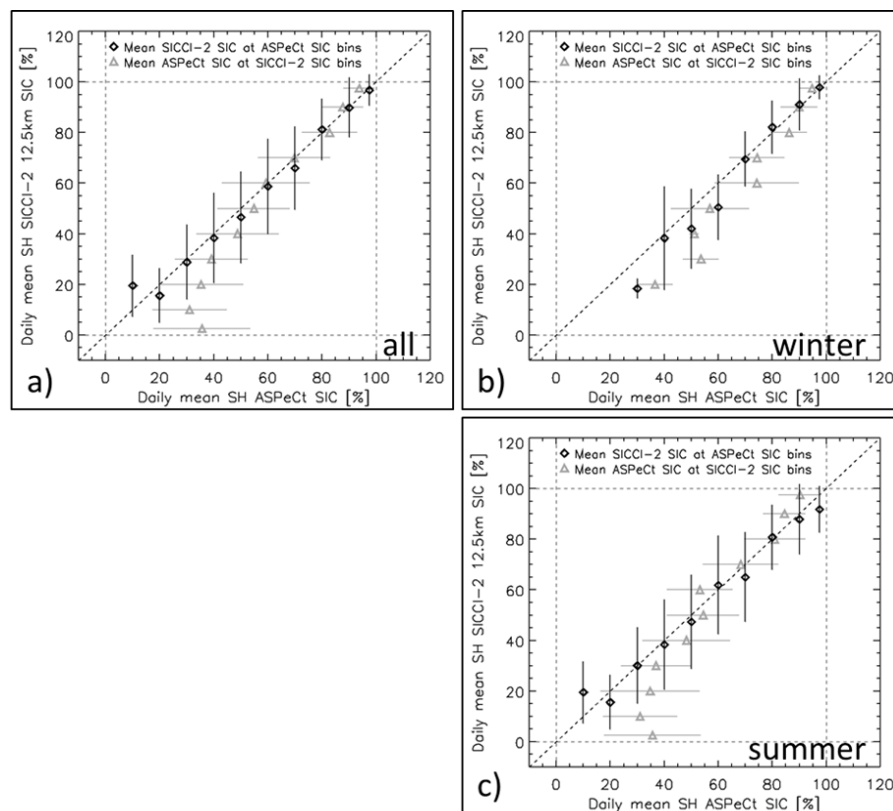
Figure 3-64: Mean SICCI-2 (here: SICCI-HF, 12.5 km resolution) SIC plus/minus one standard deviation (vertical bars) computed for each ASPeCt SIC bin used in the histograms in Figure 3-60 (black symbols) and mean ASPeCt SIC plus/minus one standard deviation (horizontal bars) computed for SICCI-2 SIC bins of the same bin widths (grey symbols) for the Southern Hemisphere.
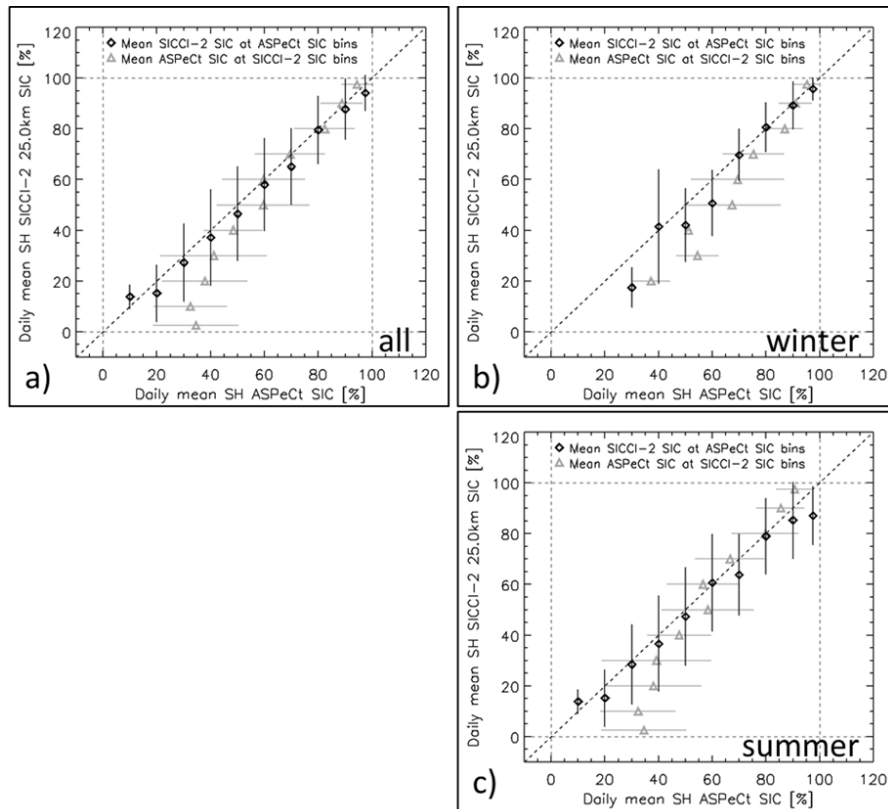
Figure 3-65: As Figure 3-64, using SICCI-2 SIC of SICCI-LF (25.0 km).
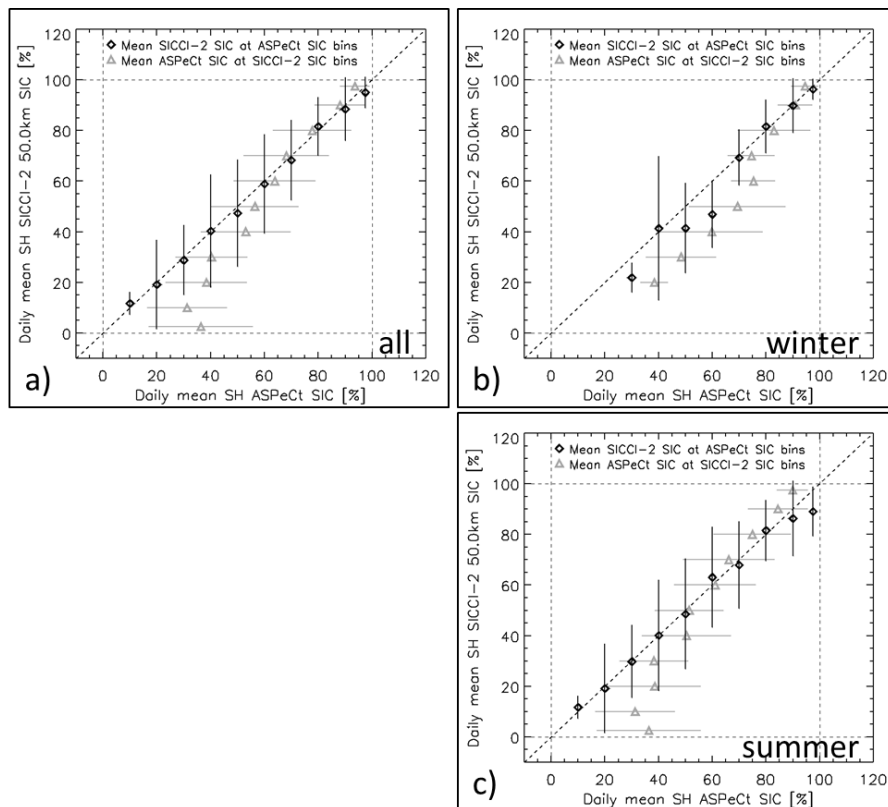
Figure 3-66: As Figure 3-64, using SICCI-2 SIC of SICCI-LF (50.0 km).

Summary:

Ship-based visual observations of the sea-ice cover (8280 for the Northern Hemisphere, 7012 for the Southern Hemisphere), ASPeCt SIC, were collocated with the three SICCI-2 SIC products. From both ship-based and satellite data the daily average along-track SIC was computed (~660 for the Northern Hemisphere, ~520 for the Southern Hemisphere) following the methodology of Beitsch et al. [RD-17]. These daily mean values were compared by means of their difference, correlation, root mean square difference (RMSD), and a linear regression analysis. Main results are summarized in Table 3-25 and Table 3-26.

Table 3-25: Summary of the ASPeCt SIC to SICCI-2 SIC intercomparison for the Northern Hemisphere. "N" is number of valid daily mean SIC values, "DIFF" is the mean difference SICCI-2 SIC minus ASPeCt SIC, "SDEVDIFF" is the standard deviation of the mean difference, "RMSD" is the root mean square difference, R^2 is the squared linear correlation coefficient, and "b" and "a" are intercept and slope of the linear regression. See text for definition of "summer" and "winter".

	HF (12.5 km)			LF (25 km)			VLF (50 km)		
	all	winter	summer	all	winter	Summer	all	winter	summer
N	670	210	459	666	209	456	650	203	446
DIFF	-7.1%	-8.4%	-6.5%	-8.0%	-9.0%	-7.5%	-7.6%	-7.9%	7.5%
SDEVDIFF	14.0%	14.0%	14.0%	14.1%	13.5%	14.4%	14.8%	14.2%	15.1%
RMSD	15.7%	16.3%	15.4%	16.2%	16.1%	16.3%	16.7%	16.2%	16.8%
R²	0.73	0.57	0.74	0.73	0.58	0.73	0.72	0.55	0.72
b	-6.9%	-13.4%	-7.0%	-7.9%	-11.3%	-8.2%	-9.3%	-16.1%	-9.0%
A	0.998	1.057	1.007	0.999	1.027	1.010	1.022	1.093	1.022

Table 3-26: As Table 3-25 but for the Southern Hemisphere.

	HF (12.5 km)			LF (25 km)			VLF (50 km)		
	all	winter	summer	all	winter	summer	all	winter	summer
N	528	225	302	519	225	293	503	225	277
DIFF	-0.8%	-0.1%	-1.3%	-2.5%	-1.7%	-3.1%	-1.1%	-1.3%	-0.9%
SDEVDIFF	13.3%	9.8%	15.4%	13.5%	9.2%	16.0%	14.2%	10.4%	16.6%
RMSD	13.3%	9.7%	15.4%	13.7%	9.3%	16.3%	14.2%	10.4%	16.6%
R²	0.76	0.74	0.69	0.74	0.74	0.66	0.71	0.70	0.63
b	-2.8%	-10.3%	-0.5%	-3.0%	-7.2%	-0.9%	-0.2%	-7.7%	+1.7%
A	1.027	1.118	0.987	1.007	1.064	0.965	0.988	1.075	0.959

- Mean differences between ASPeCt SIC and SICCI-2 SIC are smaller in the Southern than in the Northern Hemisphere. This is in line with the result of the intercomparison of SICCI-2 SIC at ~100% sea-ice concentration reported in section 3.2 of this report.
- Standard deviation of the difference ASPeCt SIC minus SICCI-2 SIC and the RMSD are smaller by ~1% to ~2% in the Southern than in the Northern Hemisphere. In the Southern Hemisphere both parameters are considerably smaller in winter than in summer.
- Linear regression analysis suggests best agreement between ASPeCt SIC and SICCI-2 SIC for the 25.0 km product of SICCI-LF in both hemispheres during winter; during summer the 12.5 km product of SICCI-HF yield the best regression.

Net ice surface fraction (ISF) computed from a combination of ship-based SIC and melt-pond fraction observations are overestimated considerably by all three algorithms; considerably means 20% to 30% for ASPeCt SIC values between ~50% and 100% (see Figure 3-55). This is in agreement with results from the intercomparison of SICCI-2 SIC with ISF derived from MODIS observations of melt-pond fraction and ISF (see section 3.4).

ESA UNCLASSIFIED - For Official Use

3.6   SICCI 2 SIC distribution around SIC=0% and SIC=100%

In this section we show results of our investigation of the distribution of the unfiltered sea-ice concentrations around SIC = 0% and SIC = 100%. The aim of this investigation is to show how accurately, with the three different algorithms (products), open water (SIC = 0%) and completely closed pack ice (SIC = 100%) is retrieved. This investigation does not include independent data against which SICCI-2 SIC have been compared.

In the following we consider sea-ice concentrations of the range -15% through 15% for the SIC = 0% cases and of the range 85% through 115% for the SIC=100% cases. To do so the variable "raw_icecon" is read together with the status flag variable and with the "clean" icecon variable. A combined SIC field is obtained by inserting "icecon" values into those gaps in the variable "raw_icecon" where "icecon" has valid values. Open water outside the climatological sea-ice extent is excluded as well as land and grid cells with a flag value greater or equal to 64, and any grid cells where SIC values were subject to too high 2m air temperatures and/or the additional land-spillover correction.

The distribution of the sea-ice concentrations around 0% and 100% is realized in form of histograms with 0.5% bin width; in case of 0% this is -14.9999 to -14.5; -14.4999 to -14.0, … . The investigation is carried out per month, i.e. all daily data files of one month are read and sea-ice concentrations are binned into the respective bins for every month of the time series.

We computed whole-period averages of the monthly histograms and present all of these for all three algorithms for every month, first for the Northern Hemisphere and then for the Southern Hemisphere. Note that October 2011 and July 2012 are not included into these average histograms because of the small number of days with observations (4 and 9).

Showing these histograms instead of mean numbers and standard deviations of the SIC has two advantages. First, by only computing a mean SIC value for the two considered SIC ranges would preclude that the SIC is distributed symmetrical around 0% and 100%. Secondly, only by showing the histograms the degree of asymmetry can be quantified and it can further be figured out whether and how much the actual modal SIC deviates from 0% and 100%.

The SIC = 0% cases will be presented in the subsection "open water"; those of the SIC = 100% cases in the subsection "pack ice"

3.6.1   *Open water*
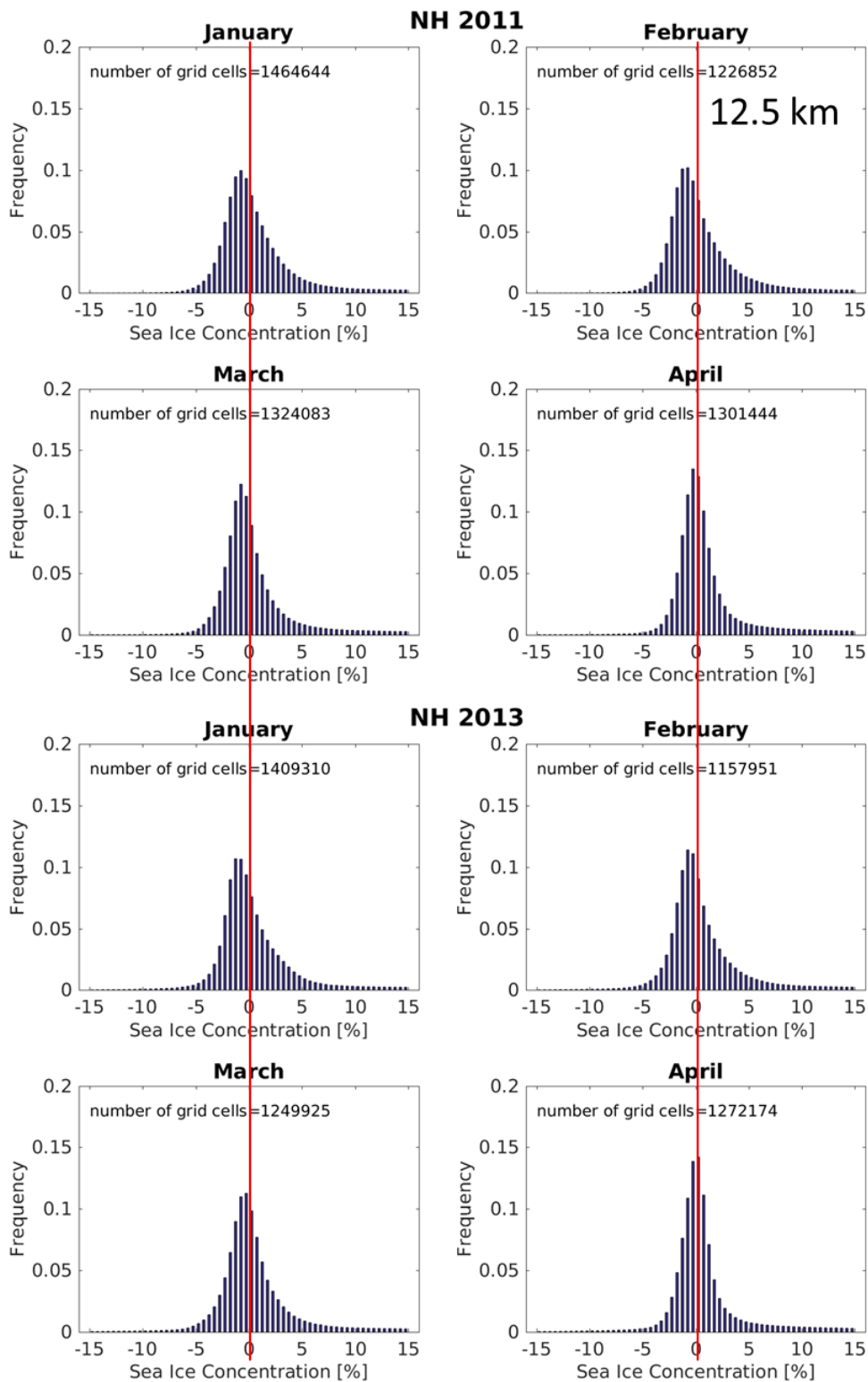
Figure 3-67: Sample set of SIC histograms around SIC=0% for SICCI-HF (12.5 km) for Jan. through Apr. 2011 and 2013 for the Northern Hemisphere. Red vertical line denotes location of SIC=0%. Binsize: 0.5%.
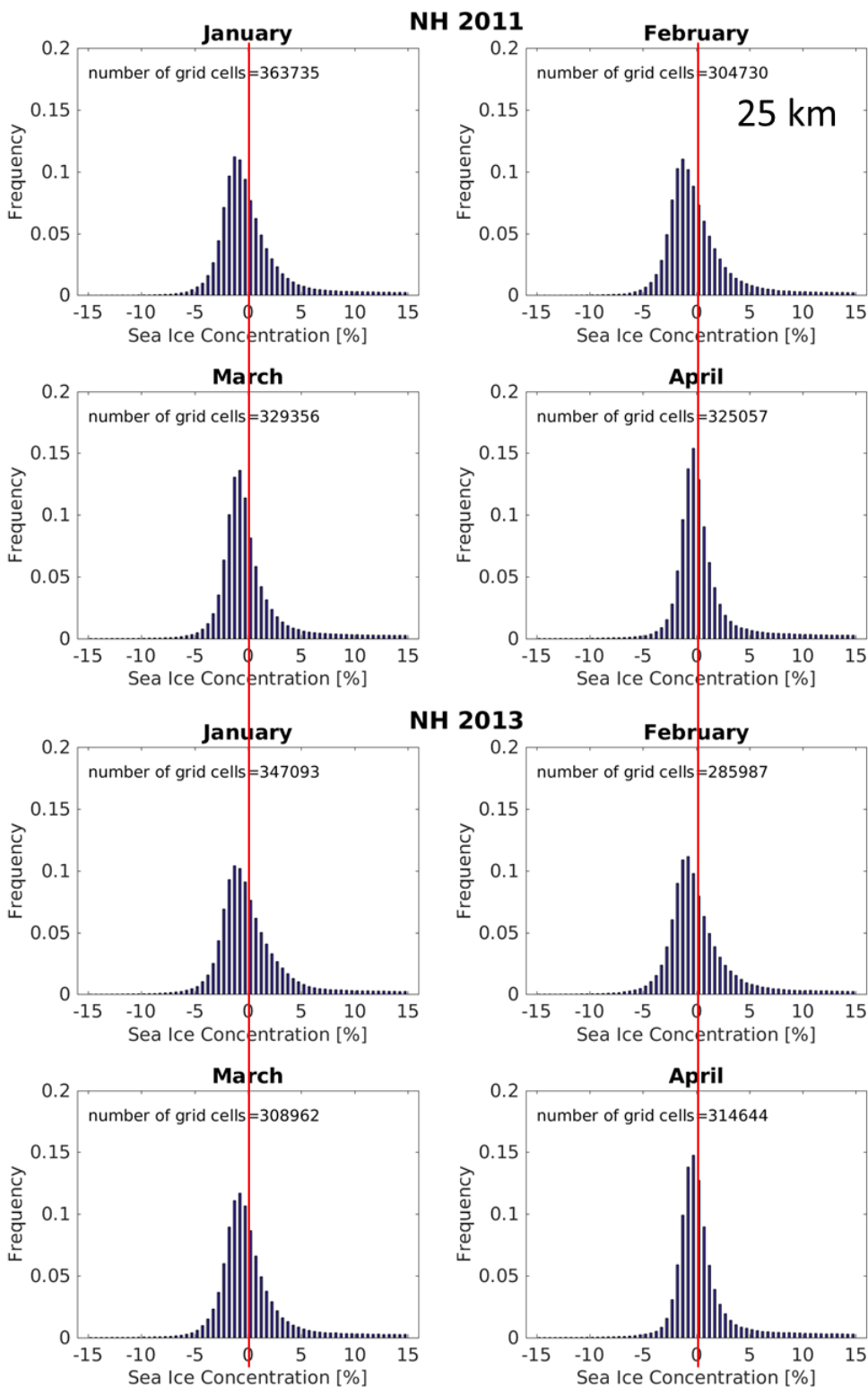
Figure 3-68: As Figure 3-67, using SICCI-LF (25.0 km).
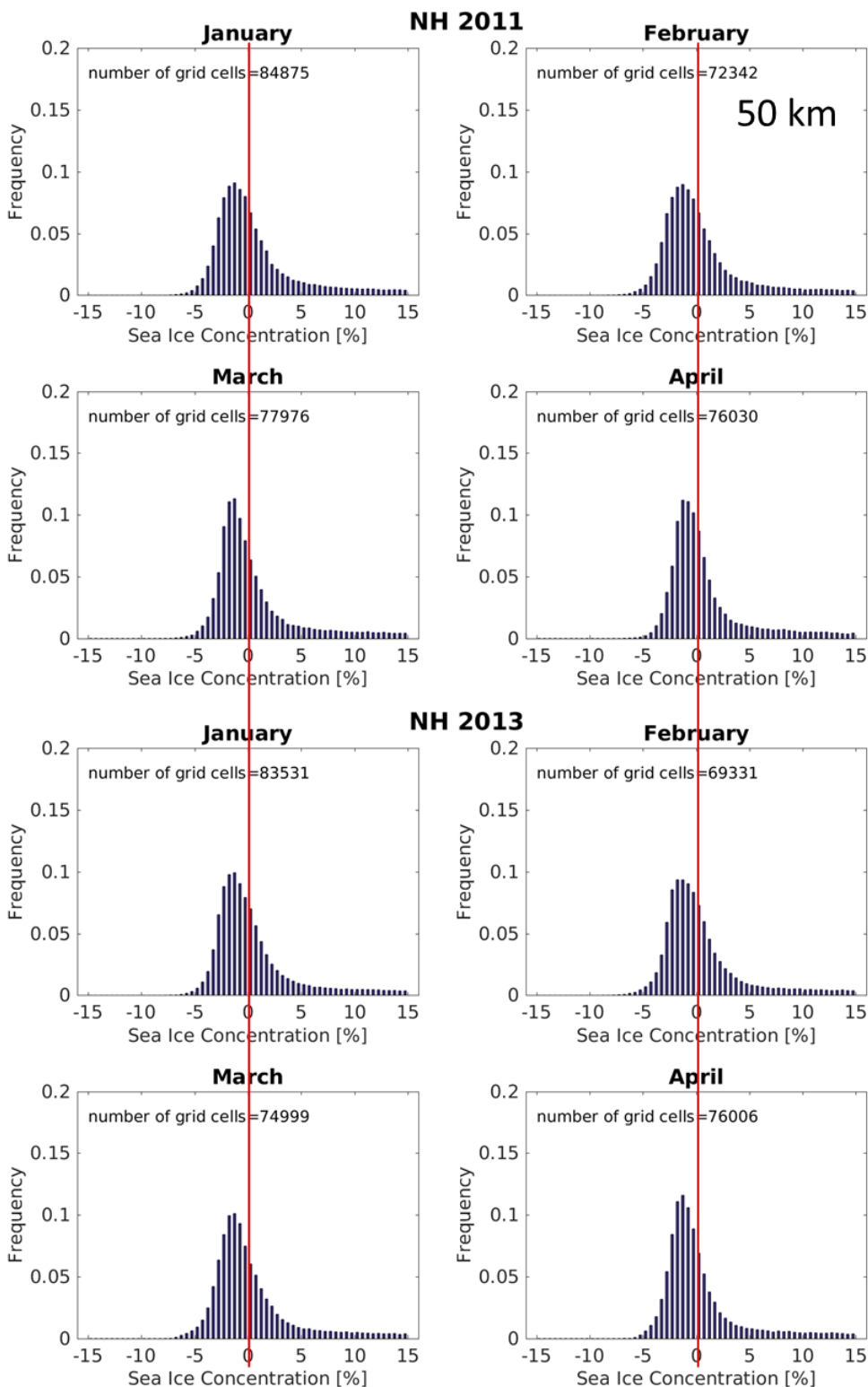
Figure 3-69: Figure 3-67, using SICCI-VLF (50.0 km).

We begin with showing a sample set of SIC distributions for the winter months January through April of two arbitrary years for the Northern

Hemisphere for all three algorithms in Figure 3-67 through Figure 3-69. In these figures we can identify that the modal peak of the SIC distribution is situated left of the red line (SIC=0%), i.e. at negative SIC, for all three algorithms. The modal peak moves towards SIC=0% in April, when SICCI-HF actually has a modal SIC either in bin -0.5% … 0.0% or 0.0% … 0.5% (Figure 3-67). We observe most negative modal SIC for SICCI-VLF (Figure 3-69) when the modal values are located in bin -1.5% … -1.0% or even in bin -2.0% … -1.5% in all months shown.
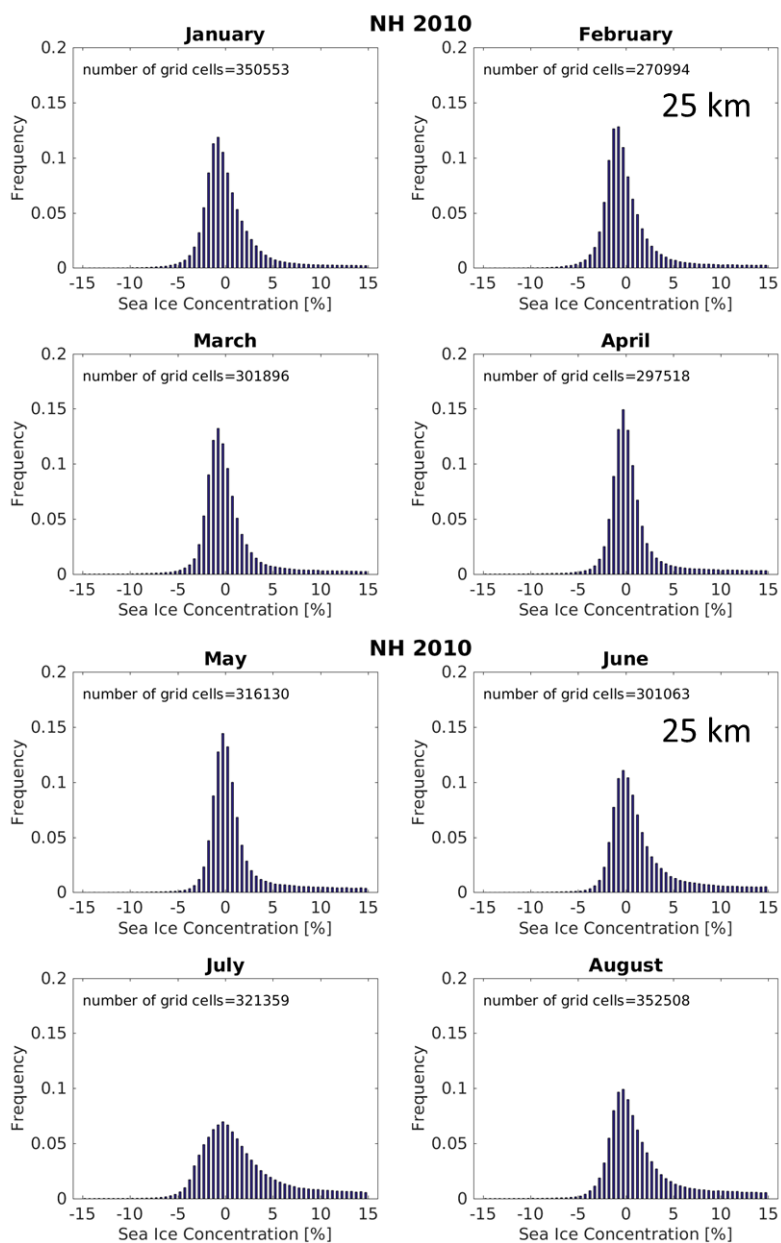
Figure 3-70: Sample seasonal evolution of the SIC distribution around SIC=0% using SICCI-LF (25.0 km). Binsize: 0.5%. Shown are months January through August of the year 2010 for the Northern Hemisphere.

ESA UNCLASSIFIED - For Official Use

With Figure 3-70 we illustrate one seasonal cycle of the SIC distribution around SIC=0% using the SICCI-LF (25.0 km) product as an example. We find, as already evident in Figure 3-67 through Figure 3-69, a quite narrow distribution around SIC = 0% - except during July. SIC values below -5% are hardly observed and constitute a very small fraction. The modal peak is slightly on the negative side throughout the entire year. During the summer months the contribution of SIC values in the range between ~2% and 15% is higher than during the rest of the year; this can possibly be attributed to a larger fraction of low sea-ice concentration cases from very open ice covers as are typical during this time of the year. It is unlikely that this higher fraction of non-zero SIC values are caused by enhanced weather influence; this is more common to observe during the winter months when low pressure systems are particularly vigorous thanks to the elevated meridional temperature gradients.
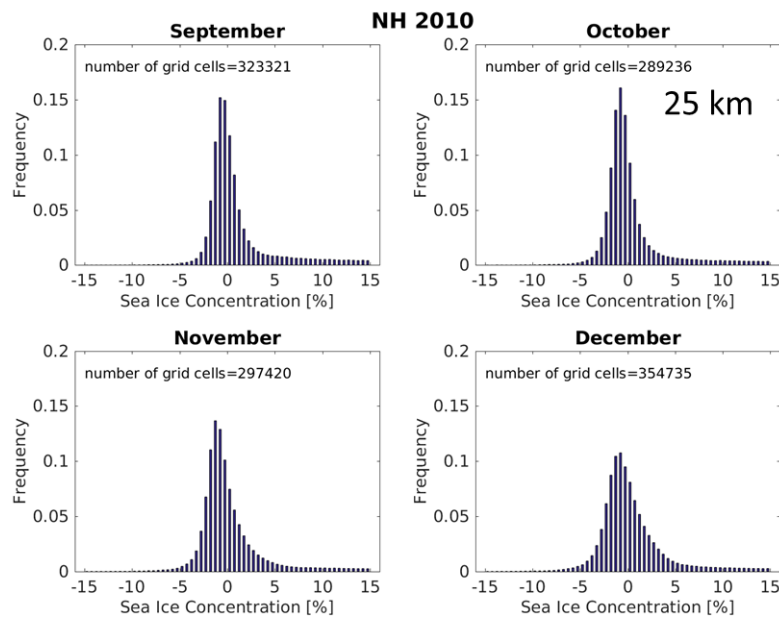
Figure 3-70 continued Months September through December
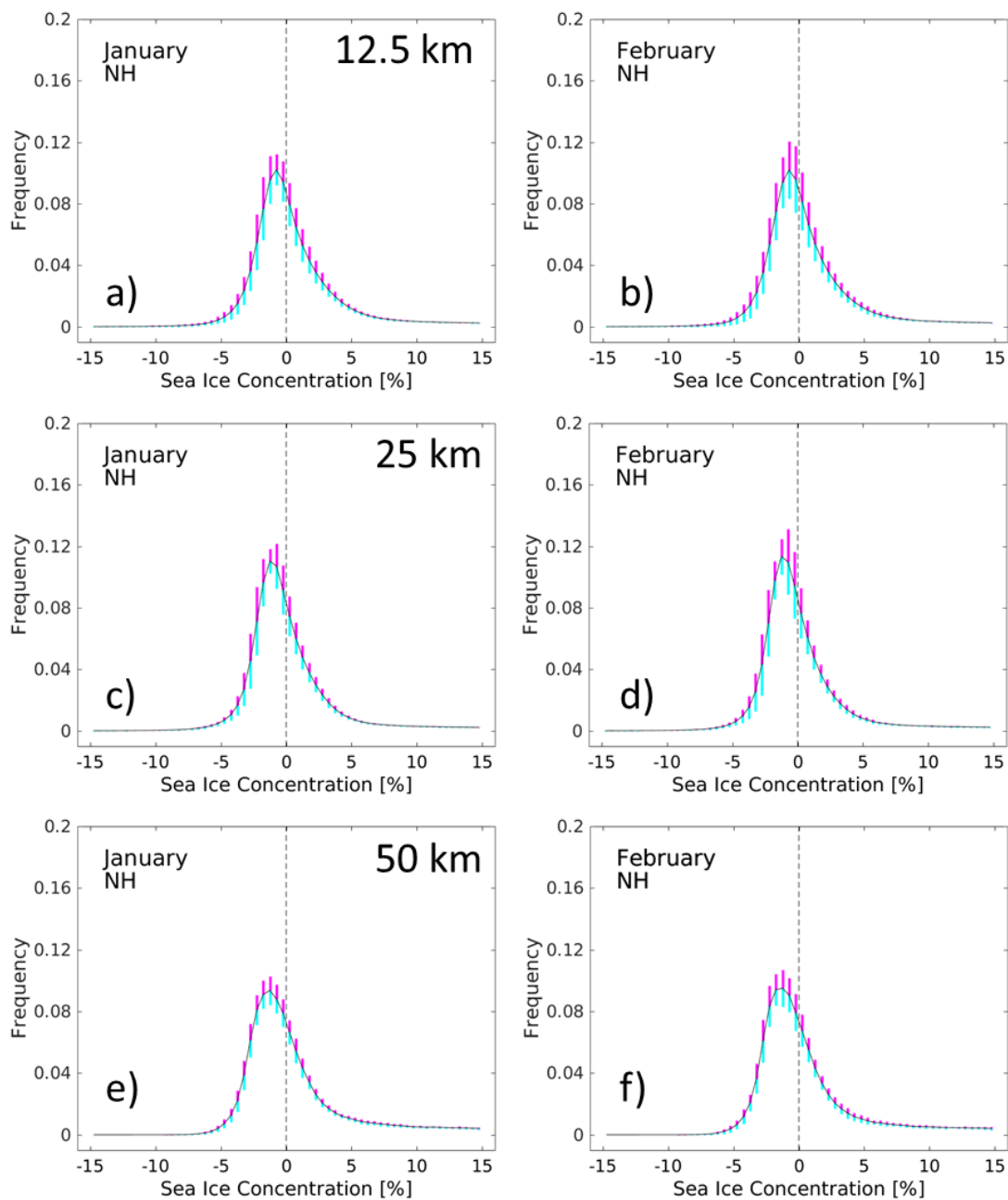
Figure 3-71: Whole-period (2002-2015) average monthly histograms of the sea-ice concentration around 0% for the 12.5 km (a,b), 25 km (c,d), and 50 km (e,f) product for January and February for the Northern Hemisphere. Bin size is 0.5%. Bars in cyan and magenta denote one standard deviation of the probability with which a SIC value falls into the respective bin. Similar figures to this one are Figure 3-72 through Figure 3-76, which are showing the other months.
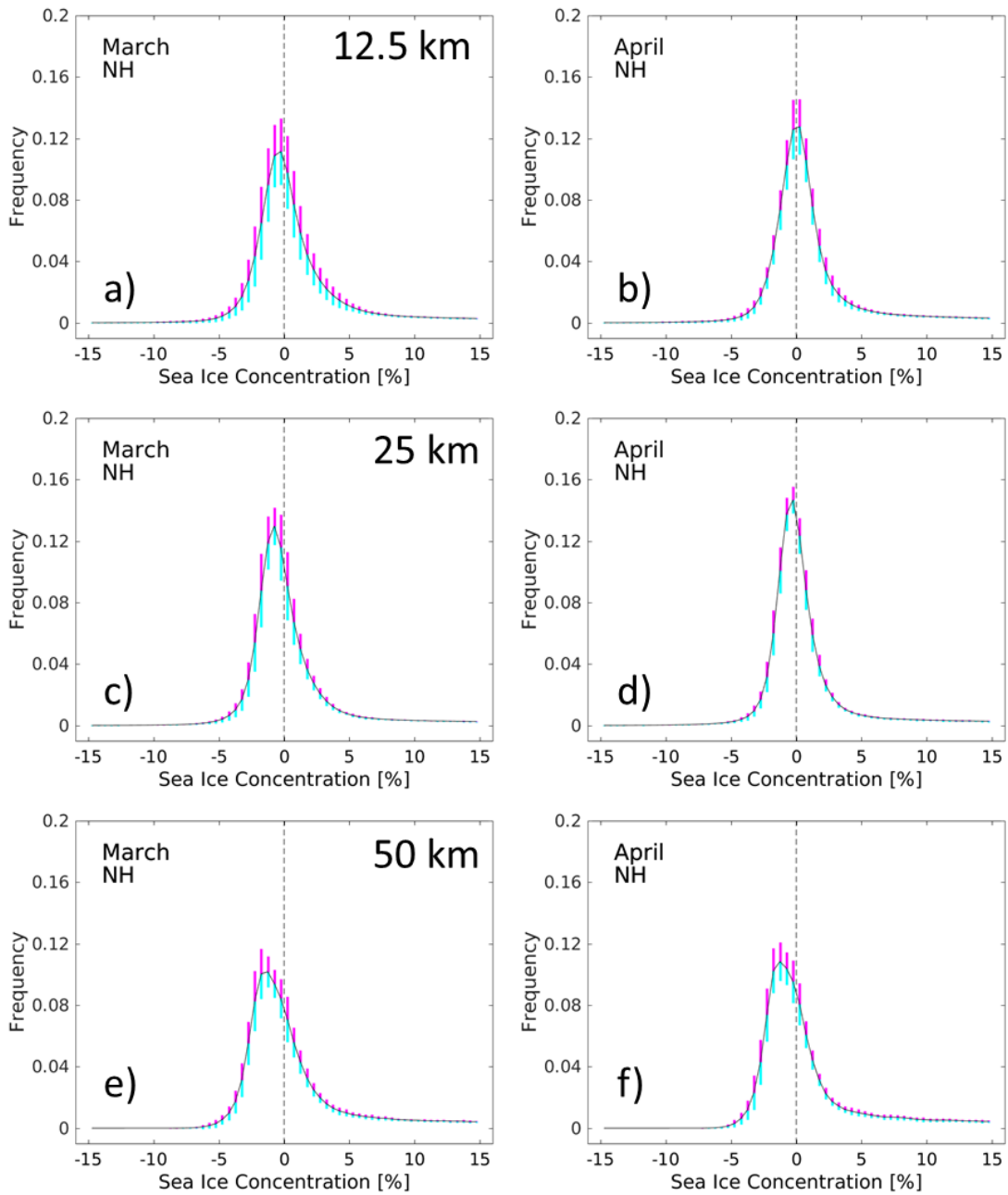
Figure 3-72: As Figure 3-71 for March and April.
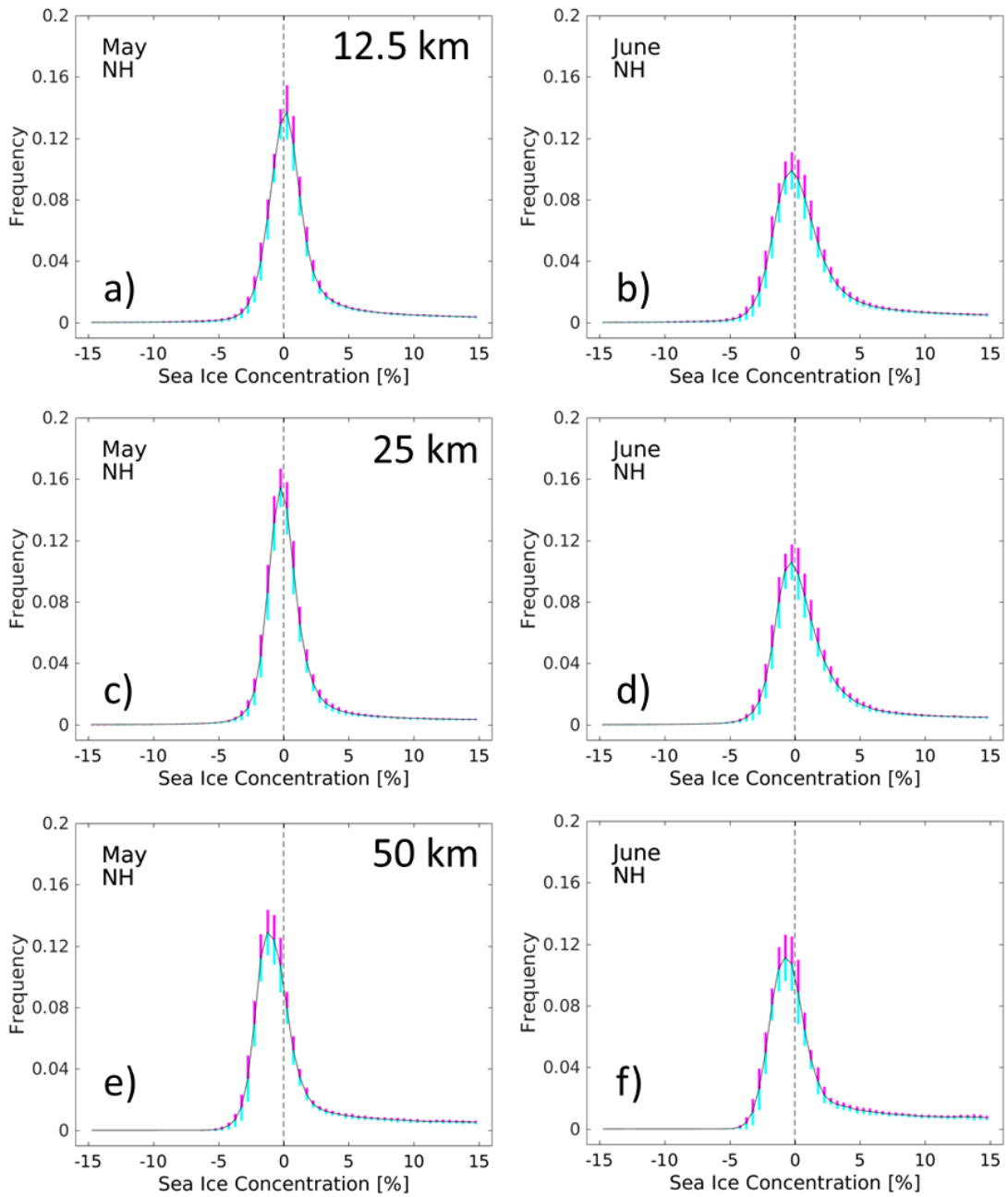
Figure 3-73: As Figure 3-71 for May and June.
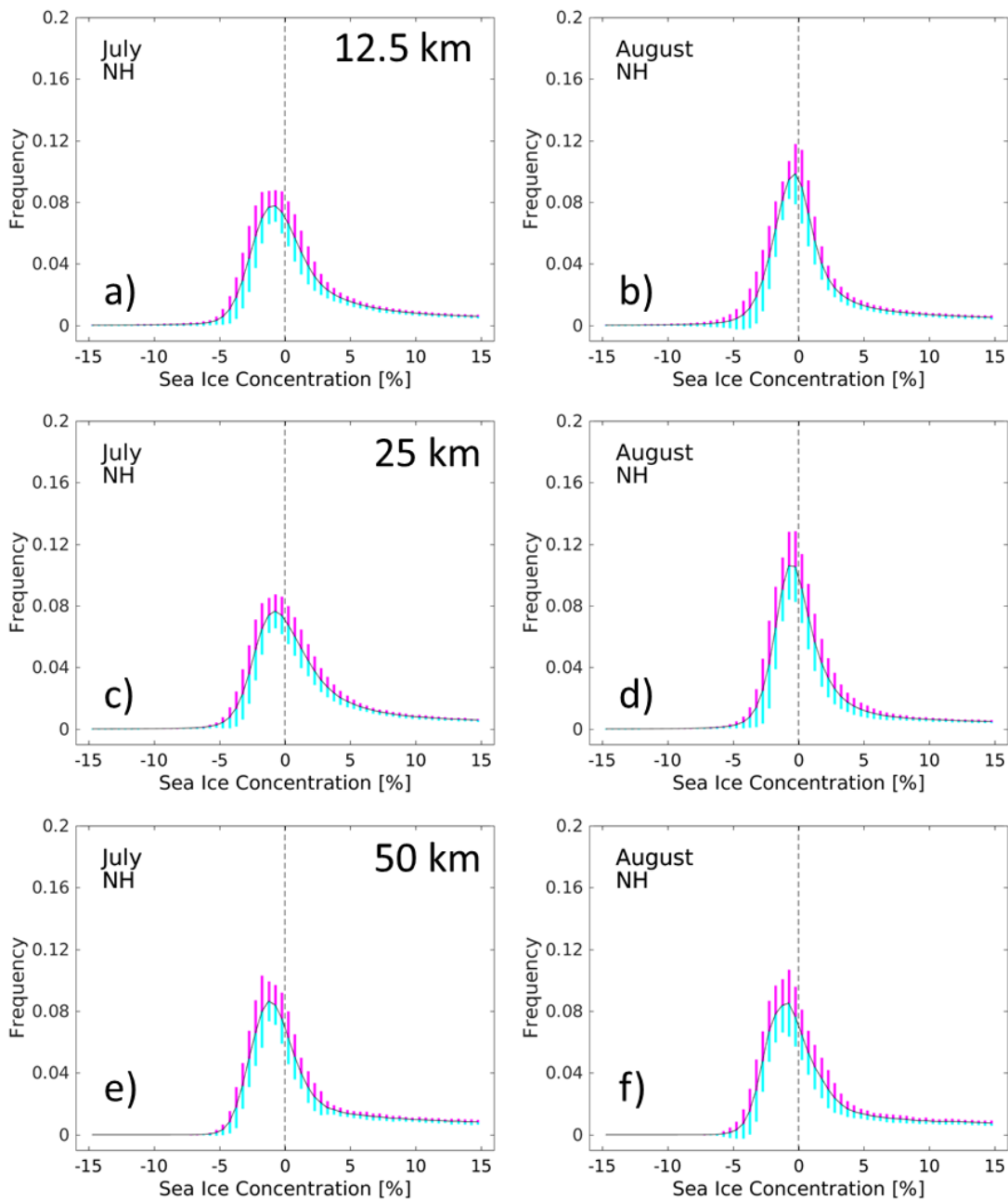
Figure 3-74: As Figure 3-71 for July and August.
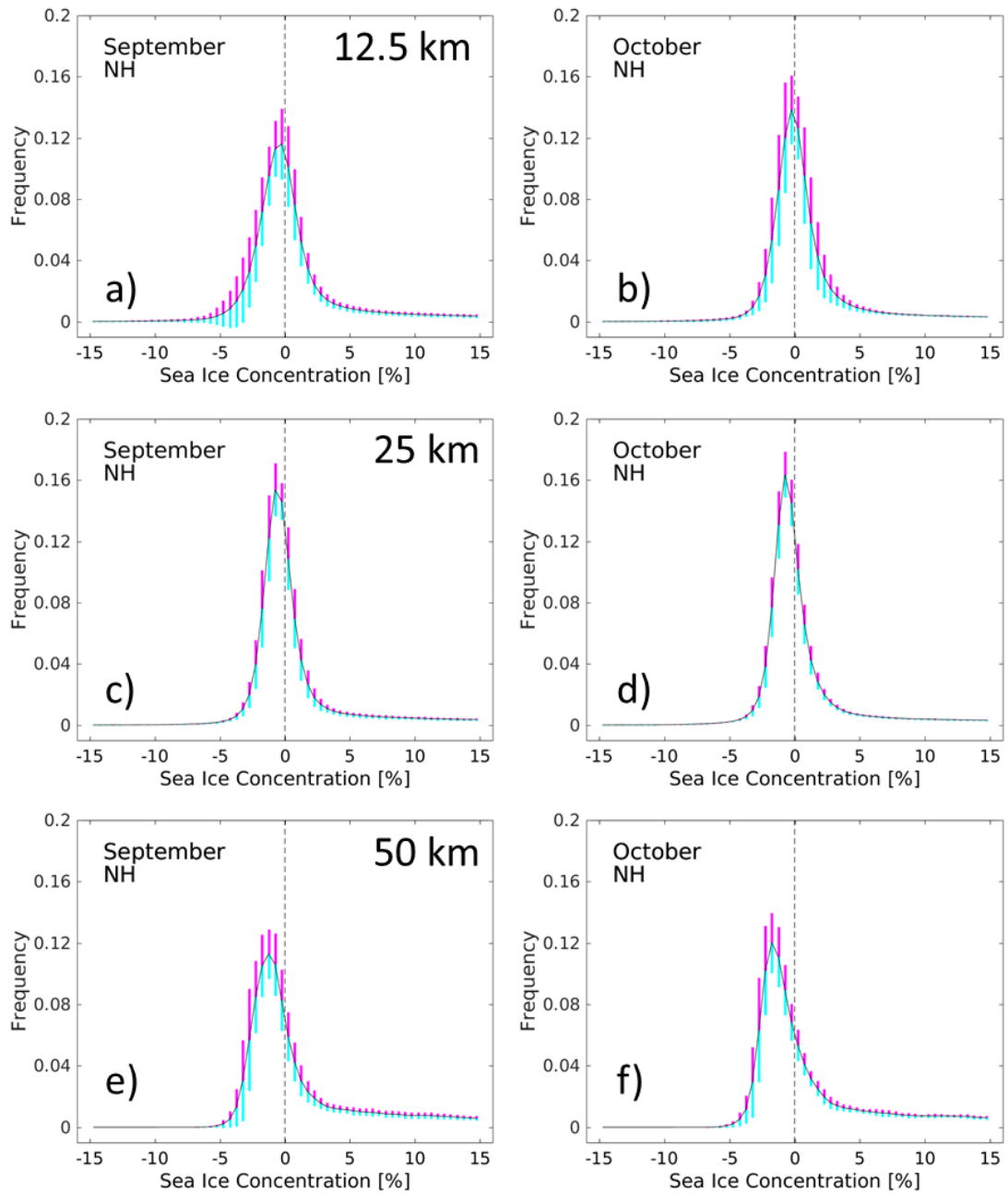
Figure 3-75: As Figure 3-71 for September and October.
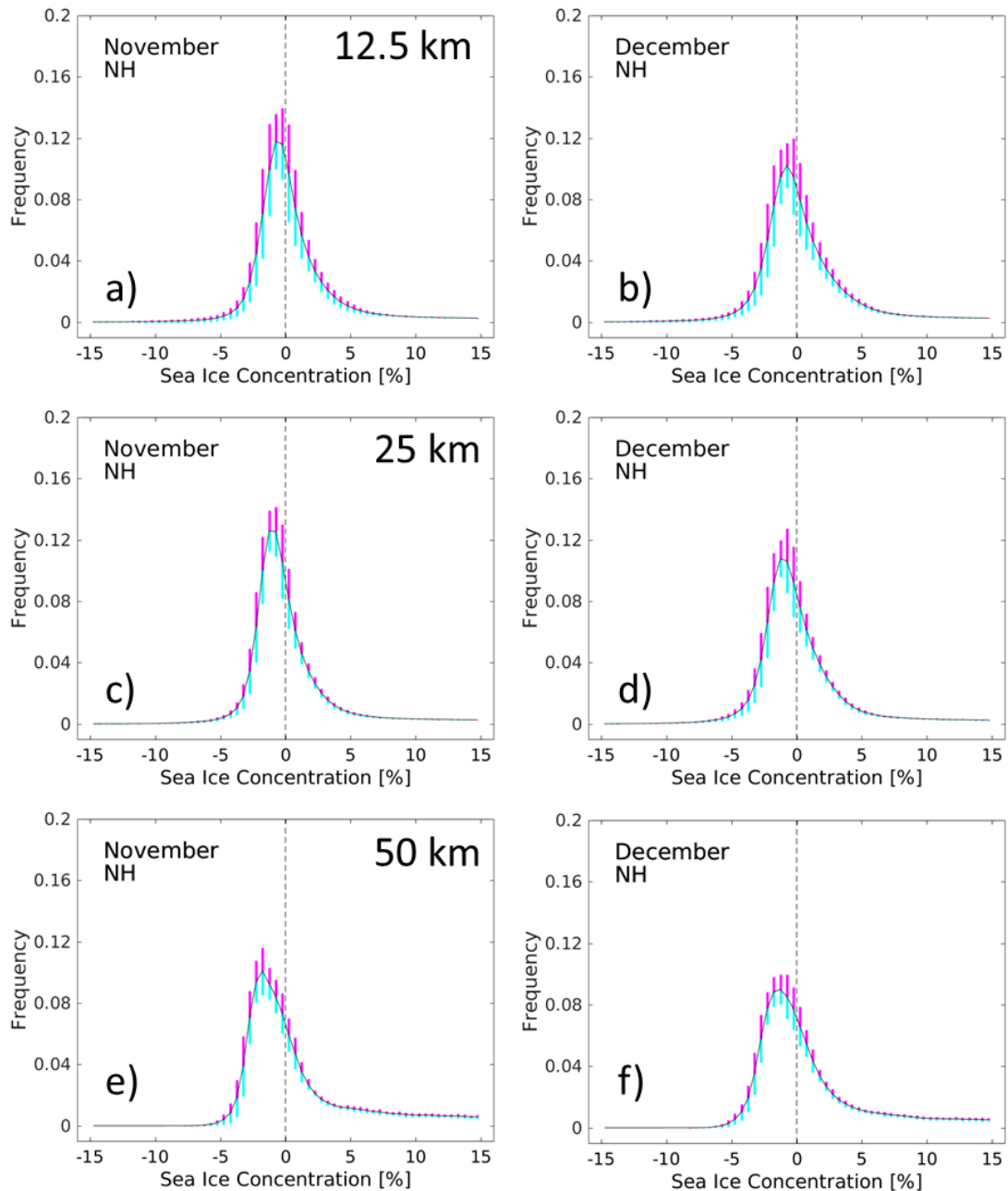
Figure 3-76: As Figure 3-71 for November and December.

All histograms shown in Figure 3-71 through Figure 3-76 reveal a narrow, well focused distribution near or around 0% sea-ice concentration.

SIC values rarely fall below -5%, particularly for the 25 km and the 50 km products (images c) through f) in Figure 3-71 through Figure 3-76). The largest and also most variable fraction of SIC < -5% is observed for the 12.5 km product (Figure 3-71 through Figure 3-76, a), b); especially during August and September.

Throughout the year, the histogram of the 50 km product is the most stable one (images e), f) in Figure 3-71 through Figure 3-76). Its shape stays

pretty constant most of the year with little variation in maximum frequency. The modal sea-ice concentration peak is most often located in bin -1.5% to -1.0%. Months April and May feature the most stable monthly histograms as illustrated by the small standard deviations (cyan and magenta bars) in these months. Elevated standard deviations seem to occur more often on the negative than the positive side of the histograms, indicating considerable inter-annual variation in the distribution of SIC around its modal value.

Histograms of the 25 km product are the second most stable ones (images c), d) in Figure 3-71 through Figure 3-76). They are a bit less shifted towards negative SIC than the 50 km histogram. Modal SIC peaks in bin -1.0% to -0.5% from September through March and closer to 0% otherwise. all months except in January and February, when it is located in bin -1.5% to -1.0%. Histogram shapes have relatively little seasonal variation. Histograms are narrower than for the 50 km product except for July. Of the three algorithms the 25 km product seems to have the most stable SIC distribution around SIC = 0% because it gives the narrowest histogram and the smallest variability off the main peak (i.e. SIC > ~3%) for most months.

Histograms of the 12.5 km product (images a), b) in Figure 3-71 through Figure 3-76) show modal SIC values which are closest to zero of the three products investigated; from this point of view SICCI-HF has the smallest error at SIC=0%. Histograms of the 12.5 km product are, however, less narrow than those of the 25 km product and exhibit larger contributions and inter-annual variability from off-peak SIC values, e.g. for September and Oktober (Figure 3-75). It is also the only product which has notable contributions from SIC < -5% during most of the year.

ESA UNCLASSIFIED - For Official Use
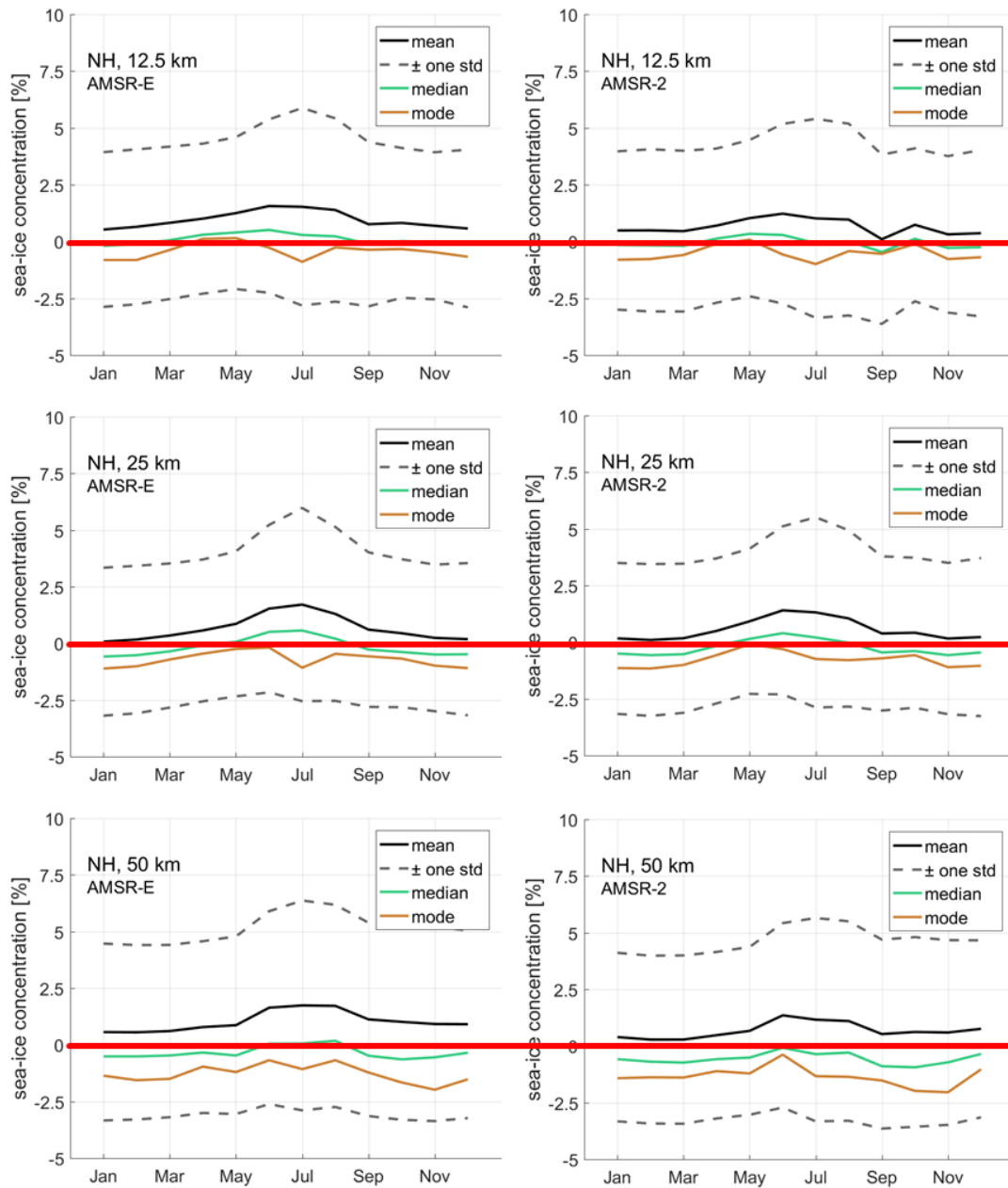
Figure 3-77: Multi-annual average monthly mean, median, and modal SIC of the three algorithms summarized from the histograms of Figure 3-71 through Figure 3-76 for the Northern Hemisphere – separately for AMSR-E (left) and AMSR2 (right). The dashed lines display ± 1 standard deviation around the mean.

With Figure 3-77 and Figure 3-78 we summarize the above findings. SICCI-LF (25 km) provides the smallest SIC error at SIC = 0% during most of the year when taking the range -15% … +15% into account; but SICCI-HF (12.5 km) and SICCI-VLF (50 km) are pretty similar (Figure 3-77). The same applies to the median SIC for the mentioned range. However, when taking the modal SIC then SICCI-VLF performs notably worse than the other

two algorithms with a year-round SIC error between -1% and -2%, and SICCI-HF performs best (Figure 3-77).

We did not find any notable difference in the performance between AMSR-E and AMSR2 (compare left and right images in Figure 3-77).
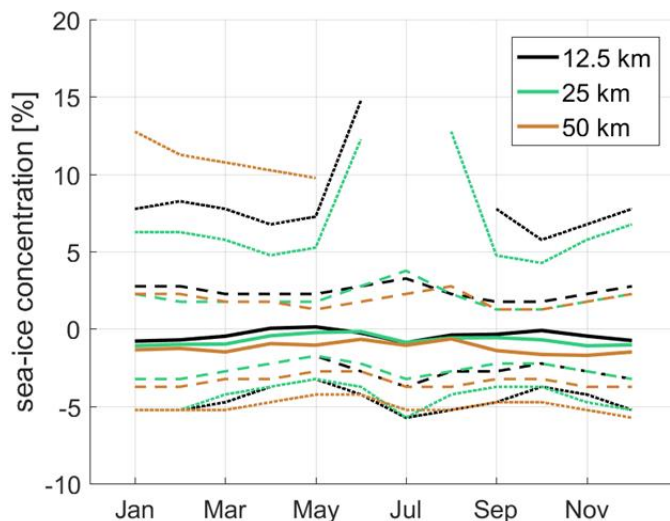
Figure 3-78: Multi-annual (AMSR-E and AMSR2 periods together) average modal SIC of the three algorithms at SIC = 0% (solid lines) for the Northern Hemisphere. The dashed and dotted lines mark the SIC where the frequency of the distribution as decreased by 66% and 95%, respectively, from the peak value. The distance between the solid and the dashed and/or dotted lines are a measure of the steepness of the histograms and hence of of confined the SIC values are around the respective modal SIC.

Figure 3-78 illustrates (see explanation in the caption) that for most months the SIC distribution provided by SICCI-LF (25 km) is best confined around the modal SIC value. In other words, during our investigation of SICCI-2 SIC values of the SIC range -15% … 15% the modal SIC value provided by the SICCI-LF (25 km) algorithm has the highest precision.
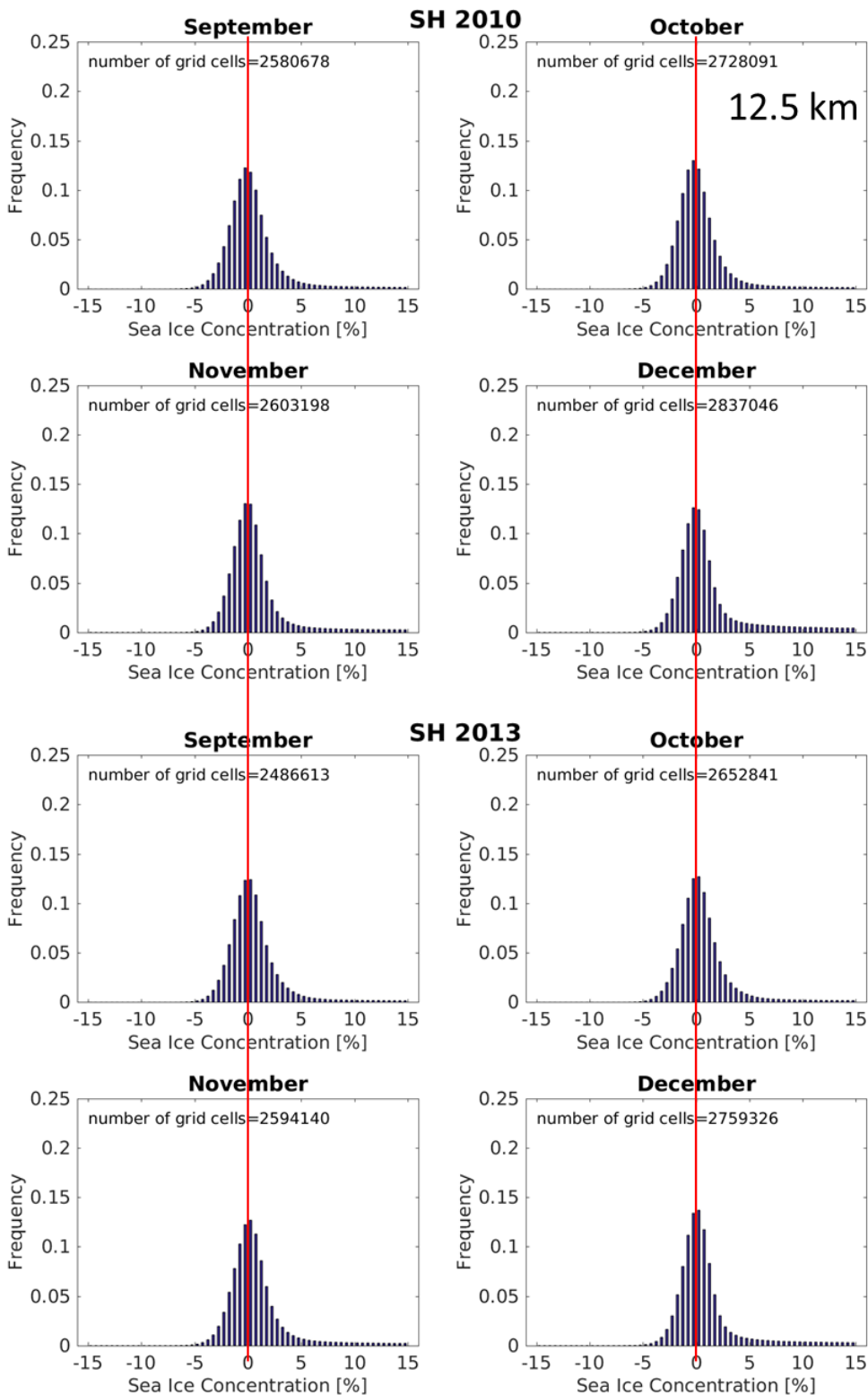
Figure 3-79: Sample set of SIC histograms around SIC=0% for SICCI-HF (12.5 km) for Sep. through Dec. 2010 and 2013 for the Southern Hemisphere. Red vertical line denotes location of SIC=0%. Binsize: 0.5%.
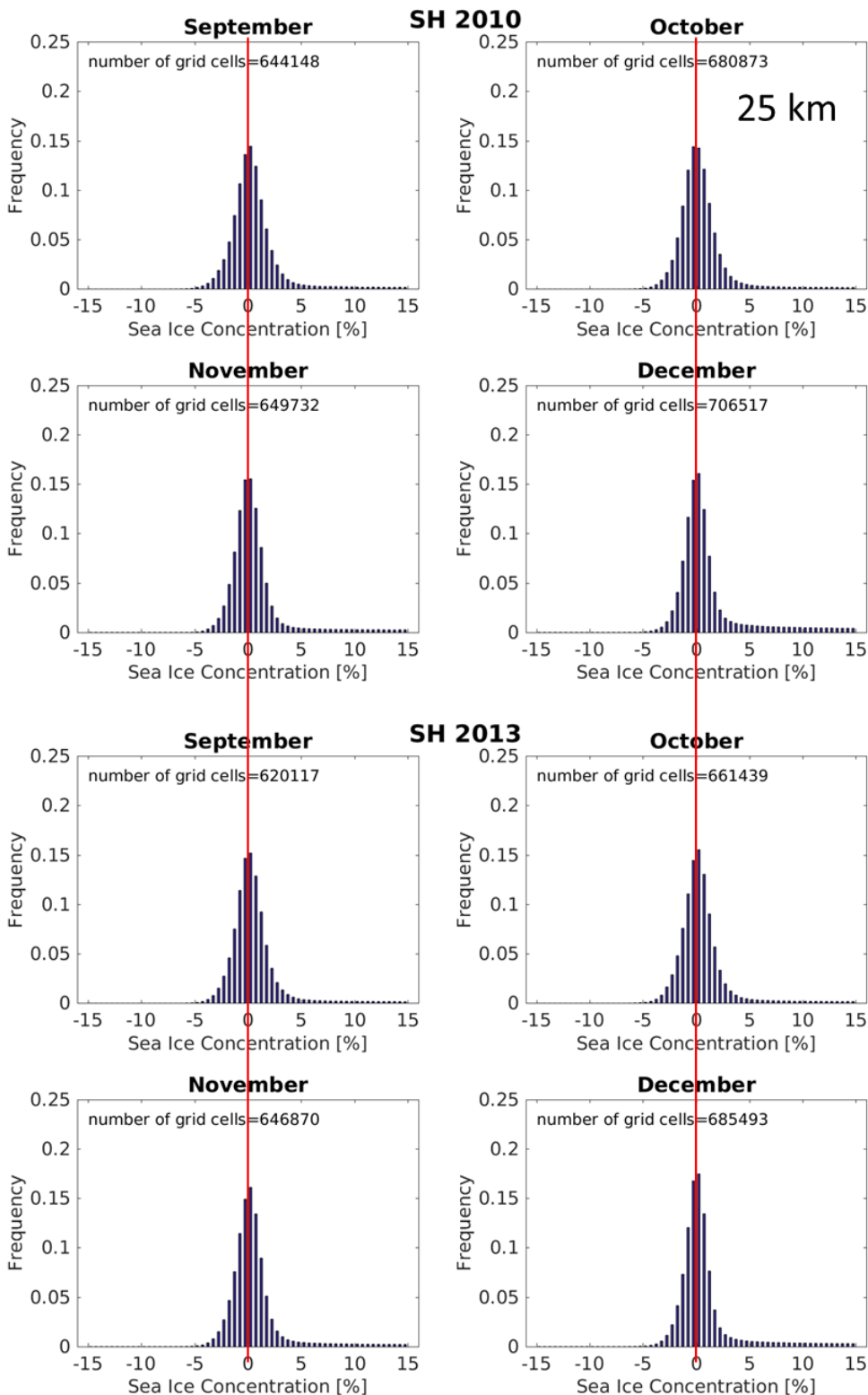
Figure 3-80: As Figure 3-79, using SICCI-LF (25.0 km).
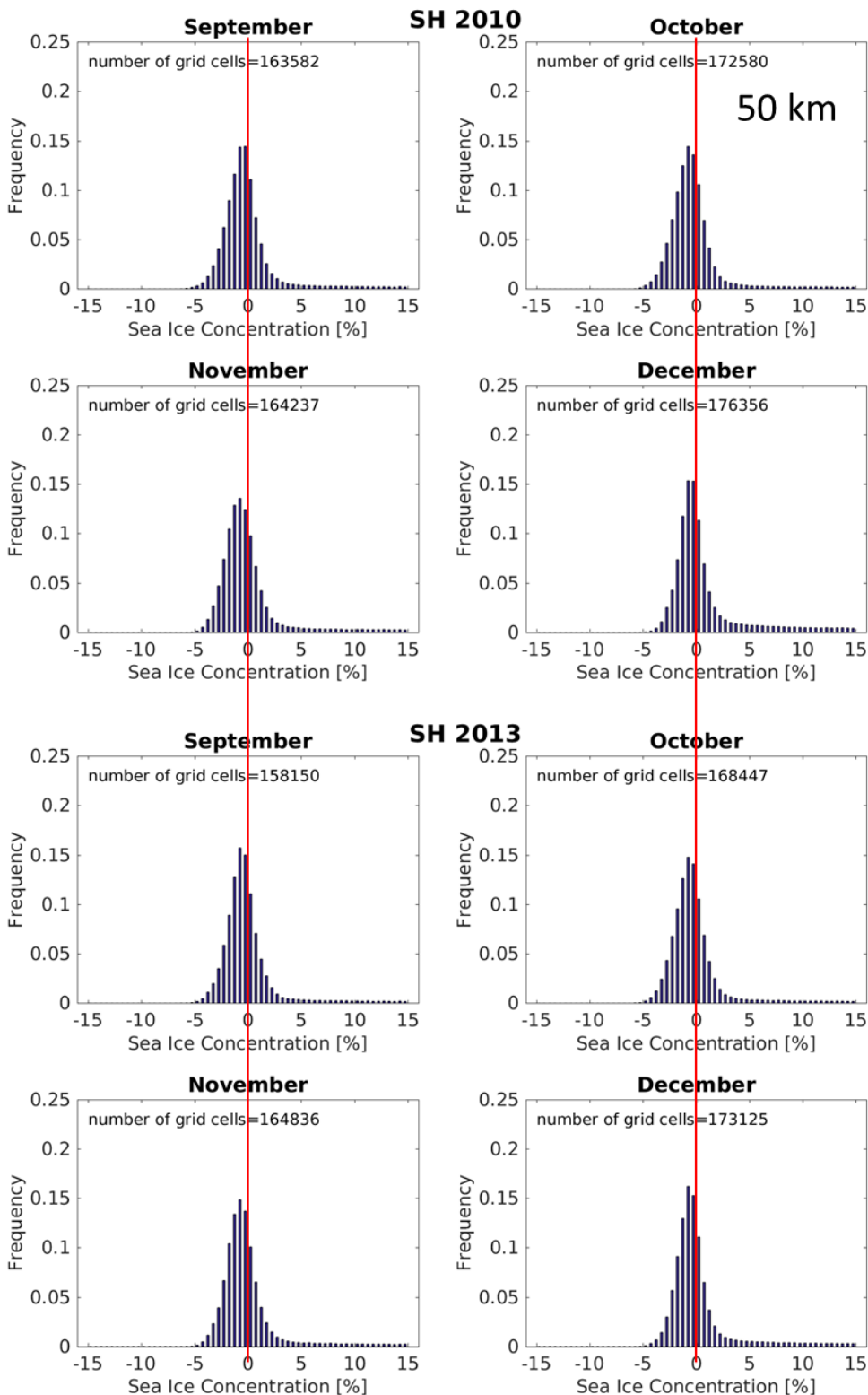
Figure 3-81: As Figure 3-79, using SICCI-VLF (50.0 km).

We show SIC distributions for the months September through December of two arbitrary years for the Southern Hemisphere for all three algorithms in

Figure 3-79 through Figure 3-81. We find quite symmetric SIC distributions around SIC=0% for SICCI-HF (12.5 km) and SICCI-LF (25.0 km); modal peaks are in bin -0.5% to 0.0% or 0.0% to 0.5%. SICCI-VLF (50.0 km) in contrast, has a SIC distribution slightly shifted to negative SIC values with a modal peak in bin -1.0% to -0.5% in almost all cases shown.
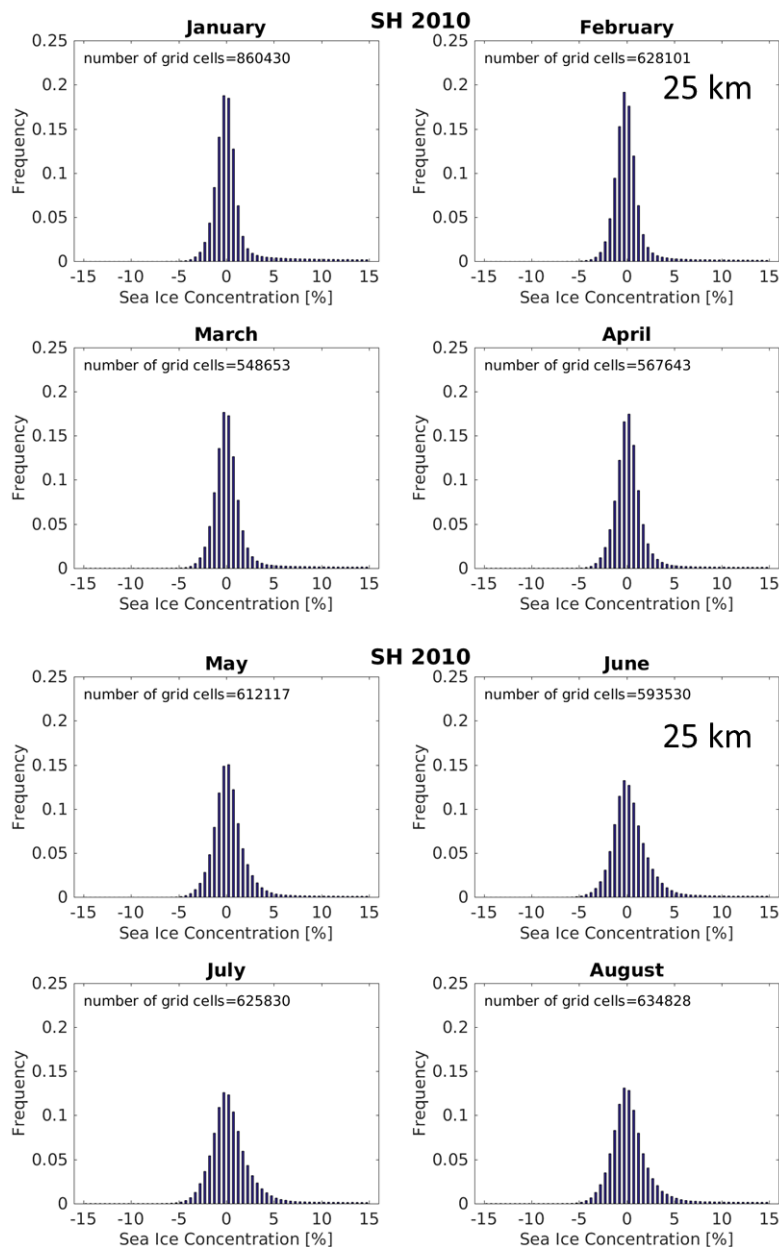
Figure 3-82: Sample seasonal evolution of the SIC distribution around SIC=0% using SICCI-LF (25.0 km). Binsize: 0.5%. Shown are months January through August of the year 2010 for the Southern Hemisphere.

The sample seasonal cycle shown for SICCI-LF in Figure 3-82 underlines how stable the SIC histograms are around SIC=0% also during the coarse of a full year. The histograms get a bit wider during winter, owing to the

ESA UNCLASSIFIED - For Official Use

higher variability in the weather influence but the modal SIC still remains in the two bins adjacent to SIC = 0%.
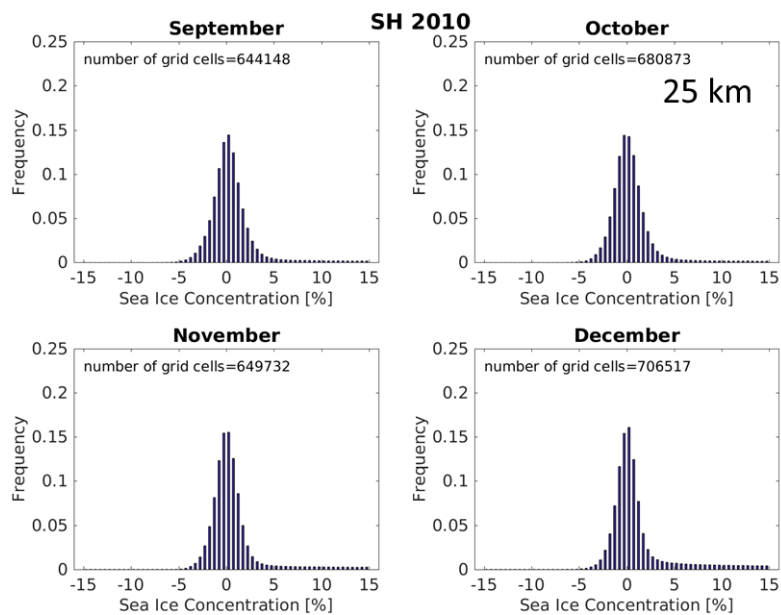
Figure 3-82 continued Months September through December

ESA UNCLASSIFIED - For Official Use
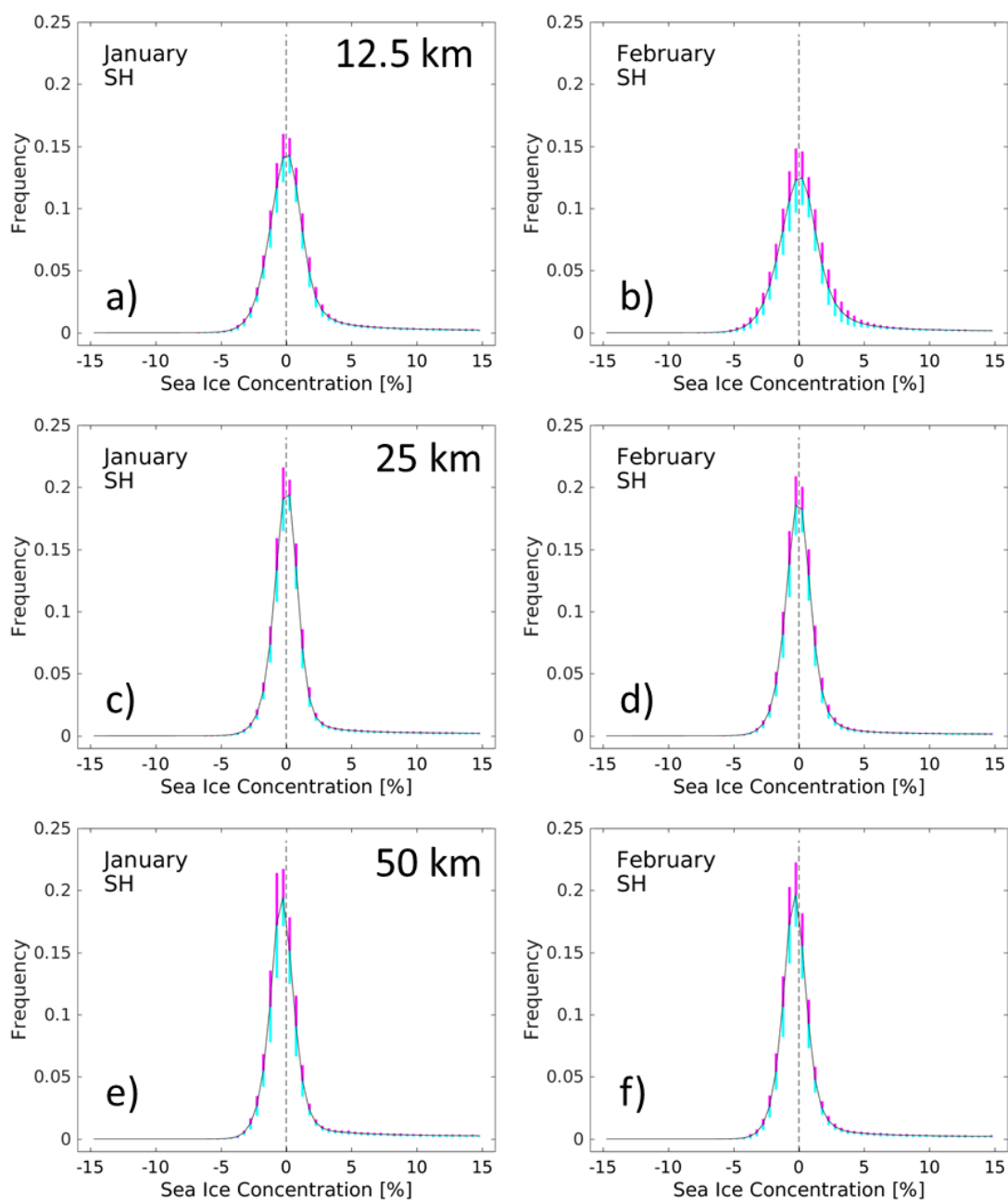
Figure 3-83: Whole-period (2002-2015) average monthly histograms of the sea-ice concentration around 0% for the 12.5 km (a,b), 25 km (c,d), and 50 km (e,f) product for January and February for the Southern Hemisphere. Bin size is 0.5%. Bars in cyan and magenta denote one standard deviation of the probability with which a SIC value falls into the respective bin. Similar figures to this one are Figure 3-84 through Figure 3-88, which are showing the other months.

The observations formulated in the context of Figure 3-79 through Figure 3-82 also hold for the multi-annual average monthly histograms shown in Figure 3-83 through Figure 3-88. For SICCI-HF (images a), b)) and SICCI-LF (images c), d)) SIC histograms are quite symmetric around SIC = 0% while for SICCI-VLF (image e), f)) the histogram is shifted towards negative

SIC values. We find that this shift is only ~0.5% during January through April but 1% during the other months.
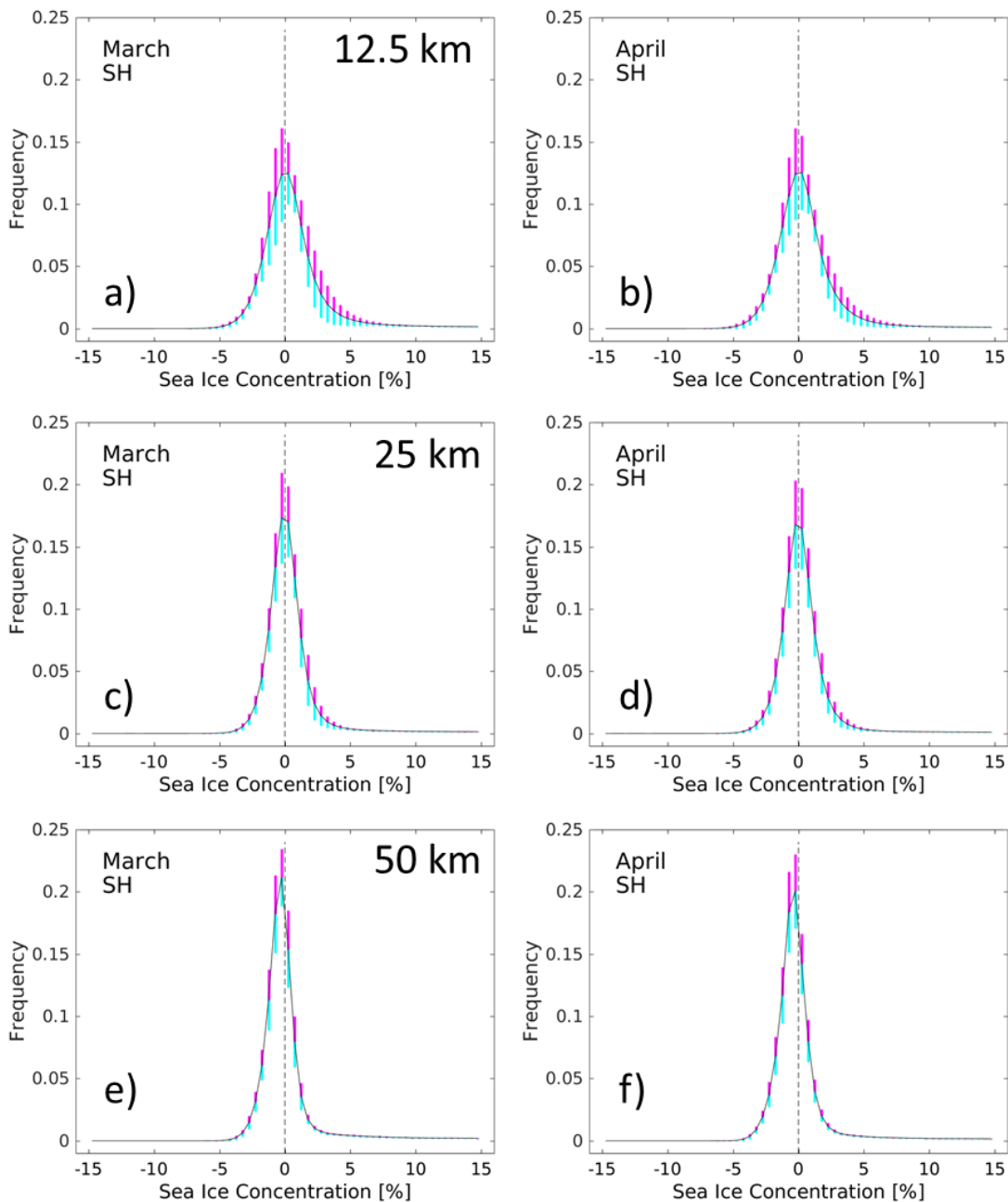
Figure 3-84: As Figure 3-83 for March and April.

We find that histograms tend to be broadest for SICCI-HF (images a), b) in Figure 3-83 through Figure 3-88) – particularly during winter. This can be attributed to the larger SIC variability caused by residual weather effects which are more pronounced at algorithms involving near-90 GHz frequencies such as SICCI-HF. Accordingly, during most of the fall and winter months SICCI-VLF provides the narrowest histograms (images e), f) in Figure 3-83 through Figure 3-88). The distribution of the standard deviations is relatively similar among the three algorithms. One exception is

ESA UNCLASSIFIED - For Official Use

SICCI-HF which shows elevated standard deviations over a considerably larger SIC range than the other two algorithms during months February through May (Figure 3-83 b), Figure 3-84 a), b), and Figure 3-85 a).
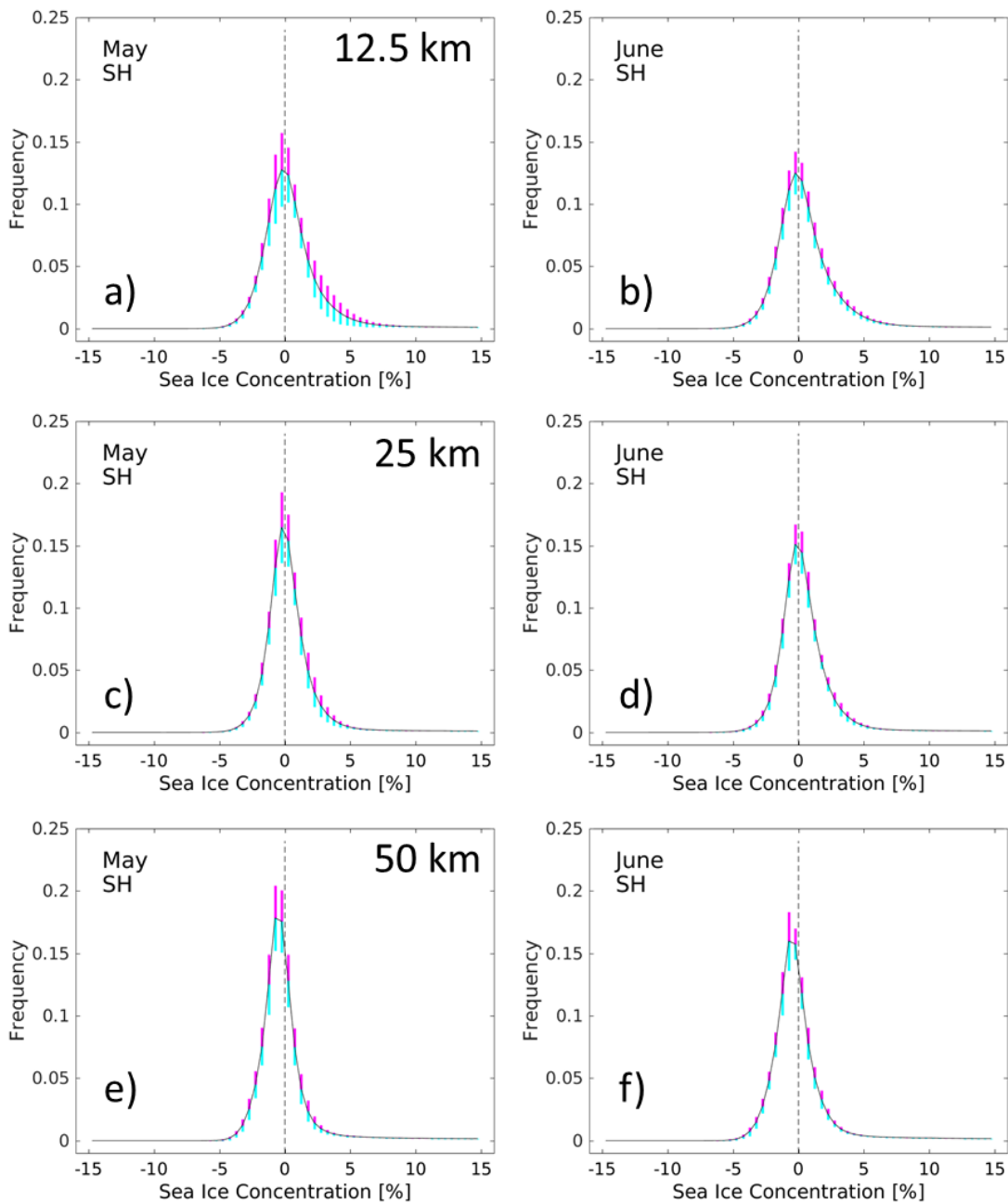
Figure 3-85: As Figure 3-83 for May and June.
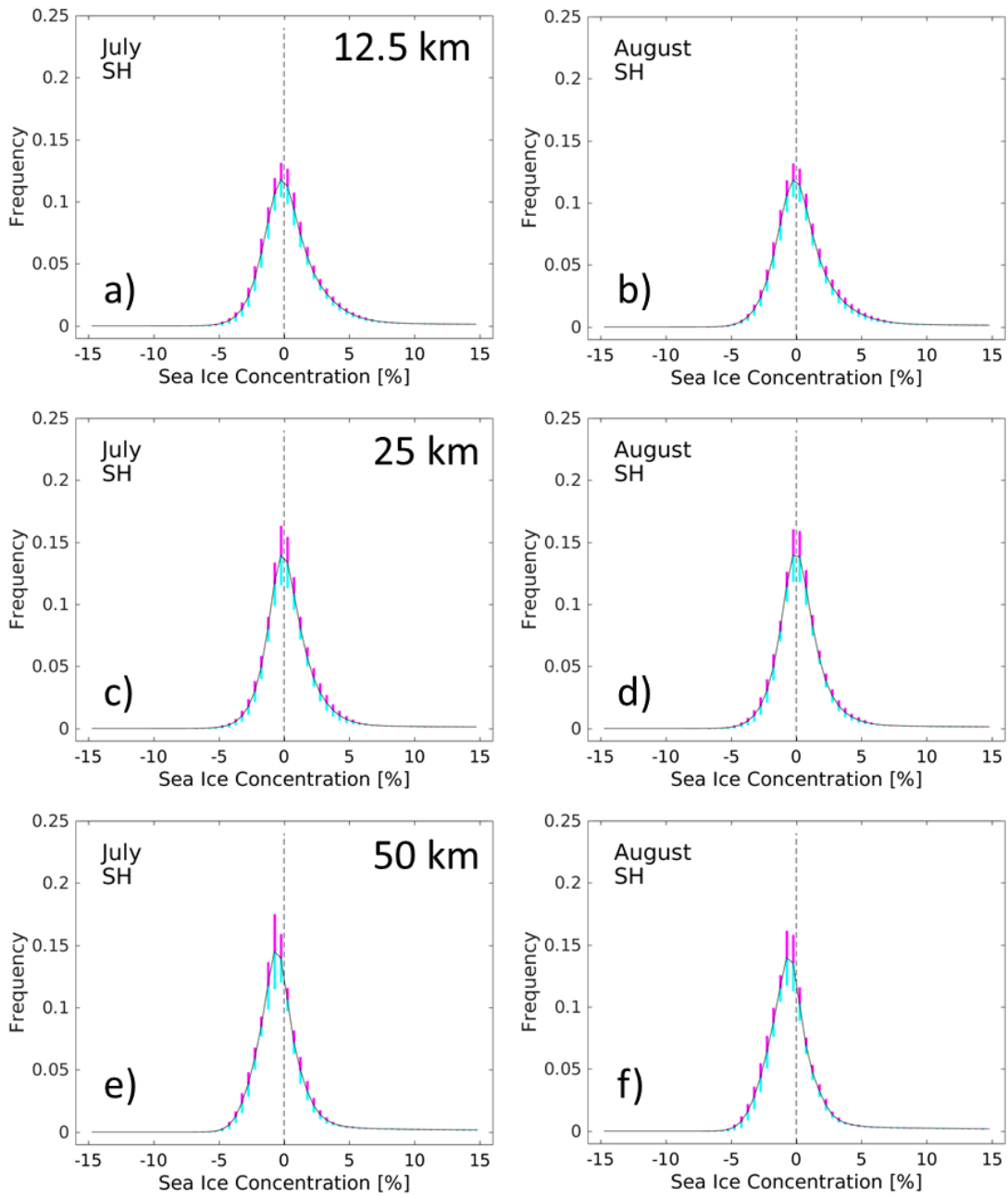
Figure 3-86: As Figure 3-83 for July and August.
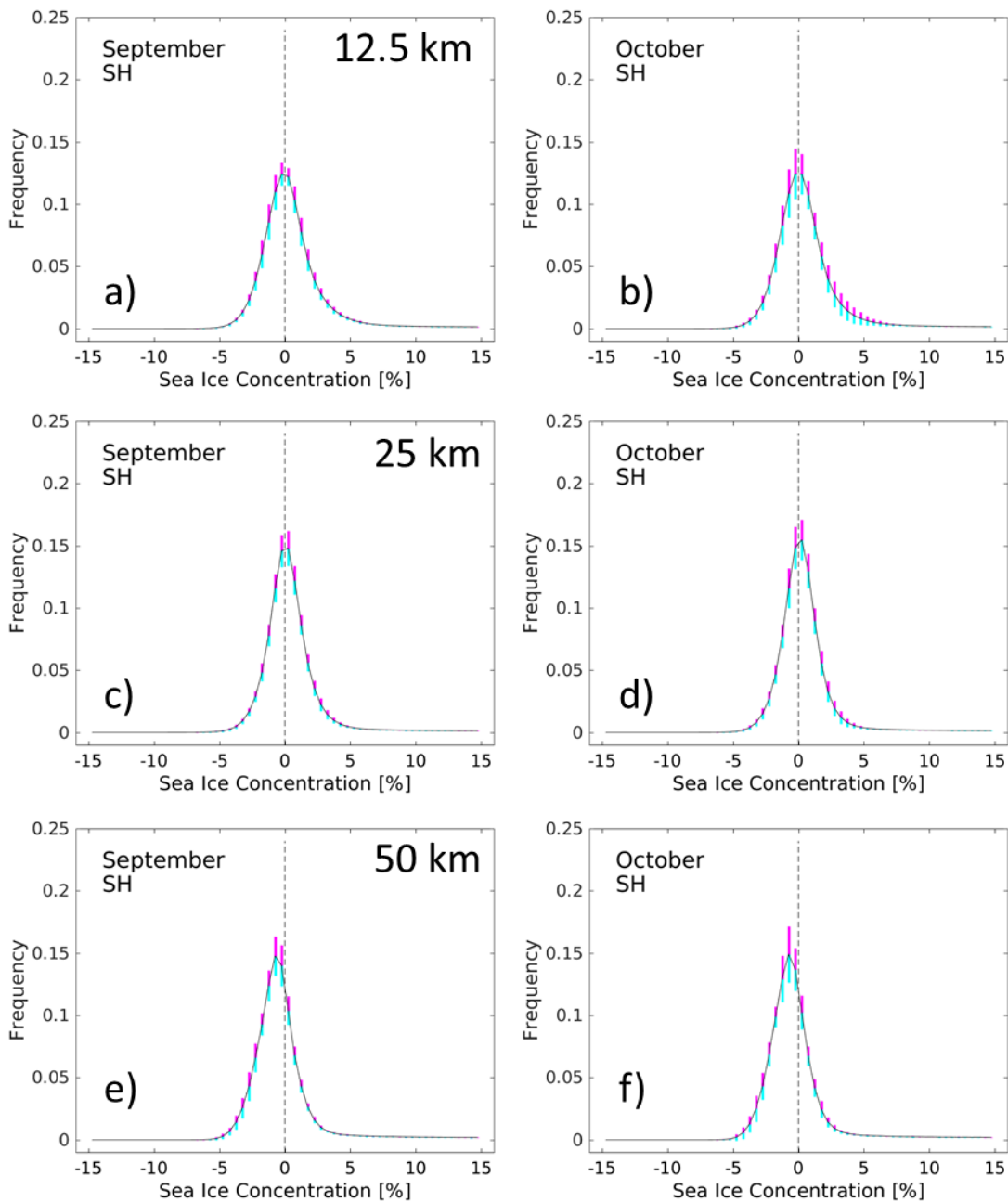
Figure 3-87: As Figure 3-83 for September and October.
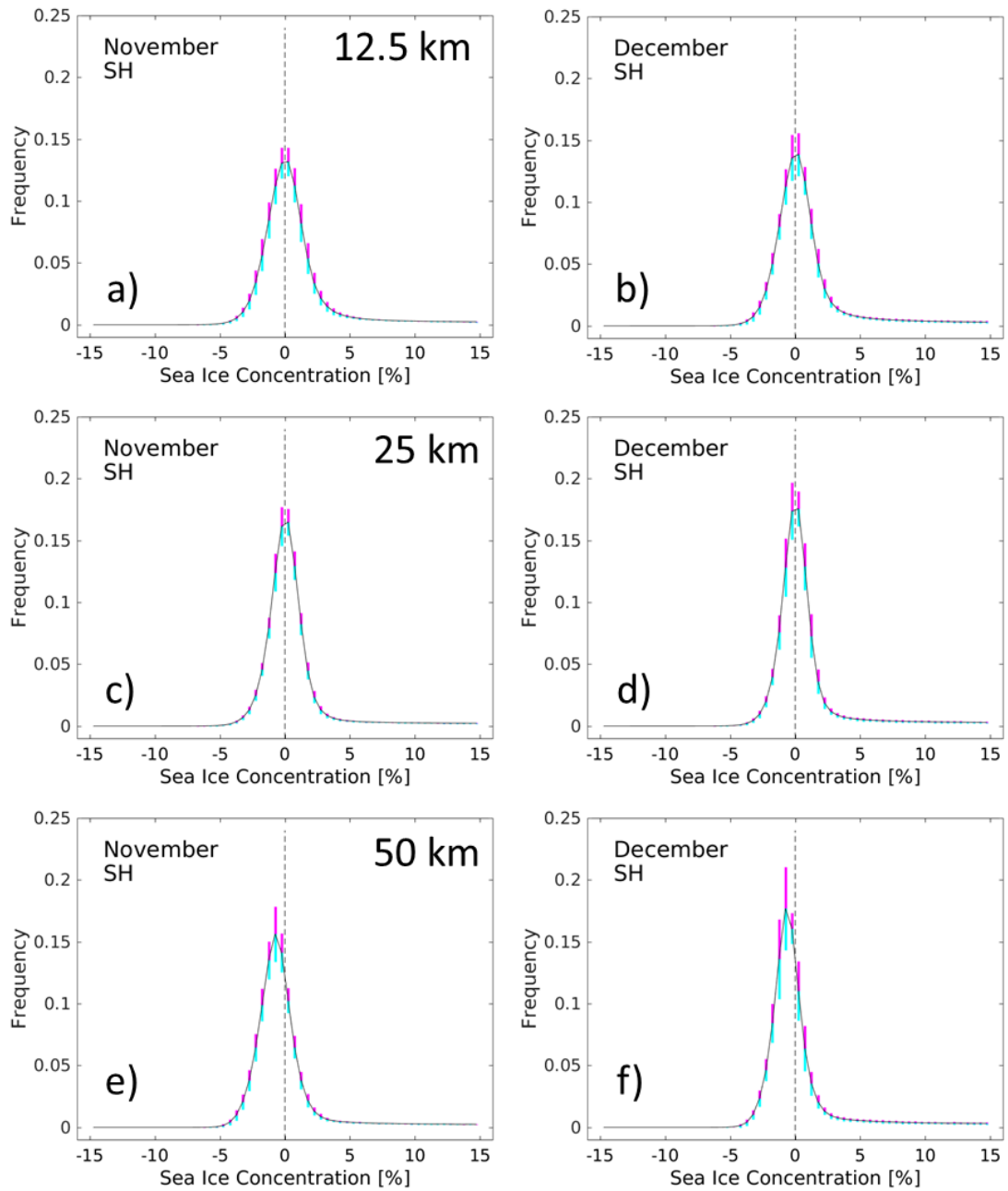
Figure 3-88: As Figure 3-83 for November and December.
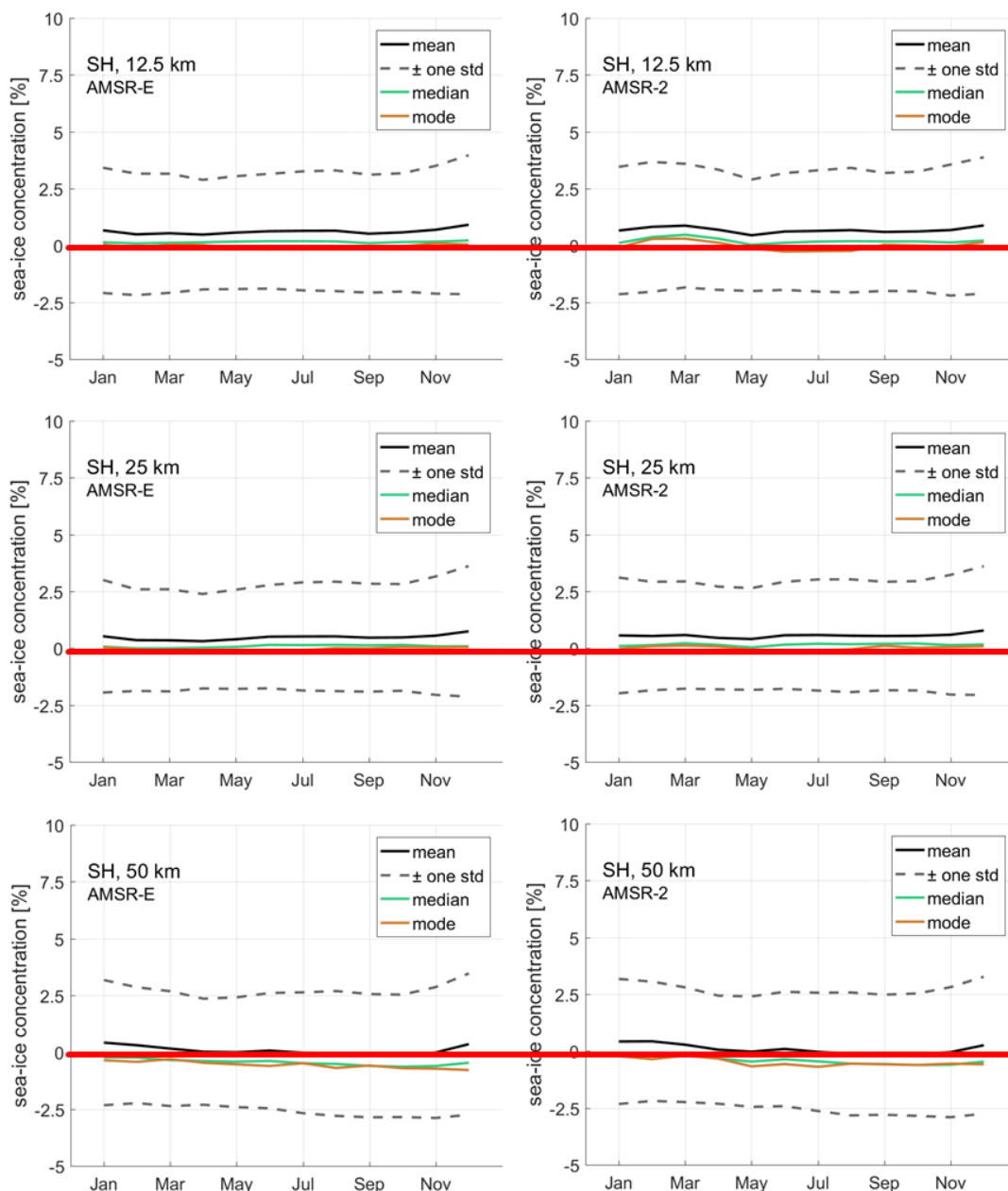
Figure 3-89: Multi-annual average monthly mean, median, and modal SIC of the three algorithms summarized from the histograms of Figure 3-83 through Figure 3-88 for the Southern Hemisphere – separately for AMSR-E (left) and AMSR2 (right). The dashed lines display ± 1 standard deviation around the mean.

With Figure 3-89 and Figure 3-90 we summarize the above findings. SICCI-VLF (50 km) provides the smallest SIC error at SIC = 0% during most of the year when taking the range -15% … +15% into account and computing the mean SIC (Figure 3-89, bottom); SICCI-HF (12.5 km) and SICCI-LF (25 km) are pretty similar but have an error of +1% (Figure 3-89, top and middle). However, when taking the median or the modal SIC then SICCI-VLF performs worse than the other two algorithms with a year-round SIC error between -0.5% and -1.

We did not find any notable difference in the performance between AMSR-E and AMSR2 (compare left and right images in Figure 3-89).
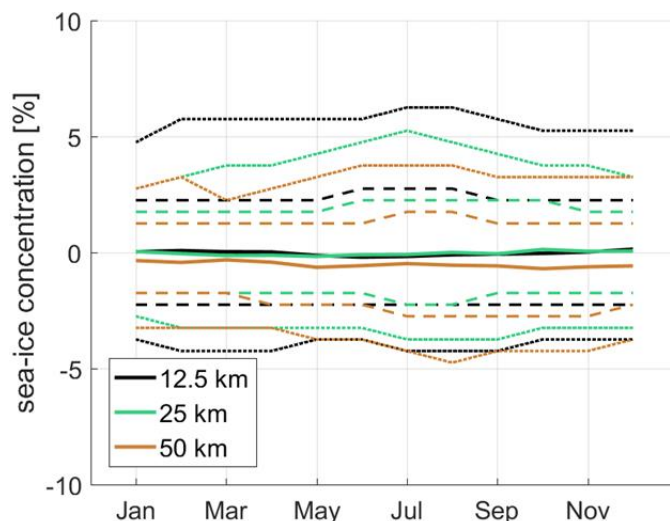
Figure 3-90: Multi-annual (AMSR-E and AMSR2 periods together) average modal SIC of the three algorithms at SIC = 0% (solid lines) for the Southern Hemisphere. The dashed and dotted lines mark the SIC where the frequency of the distribution as decreased by 66% and 95%, respectively, from the peak value. The distance between the solid and the dashed and/or dotted lines are a measure of the steepness of the histograms and hence of of confined the SIC values are around the respective modal SIC.

Finally, Figure 3-90 illustrates that the SICCI-HF SIC-distributions are the least confined around SIC = 0% of the three products; in other words: SICCI-HF SIC is least precise. Most of the time it is SICCI-VLF which is most confined around SIC = 0%, and hence is the most precise of the three algorithms.

3.6.2   *Pack ice*

We begin with the notion that not too much focus should be given on discussing the seasonal and inter-annual variation of the sea-ice concentrations below the modal SIC value because these, lower SIC values simply represent the actual sea-ice concentration and do not inform about the skill of the algorithms. The reader needs to keep in mind that we are looking in general at the sea-ice concentration range from 85% through 115% and that the focus is on the behavior of the products above 100% sea-ice concentration. We are interested in i) the scatter around the modal SIC facing SIC values > 100%, ii) whether the modal SIC is located at SIC < 100% throughout the year, and iii) whether the modal SIC is the same for the three products.

One period of the year with a high likelihood for algorithms to provide SIC > 100% is during spring / summer before substantial formation of melt ponds has commenced (see e.g. [RD-14]). Accordingly we show a sample set of

SIC distributions around 100% for two arbitrary years for months May through August in Figure 3-91 through Figure 3-93.
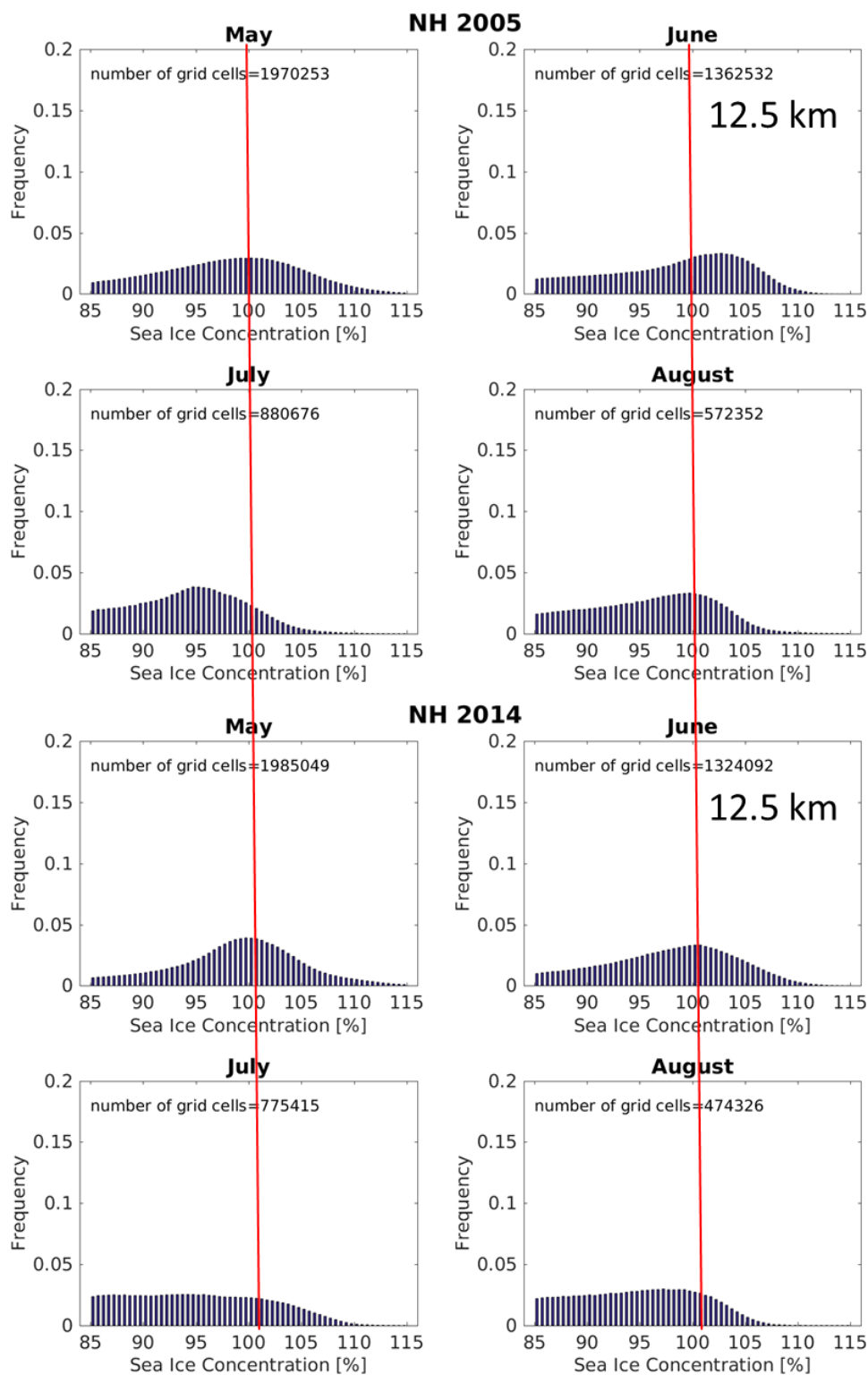
Figure 3-91: Sample set of SIC histograms around SIC=100% for SICCI-HF (12.5 km) for May through Aug. 2005 and 2014 for the Northern Hemisphere. Red vertical line denotes location of SIC=100%. Binsize: 0.5%.

ESA UNCLASSIFIED - For Official Use
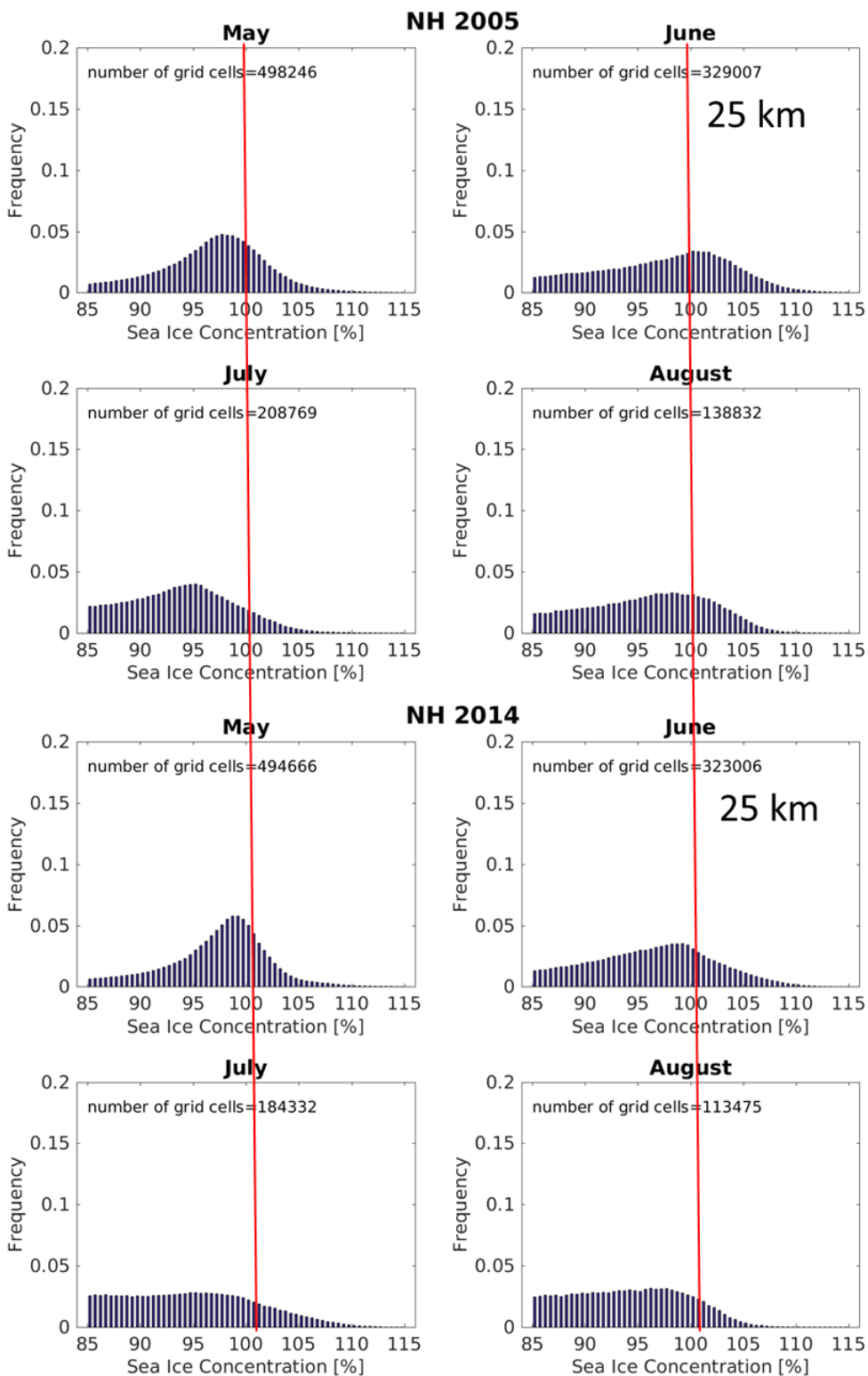
Figure 3-92: As Figure 3-91, using SICCI-LF (25.0 km).
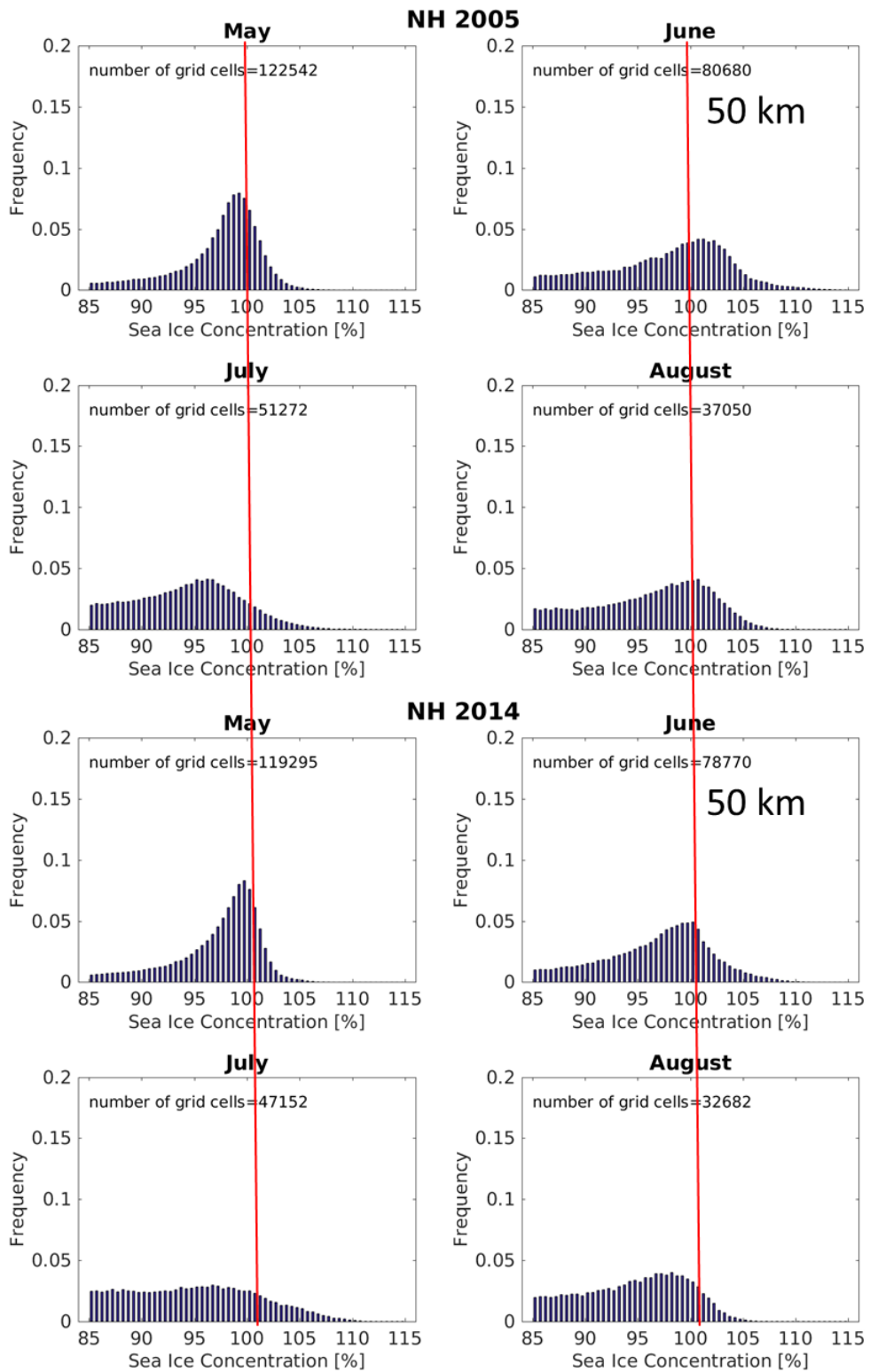
Figure 3-93: As Figure 3-91, using SICCI-VLF (50.0 km).

We find two things. First, all three algorithms provide a substantial fraction of SIC values > 100% - particularly for months May and June and less so for months July and August. We find the largest fraction of SIC > 100% using SICCI-HF. Secondly, modal SIC values may exceed 100% in May and/or June, e.g. in 2005 (Figure 3-91 through Figure 3-93, top panel) but this is not necessarily the case in every year (Figure 3-91 through Figure 3-93, bottom panel). Very high SIC values obtained with SICCI-HF, i.e. > 110%, occur more often in May than in June. In contrast, very high SIC values obtained with SICCI-LF and SICCI-VLF, i.e. > 105%, occur more often in June than in May. This can be explained with the different sensitivity to melt processes in the snow and at the snow surface. Lower frequencies as used in SICCI-LF and SICCI-VLF are less sensitive to the early stages of melt.
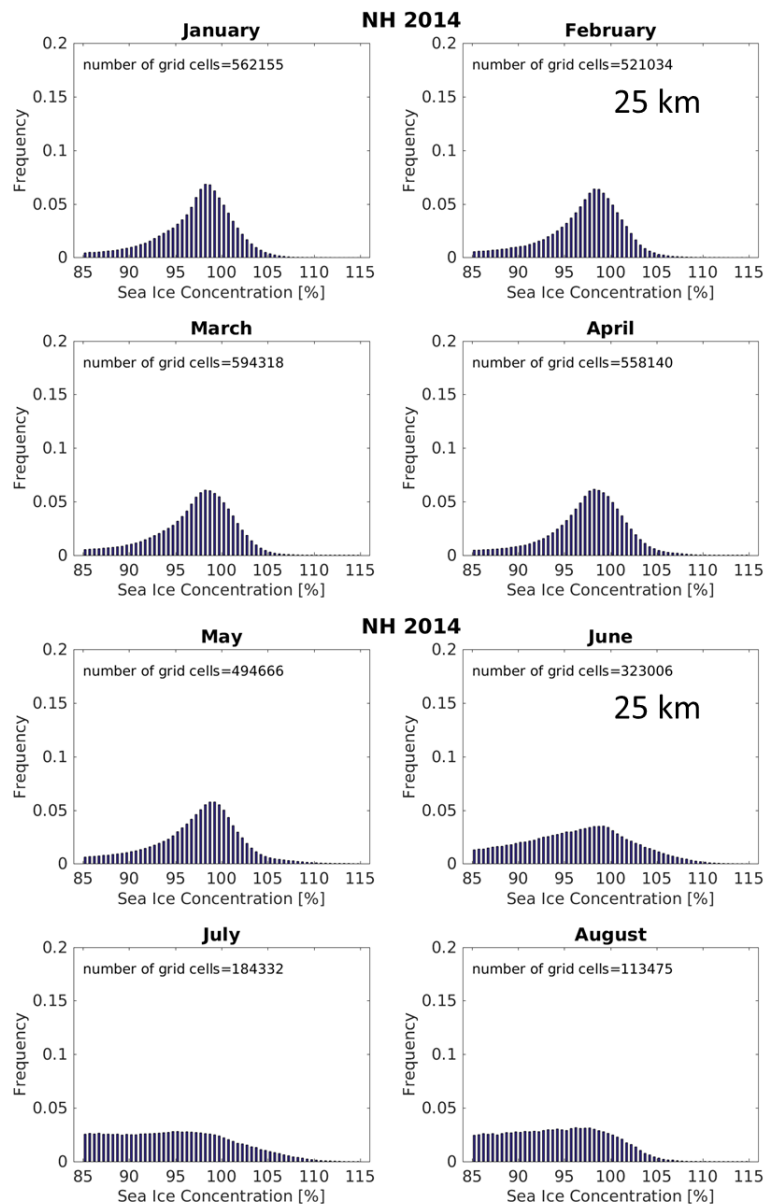
Figure 3-94: Sample seasonal evolution of the SIC distribution around SIC=100% using SICCI-LF (25.0 km). Binsize: 0.5%. Shown are months January through August of the year 2014 for the Northern Hemisphere.
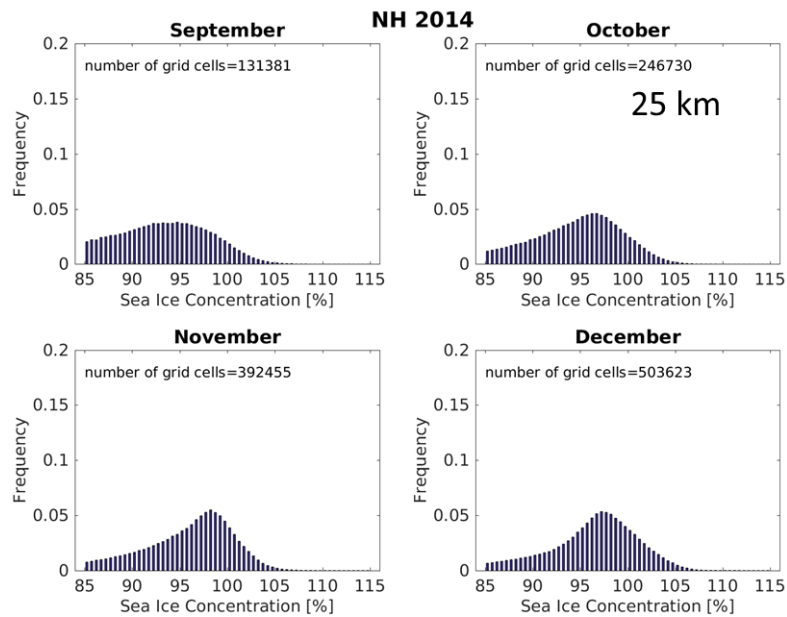
Figure 3-94 continued Months September through December.

The sample seasonal cycle shown in Figure 3-94 for SICCI-LF shows a well defined peak at SIC between 95% and 100% during winter, i.e. from about November through May. The peak maximum seems to be located relatively stable at ~98.0% - except in May when it is shifted closer to 100%. During the melt season the peak flattens and for the year shown no distinct modal SIC value can be found for monthy July and August.
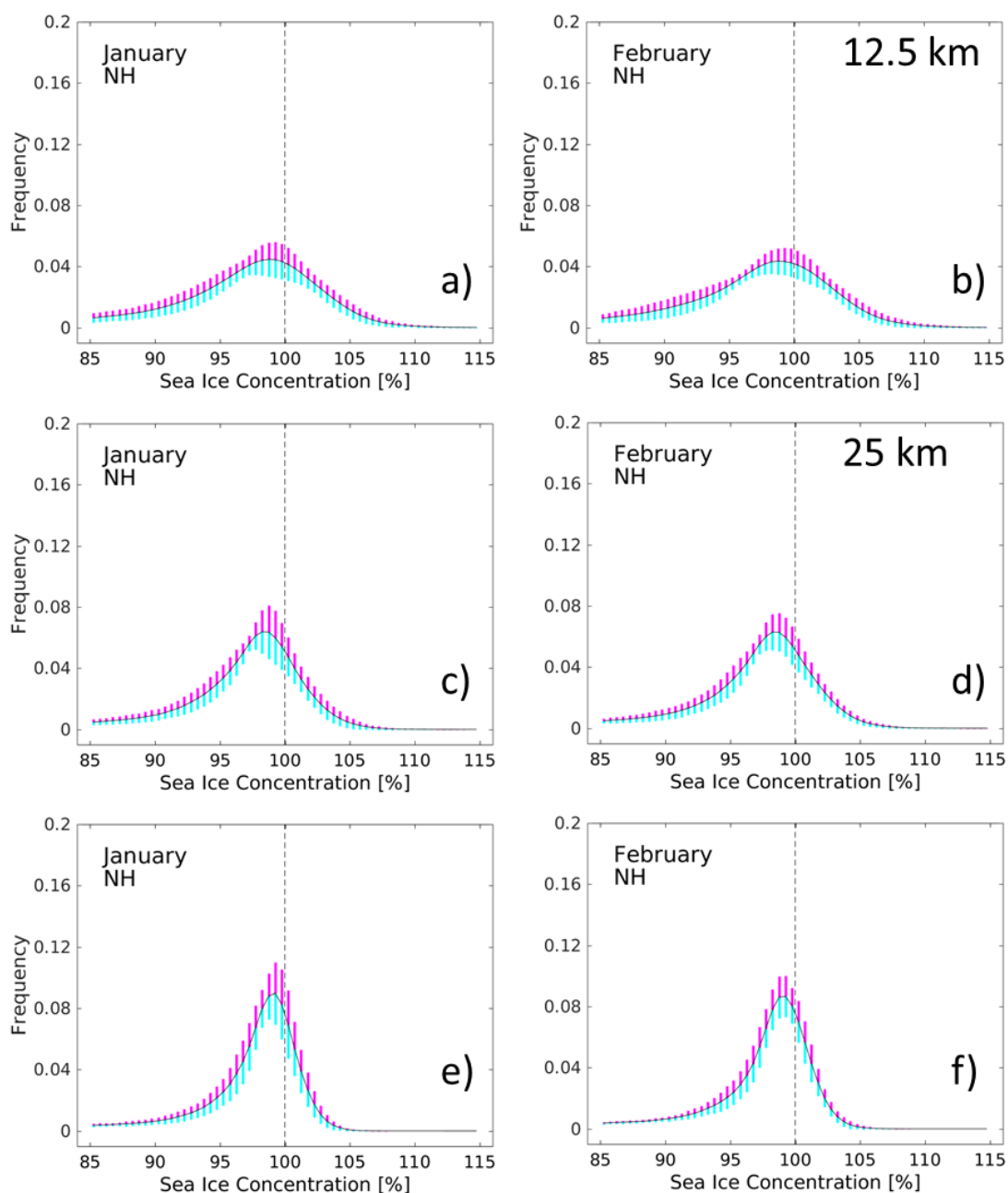
Figure 3-95: Whole-period (2002-2015) average monthly histograms of the sea-ice concentration around 100% for the 12.5 km (a,b), 25 km (c,d), and 50 km (e,f) product for January and February for the Northern Hemisphere. Bin size is 0.5%. Bars in cyan and magenta denote one standard deviation of the probability with which a SIC value falls into the respective bin. Similar figures to this one are Figure 3-96 through Figure 3-100, which are showing the other months.

When looking at the multi-annual average monthly histograms shown in Figure 3-96 through Figure 3-100 we see the findings of Figure 3-91 through Figure 3-93 mostly confirmed. None of the SIC algorithms provides SIC centered at 100%. Closest to 100% are SICCI-VLF SIC values (images e), f) in Figure 3-95 through 3.6.2.10), peaking on average in bin 99.0% to

99.5% during winter. SICCI-VLF is also the algorithm with the steepest decline in SIC towards SIC > 100% and/or a most narrow histogram around its modal SIC value. Next close to 100% are the SIC values of the SICCI-HF algorithm (images a), b) in Figure 3-95 through Figure 3-100); this algorithms' SIC peak in bin 98.5% to 99.0% during winter. At the same time SICCI-HF SIC exhibit the shallowest slopes towards SIC > 100%. Least close to 100% are the modal SIC values of SICCI-LF (images c, d) in Figure 3-95 through Figure 3-100); these are in bin 98.0% to 98.5% during winter. During summer (Figure 3-98) none of the algorithms provide a SIC distribution which would allow – within the range used (85% … 115%) – to obtain a modal SIC value.
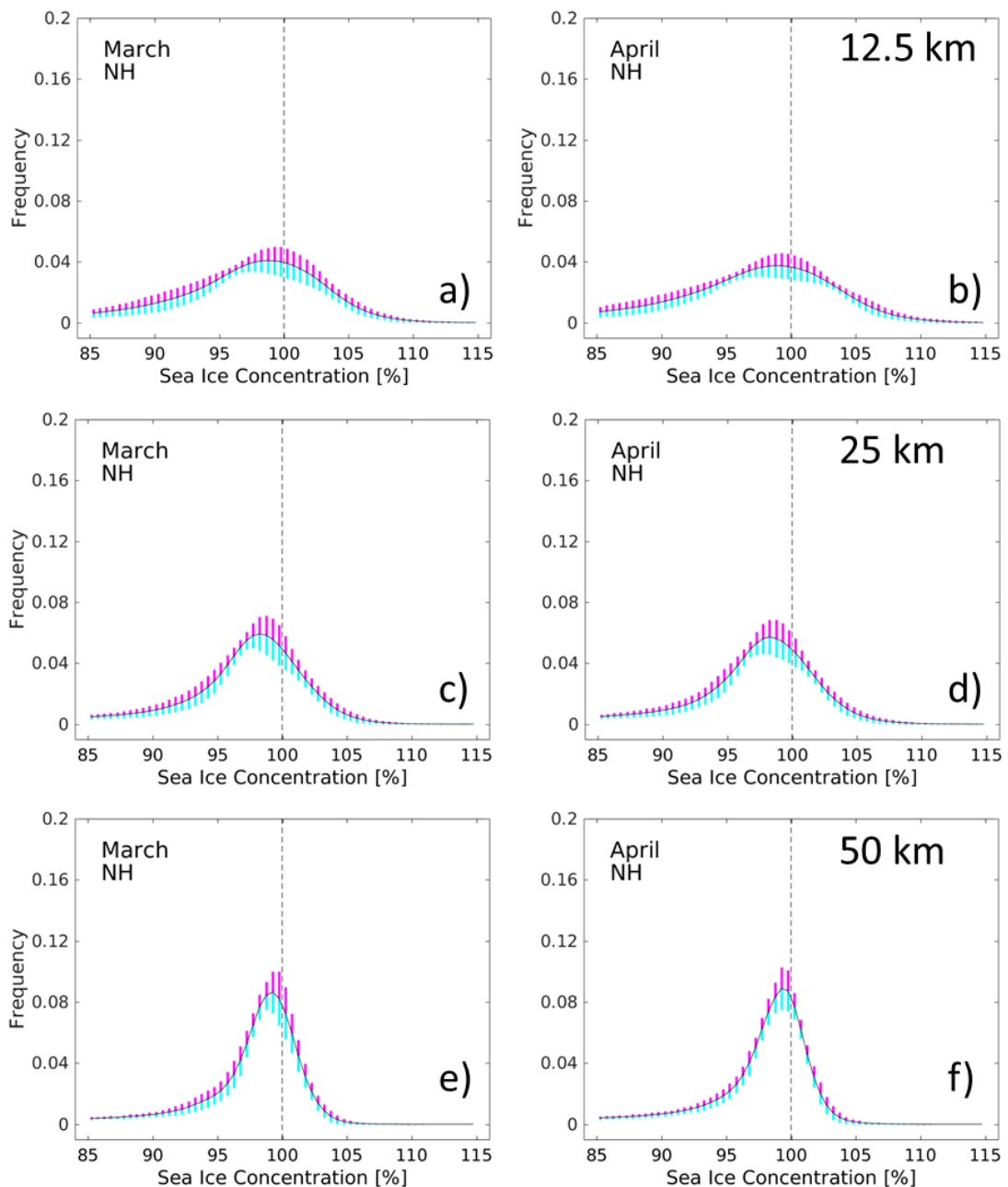
Figure 3-96: As Figure 3-95 for March and April.

Modal SIC values from all three algorithms get closer to SIC = 100% in May and/or June (Figure 3.6.2.9). SICCI-HF SIC peaks at 100% in May and 101% in June, followed by SICCI-VLF (99.5% to 100.0% in May). SICCI-LF stays at bin 98.5% to 99.0% in May and June. One could state that, compared to winter, SICCI-VLF is least sensitive to the changing conditions during late spring / summer while SICCI-HF is most sensitive.
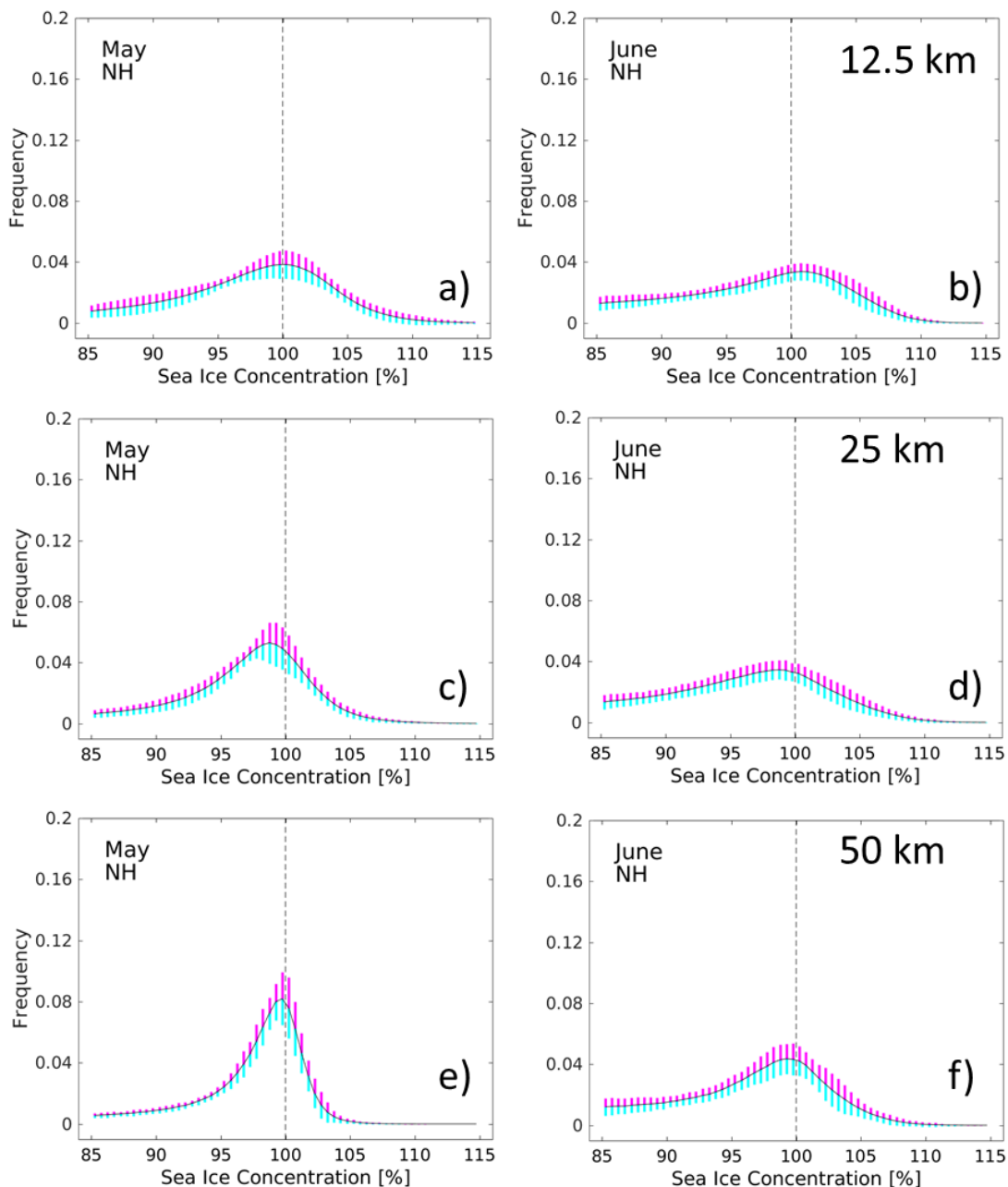
Figure 3-97: As Figure 3-95 for May and June.

Note that SIC > 105% are practically absent during winter for SICCI-VLF while a considerable fraction of SIC > 105% is observed for SICCI-LF and most so for SICCI-HF. This could be attributed to the larger sensitivity to

surface property changes at near-90 GHz frequencies when compared to the other frequencies predominantly used by the other two algorithms.
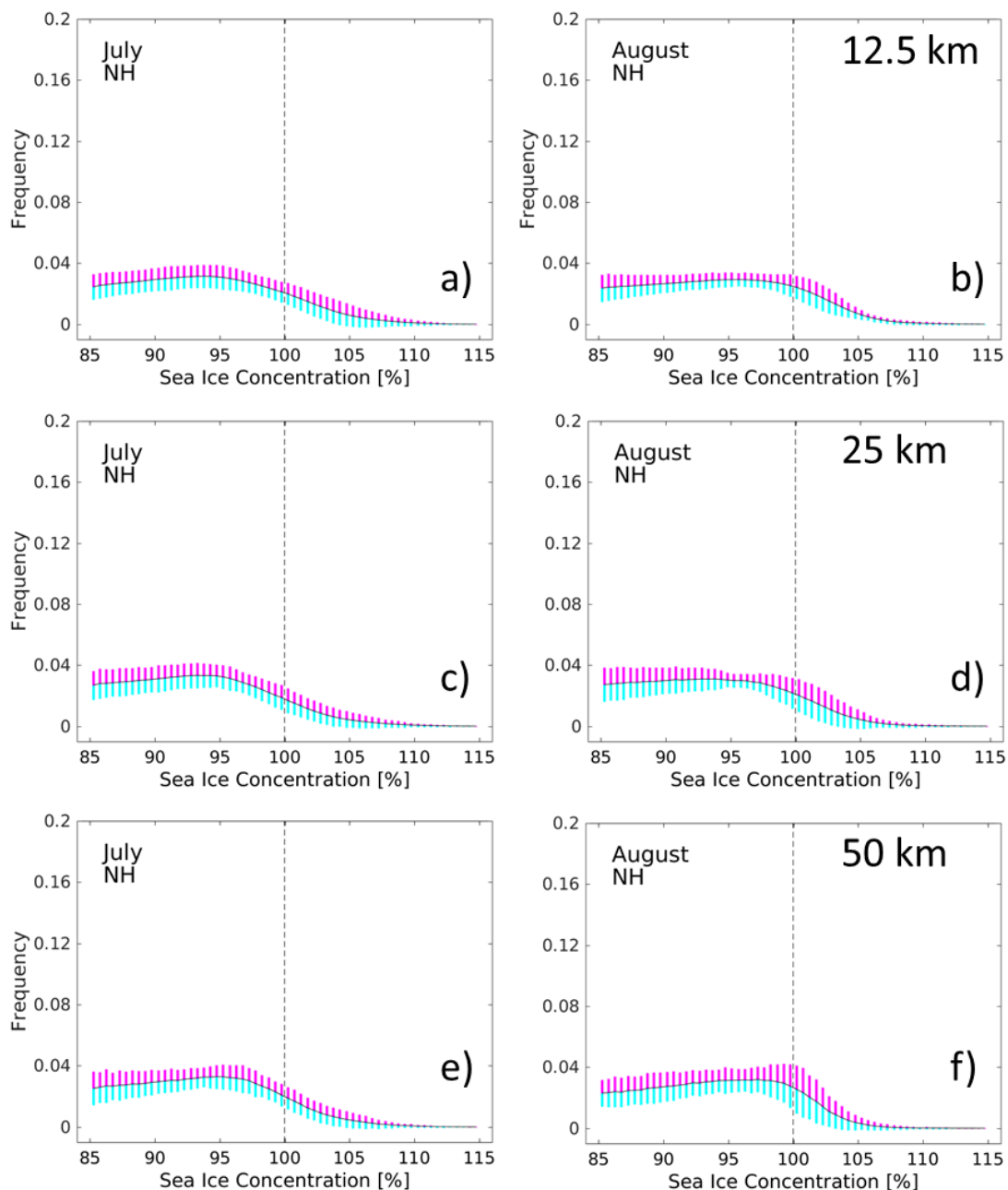
Figure 3-98: As Figure 3-95 for July and August.

Note further that from August to October (Figure 3-98 b),d),f), and Figure 3-99), the standard deviation is largest for SICCI-VLF, suggesting that the SIC distribution around SIC = 100% is more variable for SICCI-VLF during these months than it is for the other algorithms. An explanation for this is pending at the moment. One reason could perhaps be the larger sensitivity at the lower frequencies to ice-covered melt ponds. Another reason could be the larger sensitivity of lower frequencies to thin ice which occupies a considerable fraction of the sea-ice cover during these three months. Over

thin ice the SIC is under-estimated by algorithms based on lower frequency channels. If a large fraction of thin ice exists, then it could be that SICCI-VLF provides a larger fraction of lower SIC values than the other two algorithms.
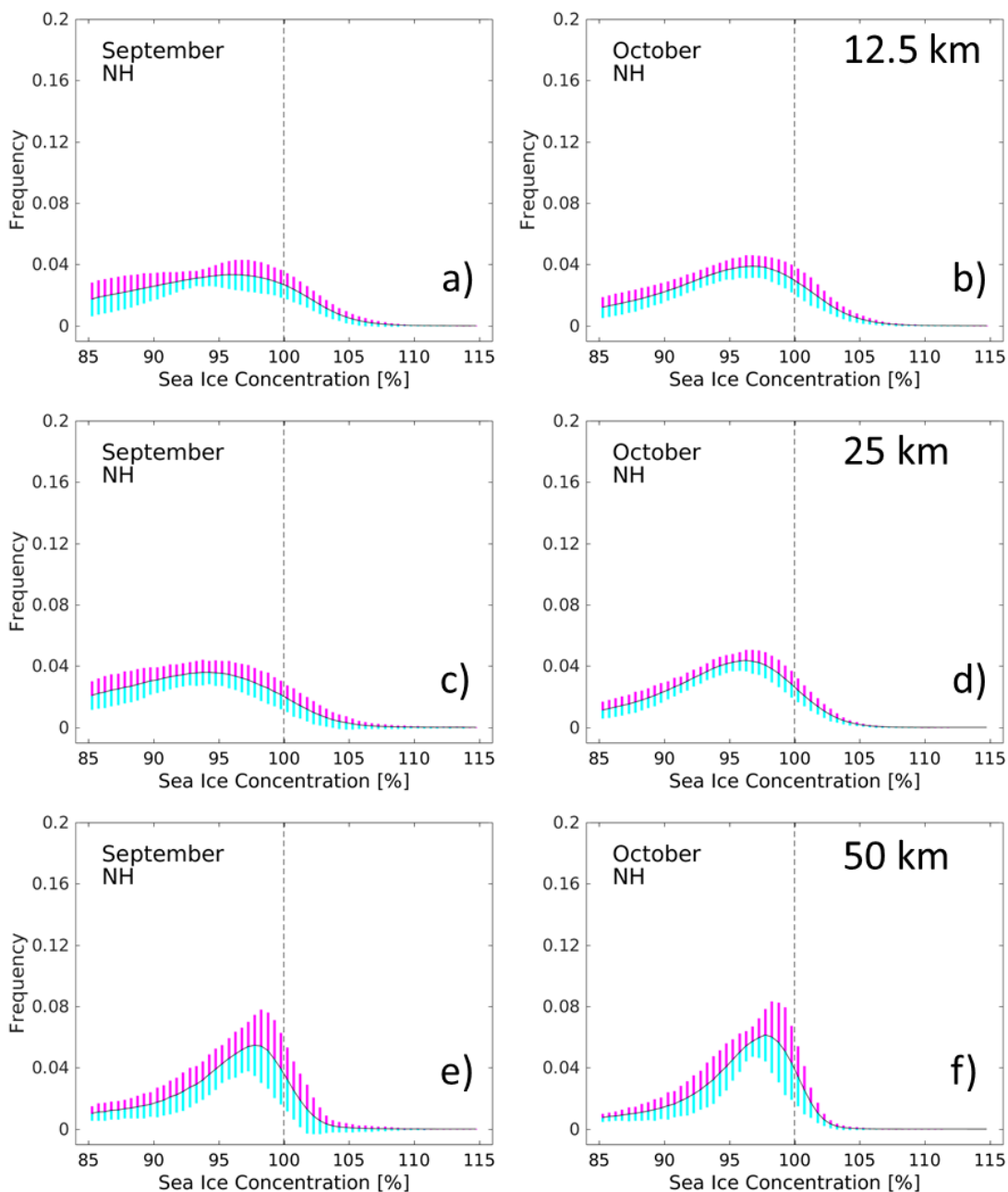
Figure 3-99: As Figure 3-95 for September and October.
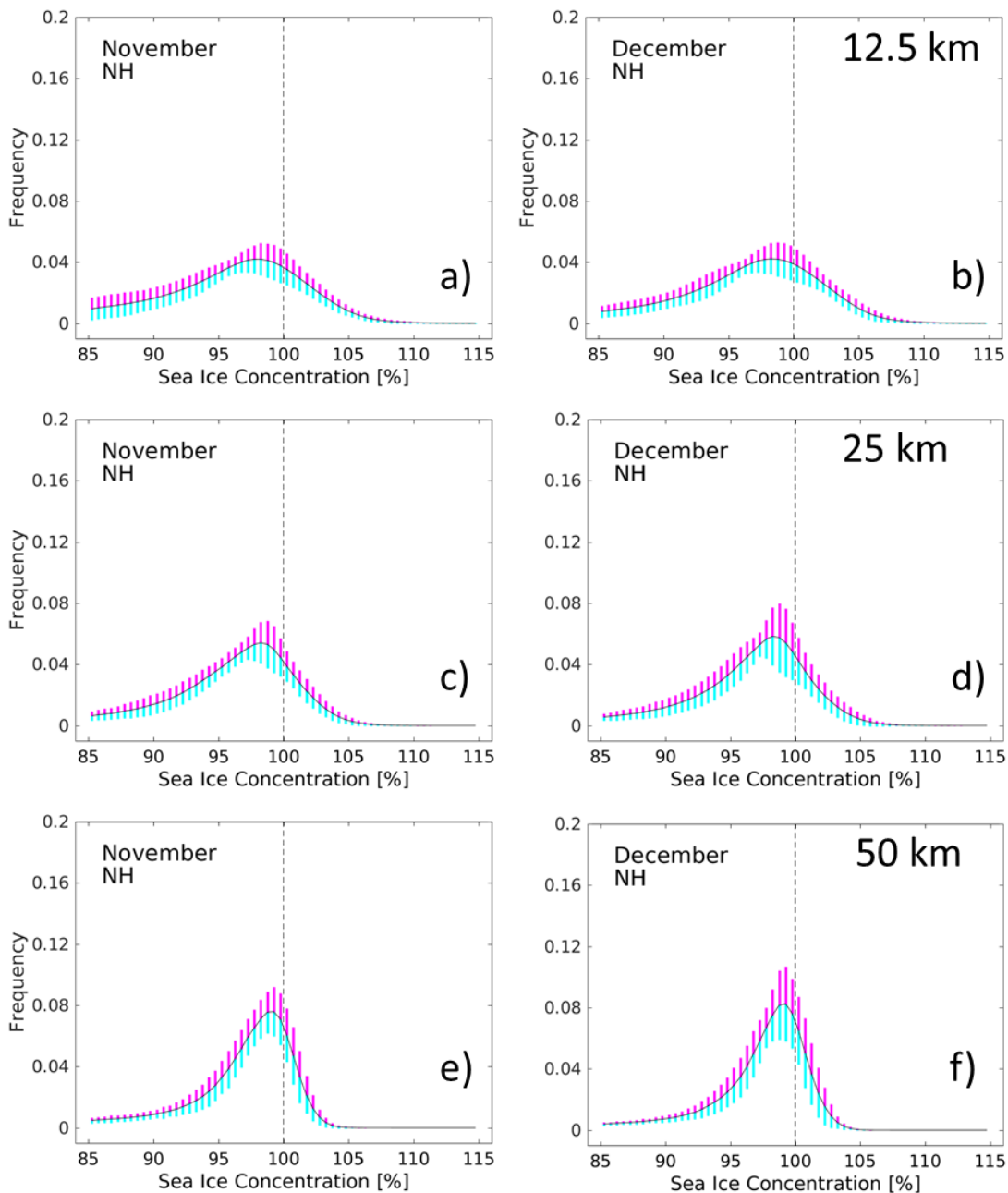
Figure 3-100: As Figure 3-95 for November and December.
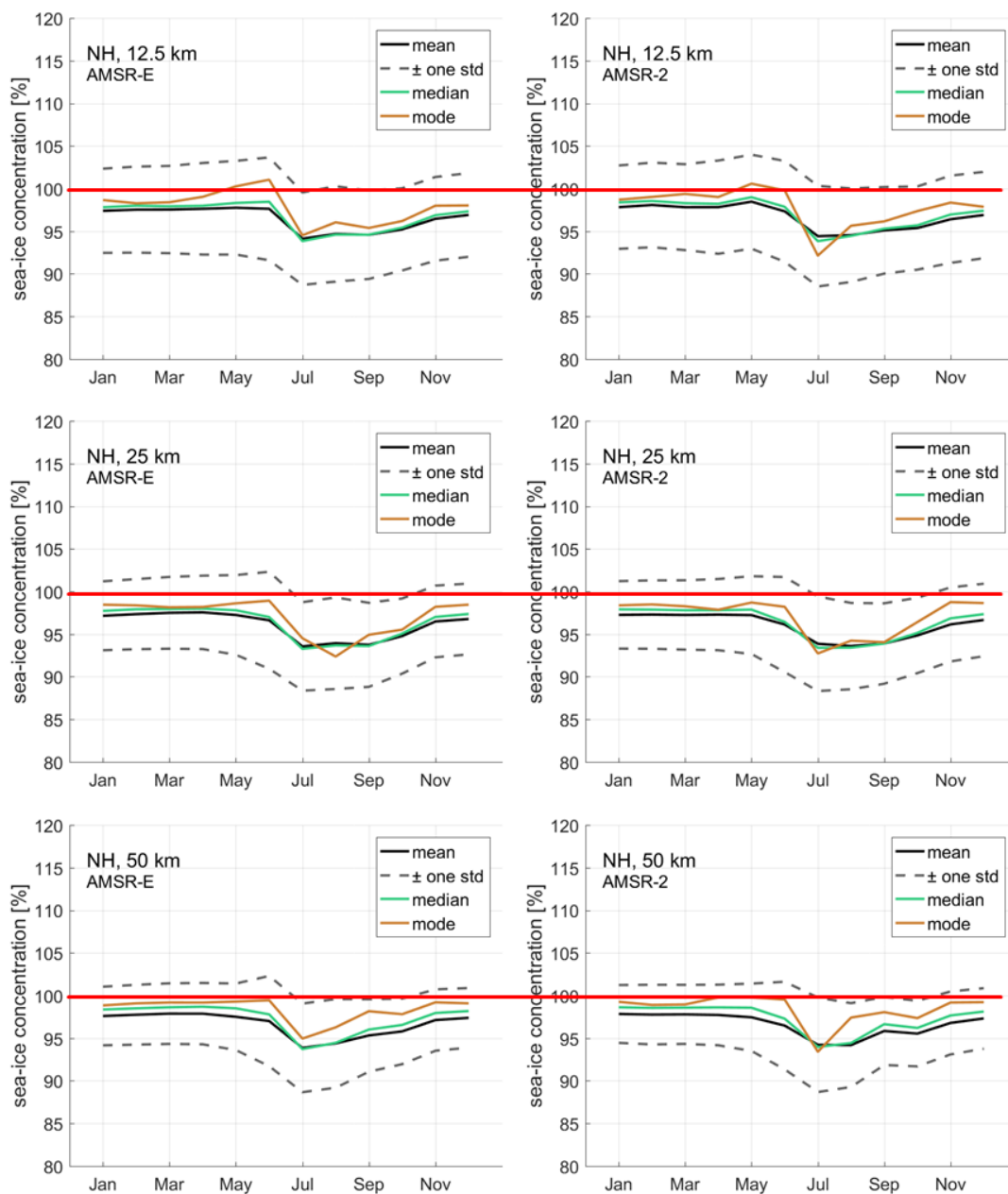
Figure 3-101: Multi-annual average monthly mean, median, and modal SIC of the three algorithms summarized from the histograms of Figure 3-95 through Figure 3-100 for the Northern Hemisphere – separately for AMSR-E (left) and AMSR2 (right). The dashed lines display ± 1 standard deviation around the mean.

Figure 3-101 summarizes the seasonal variability of the SIC distribution around SIC = 100% for the three algorithms. When considering the mean SIC of the range 85% … 115% all algorithms display more or less the same picture: SIC are ~ 97.5% during winter and dip down to ~94% during summer. Median SIC values are about 0.5% higher. Modal SIC values are closest to SIC = 100% throughout the year for SICCI-VLF but show larger intra-annual variation for SICCI-LF and SICCI-HF ranging between 92% and 99%, and 95% and 101%, respectively.
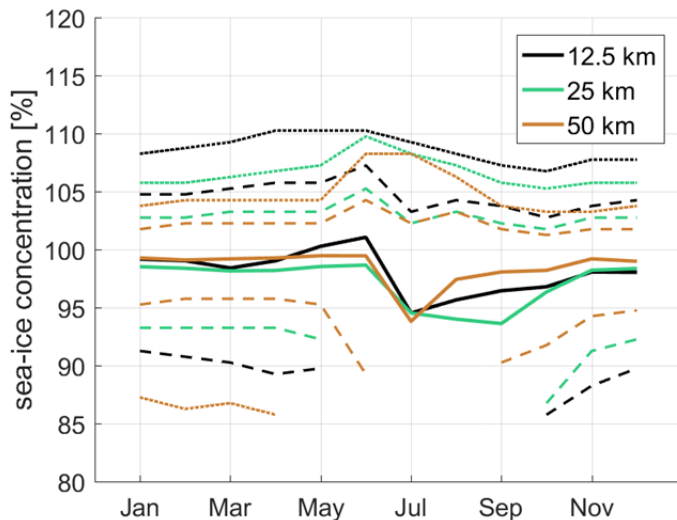
Figure 3-102: Multi-annual (AMSR-E and AMSR2 periods together) average modal SIC of the three algorithms at SIC = 100% (solid lines) for the Northern Hemisphere. The dashed and dotted lines mark the SIC where the frequency of the distribution as decreased by 66% and 95%, respectively, from the peak value. The distance between the solid and the dashed and/or dotted lines are a measure of the steepness of the histograms and hence of of confined the SIC values are around the respective modal SIC.

Finally, Figure 3-102 confirms that during winter SICCI-VLF offers SIC values which are most confined around the modal value, i.e. SICCI-VLF SIC is most precise compared to the other two algorithms. SICCI-HF provides the smallest (or worst) precision for SIC values around 100% during winter.
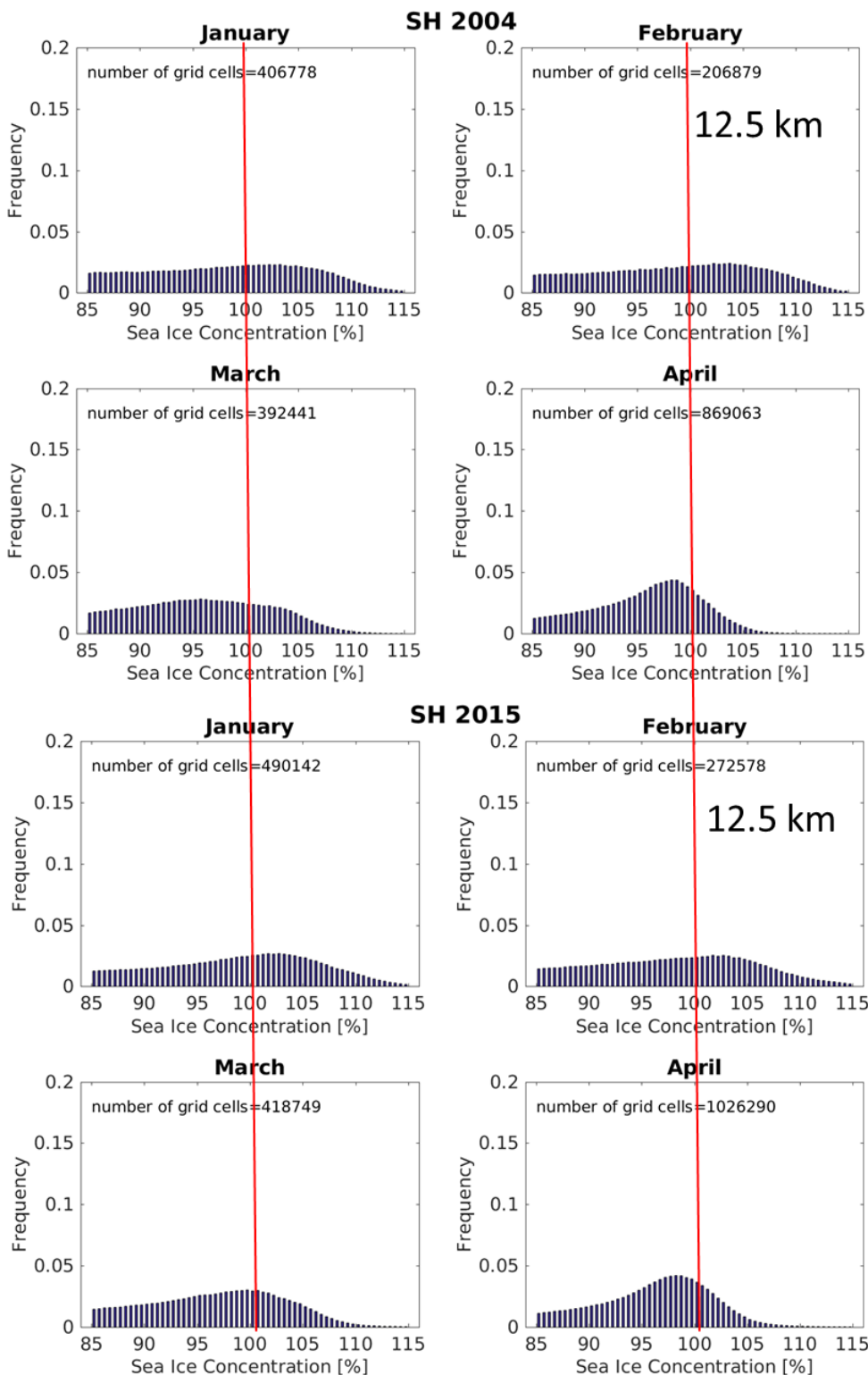
Figure 3-103: Sample set of SIC histograms around SIC=100% for SICCI-HF (12.5 km) for Jan. through Apr. 2004 and 2015 for the Southern Hemisphere. Red vertical line denotes location of SIC=100%. Binsize: 0.5%.
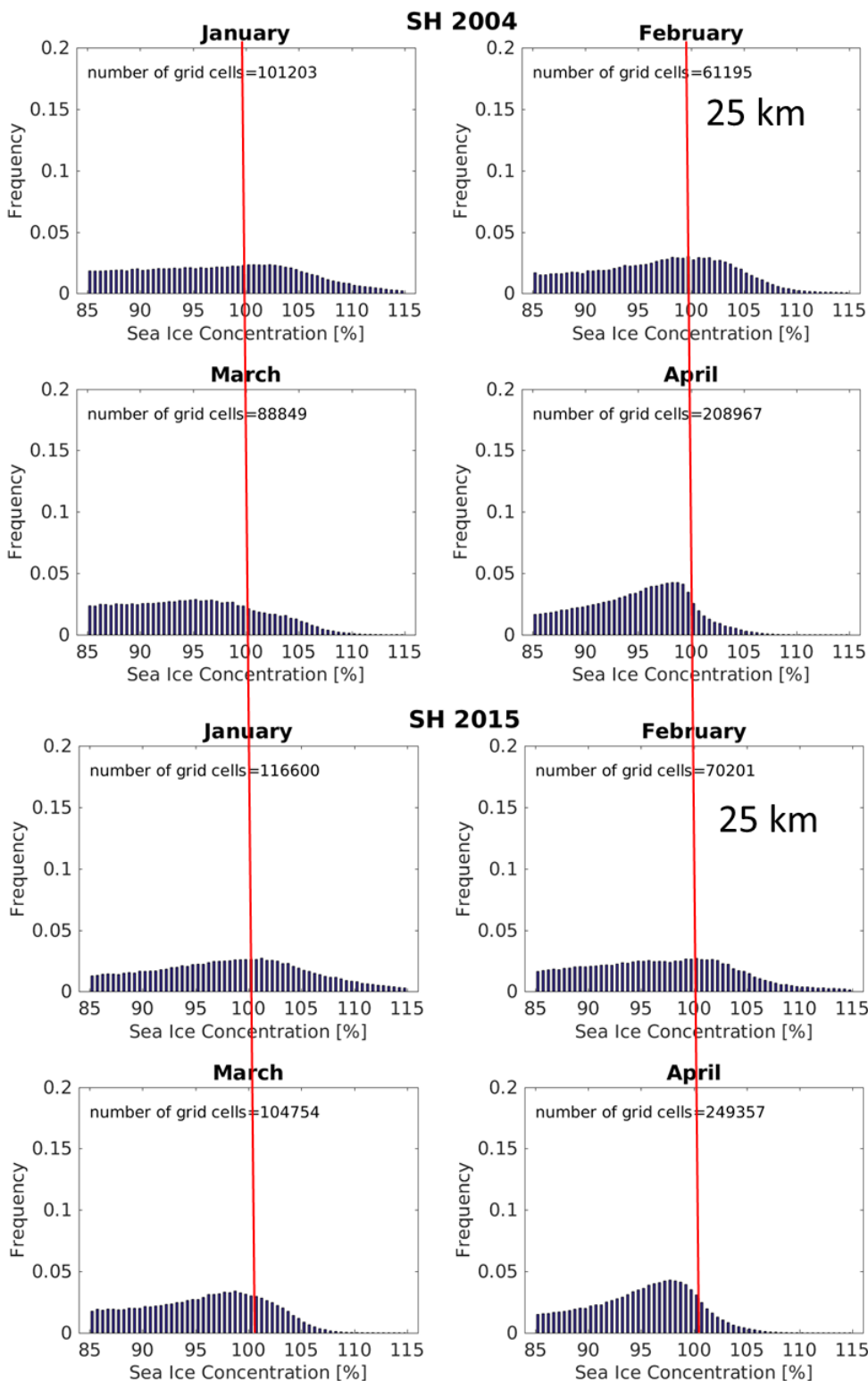
Figure 3-104: As Figure 3-103, using SICCI-Lf (25.0 km).
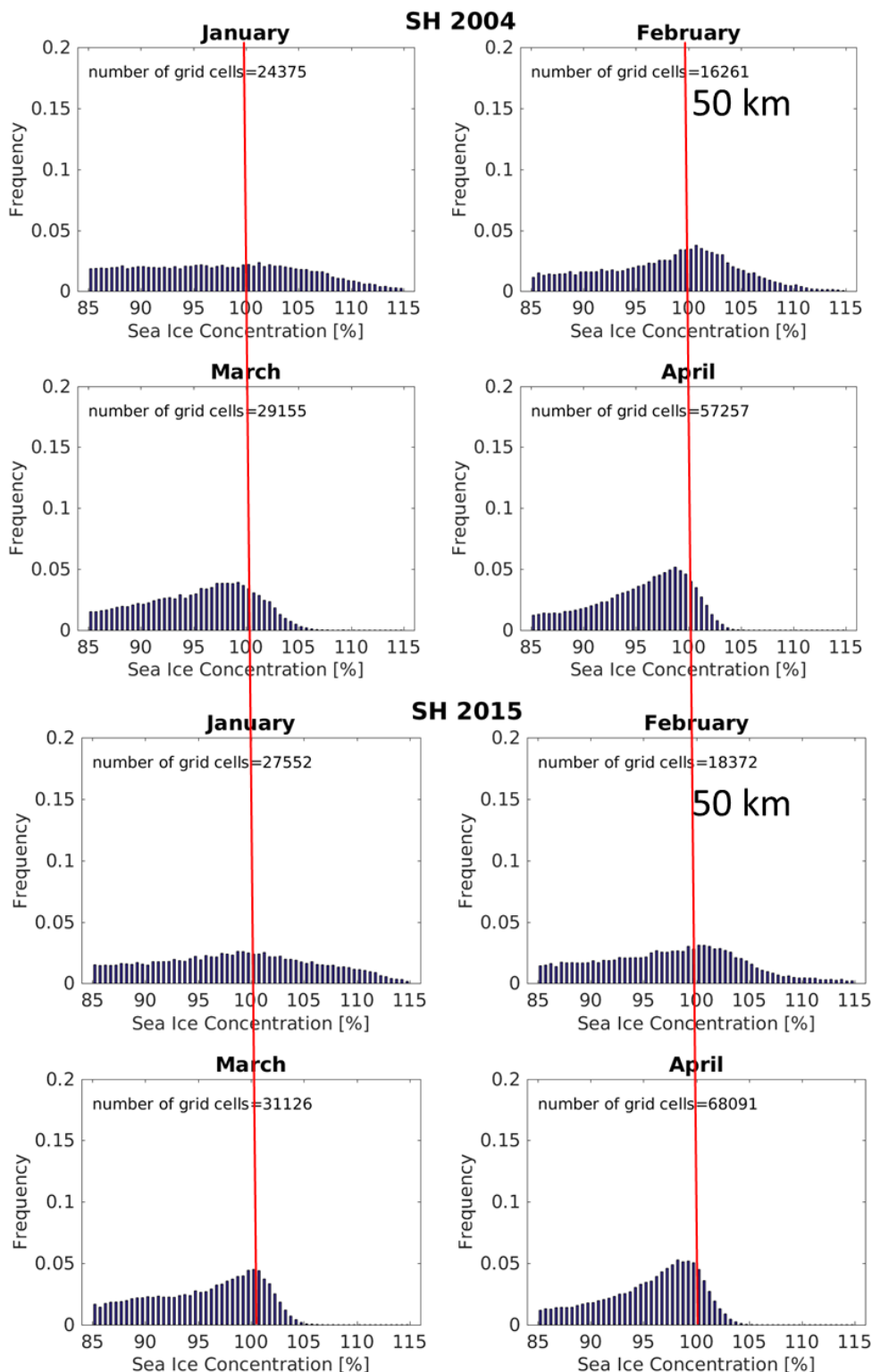
Figure 3-105: As Figure 3-103, using SICCI-VLF (50.0 km).

Figure 3-103 through Figure 3-105 illustrate for two arbitrary years how, in the Southern Ocean, the SIC distribution around SIC = 100% changes from

ESA UNCLASSIFIED - For Official Use

summer (January/February) to fall (March/April). Similar to the Northern Hemisphere, SICCI-HF provides the most broad and least confined around its modal value SIC distribution while SICCI-VLF seems to provide an as precise SIC distribution around 100% towards winter as in the Northern Hemisphere. Modal values are difficult to identify for the summer months. Still it seems evident that all algorithms may provide modal SIC values > 100% during January and February, e.g. SICCI-HF in February 2004: ~103%, SICCI-LF in January 2015: ~101%, and SICCI-VLF in February 2004: ~101%. All algorithms may have a substantial fraction of SIC values > 110%.
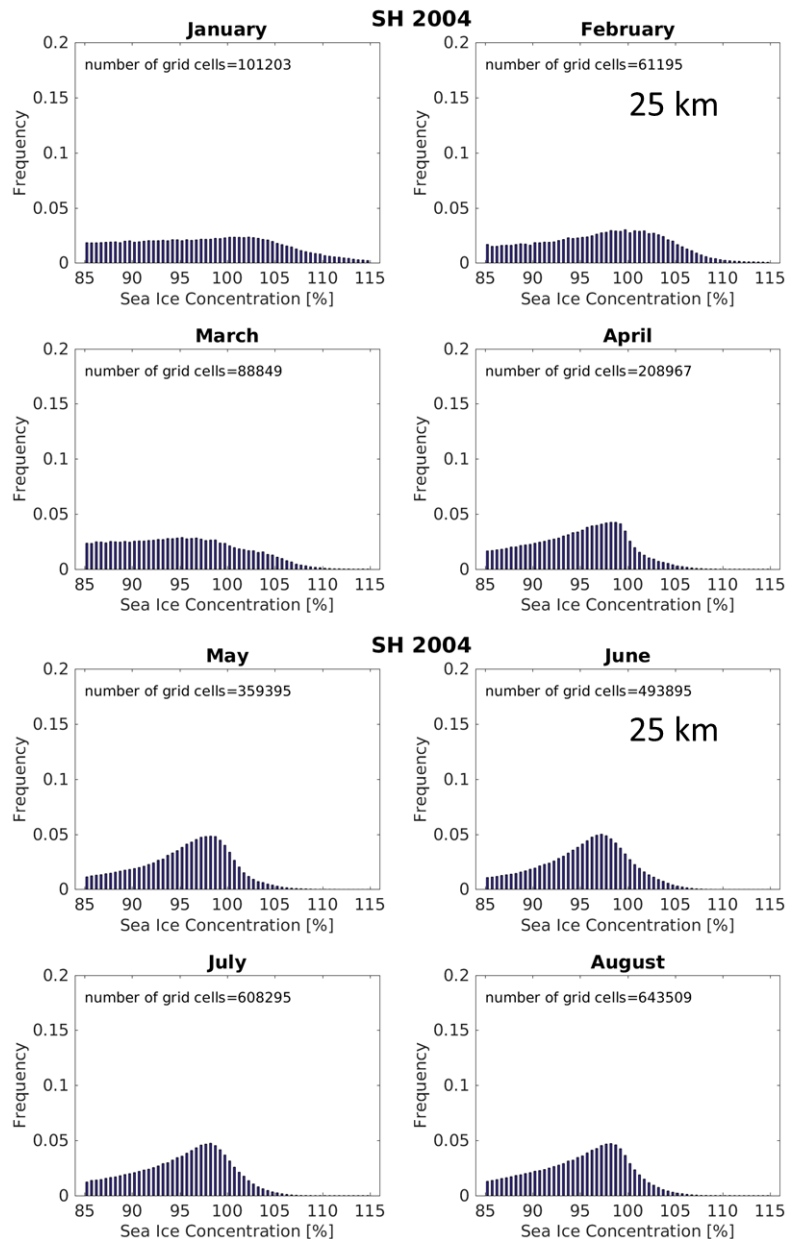
Figure 3-106: Sample seasonal evolution of the SIC distribution around SIC=100% using SICCI-LF (25.0 km). Binsize: 0.5%. Shown are months January through August of the year 2004 for the Southern Hemisphere.
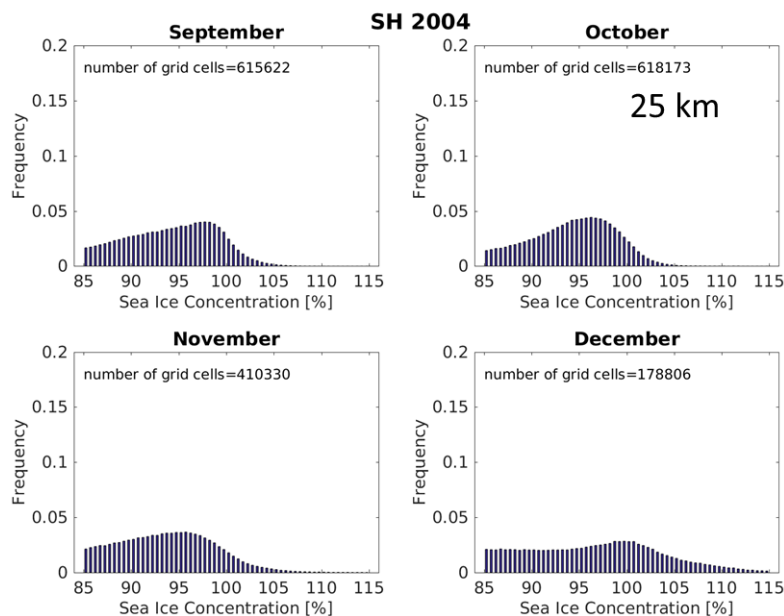
Figure 3-106 continued for months September through December

The sample seasonal cycle of the monthly SIC distribution around SIC = 100% shown for SICCI-LF for the Southern Hemisphere in Figure 3-106 reveals a distinct modal SIC value during winter, i.e. from May through October with, with a relatively steep SIC decline towards SIC > 100%. The modal SIC seems to vary more during winter than it does for the Northern Hemisphere (compare with Figure 3-94). Interesting to note is also that during spring the modal SIC value first decreases (in October/November) to ~ 96% and subsequently increases (in December) to ~ 100%. Such a decrease is not observed in the Northern Hemisphere. During winter, cases with SIC > 105% are relatively rare while during summer/fall (after including December) a considerable fraction of SIC values is > 105%.
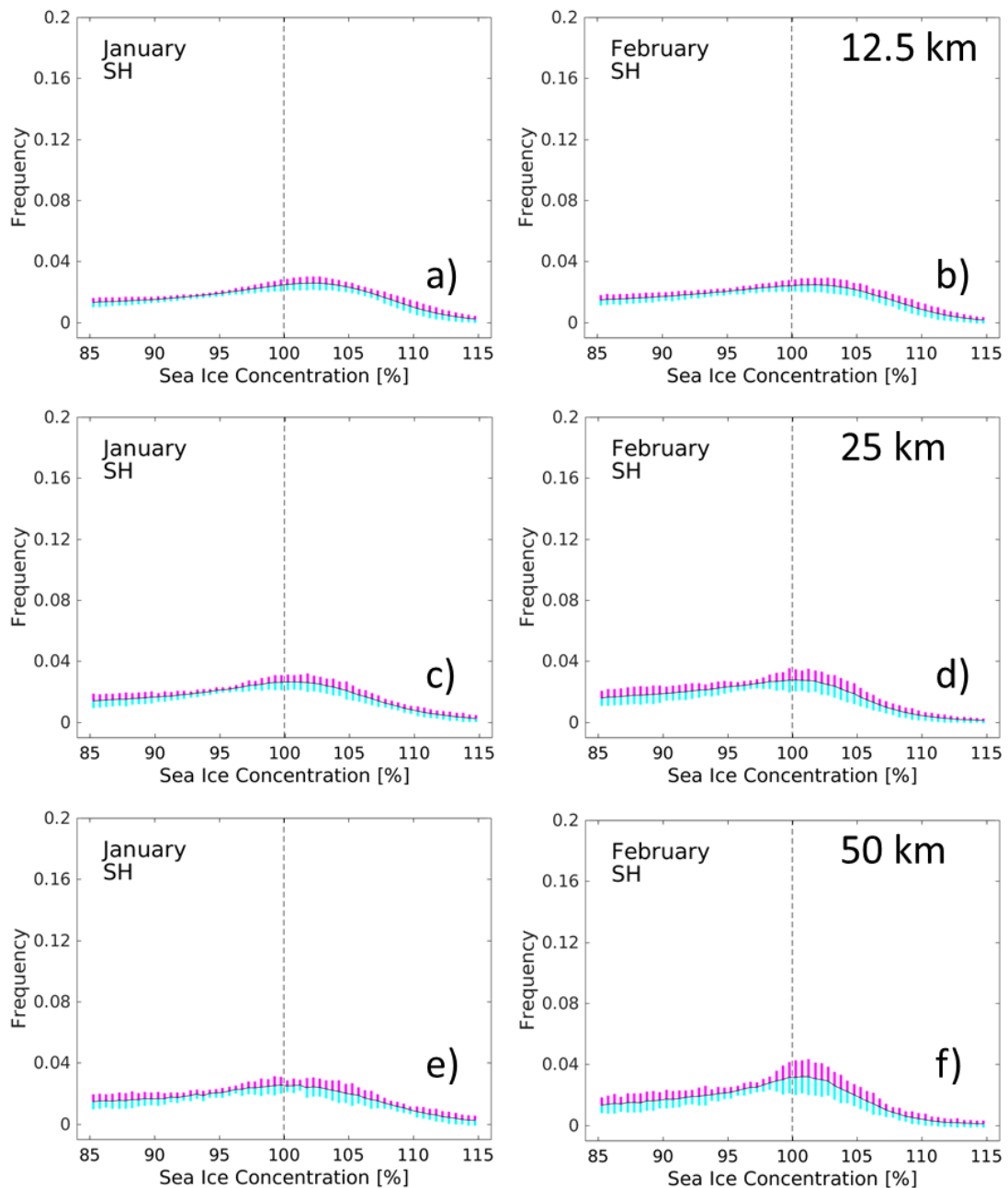
Figure 3-107: Whole-period (2002-2015) average monthly histograms of the sea-ice concentration around 100% for the 12.5 km (a,b), 25 km (c,d), and 50 km (e,f) product for January and February for the Southern Hemisphere. Bin size is 0.5%. Bars in cyan and magenta denote one standard deviation of the probability with which a SIC value falls into the respective bin. Similar figures to this one are Figure 3-108 through Figure 3-112, which are showing the other months.

The multi-annual average monthly histograms shown in Figure 3-107 through Figure 3-112 further illustrate and confirm findings from Figure 3-103 through Figure 3-106. None of the algorithms provides a SIC centered around SIC = 100% during winter in the Southern Hemisphere. Modal SIC are without exception shifted to lower SIC values with modal values being

closest to SIC = 100% for SICCI-HF and SICCI-VLF: 98.5% to 99.0% and
0.5% to 1.0% further off for SICCI-LF. SIC distributions obtained with
SICCI-VLF are most confined around the modal SIC value, SICCI-HF tend to
be least confined. This is not only visible from the shape of the histograms
but also from the fraction of SIC > 105%; the latter is essentially zero for
SICCI-VLF but notable for SICCI-HF also during winter.
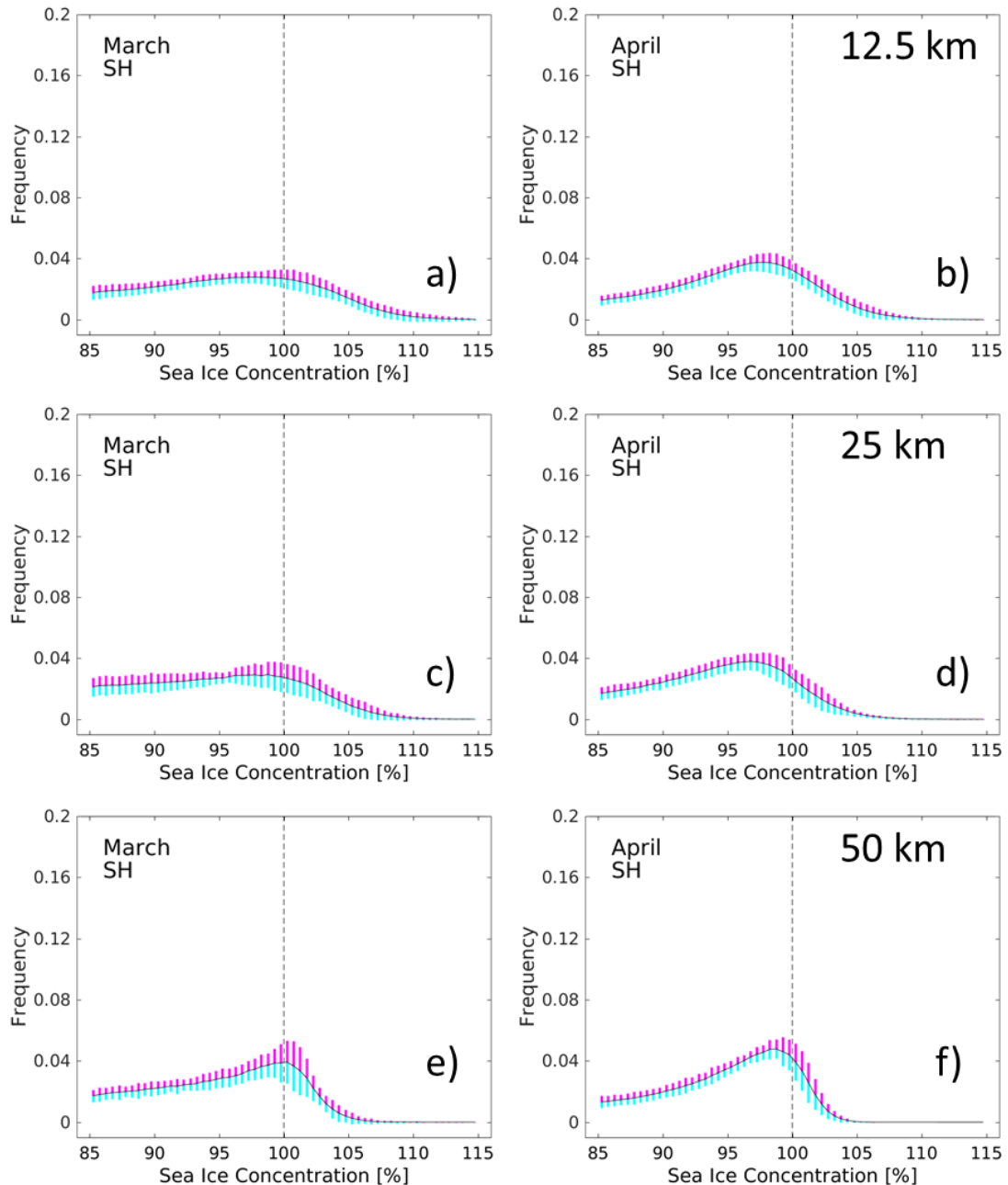
Figure 3-108: As Figure 3-107 for March and April.

During summer (December through February) modal SIC values approach
or even exceed 100%; SICCI-VLF modal SIC is ~101% for February and for
SICCI-HF it is ~102% for January and February. SICCI-LF has least
tendency for a SIC mode > 100% (Figure 3-107).

ESA UNCLASSIFIED - For Official Use
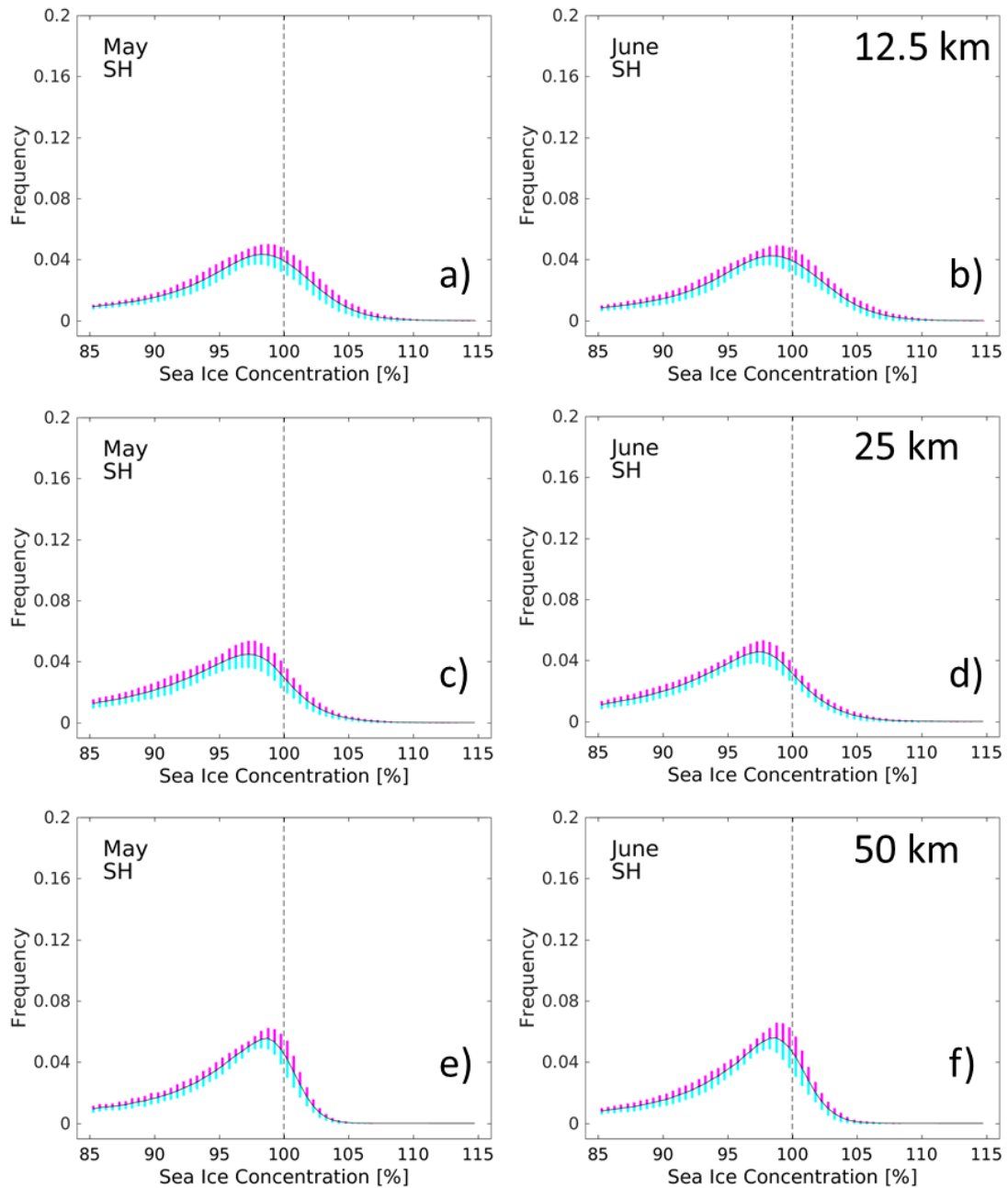
Figure 3-109: As Figure 3-107 for May and June.

Note that for most months the standard deviation of the SIC distribution per bin is smallest for SICCI-HF and often considerably smaller than the one for SICCI-VLF. While this could simply be attributed a small number of cases per bin in months February and March this has certainly a different cause during September / October (Figure 3-111). During these months the sea-ice cover of the Southern Hemisphere reaches its maximum extent. At the same time the weather induced influence could also be at maximum "efficiency". One particularly relevant influence is snow load induced flooding of the snow-ice interface and subsequent re-freezing of the potentially slushy basal snow layer. These two processes happening below

the snow cover often do not influence the near-90 GHz frequencies but are influencing the lower frequencies, suggesting variations in the retrieved SIC.
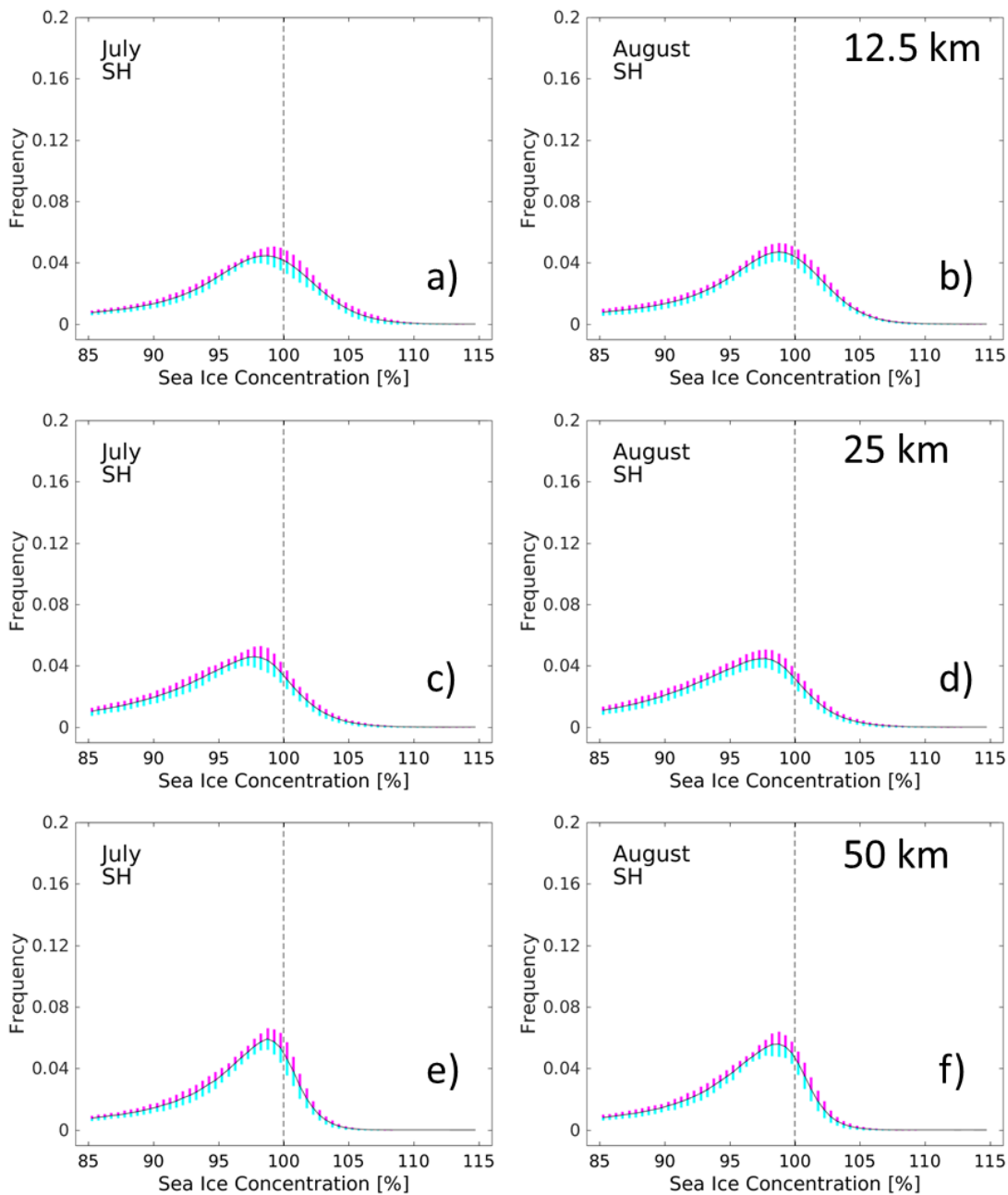
Figure 3-110: As Figure 3-107 for July and August.

ESA UNCLASSIFIED - For Official Use
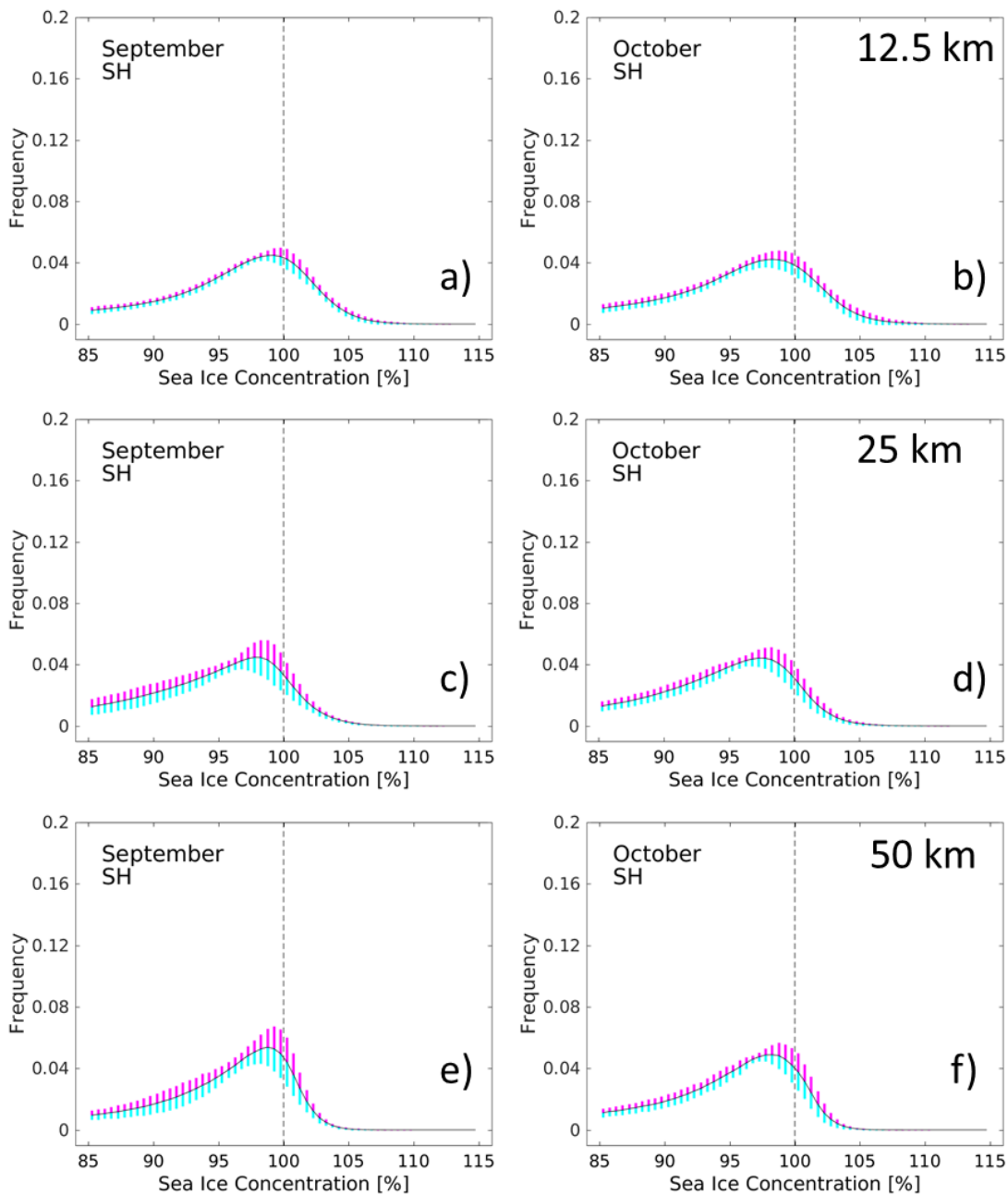
Figure 3-111: As Figure 3-107 for September and October.
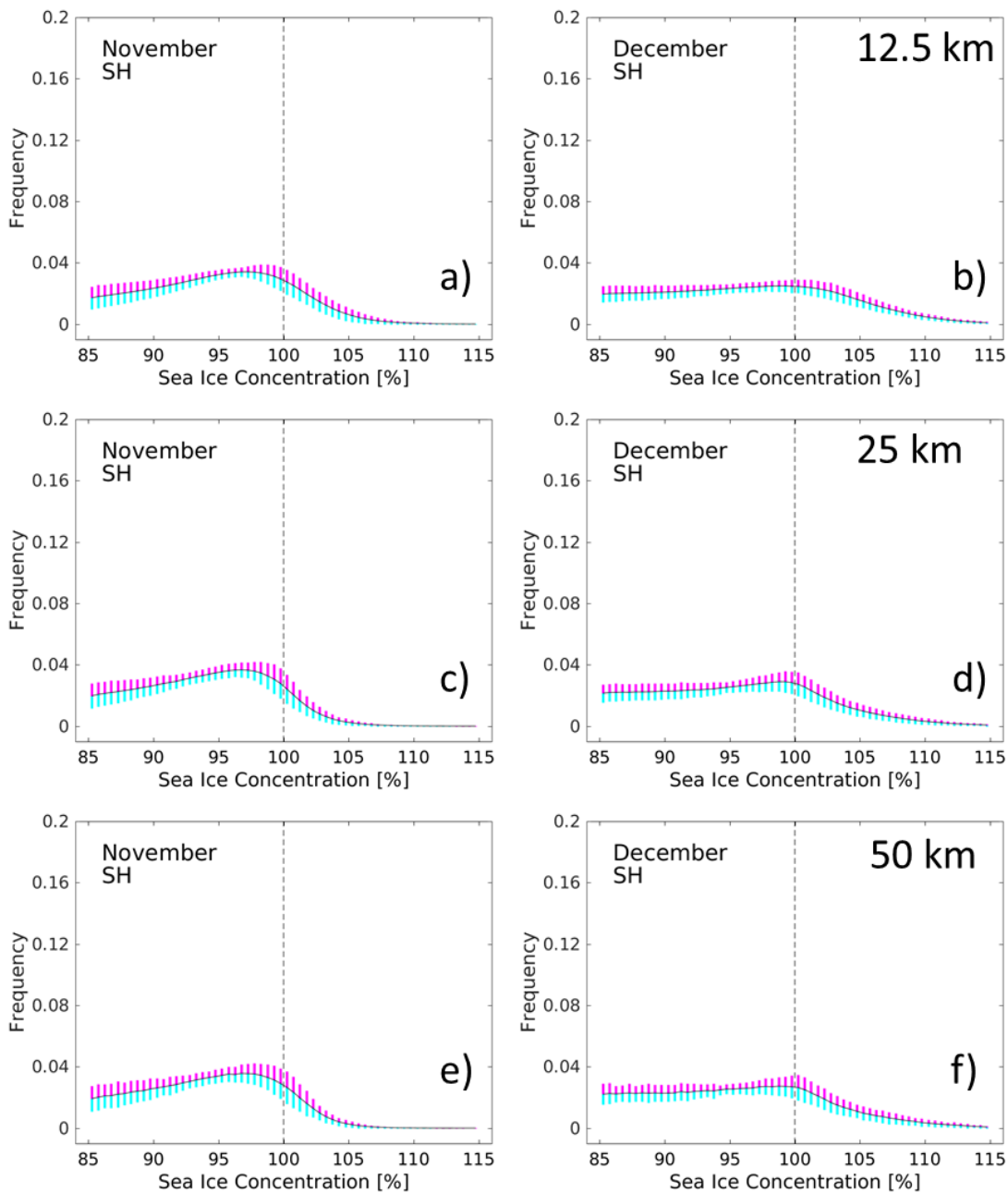
Figure 3-112: As Figure 3-107 for November and December.
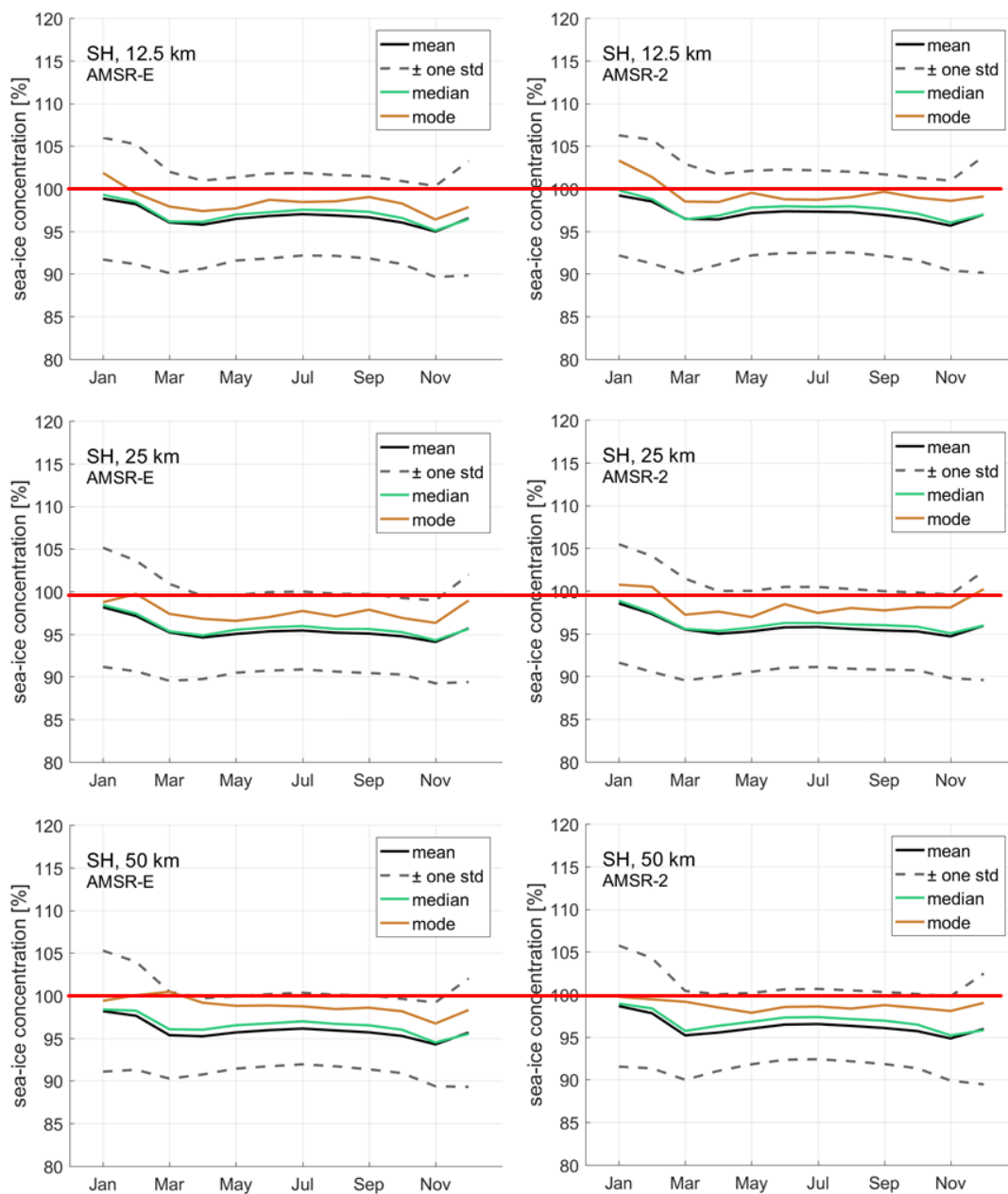
Figure 3-113: Multi-annual average monthly mean, median, and modal SIC of the three algorithms summarized from the histograms of Figure 3-107 through Figure 3-112 for the Southern Hemisphere – separately for AMSR-E (left) and AMSR2 (right). The dashed lines display ± 1 standard deviation around the mean.

The seasonal development of the multi-annual monthly mean SIC values shown in Figure 3-113 for the Southern Hemisphere illustrates that SICCI-HF has the smallest deviation from SIC = 100%, followed by SICCI-VLF and SICCI-LF – when considering the SIC range 85% … 115%. Median SIC values are similar to the mean SIC values. Modal SIC values are closest to SIC = 100% and exhibit least intra-annual variation for SICCI-VLF, followed by SICCI-HF.

In contrast to all previous cases, here we have more obvious differences between AMSR2 and AMSR-E (compare with Figure 3-77, 3Figure 3-89, and Figure 3-101). Modal SIC values seem to be larger for AMSR2 than for AMSR-2, particularly for SICCI-LF and SICCI-HF.
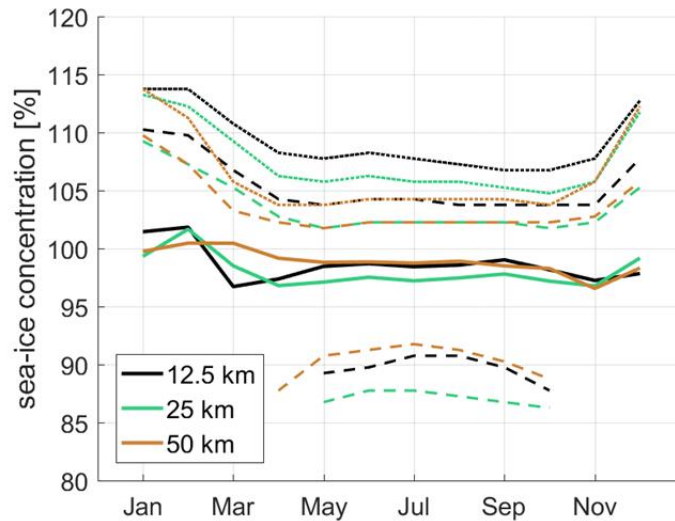
Figure 3-114: Multi-annual (AMSR-E and AMSR2 periods together) average modal SIC of the three algorithms at SIC = 100% (solid lines) for the Southern Hemisphere. The dashed and dotted lines mark the SIC where the frequency of the distribution as decreased by 66% and 95%, respectively, from the peak value. The distance between the solid and the dashed and/or dotted lines are a measure of the steepness of the histograms and hence of of confined the SIC values are around the respective modal SIC.

Finally, Figure 3-114 underlines that during winter modal SIC of SICCI-HF (12.5 km) and SICCI-VLF (50.0 km) are closer to SIC = 100% than SICCI-LF and that SICCI-VLF SIC are most confined around their modal values and are hence most precise.

ESA UNCLASSIFIED - For Official Use

3.7   SICCI 2 sea-ice concentration uncertainties

The SICCI 2 SIC products come with a per-grid cell uncertainty estimate. Two types of uncertainties can be distinguished. One is the gridding or smearing uncertainty which is caused by the insufficient representation of variations in SIC on spatial scales smaller than the grid resolution. The smearing uncertainty is given separately in the SICCI SIC product. It is zero for 0% and 100% sea-ice concentration and increases non-linearly with increasing deviation of the SIC from the above-mentioned limits. The other uncertainty is the retrieval uncertainty which is basically based on tie point and brightness temperature uncertainties. It is computed individually for each grid cell using error propagation methods. It is independent from the smearing uncertainty and grid resolution. At 0% and 100% it is the only contribution to the total SIC uncertainty.

In this section we first illustrate the uncertainties at the RRDP2 locations, i.e. the SIC uncertainties at SIC = 0% and SIC = 100% locations as used in section 3.2. Subsequently we illustrate and discuss the seasonal cycle of the uncertainties. In the revised version of the PVIR, this section will close with an investigation following the approach of Bulgin et al. ([RD-46]) in which we assess the SIC error over open water in the context of the SIC retrieval uncertainty.

3.7.1   *Open water SIC uncertainty at SIC = 0%*
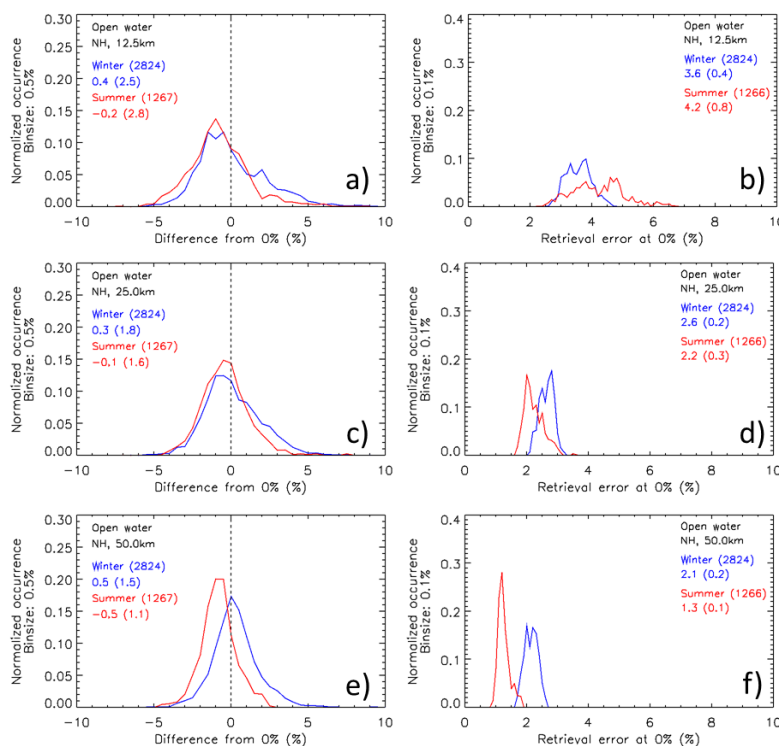
Figure 3-115: Distribution of the difference 0% minus SICCI 2 SIC (SIC error) at the RRDP 2 open water locations in the Northern Hemisphere (left hand side) together with the distribution of the SIC retrieval error at these locations (right hand side). Winter (Jan./Feb.) and summer (Aug./Sep.) values are denoted in blue and red, respectively. Grid resolution decreases from 12.5 km (a,b) through 25 km (c,d) to 50 km (e,f). Note that this figure is identical to Figure 3-3.

The distributions of the SICCI 2 SIC retrieval uncertainty shown in Figure 3-115 for the Northern Hemisphere for winter (blue) and summer (red) for the 12.5 km (b), 25 km (d) and 50 km (f) products reveal modal values between ~3.8% (12.5 km product) and ~2% (50 km product) in winter. In summer the modal retrieval uncertainty is also largest for the 12.5 km: ~4.6% and smallest for the 50 km product: ~1.2%. Modal retrieval uncertainties in summer are smaller than winter ones for the 50 km and 25 km products but not for the 12.5 km product. Also the uncertainty distributions are quite narrow for the 50 km product but comparably wide for the 12.5 km product. The mean values and standard deviations of the retrieval uncertainties are summarized in Table 3-27 together with the respective values computed for the total uncertainty. Note that the total uncertainty contains the smearing uncertainty which, however, is only relevant if unaccounted weather influences cause a substantial amount of spurious sea ice off the ice edge. The smallest retrieval uncertainty is obtained for the 50 km product, the largest for the 12.5 km product; the increase in the mean retrieval uncertainty is smaller between the 50 km and 25 km products than between the 25 km and 12.5 km products; this applies particularly for summer.

Table 3-27: Mean SIC retrieval uncertainty at the Northern Hemisphere open water locations with the respective standard deviation in parentheses for seasons winter and summer for the grid resolutions given (top two datta rows); the bottom two data rows give the respective values of the total error. All quantities – except N – are given in percent. Highlighted in bold font are results of the 25 km product.

season	12.5 km	**25 km**	50 km	N
winter	3.6 (0.4)	**2.6 (0.2)**	2.1 (0.2)	2824
summer	4.2 (0.8)	**2.2 (0.3)**	1.3 (0.1)	1266
winter	3.7 (1.0)	**2.8 (0.6)**	2.3 (0.5)	2824
summer	4.4 (1.3)	**2.4 (0.9)**	1.3 (0.3)	1266
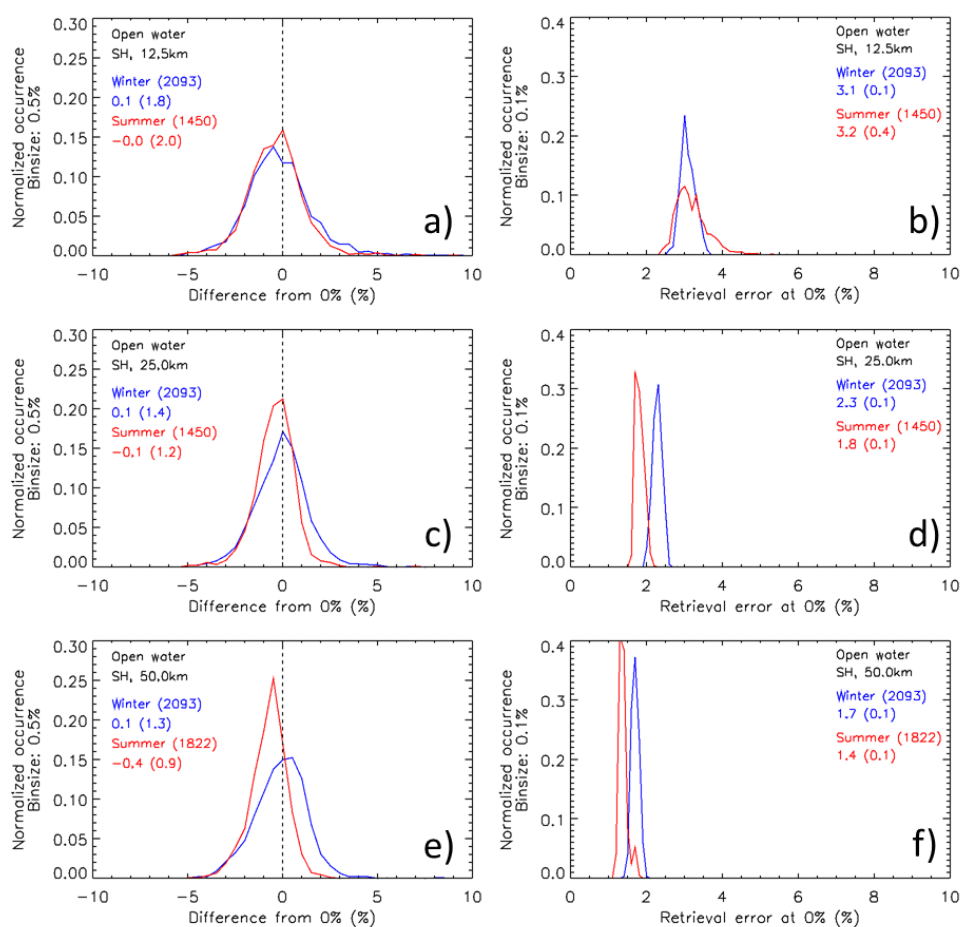
Figure 3-116: Distribution of the difference 0% minus SICCI 2 SIC (SIC error) at the RRDP 2 open water locations in the Southern Hemisphere (left hand side) together with the distribution of the SIC retrieval uncertainty at these locations (right hand side). Winter (Aug./Sep.) and summer (Jan./ Feb.) values are denoted in blue and red, respectively. Grid resolution decreases from 12.5 km (a,b) through 25 km (c,d) to 50 km (e,f). This figure is identical to Figure 3-2.

Table 3-28: Mean SIC retrieval uncertainty at the Southern Hemisphere open water locations with the respective standard deviation in parentheses for seasons winter and summer for the grid resolutions given (top two datta rows); the bottom two data rows give the respective values of the total error. All quantities – except N – are given in percent. Highlighted in bold font are the results for the 25 km product. See also caption for Table 3-2.

season	12.5 km	**25 km**	50 km	N
winter	3.1 (0.1)	**2.3 (0.1)**	1.7 (0.1)	2093
summer	3.2 (0.4)	**1.8 (0.1)**	1.4 (0.1)	1450 / 1822
winter	3.3 (1.3)	**2.4 (1.5)**	1.8 (0.8)	2093
summer	3.4 (1.1)	**2.0 (1.1)**	1.6 (1.7)	1450 / 1822

The distributions of the SICCI 2 SIC retrieval uncertainties for SIC = 0% shown in Figure 3-116 for the Southern Hemisphere for winter (blue) and summer (red) for the 12.5 km (b), 25 km (d) and 50 km (f) product reveal modal values between ~3.0% (12.5 km product) and ~1.7% (50 km product) in winter. In summer the modal retrieval uncertainty is also largest for the 12.5 km: ~3.0% and smallest for the 50 km product: ~1.3%. Modal retrieval uncertainties in summer are smaller than winter ones for the 50 km and 25 km products but not the 12.5 km product. The uncertainty distributions are quite narrow for the 50 km product but comparably wide for the 12.5 km product. Compared to the Northern Hemisphere, uncertainty distributions are extremely narrow (compare Figure 3-115). The mean values and standard deviations of the retrieval uncertainties are summarized in Table 3-28 together with the respective values computed for the total uncertainties. The smallest retrieval uncertainty is obtained for the 50 km, the largest for the 12.5 km product; the increase in the mean retrieval uncertainty is smaller between the 50 km and 25 km products than between the 25 km and 12.5 km products; this applies particularly for summer.

In contrast to the Northern Hemisphere, standard deviations of the mean total uncertainty in the Southern Ocean are substantially larger than standard deviations of the mean retrieval uncertainty (compare Table 3-27 and Table 3-28) indicating that the smearing uncertainty plays a larger role for the open water locations in case that weather effects are not properly accounted for. The difference of the mean values of retrieval uncertainty and total uncertainty is, however, similar to that for the Northern Hemisphere.

3.7.2   *Pack ice SIC uncertainty around SIC = 100%*
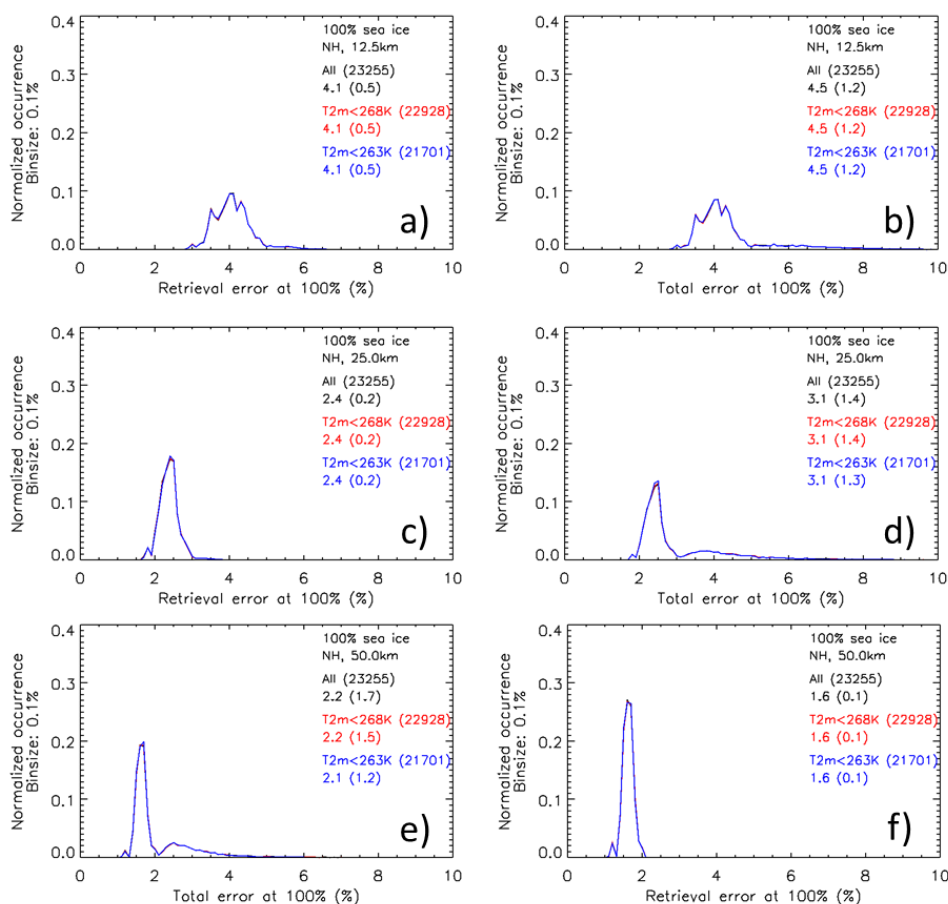
Figure 3-117: Histograms of the retrieval (a, c, e) and the total (b, d, f) sea-ice concentration uncertainty at the RRDP2 SIC=100% locations in the Northern Hemisphere for the 12.5 km (a,b), 25 km (c,d), and 50 km (e,f) product.

Table 3-29: Northern Hemisphere SICCI 2 mean SIC retrieval uncertainty at RRDP2 SIC=100% locations computed for the entire AMSR-E – AMSR2 time series for the three products. Values in parentheses are one standard deviation of the mean. All quantities – except N – are given in percent. Highlighted in bold font are results of the 25 km product.

	12.5 km	**25 km**	50 km	N
all	4.1 (0.5)	**2.4 (0.3)**	1.7 (0.1)	23255
T2m < -10°C	4.1 (0.5)	**2.4 (0.3)**	1.7 (0.1)	21701

The retrieval and total SIC uncertainties for SIC = 100%, i.e. computed at the RRDP 2 SIC = 100% locations in the Northern Hemisphere, peak at modal values between 1.5% and 2%, 2.5%, and 4% for the 50 km, 25 km and 12.5 km product, respectively (Figure 3-117). Mean uncertainties are larger only for the 50 km product (Figure 3-117 and Table 3-29 and Table

ESA UNCLASSIFIED - For Official Use

3-30). The distributions are quite narrow for the 50 km product and relatively wide for the 12.5 km product. The contribution of smearing uncertainties to the total error is small but discernible by means of the histogram shape (compare Figure 3-117 c,e with d,f), and by means of larger mean values and particularly their standard deviations (Table 3-30.

Table 3-30: As Table 3-29 but for the Northern Hemisphere SICCI 2 mean sea-ice concentration total uncertainty.

	12.5 km	**25 km**	50 km	N
all	4.6 (1.3)	**3.2 (1.4)**	2.2 (1.7)	23255
T2m < -10°C	4.6 (1.3)	**3.1 (1.4)**	2.1 (1.3)	21701
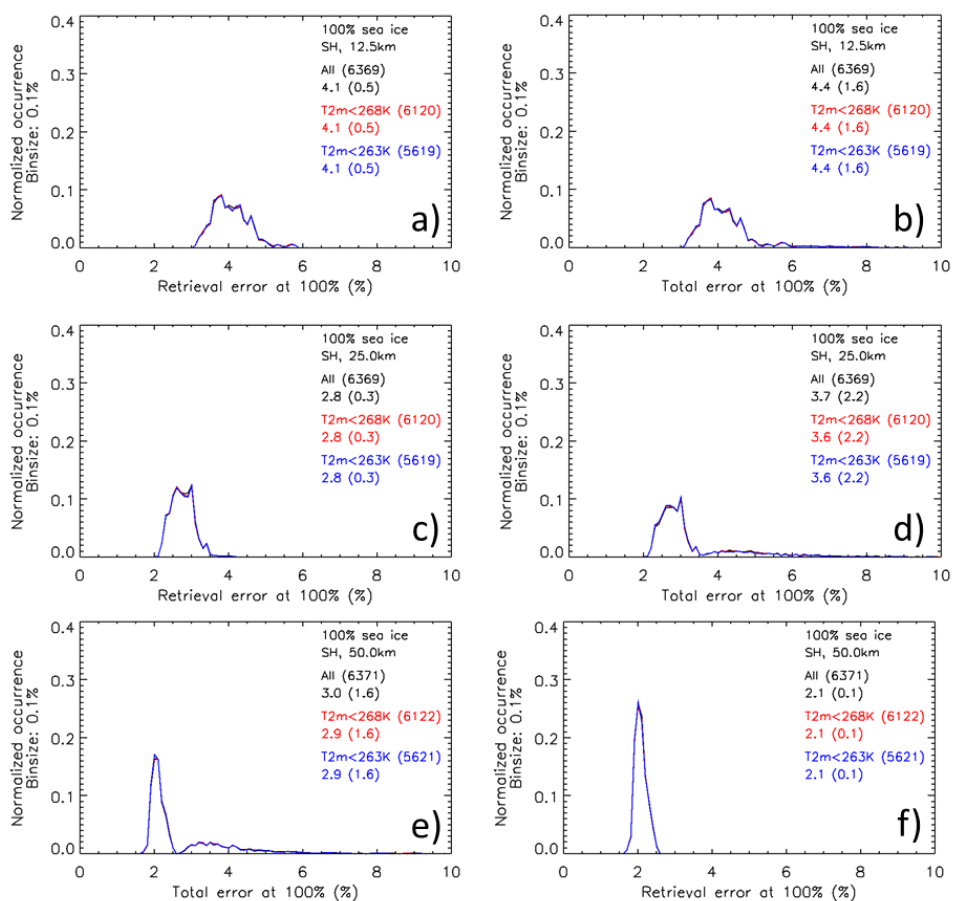
Figure 3-118: Histograms of the retrieval (a, c, e) and the total (b, d, f) sea-ice concentration uncertainty at the RRDP2 SIC=100% locations in the Southern Hemisphere for the 12.5 km (a,b), 25 km (c,d), and 50 km (e,f) product.

The retrieval and total SIC uncertainties of the Southern Hemisphere peak at modal values of 2.0%, between 2.5% and 3.0%, and 3.7% for the 50 km, 25 km and 12.5 km product, respectively (Figure 3-118). These values are slightly larger than in the Northern Hemisphere for the 25 km and 50

km products. Mean uncertainties are mostly larger than the modal values (Figure 3-118 and Table 3-31 and Table 3-32). The distributions are quite narrow for the 50 km product and relatively wide for the 12.5 km product. The contribution of smearing uncertainties to the total uncertainty is small but discernible by means of the histogram shape (compare Figure 3-118 c,e with d,f), and by means of larger mean values and particularly their standard deviations (Table 3-32).

Table 3-31: Southern Hemisphere SICCI 2 mean SIC retrieval uncertainty at RRDP2 SIC=100% locations computed for the entire AMSR-E – AMSR2 time series for the three products. Values in parentheses are one standard deviation of the mean. All quantities – except N – are given in percent. Highlighted in bold font are results of the 25 km product.

	12.5 km	**25 km**	50 km	N
all	4.1 (0.5)	**2.8 (0.3)**	2.1 (0.2)	6369
T2m < -10°C	4.1 (0.5)	**2.8 (0.3)**	2.1 (0.2)	5619

Table 3-32: As Table 3-31 but for the Southern Hemisphere SICCI 2 mean sea-ice concentration total uncertainty.

	12.5 km	**25 km**	50 km	N
all	4.5 (1.6)	**3.7 (2.3)**	3.0 (1.7)	6369
T2m < -10°C	4.4 (1.6)	**3.6 (2.2)**	2.9 (1.6)	5619

Compared to the Northern Hemisphere, the overall mean retrieval error is larger by between 0.4% for the 25km and the 50 km product. Standard deviations of the overall mean retrieval error are similar. The overall mean total errors are larger by 0.4% to 0.8% for the 25 km and 50 km product, and smaller by 0.1 to 0.2% for the 12.5 km product. Standard deviations of the overall mean total error of the Southern Hemisphere sea-ice concentration are considerably larger than in the Northern Hemisphere for the 25 km product (~0.8%) and the 12.5 km product (~0.3%) but are as large for the 50 km product (compare Table 3-30 and Table 3-32). Constraining the uncertainty analysis to cold conditions has almost no effect.

3.7.3   *Sea-ice concentration uncertainty time series & seasonal cycles*

Here we show time-series of algorithm standard error and total standard error for both hemispheres (first northern, then southern) for all three grid resolution (algorithms).

The investigation is done separately for "ice": SIC > 90% and "water": SIC < 15% grid cells, where the algorithm or the total standard error shows valid values, i.e. error value > 0 (within the sea-ice climatology mask).

Northern Hemisphere
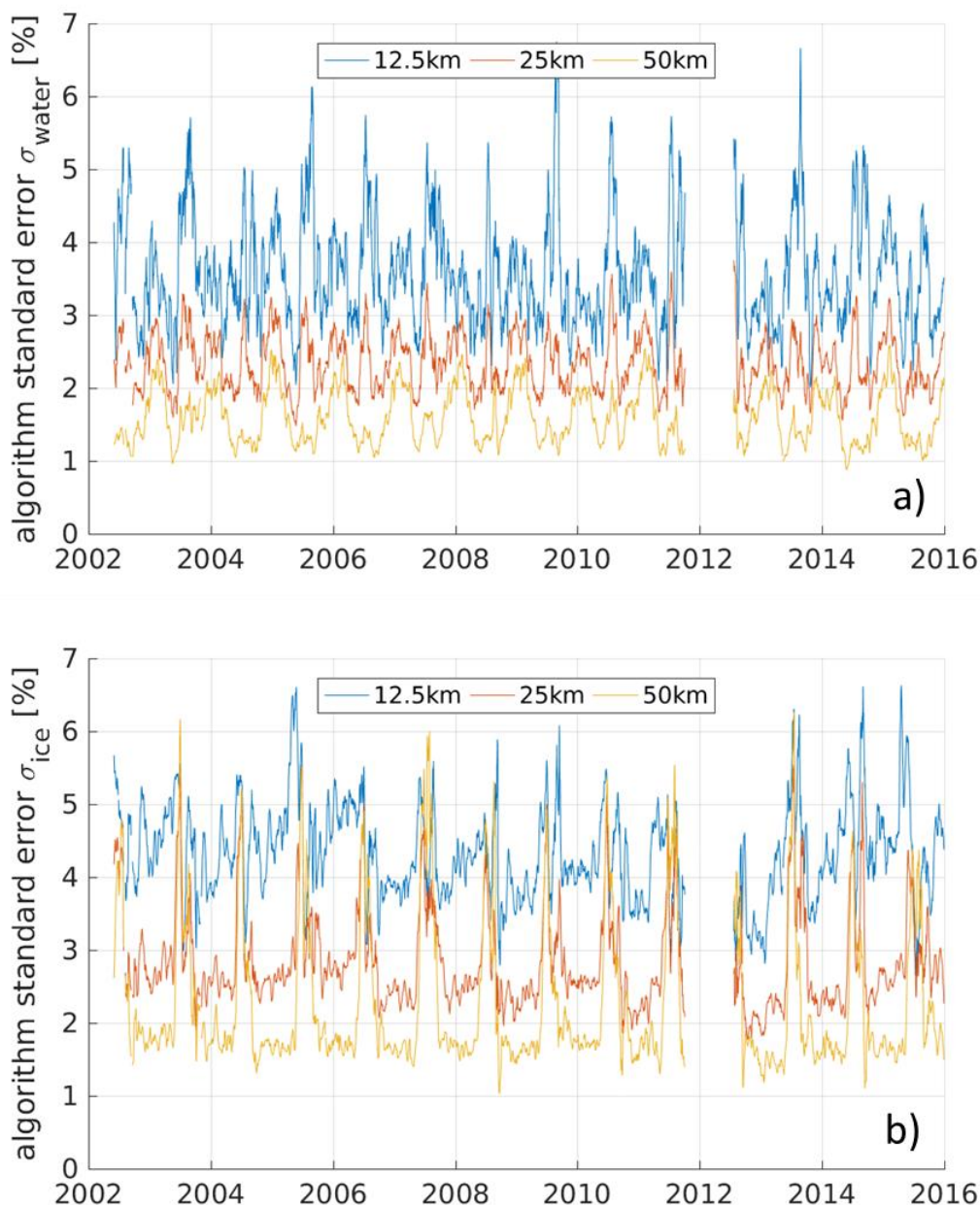
Figure 3-119: Time-series of the daily average algorithm standard error for water (a) and ice (b) grid cells computed from the algorithm standard error of the SICCI phase 2 SIC product of the Northern Hemisphere.

Figure 3-119 illustrates the long-term development of the daily average algorithm standard error of the SICCI phase 2 SIC for the Northern Hemisphere for the three different grid resolutions. The time series show strong variability of the algorithm standard error which is, however, most of the time smallest for 50 km grid resolution and largest for 12.5 km grid resolution for both water and ice grid cells. We note that during summer the algorithm standard error for 50 km might exceed the one for 25 km or even the one for 12.5 km (Figure 3-119 b); e.g. years 2003 and 2007). There seems to be no jump or inconsistency between the AMSR-E period (left of the gap) and the AMSR2 period (right of the gap).
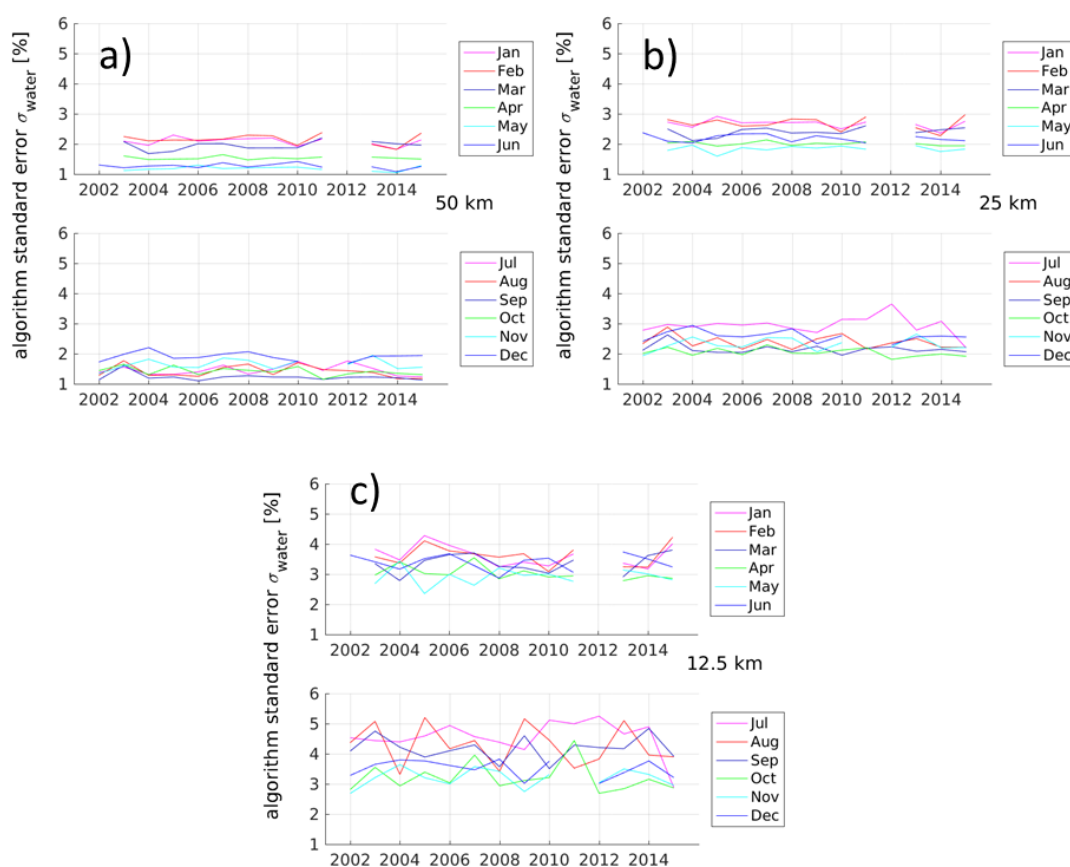
Figure 3-120: Time series of the monthly averaged algorithm standard error for 50 km (a), 25 km (b), and 12.5 km (c) for the Northern Hemisphere for water grid cells. Months with no data due to the gap between AMSR-E and AMSR2 (Oct. 2011 through June 2012) are left out.

Figure 3-120 shows the monthly averaged values of the algorithm standard error over water as shown in Figure 3-119 a) for each year. This figure confirms that the algorithm standard error is on average smallest for 50 km and largest for 12.5 km, and that the inter-annual variability of the monthly averaged algorithm standard error over water is largest for 12.5 km and smallest for 50 km. This figure confirms also, that no jump or inconsistency seems to exist in the algorithm standard error over water between the AMSR-E and the AMSR2 periods.

Figure 3-121 illustrates that also the long-term (multi-annual) monthly averaged algorithm standard error over water is smallest and has the smallest variability for 50 km, followed by the 25 km product and ending with the 12.5 km product. Common to all products is a double peak in the algorithm standard deviation with maxima during winter (January/February) and summer (July). Minimum values are observed in May and September (50 km) or October (25 km, 12.5 km). The maximum during winter can be explained by the stronger latitudinal temperature gradient supporting an enhanced frequency of low pressure systems causing variations in wind speed, water vapor and cloud liquid water (CLW) which influences are either not sufficiently mitigated by the radiative transfer model based brightness temperature correction before the retrieval or which influence (CLW) cannot

ESA UNCLASSIFIED - For Official Use

be corrected for at all. The maximum during summer, particularly for 12.5 km) is less obvious to explain.
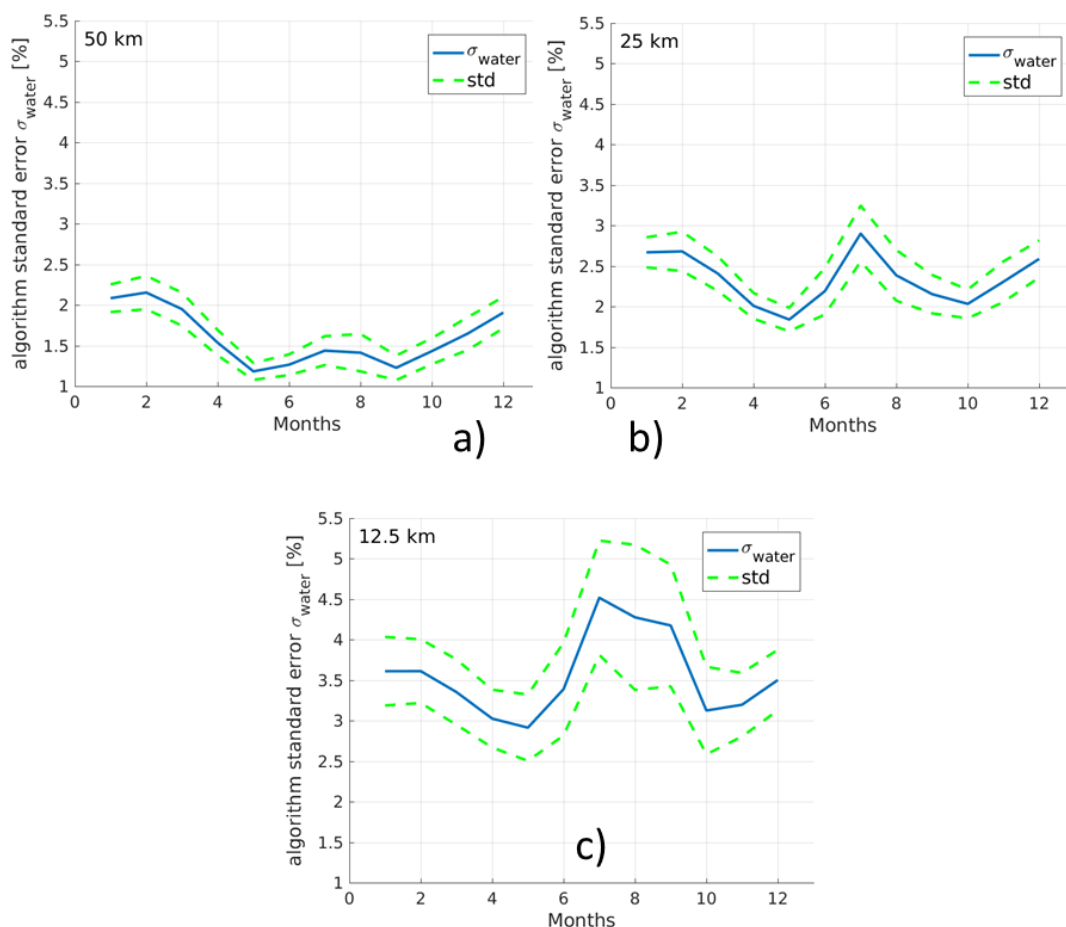
Figure 3-121: Seasonal cycle of the monthly mean algorithm standard error for 50 km (a), 25 km (b), and 12.5 km (c) over water for the Northern Hemisphere. The dashed green lines denote plus/minus one standard deviation.

On average the algorithm standard error varies around 1.5% (low: 1.2%, high: 2.1%) for 50 km, 2.3% (low: 1.9%, high: 2.9%) for 25 km and 3.5% (low: 3.0%, high: 4.5%) for 12.5 km. The standard deviations for these multi-annual monthly averages are around 0.1% to 0.2% for 50 km, 0.2% to 0.3% for 25 km and between 0.4% and 1.0% for 12.5 km, illustrating the large year-to-year variability of the impact of unaccounted weather influence over open water on the algorithm standard deviation of the 12.5 km product.

We are quite confident that the larger variability at 12.5 km is not caused by too few data samples or a substantially lower number of values. Actually the contrary is the case as is illustrated further down in Figure 3-124 showing the time series of the total number of grid cells used per day to compute the daily standard errors shown in Figure 3-119 on which the monthly averaged and multi-annual values are based.

Figure 3-122 shows – similar to Figure 3-120 – the monthly averaged values of the algorithm standard error over ice as shown in Figure 3-119 b) for each year. This figure confirms that the algorithm standard error is on average smallest for 50 km and largest for 12.5 km, and that the inter-annual variability of the monthly averaged algorithm standard error over ice largest for 12.5 km and smallest for 50 km. This is particularly valid for months October through May while the differences between the products are less obvious in the other months (see Figure 3-119 b) and Figure 3-123). Figure 3-122 confirms also, that no jump or inconsistency seems to exist in the algorithm standard error over ice between the AMSR-E and the AMSR2 periods.
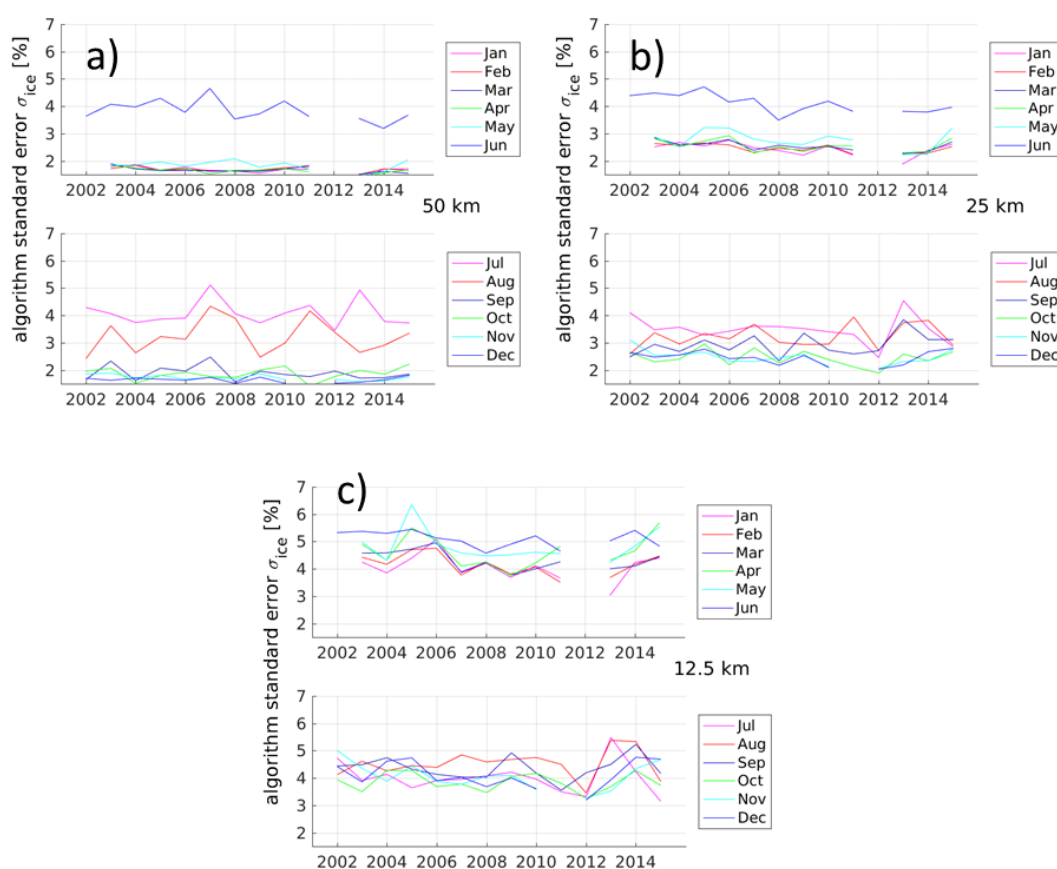
Figure 3-122: Time series of the monthly averaged algorithm standard error for 50 km (a), 25 km (b), and 12.5 km (c) for the Northern Hemisphere for ice grid cells. Months with no data due to the gap between AMSR-E and AMSR2 (Oct. 2011 through June 2012) are left out.

Figure 3-123 illustrates that indeed during winter the long-term (multi-annual) monthly averaged algorithm standard error over ice is smallest and has the smallest variability for 50 km, followed by the 25 km product and ending with the 12.5 km product. The seasonal cycle is less clear over ice than over water, though (compare Figure 3-121). For the 50 km and the 25 km product, algorithm standard errors during winter are comparably small and constant over time with little variation between October and May (Figure 3-123 a), b). This is different for 12.5 km where during same period, i.e. October through May, the algorithm standard deviation increases

ESA UNCLASSIFIED - For Official Use

monotonically (Figure 3-123 c). For 50 km, the summer months June, July, August show algorithm standard errors which are twice as large as those during winter. For 25 km, the main peak in algorithm standard error occurs in June after which the algorithm standard error decreases monotonically through summer to fall (Figure 3-123 b). For 12.5 km, the peak algorithm standard errors does also occur in June. Afterwards it drops to a typical winter value in July before reaching a second peak in August (Figure 3-123 c).
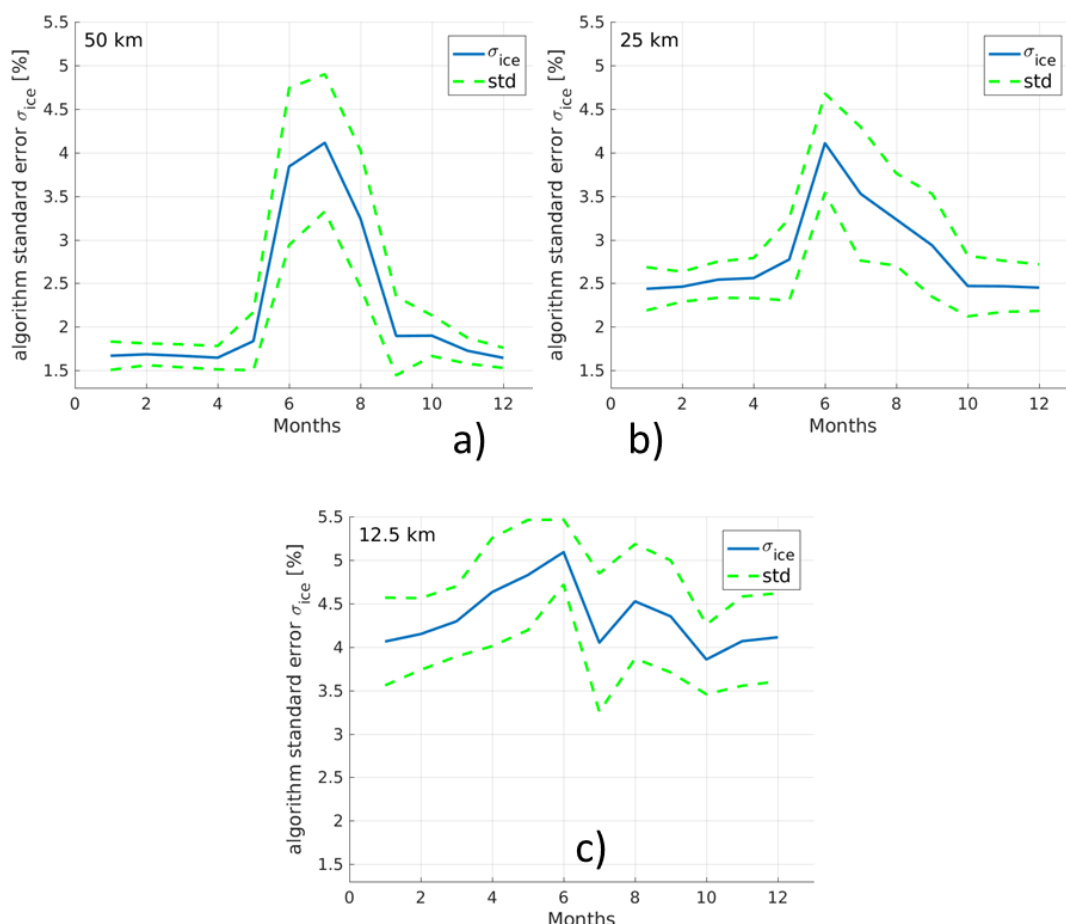
Figure 3-123: Seasonal cycle of the monthly mean algorithm standard error for 50 km (a), 25 km (b), and 12.5 km (c) over ice for the Northern Hemisphere. The dashed green lines denote plus/minus one standard deviation.

On average, the algorithm standard error over ice is ~1.7% for 50 km, ~2.5% for 25 km, and ~4.1% for 12.5 km during winter. During summer (June-July-August) the algorithm standard error over ice is ~ 3.6% for both 50 km and 25 km, and 4.5% for 12.5 km; note that the algorithm standard error for 50 km equals the one for 12.5 km in July. During winter, the standard deviations for these multi-annual monthly averages are around 0.1% to 0.2% for 50 km, and 0.2% to 0.3% for 25 km. For these two products, standard deviations are increasing substantially for late spring through fall to values between 0.5% and 0.9%. On the contrary, the standard deviation is relatively high throughout the year for 12.5 km with values between 0.4% (March, June) and 0.8% (May, July).
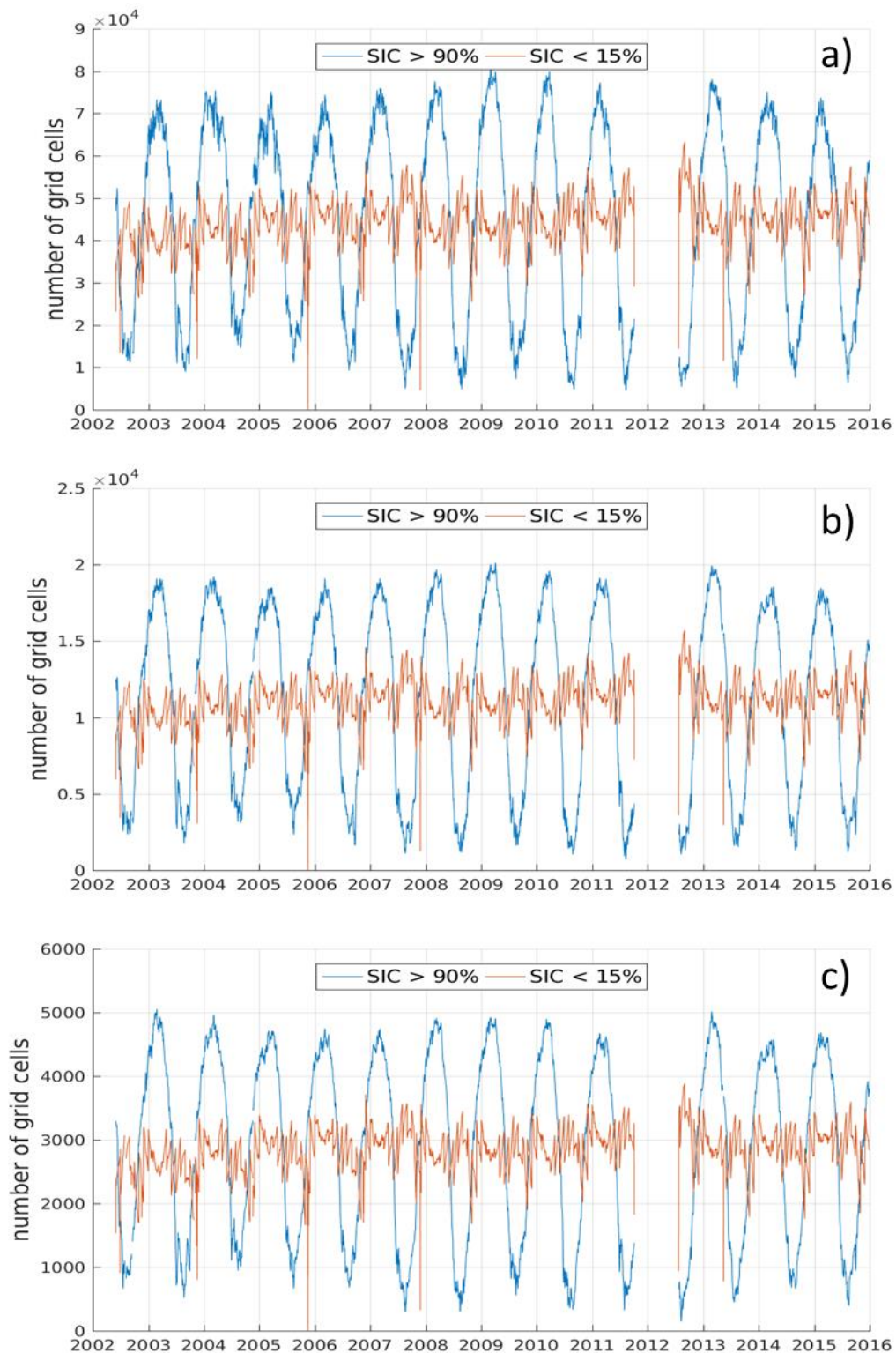
Figure 3-124: Time series of the number of grid cells used to compute the daily algorithm standard deviation shown in Figure 3-119 for 12.5 km (a), 25 km (b) and 50 km (c) for the Northern Hemisphere. Dips visible particularly in the SIC < 15 % time series are caused by missing scan lines.

The following explanations can be given

to a) the year-round large multi-annual algorithm standard error for 12.5 km: Usage of the 85 GHz data makes the algorithm much more sensitive to melt and refreeze processes at the snow and ice surface as well as to snow metamorphism and to disturbances by cloud liquid water;

to b) the comparably low algorithm standard error for 12.5 km during July: Low penetration depth and large sensitivity to surface properties reduces the uncertainty   during pan-Arctic melt conditions as encountered during July compared to the adjacent months June and August when parts of the surface are still frozen / again frozen;

to c) the much more pronounced increase in algorithm standard error during summer for 50 km compared to the other two products: Usage of the 6 GHz data makes the algorithm almost insensitive to any processes happening within the snow and topmost sea-ice layer – unless it is related to wetness or presence of liquid water. At this frequency the signal caused by the liquid water is a very clear one, not modified / counterbalanced too much by melt-refreeze cycles, snow metamorphism, surface crusts or similar; also the weather influence is almost negligible.
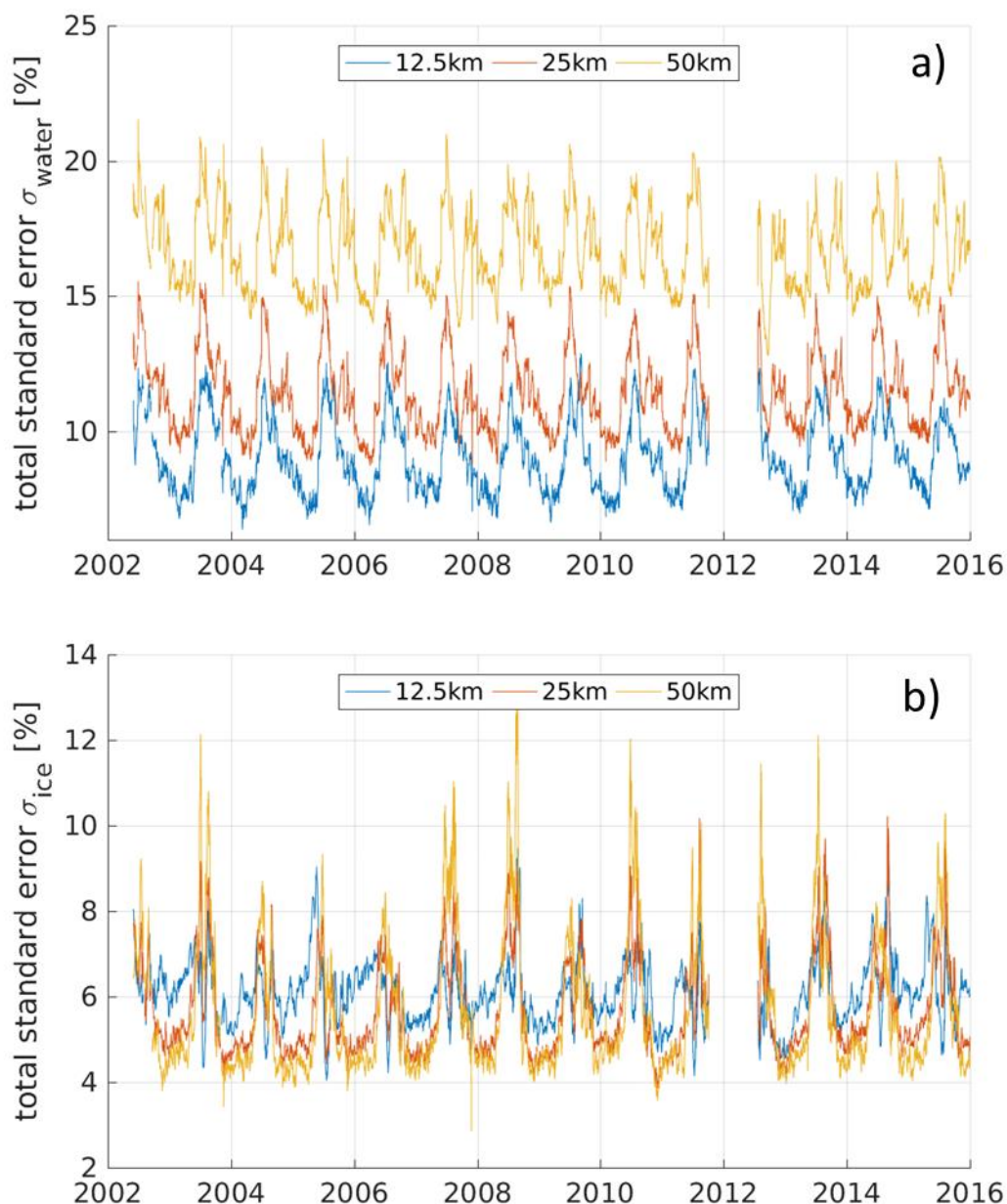
Figure 3-125: Time-series of the daily average total standard error for water (a) and ice (b) grid cells computed from the total standard error of the SICCI phase 2 SIC product of the Northern Hemisphere.

In Figure 3-125 through Figure 3-128 we repeat Figure 3-119 through Figure 3-123, but instead of showing the algorithm standard error we show the total standard error. The total standard error is substantially larger than the algorithm standard error because it includes the contribution of the smearing standard error which is tied to sea-ice concentration gradients being blurred by the gridding process. The smearing standard error can be as large as 40 % in the marginal ice zone.

Figure 3-125 illustrates – like Figure 3-119 – the pronounced seasonal variation of the total standard error for all three grid resolutions and for

both water and ice grid cells with maximum error values during summer and minimum error values during winter. However, for water grid cells the order of which product is associated with the smallest / largest error is reversed (compare Figure 3-119 a). The 50 km total standard error is the largest throughout the year, followed by the 25 km, and the 12.5 km total standard errors. For ice grid cells the order remains the same but the fraction with which the 50 km total standard error exceeds the 25 km and 12.5 km total standard errors increases compared to the algorithm standard error (compare Figure 3-125 b) and Figure 3-119 b). The seasonal variation of the 50 km total standard error seems to be substantially larger than for 25 km and 12.5 km.
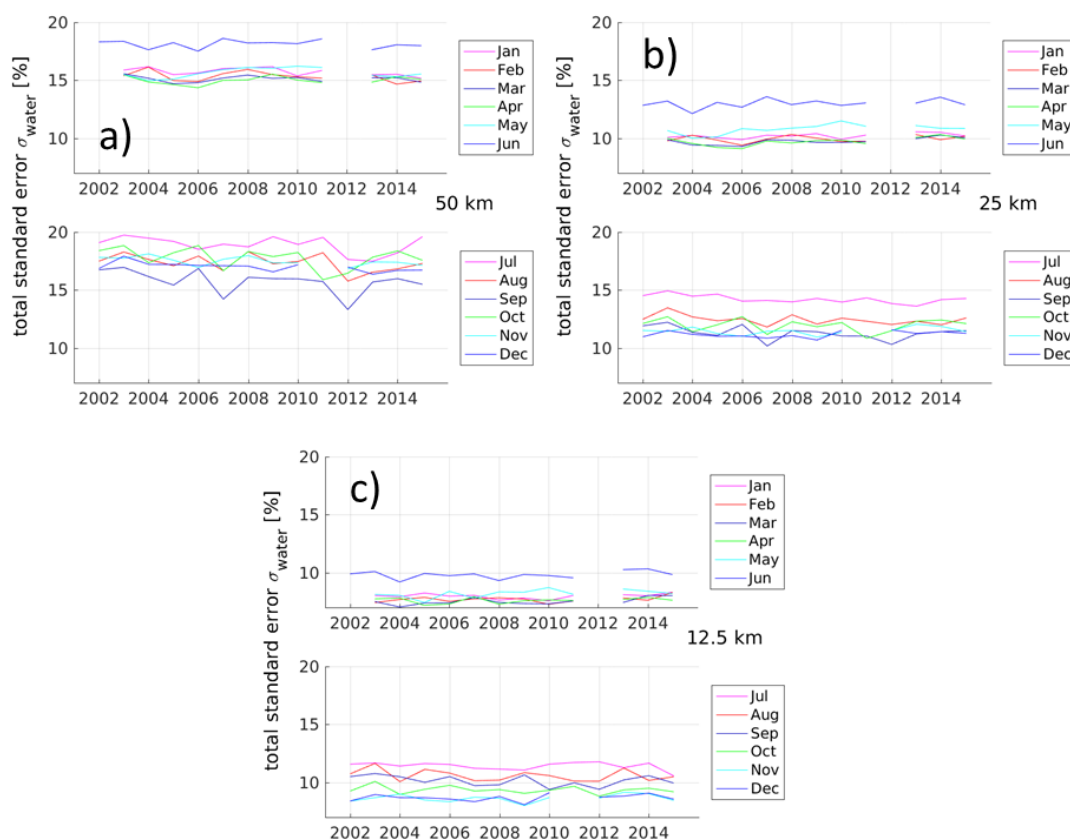
Figure 3-126: Time-series of the monthly averaged total standard error for 50 km (a), 25 km (b), and 12.5 km (c) for the Northern Hemisphere for water grid cells. Months with no data due to the gap between AMSR-E and AMSR2 (Oct. 2011 through June 2012) are left out.

Figure 3-126 shows the monthly averaged values of the total standard error over water as shown in Figure 3-125 a) for each year (compare Figure 3-120). This figure confirms that the 50 km total standard error is on average larger than the 25 km and the 12.5 km total standard errors. This figure confirms also, that no jump or inconsistency seems to exist in the total standard error over water between the AMSR-E and the AMSR2 periods.
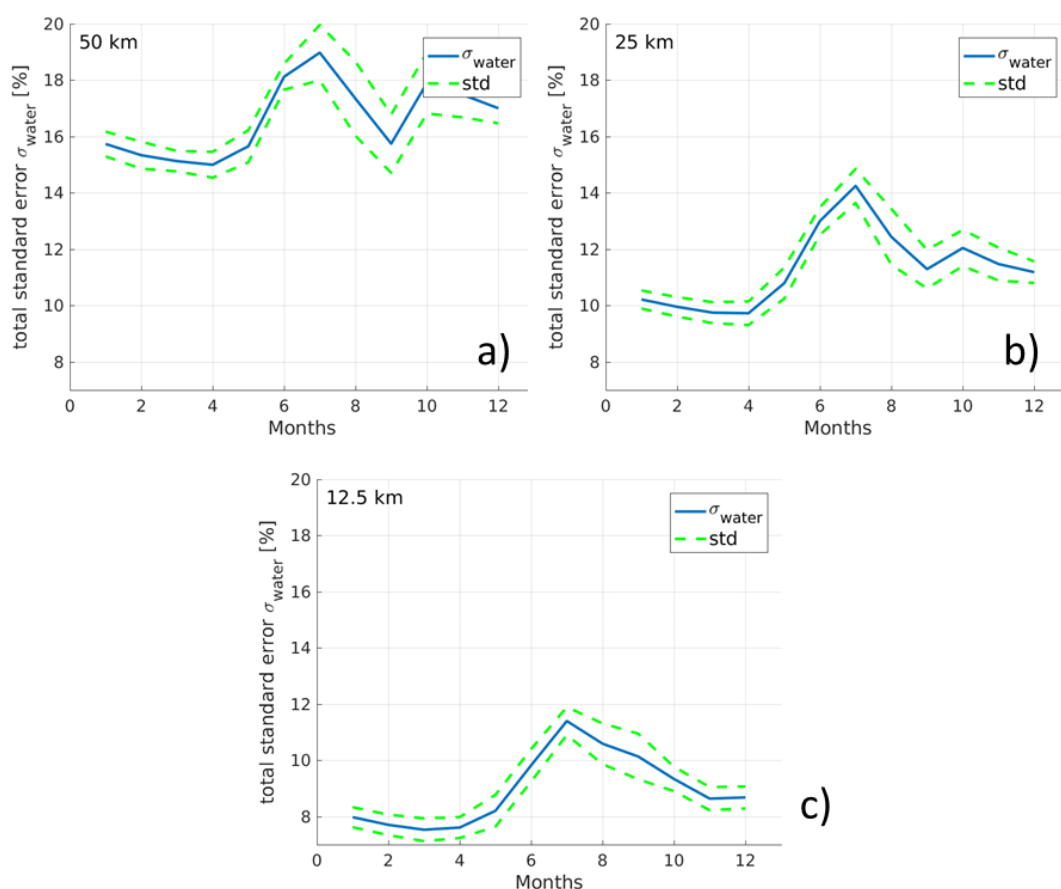
Figure 3-127: Seasonal cycle of the monthly mean total standard error for 50 km (a), 25 km (b), and 12.5 km (c) over water for the Northern Hemisphere. The dashed green lines denote plus/minus one standard deviation.

Figure 3-127 illustrates that also the long-term (multi-annual) monthly averaged total standard error over water is largest for 50 km, followed by the 25 km and 12.5 km products. The double peak observed for the algorithm standard deviation with maxima during winter (Jan./Feb.) and summer (July) (Figure 3-121) is super-seeded by the smearing error which changes the seasonal cycle of the total standard error. Common to all products is a minimum total standard error over water in March/April. ~15% for 50 km, ~ 10% for 25 km, and ~7.5% for 12.5 km. Also common to all products is a maximum total standard error in July which takes a value of 19% for 50 km, 14% for 25 km and 11.5% for 12.5 km; the multi-annual monthly average total standard error increases by the same amount of ~4% from winter to summer. Secondary maxima are observed in October for 50 km and 25 km total standard errors (Figure 3-127 a) and b). The standard deviation stays constant and relatively small (< 0.5%) during most of the cold season, increases slightly during the summer months for 25 km and 12.5 km, and increases more strongly to values around 1% during summer and fall for 50 km.

From these results it seems obvious that the smearing of sea-ice concentration gradients along the ice edge has a substantially larger impact on the total standard error at the coarser grid resolution than at the finer grid resolution. The increase in open water areas and associated ice edge

length during the melting season causes an increase in the fraction covered by sea-ice concentration gradients which are associated with a large smearing standard error. This explains the increase in total standard error towards summer.
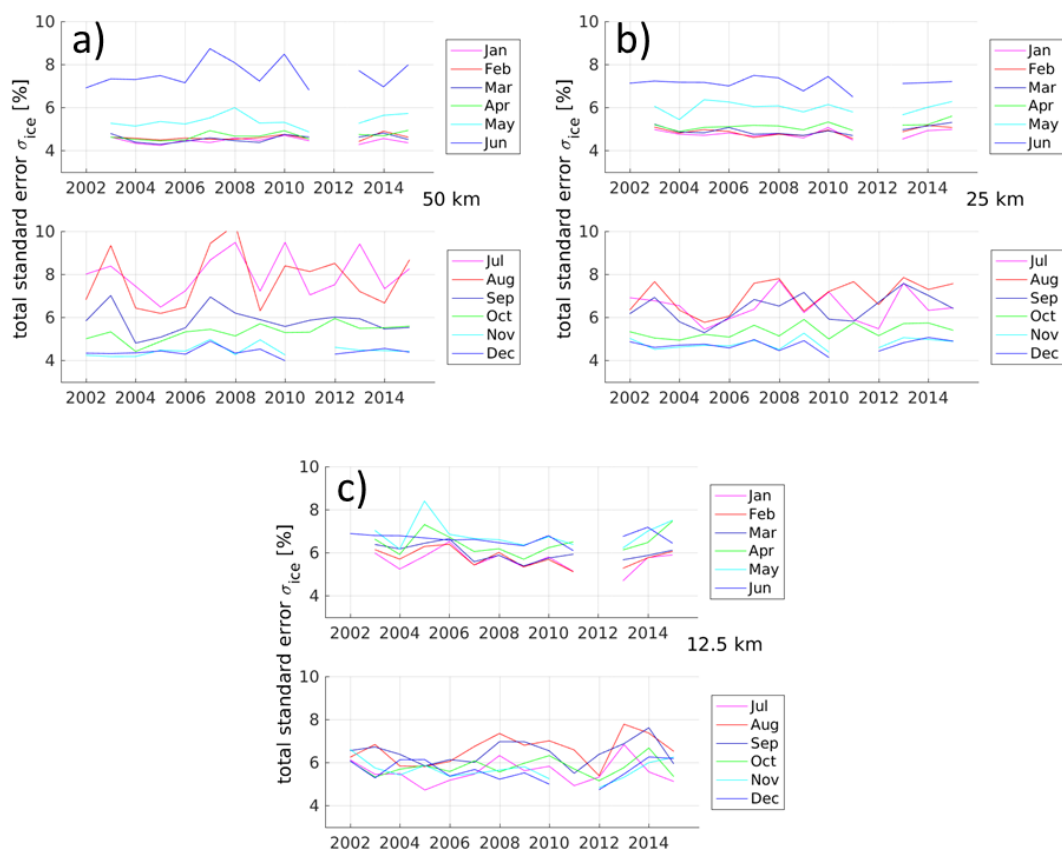
Figure 3-128: Time-series of the monthly averaged total standard error for 50 km (a), 25 km (b), and 12.5 km (c) for the Northern Hemisphere for ice grid cells. Months with no data due to the gap between AMSR-E and AMSR2 (Oct. 2011 through June 2012) are left out.

Figure 3-128 shows – similar to Figure 3-126 – the monthly averaged values of the total standard error over ice as shown in Figure 3-125 b) for each year. This figure confirms that the 50 km and the 25 km total standard error is on average smaller than for 12.5 km for most of the year. During summer months, however, the 25 km and particularly the 50 km total standard error are larger than the 12.5 km total standard error (compare Figure 3-128 a) and c). Figure 3-128 confirms also, that no jump or inconsistency seems to exist in the total standard error over ice between the AMSR-E and the AMSR2 periods.

Figure 3-129 illustrates that over ice the seasonal cycles of the multi-annual monthly average total and algorithm standard error are similar (compare Figure 3-123). The smearing standard error basically leads to an increase of the error with only marginally changing the seasonal cycle. During winter months the 50 km total standard error is ~4.5%, the 25 km one is ~5% and the 12.5 km one is ~5.8%; the contribution of the smearing standard error (= difference between total and algorithm standard error) is almost 3

% for 50 km, 2.5% for 25 km and < 2% for 12.5 km. The contribution by the smearing standard error increases to 4% and > 3% for 50 km and 25 km, respectively, but stays at the winter level for 12.5 km with average summer-time total standard errors of 7.8%, 6.7% and 6.3% for 50 km, 25 km and 12.5 km, respectively.
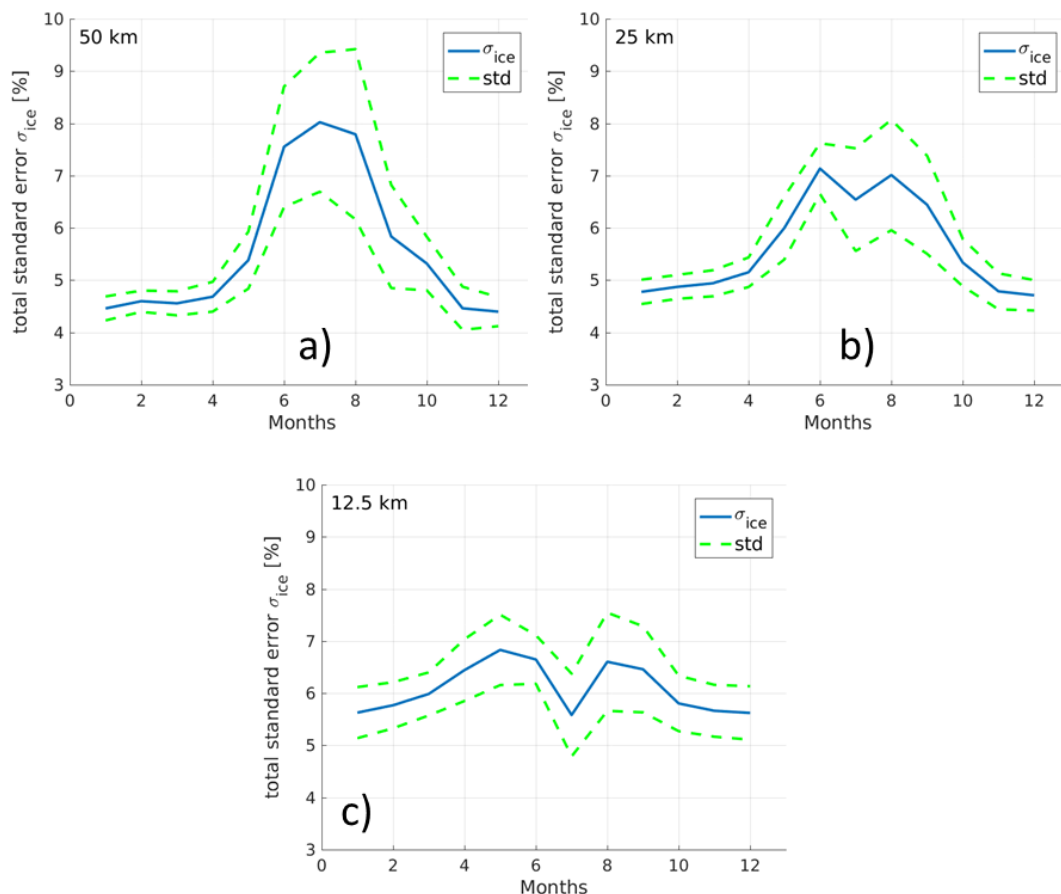
Figure 3-129: Seasonal cycle of the monthly mean total standard error for 50 km (a), 25 km (b), and 12.5 km (c) over ice for the Northern Hemisphere. The dashed green lines denote plus/minus one standard deviation.

This differing change in total standard error over ice from winter to summer between the three products can again be explained with the coarser grid resolution of the 50 km product. It is more likely that larger smearing standard errors due to sea-ice concentration gradients enter the total standard error even for > 90% sea-ice concentration (which are considered here only) for the 50 km product than for the 12.5 km product.

ESA UNCLASSIFIED - For Official Use

Southern Hemisphere
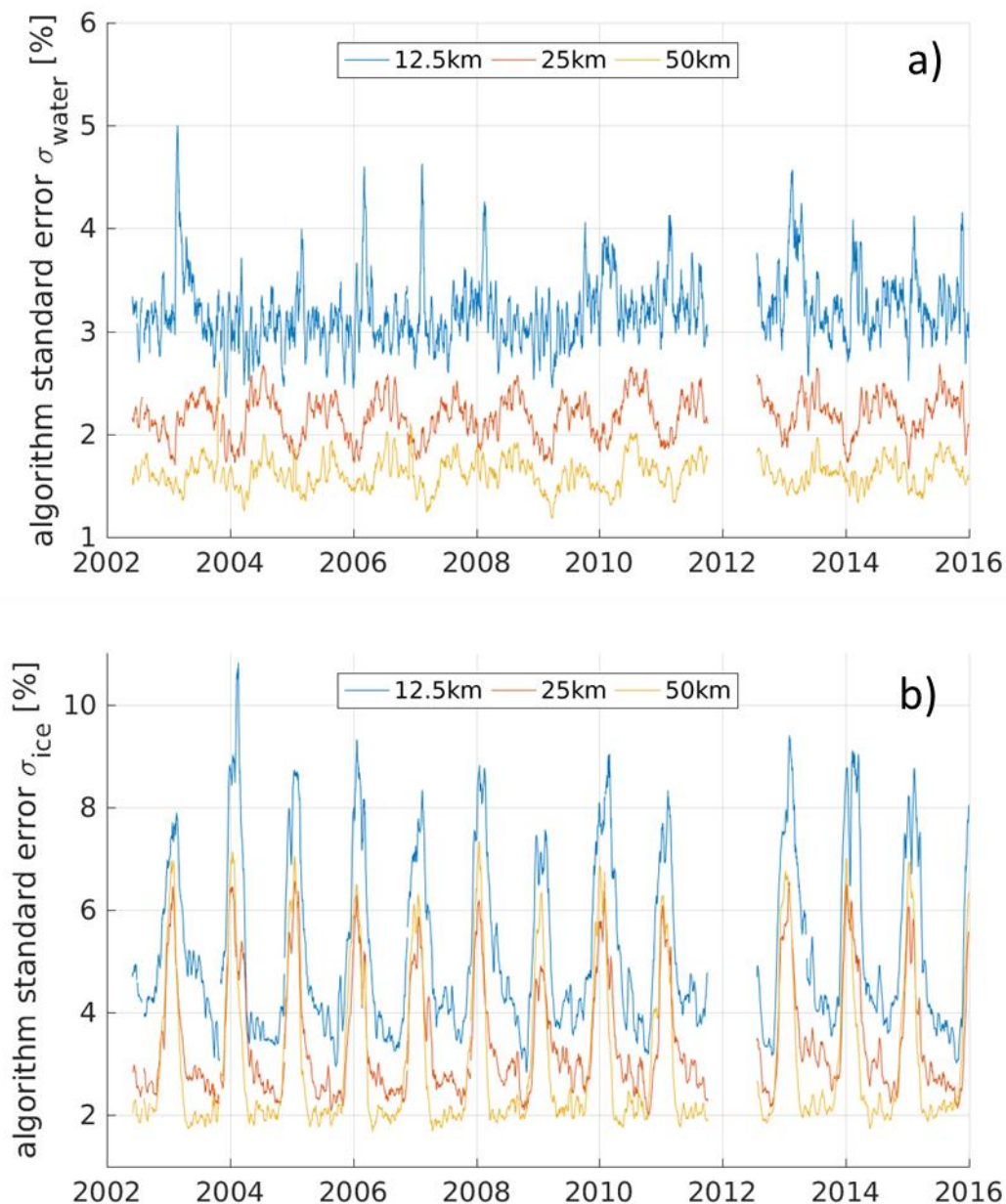
Figure 3-130: Time-series of the daily average algorithm standard error for water (a) and ice (b) grid cells computed from the algorithm standard error of the SICCI phase 2 SIC product of the Southern Hemisphere.

Figure 3-130 is the Southern Hemisphere version of Figure 3-119. It illustrates that for water (Figure 3-130 a) and ice (Figure 3-130 b) the mean 12.5 km algorithm standard error is larger than the 25 km one which is in turn larger than the 50 km one. There is much less variability in the 12.5 km algorithm standard deviation over water than in the Northern Hemisphere (Figure 3-119 a) and Figure 3-130 a). Over water largest 12.5 km algorithm standard errors occur during summer while the 25 km and 50 km algorithm standard errors are largest during winter and smallest during

ESA UNCLASSIFIED - For Official Use

summer. Over ice the algorithm standard error has a much more pronounced seasonal cycle with generally lower values during winter and maximum values during summer – in agreement with the Northern Hemisphere (Figure 3-119 b). While having the lowest values during winter, the 50 km algorithm standard errors exceed the 25 km ones in several years during summer but still remain always below the 12.5 km ones. There seems to be no jump or inconsistency between the AMSR-E period (left of the gap) and the AMSR2 period (right of the gap) neither for water nor for ice grid cells.
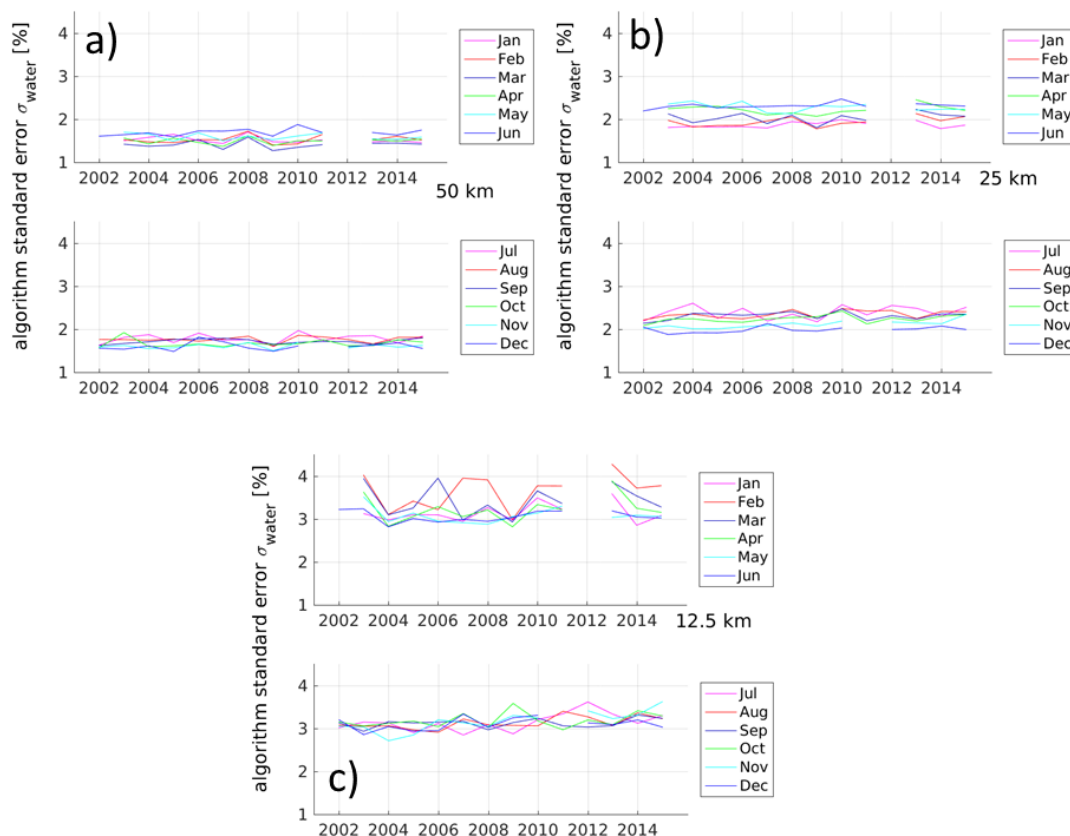
Figure 3-131: Time series of the monthly averaged algorithm standard error for 50 km (a), 25 km (b), and 12.5 km (c) for the Southern Hemisphere for water grid cells. Months with no data due to the gap between AMSR-E and AMSR2 (Oct. 2011 through June 2012) are left out.

The results shown in Figure 3-130 are nicely confirmed by the time-series of the monthly average algorithm standard error illustrated in Figure 3-131, the Southern Hemisphere version of Figure 3-120. Smallest algorithm standard error and smallest inter-annual variation is found for 50 km followed by 25 km and 12.5 km, the latter providing on average the largest values and also the largest inter-annual variability – at least during summer (Figure 3-131 c). Figure 3-131 confirms that no jump or inconsistency seems to exist in the algorithm standard error over water between the AMSR-E and the AMSR2 periods.
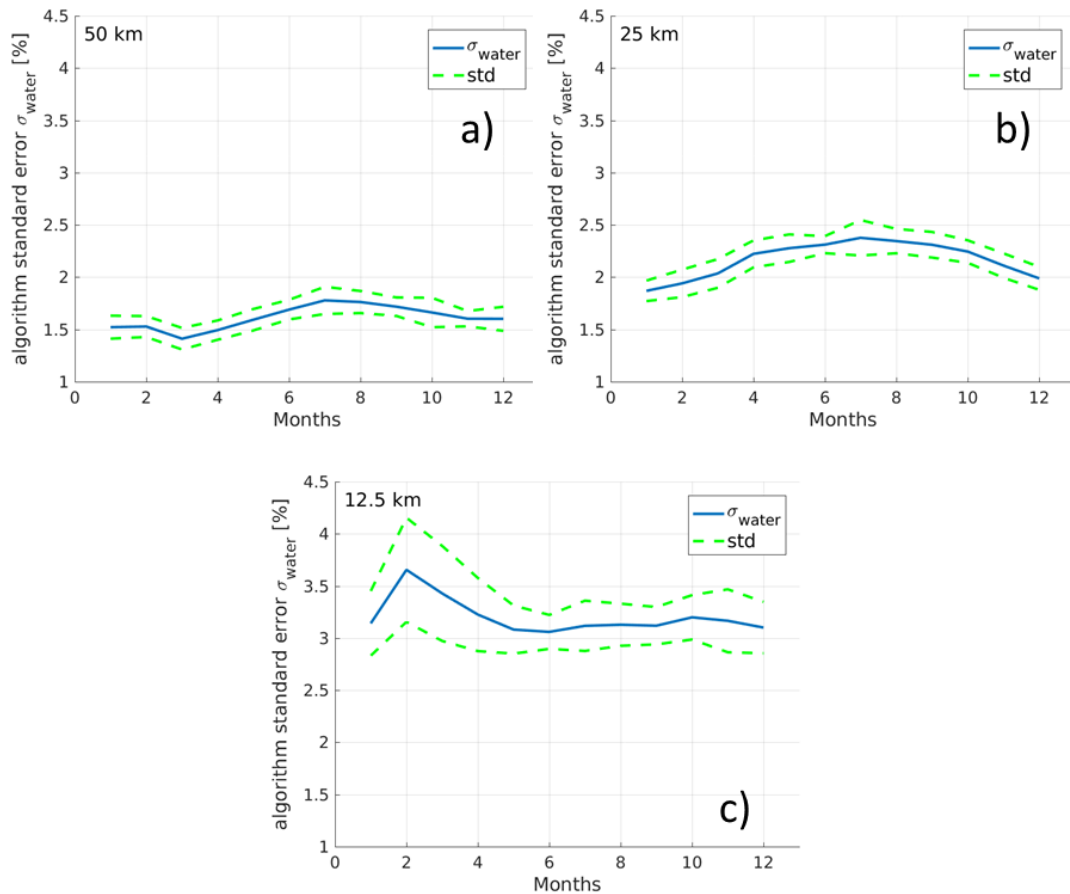
Figure 3-132: Seasonal cycle of the monthly mean algorithm standard error for 50 km (a), 25 km (b), and 12.5 km (c) over water for the Southern Hemisphere. The dashed green lines denote plus/minus one standard deviation.

Figure 3-132 illustrates that in the Southern Hemisphere the multi-annual monthly average algorithm standard error over water is bit smaller and has a weaker seasonal cycle than in the Northern Hemisphere (compare Figure 3-121) if present at all. There is only a weak increase in the 50 km and 25 km algorithm standard errors during winter with a peak value of 1.8% and 2.4%, respectively, after minimum values of 1.4% (March) and 1.9% (Jan.) for 50 km and 25 km, respectively. The 12.5 km algorithm standard error has not peak in winter but a maximum during summer: 3.6% in February. Also, the standard deviation is substantially larger, up to 0.5%, for the 12.5 km product compared to the other two products. The increase of the algorithm standard deviation over water during summer is a feature which was observed for the Northern Hemisphere as well: for the 25 km and the 12.5 km products.

ESA UNCLASSIFIED - For Official Use
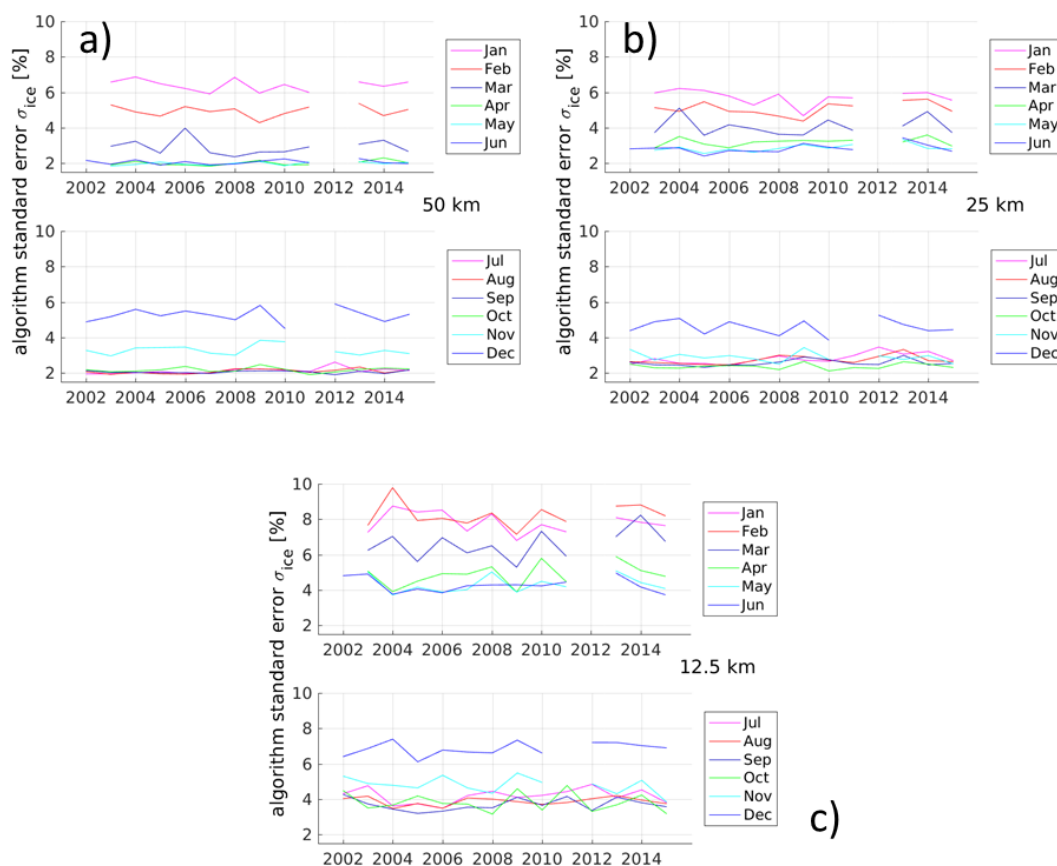
Figure 3-133: Time series of the monthly averaged algorithm standard error for 50 km (a), 25 km (b), and 12.5 km (c) for the Southern Hemisphere for ice grid cells. Months with no data due to the gap between AMSR-E and AMSR2 (Oct. 2011 through June 2012) are left out.

Figure 3-133 shows – similar to Figure 3-122 – the monthly averaged values of the algorithm standard error over ice as shown in Figure 3-130 b) for each year for the Southern Hemisphere. This figure illustrates nicely how the melting period is manifested in the algorithm standard error. For 50 km, the algorithm standard error is small and not very variable for months April through October. But then the algorithm standard error increases from November to December to January before it decreases again in February and March (Figure 3-133 a). The same can be observed for the other two products. The inter-annual variability in the monthly average algorithm standard error over ice is largest at 12.5 km and smallest at 50 km. Figure 3-133 confirms also, that no jump or inconsistency seems to exist in the algorithm standard error over ice between the AMSR-E and the AMSR2 periods in the Southern Hemisphere.
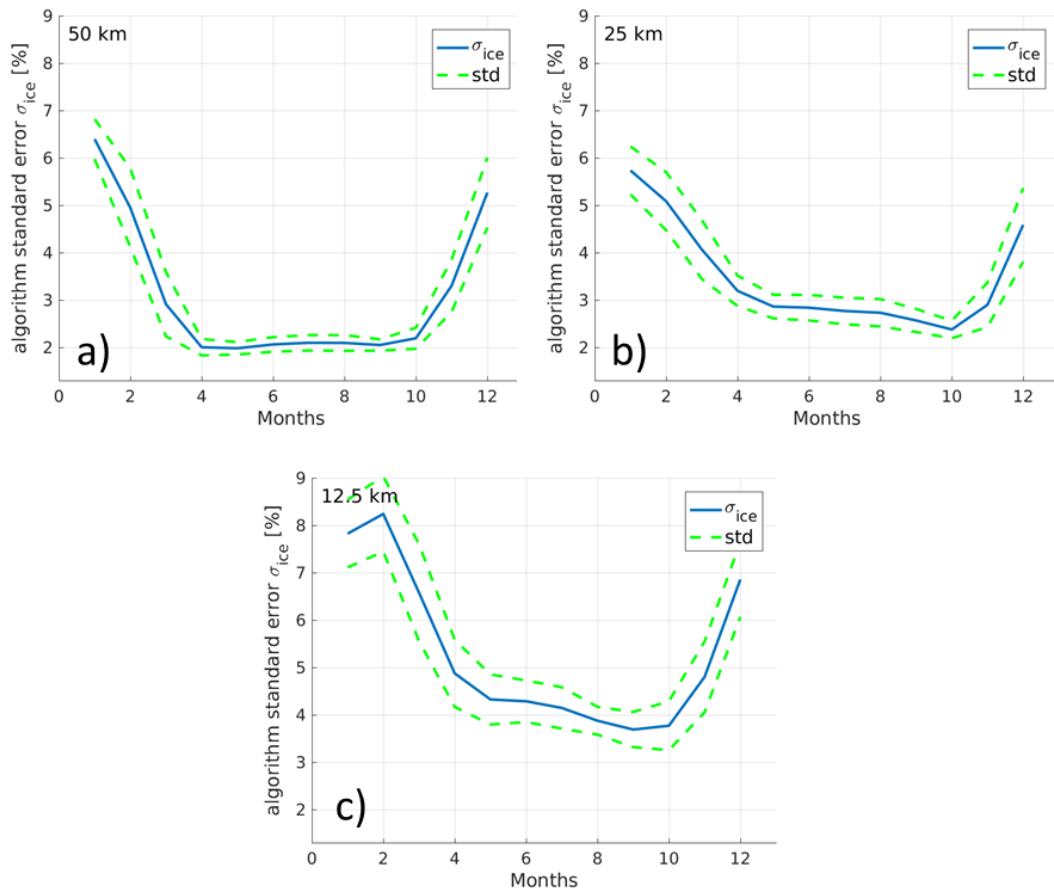
Figure 3-134: Seasonal cycle of the monthly mean algorithm standard error for 50 km (a), 25 km (b), and 12.5 km (c) over ice for the Southern Hemisphere. The dashed green lines denote plus/minus one standard deviation.

Figure 3-134 shows – similar to Figure 3-123 – the multi-annual monthly average algorithm standard error over ice in the Southern Hemisphere and shows almost the same seasonal cycle as observed in the Northern Hemisphere. During winter, say May through October, the algorithm standard error is small: ~2%, ~2.8%, and ~4% for the 50 km, 25 km and 12.5 km product, respectively. The mean winter 12.5 km algorithm standard error is as large as in the Northern Hemisphere, and the 25 km and 50 km ones are a bit larger than in the Northern Hemisphere (compare Figure 3-123While the 50 km algorithm standard error is almost constant throughout the winter, both the 25 km and the 12.5 km algorithm standard errors decrease during winter, reaching the minimum value in October and September, respectively. Late spring and summer are characterized by a substantial increase in algorithm standard error which peaks at 6.4%, 5.7 % (both in Jan.), and 8.2% (in Feb.) and mean (Dec.-Jan.-Feb.) values of 5.5%, ~5% and 7.5% for the 50 km, 25 km and 12.5 km product, respectively. With that the summer-time algorithm standard error over ice is larger in the Southern than in the Northern Hemisphere where the respective mean values are 3.6%, 3.6% and 4.5%.
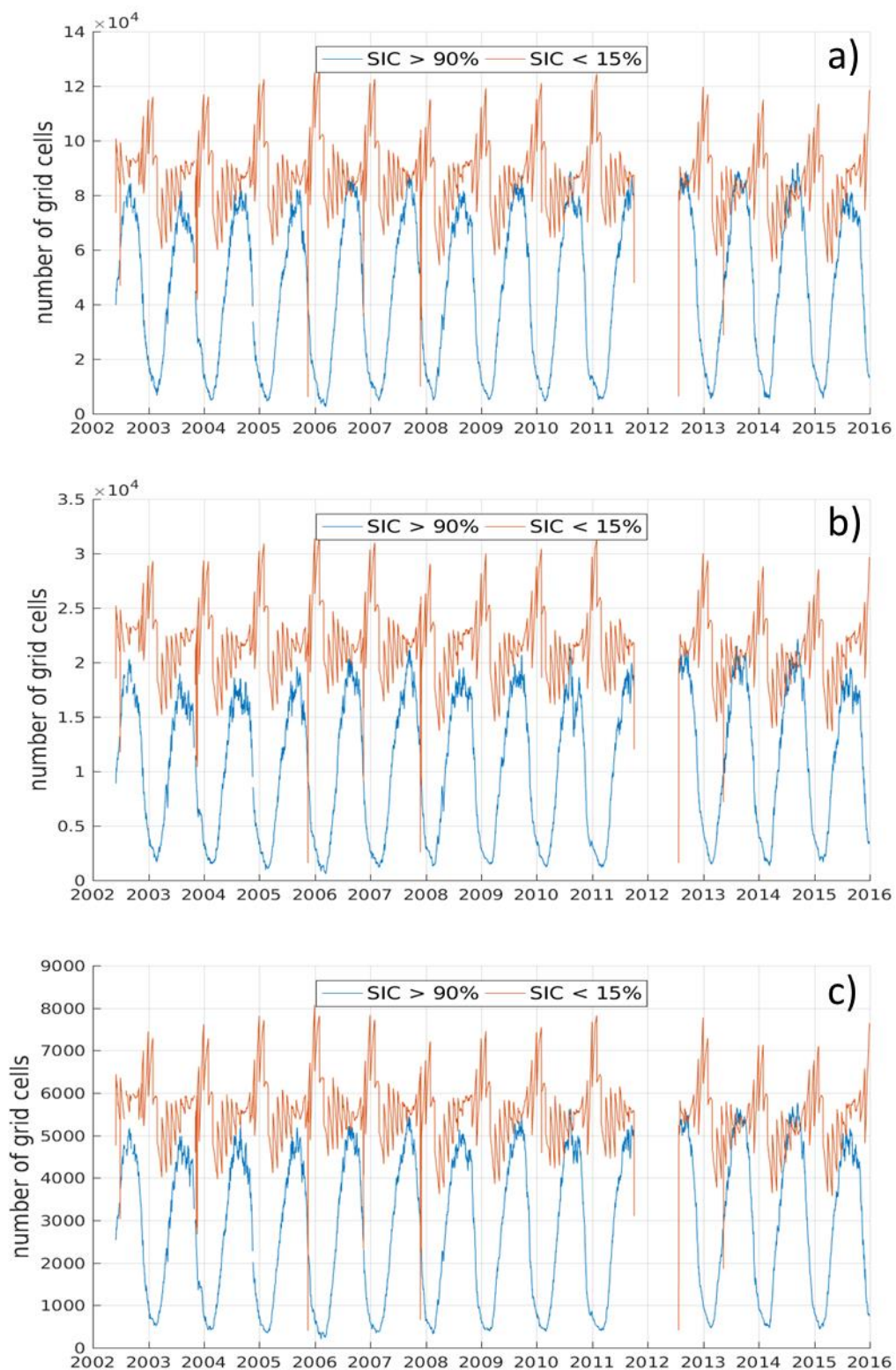
Figure 3-135: Time series of the number of grid cells used to compute the daily algorithm standard deviation shown in Figure 3-130 for 12.5 km (a), 25 km (b) and 50 km (c) for the Southern Hemisphere. Dips visible particularly in the SIC < 15 % time series are caused by missing scan lines.

The strong oscillation of the water (SIC < 15%) number of grid cells can be explained by the monthly change of the climatological ice-water boundary marking the outer limit of any ice. During most of the freezing season this increases the number of grid cells available as water area at the 1st of the respective month, a number which then gradually decreases as the ice extent increases.
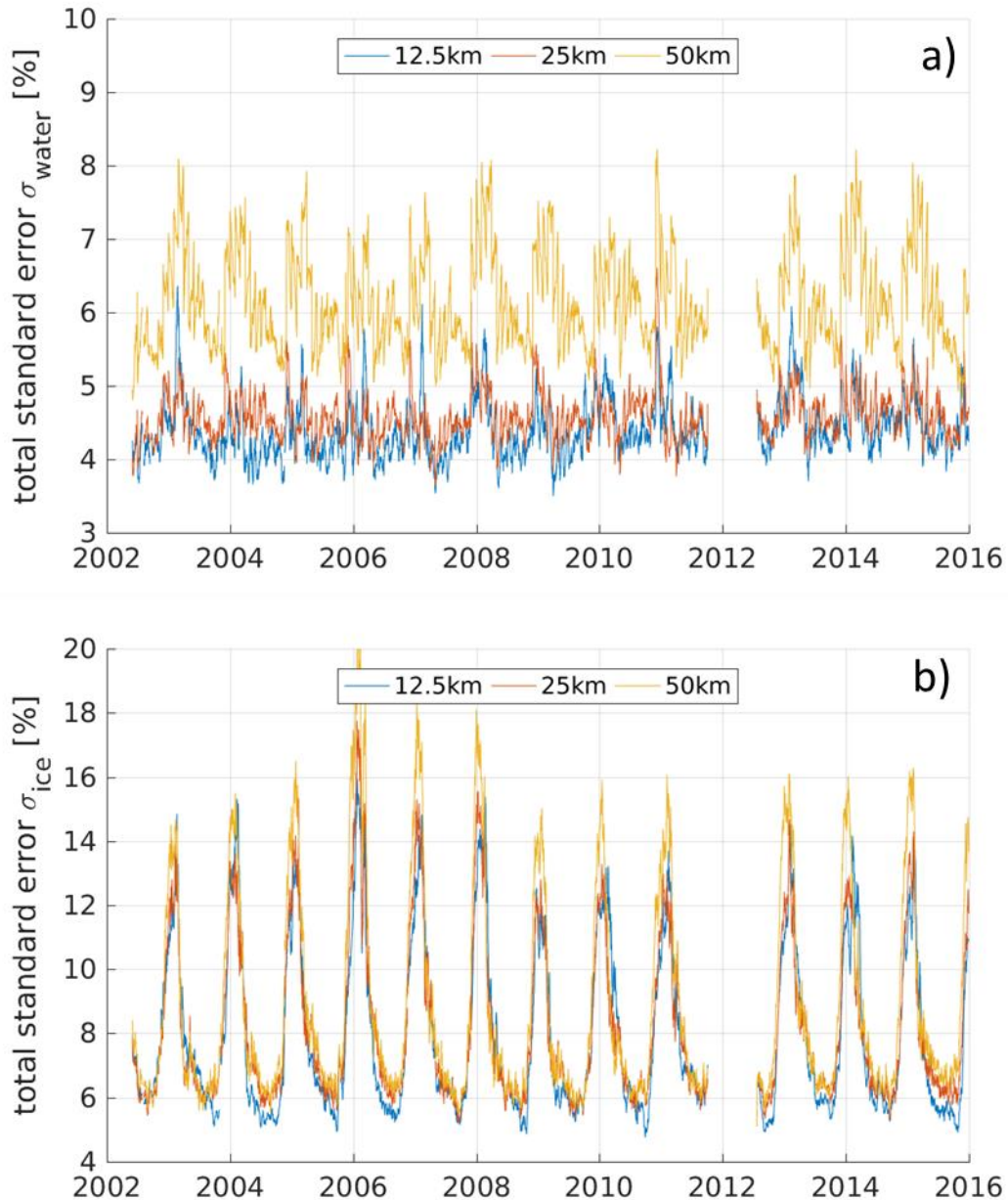
Figure 3-136: Time-series of the daily average total standard error for water (a) and ice (b) grid cells computed from the total standard error of the SICCI phase 2 SIC product of the Southern Hemisphere.

We note that there is a substantial variation of the number of grid cells which can be used every day to compute the mean algorithm standard error for water but particularly for ice grid cells (see Figure 3-135). Especially

ESA UNCLASSIFIED - For Official Use

during summer and for the 50 km product the total number of grid cells is smaller than 500 regularly. This means that the statistics of the results obtained during the summer months – especially with the 50 km product is considerably worse than during the remaining year.

In Figure 3-136 through Figure 3-140 we repeat Figure 3-130 through Figure 3-134 for the total standard error instead of the algorithm standard error (compare Figure 3-125 through Figure 3-129). Over water, the total standard error behaves similar as in the Northern Hemisphere. While the 50 km algorithm standard error is smallest and the 12.5 km algorithm error is largest, the opposite applies to the total standard error due to the contribution of the smearing standard error: the 50 km total standard error is largest, followed by the 25 km one and the 12.5 km one; the latter two don't differ too much and occasionally during summer there are peaks in the 12.5 km total standard error exceeding the one at 25 km. In addition, the 50 km total standard error varies much more seasonally than the 50 km algorithm standard error (Figure 3-136 a) and Figure 3-130 a). We note that the difference between total standard error and algorithm standard error over water is much smaller in the Southern Hemisphere than in the Northern Hemisphere (see Figure 3-119, Figure 3-125, Figure 3-130, and Figure 3-136, image a).
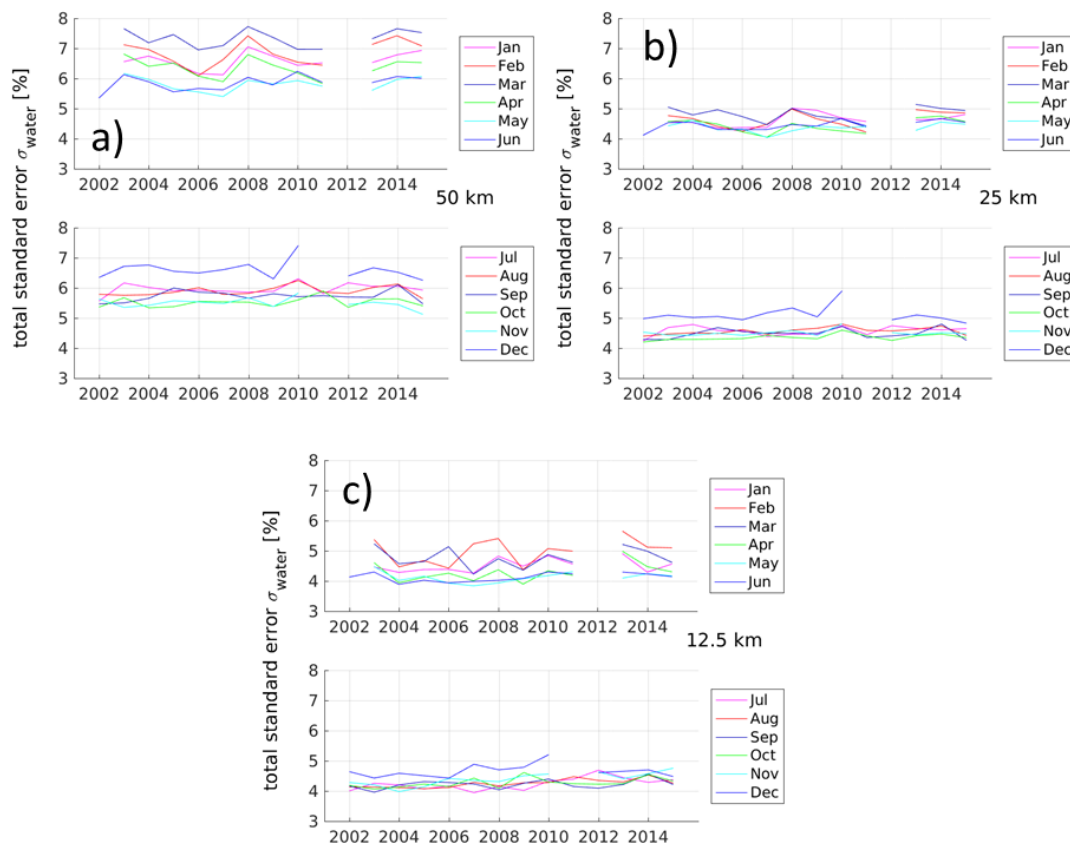
Figure 3-137: Time-series of the monthly averaged total standard error for 50 km (a), 25 km (b), and 12.5 km (c) for the Southern Hemisphere for water grid cells. Months with no data due to the gap between AMSR-E and AMSR2 (October 2011 through June 2012) are left out.

Over ice the difference between total and algorithm standard error is again most pronounced at 50 km and at 25 km. The smallest total standard errors are obtained for 12.5 km during winter – but the difference to the coarser grid resolutions is 1% at most. During summer, however, particularly the 50 km total standard error peaks at considerably larger values than the 12.5 km one and also the 25 km one.

Figure 3-137 confirms the notion from Figure 3-136. Also as monthly averages the 50 km total standard errors over water are considerably larger than for the other two products during both winter and summer in the Southern Hemisphere. The smallest overall variation is observed for 25 km.
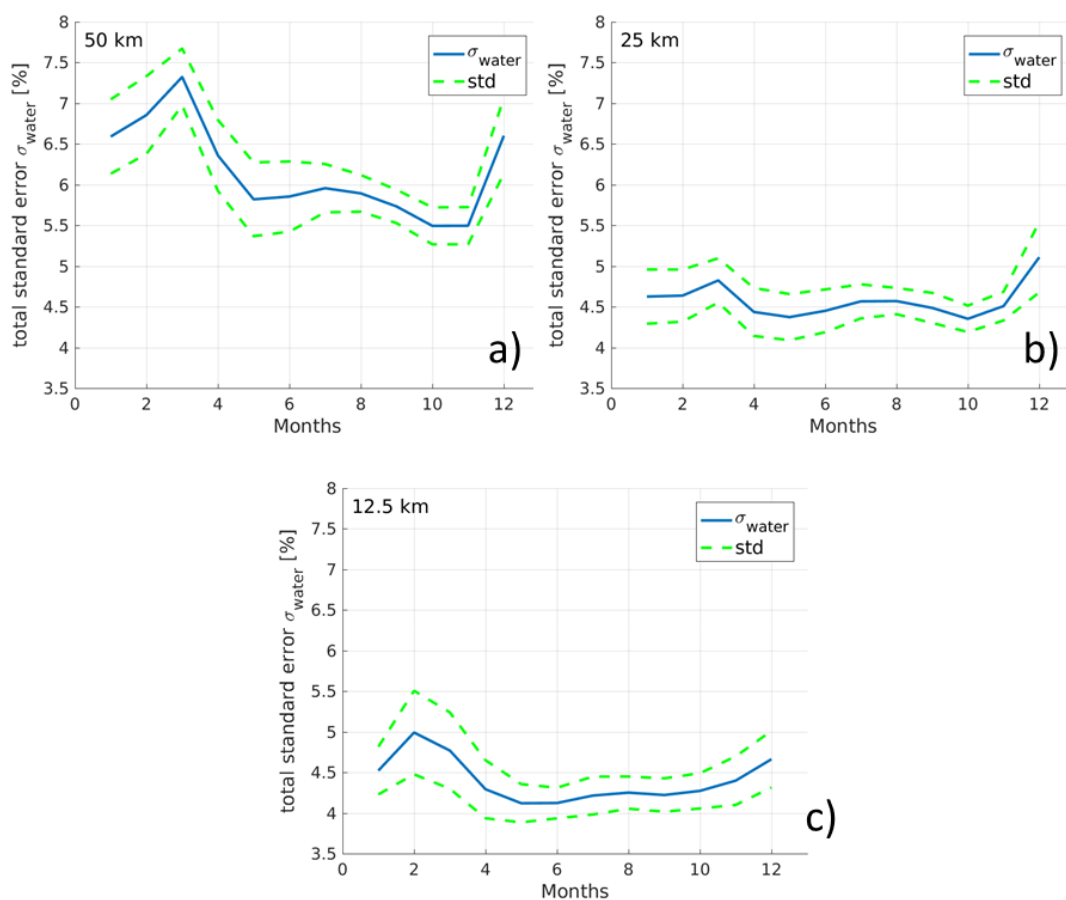
Figure 3-138: Seasonal cycle of the monthly mean total standard error for 50 km (a), 25 km (b), and 12.5 km (c) over water for the Southern Hemisphere. The dashed green lines denote plus/minus one standard deviation.

In Figure 3-138 we see that the difference between the multi-annual monthly average 12.5 km total and algorithm standard errors over open water basically is a more or less constant offset of 1 to 1.5% (compare Figure 3-138 c) and Figure 3-132 c); the peak error value still occurs in February. For the other two products the inclusion of the smearing error leads to a change in the seasonal pattern of the total standard error compared to the algorithm standard error (compare Figure 3-138 a,b) and Figure 3-132 a,b). For both coarser resolution products the peak error values occur in summer/fall (Dec. for 25 km and March for 50 km). For 25 km the difference between total and algorithm standard errors is 2% during

winter and 3% during summer; for 50 km this difference is 4% during winter and up to 5.5% during summer/fall. The explanation for this larger contribution of the smearing error at coarser grid resolutions and during summer can be explained by the reduced capability to resolve small-scale sea-ice concentration gradients and the greater length of the ice edge paired with more open water areas also inside the ice cover, respectively.
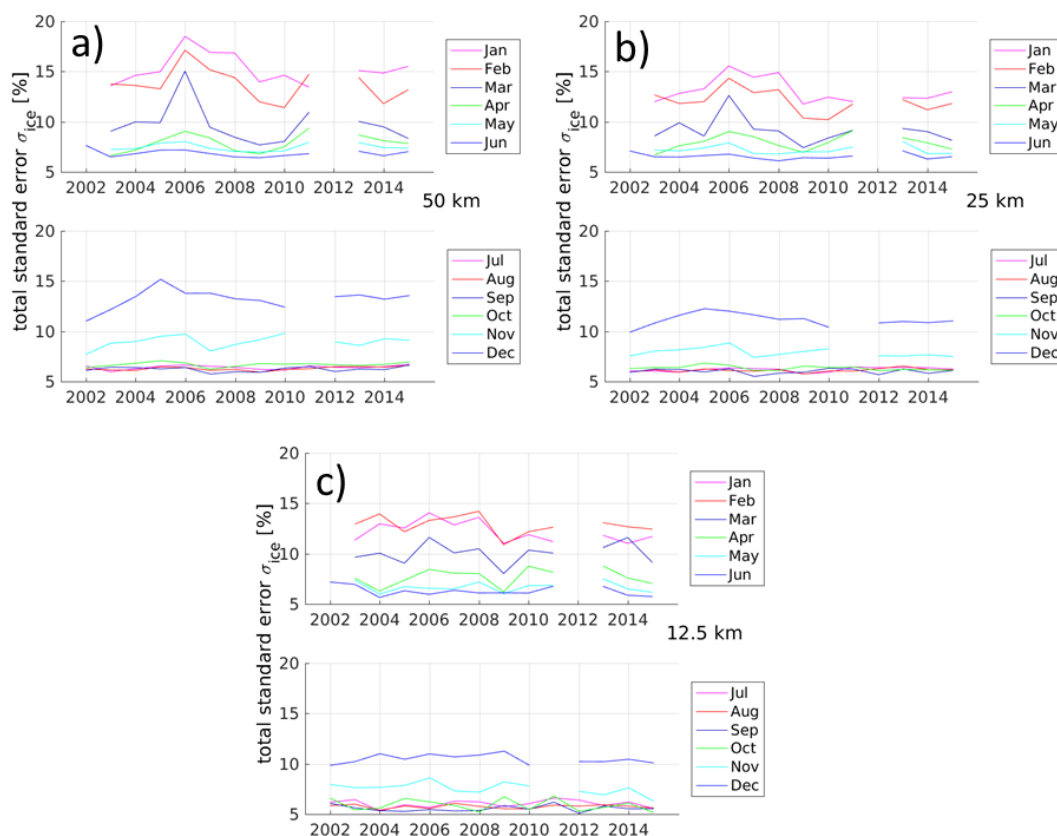
Figure 3-139: Time-series of the monthly averaged total standard error for 50 km (a), 25 km (b), and 12.5 km (c) for the Southern Hemisphere for ice grid cells. Months with no data due to the gap between AMSR-E and AMSR2 (Oct. 2011 through June 2012) are left out.

Figure 3-139 illustrates that the monthly average total standard errors over ice in the Southern Hemisphere follow basically the same pattern as the respective algorithm standard errors (see Figure 3-133), with comparably low values and small inter-annual variation during winter and elevated values and more inter-annual variation during summer. Remarkable is that over ice during summer the total standard errors are much larger in the Southern Hemisphere: 14%, 12% and 12% for 50 km, 25 km and 12.5 km, respectively, than in the Northern Hemisphere: 8%, 7% and 6% for 50 km, 25 km and 12.5 km, respectively (Figure 3-129). Also, in the Northern Hemisphere there was almost no difference in the monthly average 12.5 km total standard error over ice between winter and summer while in the Southern Hemisphere there is a difference between winter and summer by about 5%. One possible explanation for this could be that the areas with > 90% sea-ice concentration are less compact in the Southern Ocean, i.e. there is a more wide-spread distribution of relatively small patches of >

90% sea-ice concentration while in the Northern Hemisphere there are only a few larger areas with > 90% sea-ice concentration. This reduces the number of grid cells with strong sea-ice concentration gradients being responsible for elevated smearing standard errors and subsequently total standard errors.
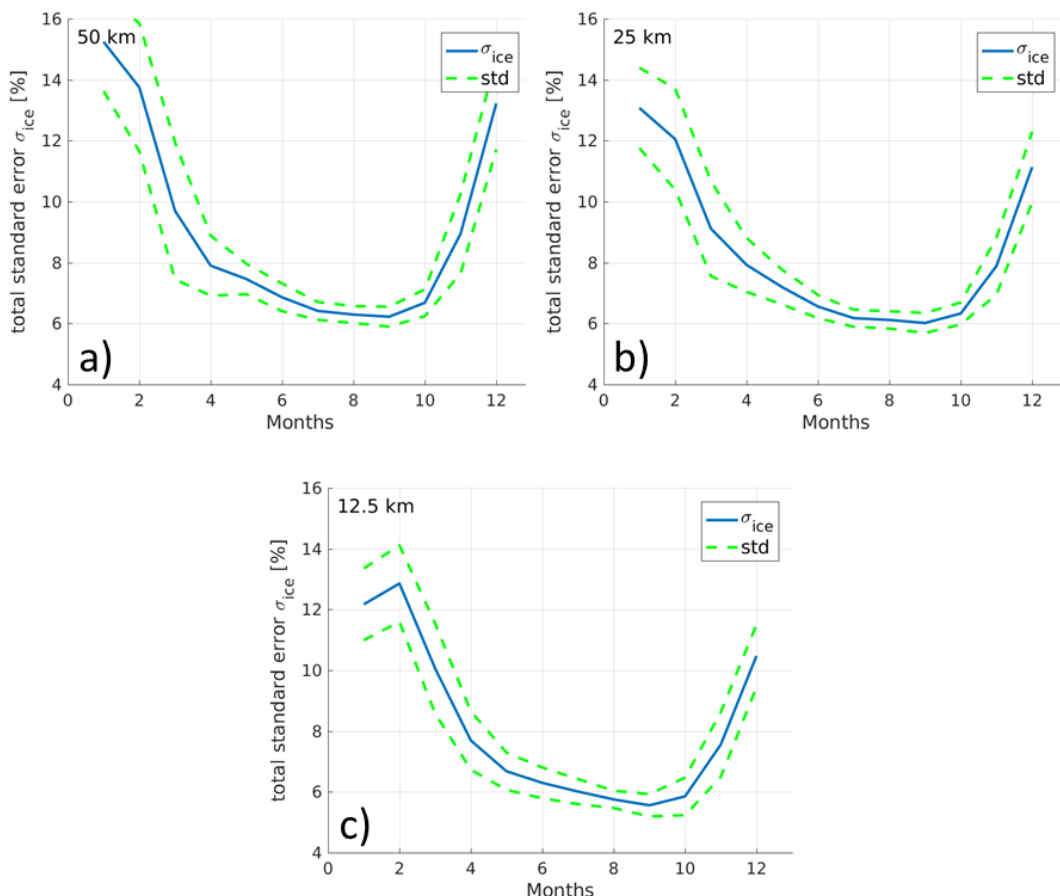
Figure 3-140: Seasonal cycle of the monthly mean total standard error for 50 km (a), 25 km (b), and 12.5 km (c) over ice for the Southern Hemisphere. The dashed green lines denote plus/minus one standard deviation.

The seasonal cycles of the multi-annual monthly average total standard error over ice in the Southern Hemisphere shown in Figure 3-140 confirm the statements made for Figure 3-139 and illustrate that during mid to late winter total standard errors are almost the same for all three products while during summer the above-mentioned differences apply. Standard deviations are small (around 0.5%) during winter and increase to between 1 and 2% during summer.

Summary

In this section we give a short summary of the multi-annual monthly average algorithm and total standard errors in tabulated form. In total we have four tables: two for the Northern Hemisphere and two for the Southern Hemisphere showing the results of the water grid cells (< 15% sea-ice concentration) and the ice grid cells (> 90% sea-ice concentration).

Table 3-33: Summary of the standard errors over water for the Northern Hemisphere.

Northern Hemisphere	Resolution	Algorithm standard error [%]	Total standard error [%]
Winter (Nov.-Apr.)	50 km	1.8	16.0
	25 km	2.5	10.5
	12.5 km	3.4	8.0
Summer (June-Aug.)	50 km	1.4	18.0
	25 km	2.5	13.0
	12.5 km	4.2	10.5

Table 3-34: Summary of the standard errors over ice for the Northern Hemisphere.

Northern Hemisphere	Resolution	Algorithm standard error [%]	Total standard error [%]
Winter (Nov.-Apr.)	50 km	1.7	4.5
	25 km	2.5	5.0
	12.5 km	4.1	5.8
Summer (June-Aug.)	50 km	3.6	7.8
	25 km	3.6	6.7
	12.5 km	4.5	6.3

Table 3-35: Summary of the standard errors over water for the Southern Hemisphere.

Southern Hemisphere	Resolution	Algorithm standard error [%]	Total standard error [%]
Winter (May-Oct.)	50 km	1.7	5.7
	25 km	2.3	4.5
	12.5 km	3.1	4.2
Summer (Dec.-Feb.)	50 km	1.5	6.7
	25 km	2.0	4.8
	12.5 km	3.4	4.7

Table 3-36: Table 3.7.3.4 Summary of the standard errors over ice for the Southern Hemisphere.

Southern Hemisphere	Resolution	Algorithm standard error [%]	Total standard error [%]
Winter (May-Oct.)	50 km	2.0	6.5
	25 km	2.7	6.2
	12.5 km	4.0	6.0
Summer (Dec.-Feb.)	50 km	5.5	14.2
	25 km	5.0	12.0
	12.5 km	7.5	12.0

3.7.4   Are the SIC uncertainties a proper measure for the SIC error?

Let's sum up the main results of sections 3.2.1 and 3.7.1 as well as of 3.2.2 and 3.7.2; for the latter we take all data into account and to not filter for the 2m air temperature.

SICCI-VLF (the 50 km product) reveals an absolute SIC error of ≤ 0.5% over open water in both hemispheres. The precision, expressed as 1 standard deviation, is ~1.0% for summer and ~1.4% for winter. The mean SIC retrieval uncertainty at SIC=0% is ~1.4% for summer and > 1.5% for winter; these values increase by ~0.2% when taking the smearing error into account. Over pack ice, SICCI-VLF exhibits a mean SIC error of ~-0.6%. The mean SIC precision at SIC=100% is 2.1% in the Northern and 2.4% in the Southern Hemisphere. The mean SIC retrieval uncertainty at SIC=100% is 1.7% in the Northern and 2.1% in the Southern Hemisphere; these values increase by 0.5% and 0.9%, respectively, when taking the smearing error into account.

Conclusion: On average, SICCI-VLF SIC retrieval uncertainties exceed the SIC standard deviation over open water but not over pack ice; however, when using the total uncertainty, i.e. including possible smearing contributions, then SIC standard deviations are within the SIC uncertainty range.

SICCI-LF (the 25 km product) reveals an absolute SIC error of ≤ 0.3% over open water in both hemispheres. The precision, expressed as 1 standard deviation, is between 1.2% and 1.6% during summer and between 1.4% and 1.8% during winter. The mean SIC retrieval uncertainty at SIC=0% is > 1.8% for summer and > 2.2% for winter; these values increase by ~0.2% when taking the smearing error into account. Over pack ice, SICCI-VLF exhibits a mean SIC error of -1.4% and -2.2% in the Southern and Northern Hemisphere, respectively. The mean SIC precision at SIC=100% is 3.7% in the Northern and 4.0% in the Southern Hemisphere. The mean SIC retrieval uncertainty at SIC=100% is 2.4% in the Northern and 2.8% in the Southern Hemisphere; these values increase by 0.8% and 0.9%, respectively, when taking the smearing error into account.

Conclusion: On average, SICCI-LF SIC retrieval uncertainties exceed the SIC standard deviation over open water. However, over pack ice, neither the retrieval nor the total SIC uncertainty exceed the SIC standard deviations.

SICCI-HF (the 12.5 km product) reveals an absolute SIC error of ≤ 0.4% over open water in both hemispheres. The precision, expressed as 1 standard deviation, is ~2.7% in the Northern and ~1.9% in the Southern Hemisphere. The mean SIC retrieval uncertainty at SIC=0% is > 3.5% in the Northern and > 3.0% in the Southern Hemisphere; these values increase by ~0.1% when taking the smearing error into account. Over pack ice, SICCI-VLF exhibits a mean SIC error of -0.7% and -4.2% in the Southern and Northern Hemisphere, respectively. The mean SIC precision at SIC=100% is 5.9% in the Northern and 4.0% in the Southern Hemisphere. The mean SIC retrieval uncertainty at SIC=100% is 4.1%; this value increases by ~0.4%, when taking the smearing error into account.

Conclusion: On average, SICCI-HF SIC retrieval uncertainties exceed the SIC standard deviation over open water. Over pack ice, Northern Hemisphere, neither the retrieval nor the total SIC uncertainty exceed the

ESA UNCLASSIFIED - For Official Use

SIC standard deviations. Over pack ice, Southern Hemisphere, however, the SIC retrieval uncertainty at SIC=100% exceeds the SIC standard deviation.

We note that the results of the total standard error over open water as shown in this report might be biased due to land-spillover effects which were not properly elimitated prior to this investigation. The way we carried out the masking of the land-spillover affected regions did not entirely remove all grid cells along the coast lines for which grid cells with spurious SIC have been set to SIC = 0% but for which the respective total standard error is high and not masked out (and cannot also not be masked out without also discarding a larger number of valid data). Hence, even though SIC is 0% the total standard error is high … and contributes particularly during summer melt as then more land-spillover affected grid cells contribute to the estimate of the average monthly total standard error for open water grid cells.

3.8   Correlation length analysis for SIC and SIC errors

Sea-ice concentration fields, their errors, and their uncertainties can exhibit substantial correlation over space and time. This is of relevance for assimilation experiments.

In this section we will therefore, as a novel part of the SICCI sea ice concentration evaluation, present results of first investigations of the correlation length scales observed for the three SICCI 2 sea-ice concentration products and their uncertainties derived for different temporal scales.

The goal is to illustrate the spatial correlation of the SICCI-2 SIC values themselves, about the SICCI-2 SIC error (*) as well as SIC retrieval standard error, smearing error, and total standard error, or in other words, to get a feeling about the correlation length scales.

(*) In order to have a measure of the SICCI-2 SIC error we carry out the investigation not just for the SIC itself but also for the difference SIC – 0% for -15% … SIC … +15% as the potential error over open water and for the difference SIC – 100% for 85% … SIC … 115% as the potential error over 100% sea ice.

For this purpose we read daily SICCI-2 data of all full annual cycles of SIC development. For the Northern Hemisphere one annual cycle begins October 1 and ends September 30 while for the Southern Hemisphere one annual cycle begins March 1 and ends February 28. We omit February 29. For the Northern Hemisphere we have 13, for the Southern Hemisphere 12 full annual cycles. We take into account data from v2.0 and v2.1 of the SICCI-2 product; hence the last cycle is 2015/2016 for the Northern and 2016/2017 for the Southern Hemisphere.

The stacks over time of the two-dimensional daily data fields are reduced in two steps into a set of vectors containing the time series of the SIC (or errors) at the respective valid grid cell to ease computation. Grid cells are termed valid if i) they are not flagged as land in the flag layer provided with the data, and if ii) the sum of the SIC values over the entire time-series is different from zero.

SIC values are further filtered using the flag layer such that inland waters, grid cells with additional filtering for contamination of the brightness temperatures by land influence, and grid cells filtered out due to too high air temperatures are set to "nan". SIC error values are treated with the same filter; in addition missing values caused by missing swaths are set to "nan". Also grid cells with a SIC < -20% or a SIC > 120% are set to "nan".

The following correlation analysis is then applied to i) the entire time series, i.e. 13 or 12 years of SIC, SIC error (see (*) above), and SIC standard error data and to ii) the multi-annual daily mean of the SIC, SIC error, and SIC standard error data. For ii) the mean SIC, mean SIC error, and mean SIC standard error values are computed from all valid data at the respective grid cell for every day. For the multi-annual daily mean 5 years of data are required. In addition, for ii) also a limitation to the winter period is made, which means that only the months December through April or the months May through October are used for the Northern and Southern Hemisphere, respectively.

The correlation analysis is carried out as follows. For each valid grid cell a search area with radius 1000 km is extracted from the data. Different radii were tested (500 km, 1600 km, 2000 km) but not found to provide more meaningful results. Each SIC, SIC error (see (*) above), and SIC standard error time series within that search area is correlated with the SIC, SIC error, and SIC standard error time series of the center grid cell of the search area. Both the linear correlation coefficient as well as the covariance is computed. Computation is only carried out if at least one quarter of the circular search area contains valid, i.e. non-"nan" SIC values. Each pair of SIC, SIC error, and SIC standard error time series, i.e. the center grid cell time series and the time series within the search area for which the correlation / covariance is computed, needs to have valid values for at least 25% of the length of the time series; this criterion is relaxed when computing correlations for the winter periods when only 10% of the time series needs to have valid data. Otherwise the correlation value is set to "nan" at the respective non-center grid cell. Covariance and correlation values are kept for each search area. Note that the restriction to 25% or 10% of the entire time series causes artifacts in the marginal ice zone in some of the results.

For each search area we compute the mean correlation and the mean covariance (and the corresponding standard deviation) and also take the maximum value of correlation and covariance to illustrate the spatial distribution – separately for SIC, the SIC error (see (*) above) and the three SIC standard error variables. The center grid cell of the search area is excluded here as the correlation is obviously 1.

In order to compute the correlation length scale we evaluate the distribution of the correlation values within each search area. We compute spatial correlation scales for correlation thresholds of 0.99, 0.95, 0.9 and 0.7. For this we first compute the mean correlation of rings around the search area center. The width of the rings is given by the grid resolution of the product; it is hence either 50 km or 25 km for SICCI-VLF and SICCI-LF, respectively. Subsequently, we find out up to which distance from the search area center the correlation stays above each of the thresholds given. For this we find all rings where the mean (of the respective ring) correlation falls below the threshold and compute their minimum distance: R_{below} to the search area center. In addition we find all rings where the mean correlation is higher than the threshold and compute their maximum distance: R_{above}. If there are no valid values for both, the correlation length is considered to be zero. If there is no valid value for R_{above}, and R_{below} is the distance of the ring right next to the search area center, the correlation length is set to half the grid resolution. If both R_{above} and R_{below} have valid values, the correlation length is set to MIN(R_{below};R_{above}) plus half the grid resolution. Finally, if there is no valid value for R_{below}, which basically means that the correlation is above the threshold for the entire search area, but R_{below} is close to the search radius, the correlation length is set to the search area radius. This occurs frequently for the threshold 0.7 in combination with the multi-annual mean daily data.

Note that cases exist, where for the search area centered at one grid cell the correlation is first above the threshold, then drops below it, and then again increases to above the threshold until the end of the search area, while for the neighboring search area the correlation stays above the threshold for the entire search area. In these cases we observe artificial jumps in the correlation length between relatively small values and values close to 1000 km, the search area radius.
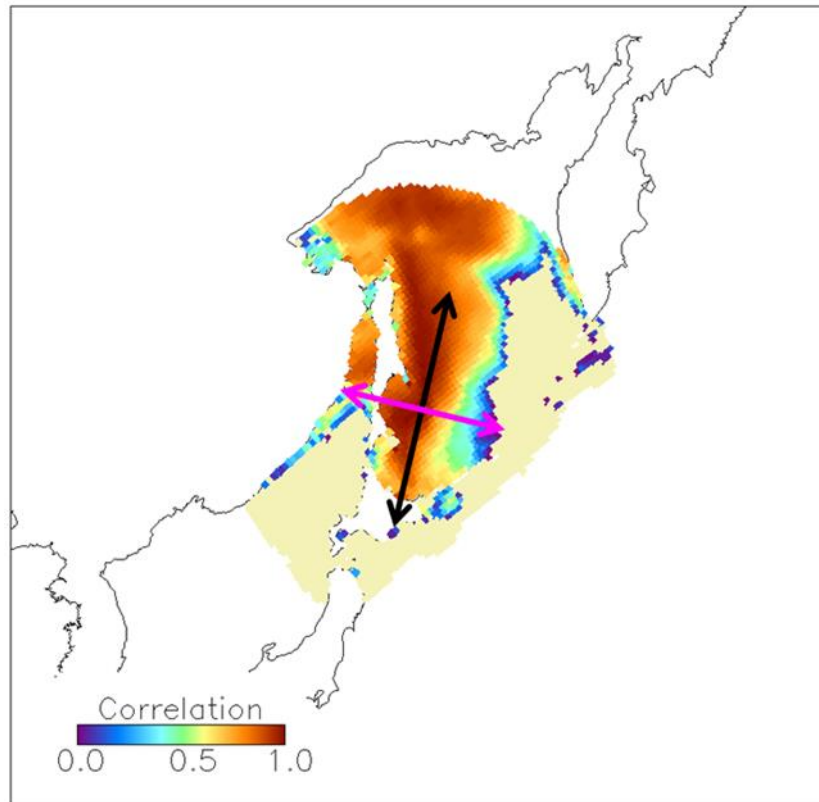
Figure 3-141: Illustration of a search area in the Sea of Ohkotsk. Shown is the correlation of the SICCI-LF (25 km) sea-ice concentration. Along the black double arrow the gradient in the correlation is relatively small and the correlation stays at or close to 0.9 for quite a distance. In contrast, along the magenta double arrow the correlation decreases quickly towards the East where the sea-ice concentration decreases as well.

Note further that usage of a circular search area and of a circular distance computation scheme is less suitable for regions of the sea-ice cover where correlations do not have circularly varying gradients, as for instance in the marginal ice zone. In these regions, the correlation length obtained might overestimate its actual value into the direction parallel to the strongest gradient while it might underestimate its actual value into the direction parallel to the weakest gradient. This is illustrated in Figure 3-141.

Northern Hemisphere

Figure 3-142 a) and b) show two examples close to Denmark Strait. In image a) the center grid cell is located close to the coast in an area of substantial sea-ice coverage. In image b) the center grid cells located just outside the sea-ice covered area and/or in the marginal ice zone with large SIC variability. The correlation shown in image a) is large, i.e. > 0.9, in all grid cells with a SIC having a similar 13-year average daily seasonal cycle than in the center grid cell. Obviously these grid cells align along the coast and kind of represent the expected average sea-ice coverage. In contrast, the area of high correlation in image b) is rather small and almost concentric around the center grid cell. This indicates small correspondence between the seasonal cycle off the SIC at this location with the surrounding

grid cells – presumably due to large intra-annual variation of the SIC around this location.
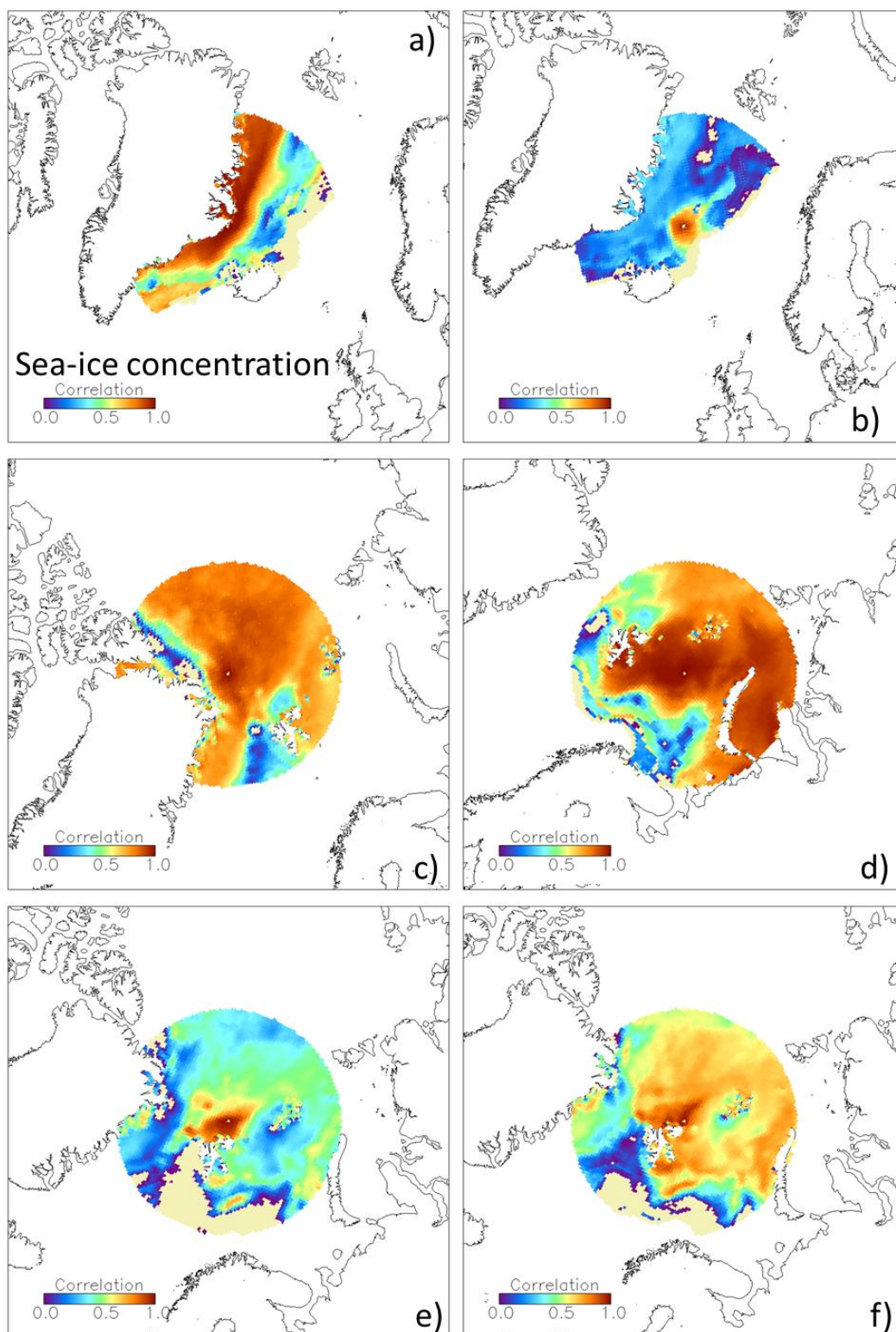
Figure 3-142: Correlation of multi-annual mean daily SICCI-LF (25 km) SIC of one seasonal cycle for six different locations in the Northern Hemisphere. Pale yellow grid cells off the dark blue indicate either that no correlation could be computed or negative correlation values.
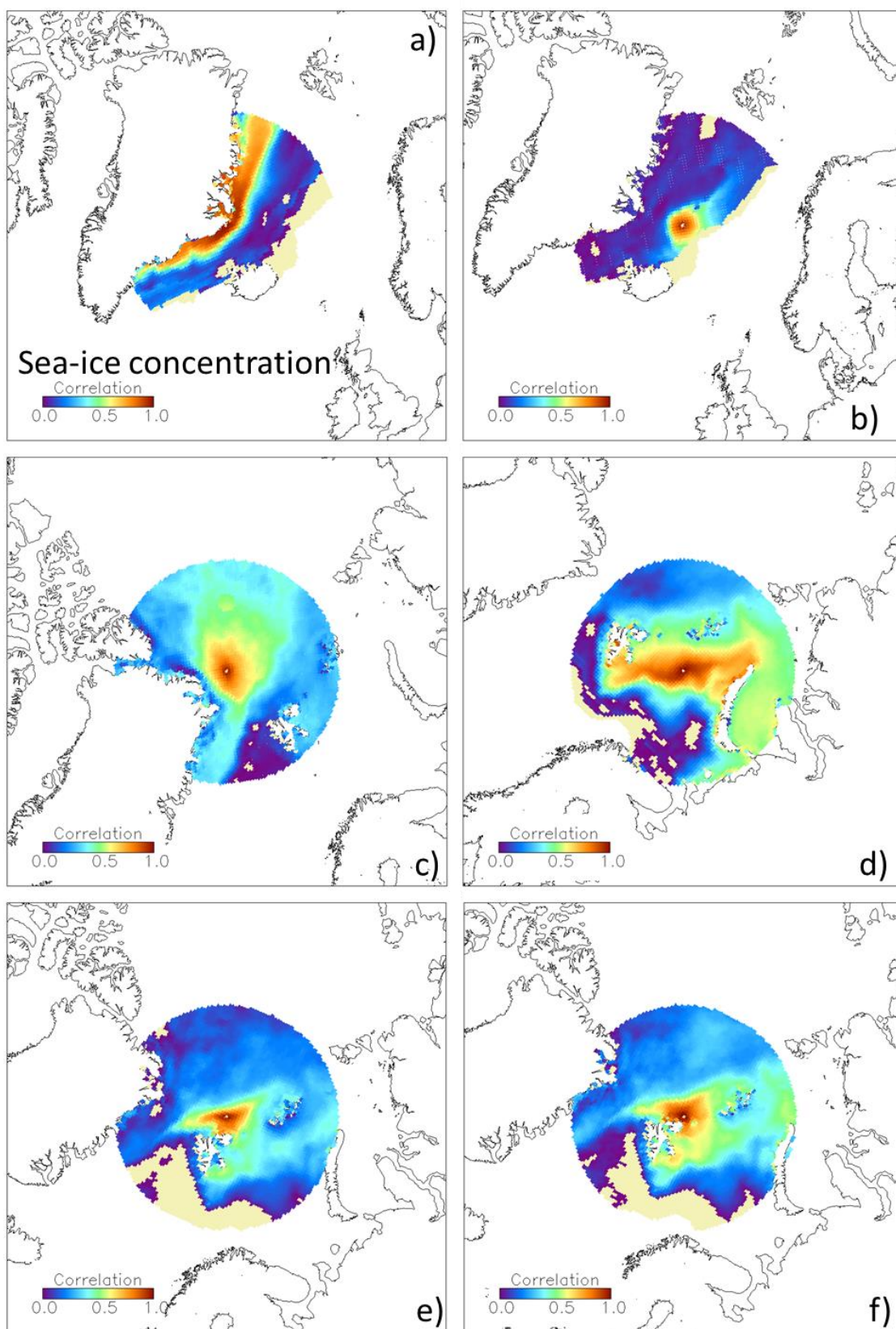
Figure 3-143: As Figure 3-142 but using the time series of daily SIC data of all 13 seasonal cycles.

Figure 3-142 c) is located north of Greenland, an area supposed to be sea-ice covered year round. This seems not to result into a too high correlation of the center grid cell SIC with the surrounding SIC values. Only the directly adjacent grid cells have a correlation close to 1; most of the remaining year-round SIC covered grid cells show correlations between 0.8 and 0.9. One reason for this is the lacking seasonal cycle (compare Figure 3-142 c)). Another reason for this is (presumably) the fact that variations in the surface properties (snow) which induce local sea-ice concentration variations have a comparably large impact on the seasonal cycle of the SIC. This seems to apply particularly for the grid cells adjacent to the Greenland coast and towards the Lincoln Sea – i.e. an area of 100% multiyear ice – where correlations drop below 0.5 or even become negative.

Figure 3-142 d) is an example from the northern Barents Sea, an area with substantial intra- and inter-annual variation in SIC. The correlation with the surrounding grid cells is quite high and seems to be > 0.8 for most of the regularly sea-ice covered area and even higher for the nearby grid cells having a more similar intra- and inter-annual variation in SIC. Areas with correlations < 0.5 are obviously open water.

Figure 3-142 e) and f) located north of Svalbard again illustrate how different the correlation pattern can be in the marginal ice zone. While the location in image e) seems to be located in a very variable area with only as small extent of high correlations (comparable to image b), the location in image f) seems to be located in a more stable region. While the pattern of higher correlation values looks similar to image e) the correlation across the search area is less variable and on average also higher than in image e).

In Figure 3-143 we repeat the same regions as shown in Figure 3-142 but this time the correlation is based on 13 years of daily data, i.e. instead of on one full seasonal cycle of 365 days it is based on 13 full seasonal cycles. We find that the main patterns observed in Figure 3-142 are repeated in Figure 3-143. This applies in particular to images a) and b). In Figure 3-143 c) high correlations are only observed for a relatively small patch. Over the majority of the search area the correlation is < 0.6 – which contrasts Figure 3-142 c) where the correlation was > 0.8 of most of the search area. In Figure 3-143 d) the area of high correlation is confined to a band extending West-East through the Barents Sea with smaller correlations (< 0.5) to the South but also to the North. Finally, Figure 3-143 e) and f) indicate that the sea-ice conditions represented by the respective center grid cells are correlated with values > 0.8 only within a 50-100 km radius. Correlations outside that neighborhood dropped substantially compared to Figure 3-142 e) and f) and are particularly small with the sea ice north of the Fram Strait towards the west.

After we have shown the examples of six different regions we now pick one region, the one of image d), to also show examples of the correlations over the search area for the retrieval standard error, the smearing error and the total standard error.
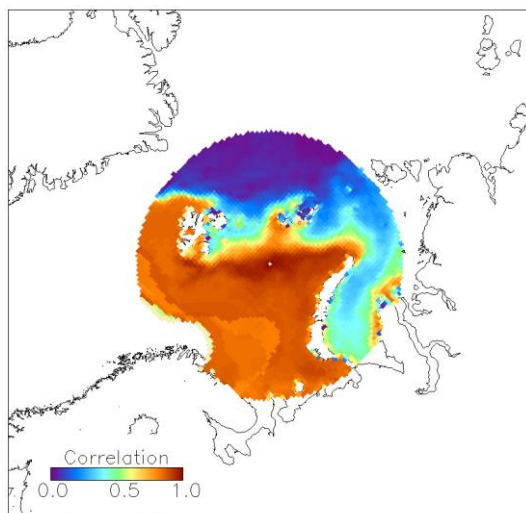
Figure 3-144: Correlation of multi-annual mean daily SICCI-LF (25 km) SIC of one seasonal cycle for the Barents Sea region (image d) in Figure 3-142 and Figure 3-143) in the Northern Hemisphere. Pale yellow grid cells off the dark blue indicate either that no correlation could be computed or negative correlation values.

Figure 3-144 exemplifies in correspondence to Figure 3-142 d) the correlation of the SICCI-LF SIC retrieval error. The retrieval error basically roots in the tie points uncertainties, sensor noise and residual noise after the correction for atmospheric influence. The main factor impacting the retrieval error is the presence of either sea ice or water and high correlations should be expected for purely sea-ice covered and pure open water grid cells. For the time period considered in the multi-annual daily mean, the center of the search area is highly correlated within a relatively large region stretching West-East between the pack ice of the Arctic Ocean north and the open water of the Norwegian Sea south, i.e. the marginal ice zone. Correlations are much lower to the pack ice region than to the open water region.
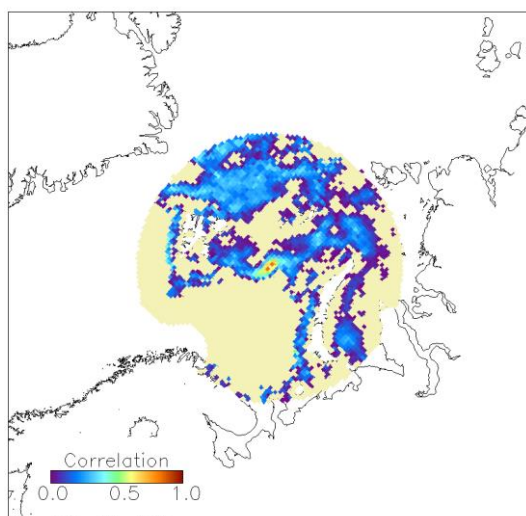
Figure 3-145: As Figure 3-144 but showing the correlation for the SIC smearing error.

Figure 3-145 exemplifying the correlation of the smearing error for the same search area as used in Figure 3-144 does not allow too many conclusions. The correlation is generally low or negative or cannot be computed and only a very small region close to the search area center exhibits elevated correlation values.
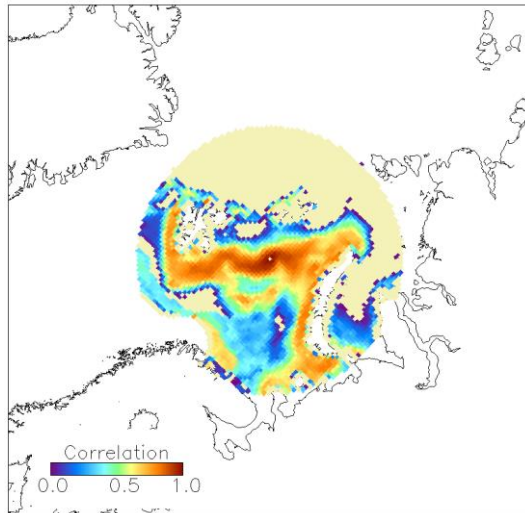
Figure 3-146: As Figure 3-144 but showing the correlation for the SICCI-LF SIC total standard error.

The correlation of the SIC total standard error exemplified in Figure 3-146 is large (~ 0.9) close to the search area center and elevated (> ~0.7) along bands marking the location of the marginal ice zone. Correlations are absent (or negative) for the pack ice area and parts of the open water area of the Norwegian Sea.

Now, what is the effect of the limitations to winter? And how does the correlation of such a search area look like for the SIC error i.e. SIC – 0% and SIC – 100% for SIC ranges -15% … +15% and 85% … 115%, respectively? We illustrate this for images a) and b) of Figure 3-142 in the following Figure 3-147 through Figure 3-149.
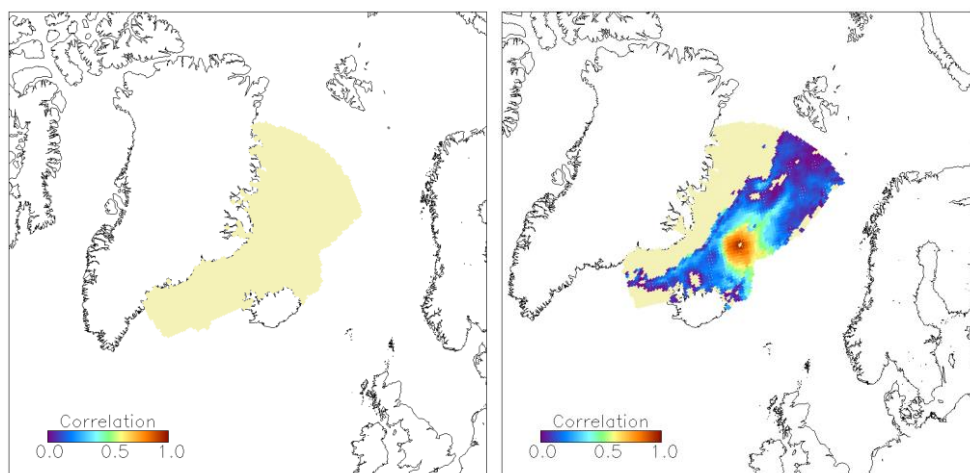
Figure 3-147: Correlation of the SIC error for open water, i.e. SIC − 0% of the range -15% … SIC … 15% for Figure 3-142 a) (left) and b) (right) for winter months using the multi-annual mean daily seasonal cycle of SICCI-LF SIC. In the left image the search area center is located over sea ice; in the right image it is located over open water.

For the search area shown in Figure 3-142 a) no correlation can be computed when restricting the analysis to i) winter months and ii) to the SIC range of -15% to 15% (Figure 3-147, left). For the search area shown in Figure 3-142 b) we find a very localized and also quite high correlation around the search area center (Figure 3-147, right).
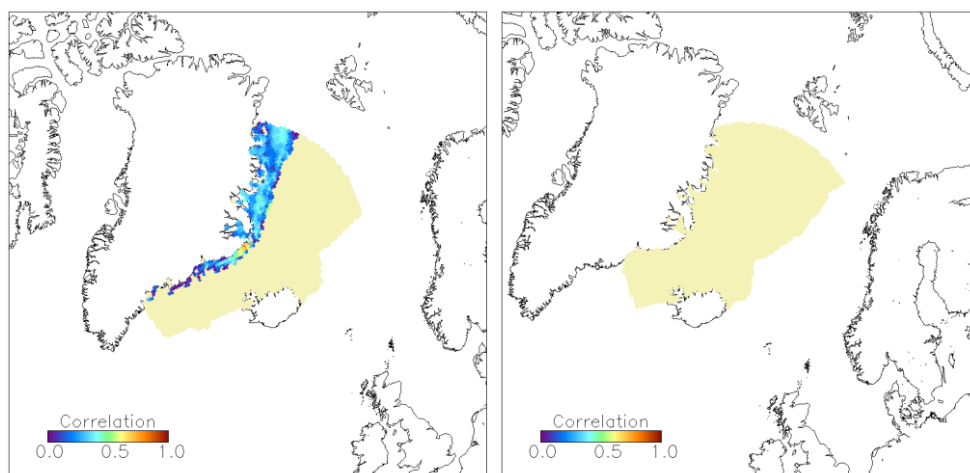
Figure 3-148: As Figure 3-147 but for the SIC error over 100% sea ice, i.e. SIC − 100% of the range 85% … SIC … 115%.

Figure 3-148 exemplifies the pendant to Figure 3-147. Now, the search area over open water exhibits no valid correlation values (Figure 3-148 right) while the search area centered over sea ice shows an region with elevated correlation values hugging the East coast of Greenland (Figure 3-148 left). Correlations are – at least in this case – much lower than for the open water case shown in the previous figure. That correlations of the SIC error can reach similar high values over sea ice than over open water is illustrated in Figure 3-149 showing the region of image c) of Figure 3-142. We find a relatively isolated region of high correlation around the center of the search area. Similarly to Figure 3-147, right, the correlation drops off quickly.
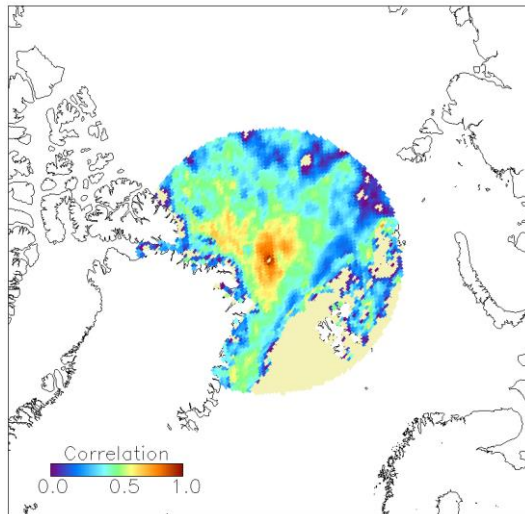
Figure 3-149: As Figure 3-148 but for the search area of image c) in Figure 3-142.

We have investigated this drop-off of the correlation values with increasing distance from the center of the search area and illustrate the results in the following figures.

ESA UNCLASSIFIED - For Official Use
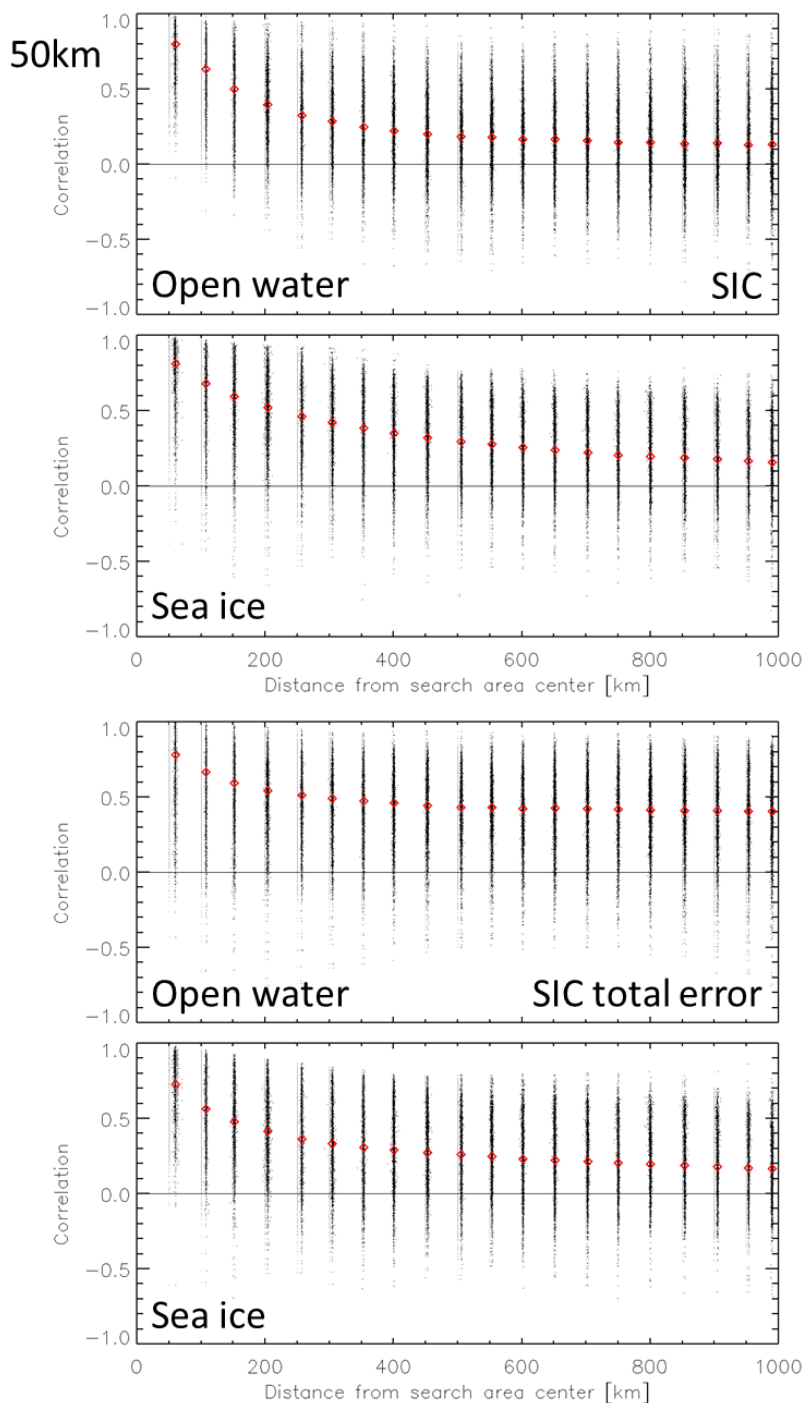
Figure 3-150: Mean correlation values computed for each distance ring around the search area center for all valid multi-annual mean daily seasonal cycle winter-time SIC error and SIC total standard error correlation values obtained using the SICCI-VLF (50.0 km) product of the Northern Hemisphere. Black dots denote individual mean correlation values while red diamonds give the average correlation of all search areas.
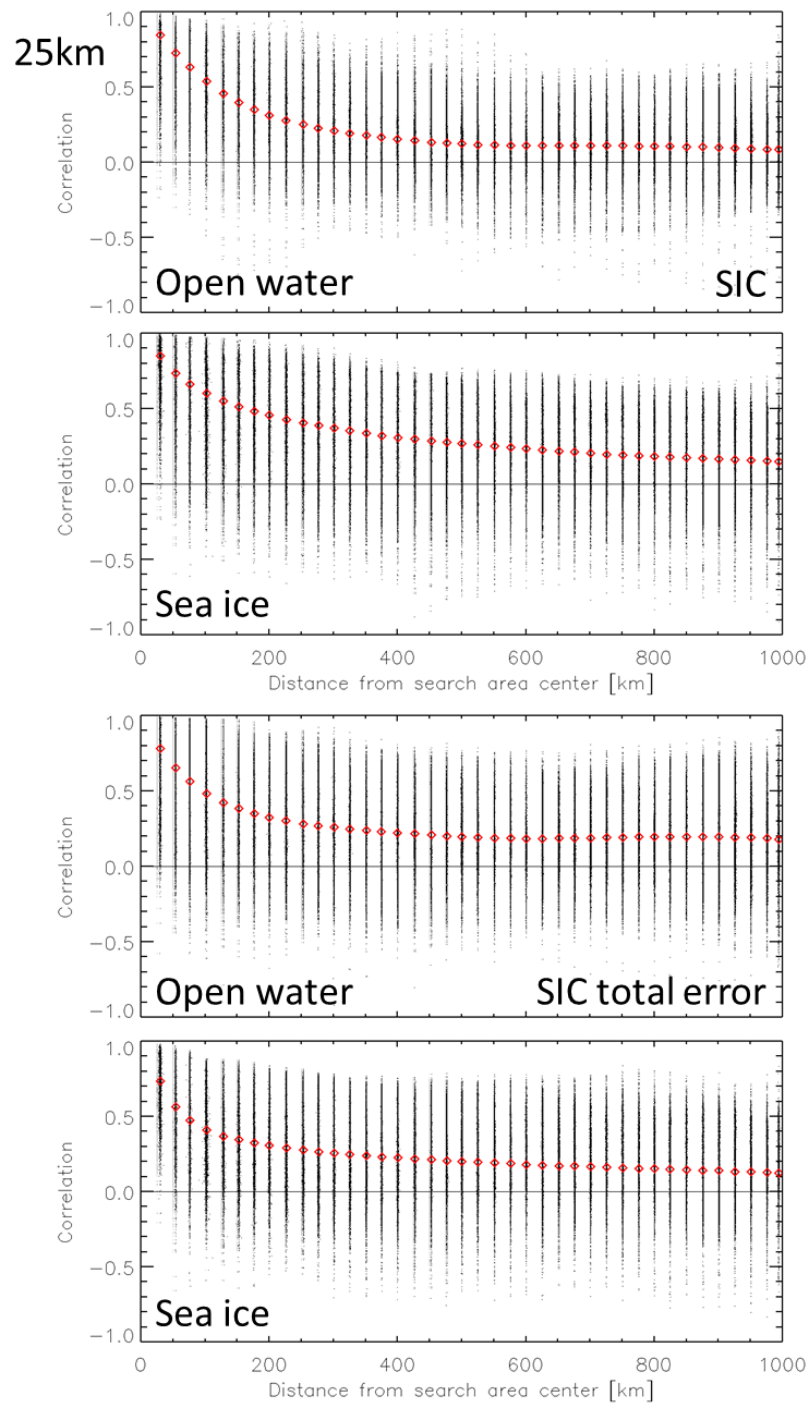
Figure 3-151: As Figure 3-150 but using SICCI-LF (25.0 km).

On average, correlations drop off faster, i.e. within a shorter distance to the search area center for SICCI-LF (25 km) than for SICCI-VLF (50 km). This applies to both the SIC error (top two images in Figure 3-150 and Figure 3-151) and the SIC total standard error (bottom two images in Figure 3-150 and Figure 3-151). The SIC error is correlated over larger distances over sea ice than over open water. Over water, correlations fall below 0.5 at ~150 km and ~120 km distance from the search area center for SICCI-VLF and SICCI-LF, respectively. Over sea ice, corresponding correlations fall

below 0.5 at ~200 km and ~170 km distance from the search area center. The SIC total standard error is correlated over larger distances over open water than over sea ice. Over water, correlations fall below 0.5 at ~320 km and ~100 km distance from the search area center for SICCI-VLF and SICCI-LF, respectively. Over sea ice, corresponding correlations fall below 0.5 at ~140 km and ~70 km distance from the search area center.

The correlation of the average SICCI-VLF SIC total standard error values stays quite high at around 0.4 over the entire remaining search area while in all other cases the correlations drop below or at least reach 0.2 towards the margin of the search area, i.e. in ~ 1000 km distance to the search area center.

We note that not constraining this analysis to the winter-time does not change the results shown in Figure 3-150 and Figure 3-151 notably.
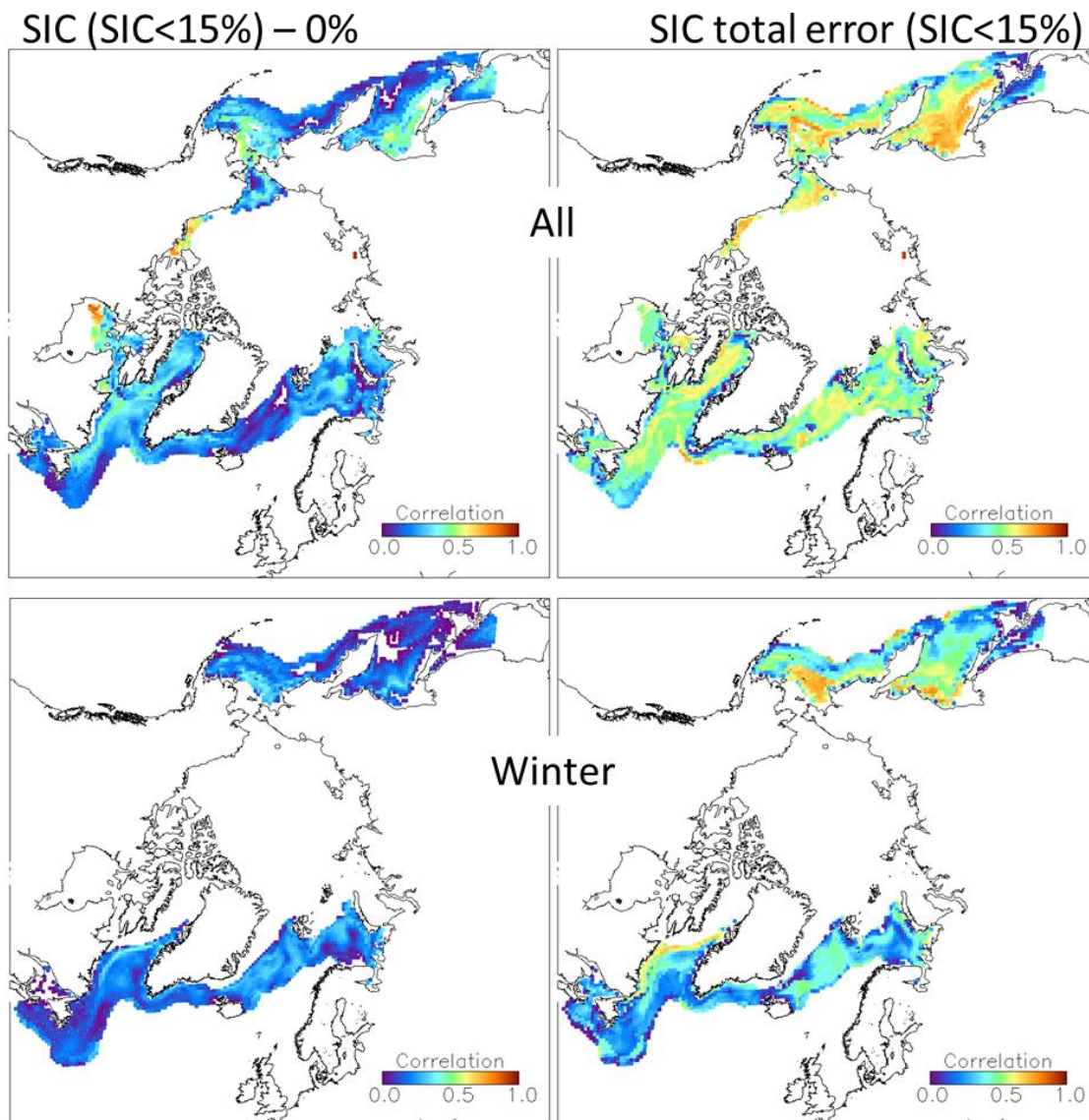
Figure 3-152: Correlation of the SIC error over open water, i.e. SIC – 0% computed for the range -15% … SIC … 15%, for all (top) and winter-time (bottom) valid multi-annual mean daily seasonal cycle values obtained using the SICCI-LF (25.0 km) product of the Northern Hemisphere.

ESA UNCLASSIFIED - For Official Use
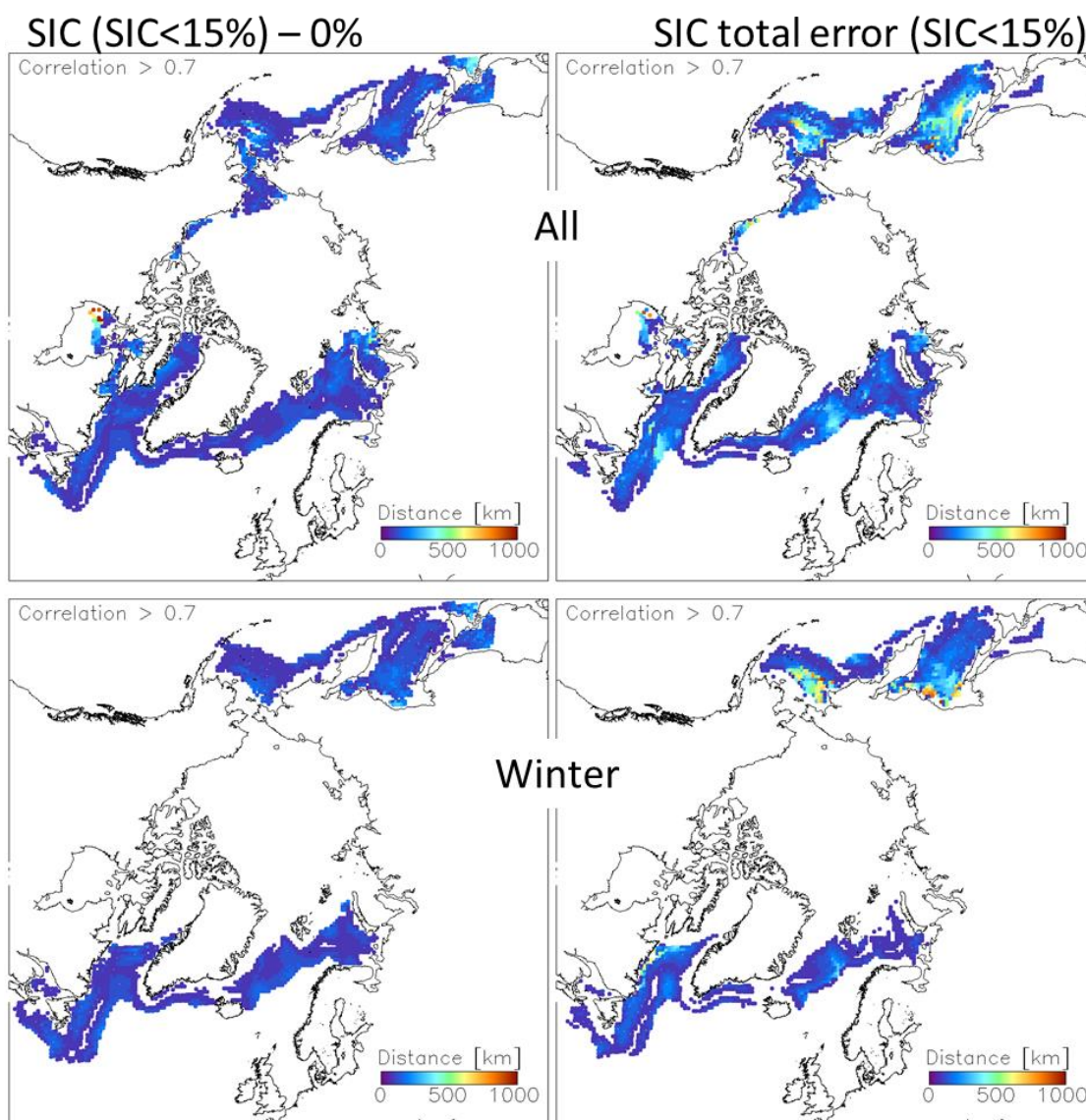
Figure 3-153: Correlation length = Distance from the search area center at which the correlations shown in Figure 3-152 fall below 0.7.

In Figure 3-152 and Figure 3-153 we show the spatial distribution of the correlation of the SIC error over open water and of the respective SIC total standard error and the distribution of the correlation length scale – here the distance from the search area center beyond which the correlation is below 0.7 – using all and only the winter-time multi-annual mean daily seasonal cycle SICCI-LF product. These maps illustrate that the little sea ice in the marginal ice zone (SIC < 15%) seem to dominate the correlation in regions such as the Sea of Okthosk, Bering Sea and Labrador Sea. The best area to take meaningful, i.e. least influenced by sea ice, information about the correlation over open water seems to be the eastern Greenland Sea as well as the southern Barents Sea. The maps of the correlation length scale (Figure 3-153) confirm the view given in Figure 3-151.
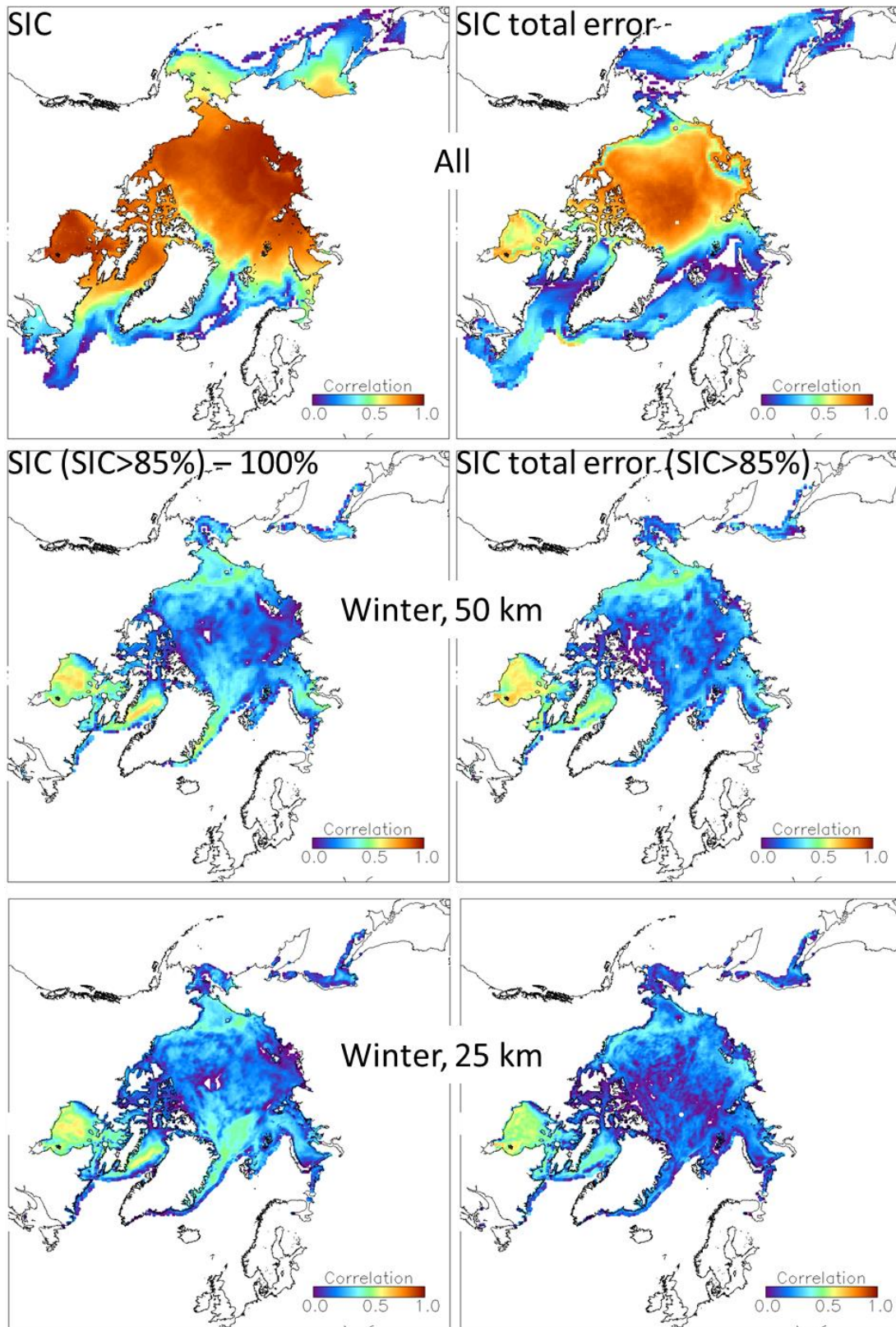
Figure 3-154: Correlation of SIC and SIC total standard error without any constraints (top), and of the SIC error over sea ice, i.e. SIC − 100% computed for the range 85% … SIC … 115%, for winter-time valid multi-annual mean daily seasonal cycle values obtained using SICCI-VLF (50 km, middle) and SICCI-LF (25 km, bottom) SIC of the Northern Hemisphere.
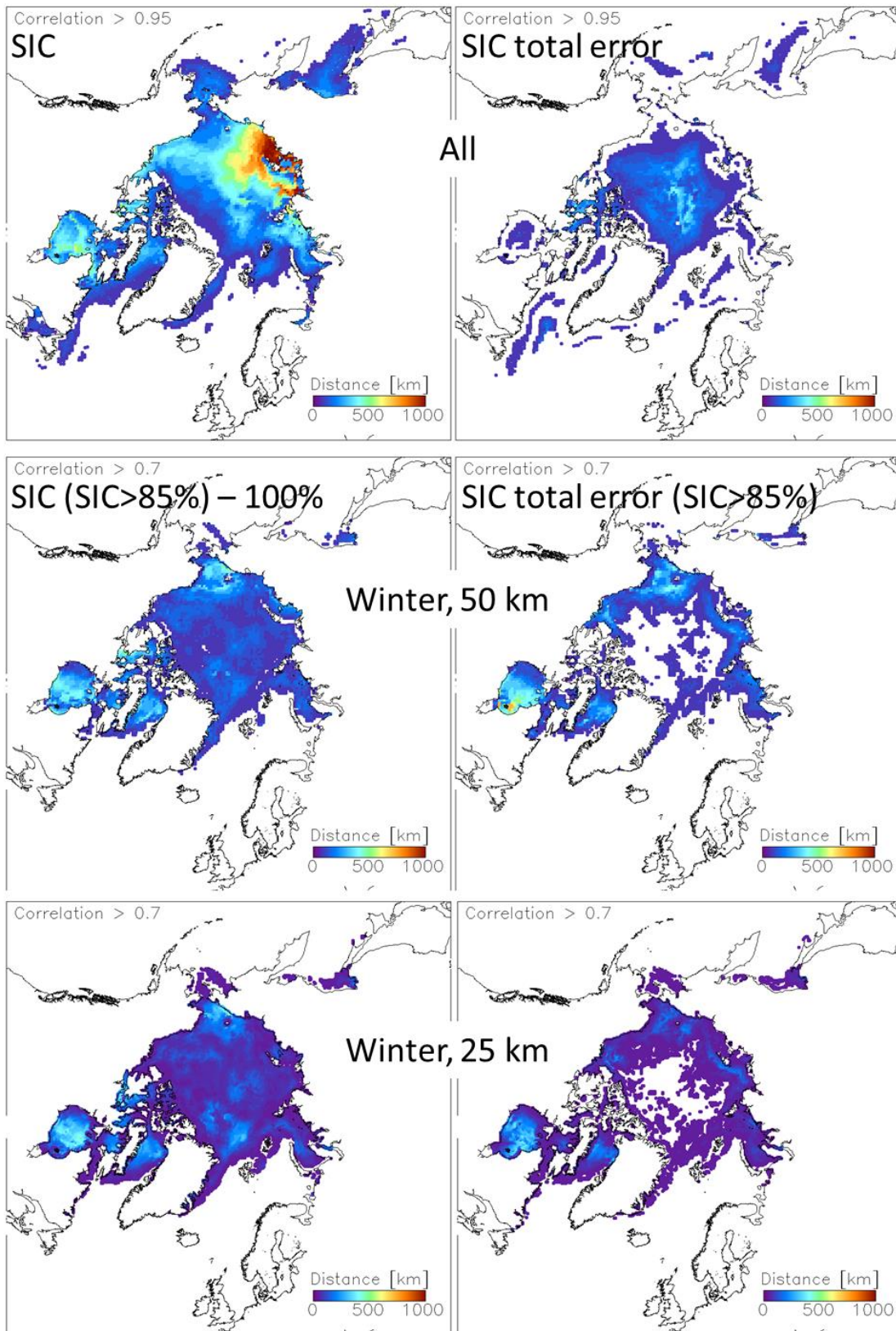
Figure 3-155: Correlation length = Distance from the search area center at which the correlations shown in Figure 3-154 fall below 0.95 (top) or below 0.7 (middle and bottom).

We find especially high correlations where the seasonal cycle is highly stable or, in other words, where the single seasonal cycles are very well represented by the multi-annual daily mean seasonal cycle. Such areas of high correlations we find in the Laptev and East Siberian Seas and the areas north of these, in the eastern Kara Sea, in parts of the Beaufort Sea and in the Hudson Bay (Figure 3-154, top left).

We find lower correlations in regions where the seasonal cycle has a lot of interannual variation, for instance due to i) a variable open water fraction thanks to variable melt and refreeze onset, or due to ii) variable snow and sea-ice surface properties thanks to weather-effect induced snow or ice-snow interface metamorphism. Regions subject to i) are, e.g. the western Kara Sea, and all peripheral seas, such as the Bering Sea. The main region subject to ii) is located north of Greenland and the Canadian Arctic Archipelago (Figure 3-154, top left).

The correlation of the respective SIC total standard error is highest (~0.9) in the central Arctic Ocean and exhibits a north-south gradient. Outside the Arctic Ocean and in the peripheral seas the correlation of the SIC total standard errors is below 0.5 (Figure 3-154, top right).

It turns out that the distribution of the correlation for SIC (Figure 3-154, top left) results in an East-West gradient in correlation length across the Arctic Ocean when applying a correlation threshold of 0.95. Then we find correlation length of over 500 km in the Laptev and East Siberian Seas which decrease to below 100 km when reaching the Lincoln Sea or Fram and Bering Straits (Figure 3-155, top left). Actually, no correlation lengths can be obtained using this correlation threshold north of Greenland. In accordance with Figure 3-154, top right, we find highest correlation lengths in the central Arctic Ocean, actually close to the pole, which decrease towards the south (Figure 3-155, top right); note that we used a similarly high correlation threshold of 0.95 and that the correlation lengths would be substantially larger if we would have chosen a lower correlation threshold.

This picture changes when constraining the analysis to winter and when using the SIC error over sea ice, i.e. SIC – 100% for the range 85% … SIC … 115%. For SICCI-VLF (50 km), we find that correlations of the SIC error are below 0.5 in most of the Arctic Ocean; only in the Hudson Bay and in the Baffin Bay as well as some smaller regions in the Chukchi Sea, the East Greenland Sea and the western Kara Sea correlations of the SIC error exceed 0.5. We note an area of elevated correlation (~0.4) which extends northward from the Fram Strait (Figure 3-154, middle left). The correlation of the respective SIC total standard error has a surprisingly similar pattern and also surprisingly similar correlation values (Figure 3-154, middle right). One could hypothesize that this is an indication of the SIC total standard error to properly represent to SIC error over sea ice. For SICCI-LF (25 km), we find a distribution of the SIC error correlation which is quite similar to the one of SICCI-VLF. While some regions in the central Arctic Ocean have a slightly higher correlation, some other regions, e.g. Baffin Bay and Chukchi Sea, have slightly lower correlations. The area of elevated correlations north of Fram Strait is more pronounced for SICCI-LF (Figure 3-154, bottom left). The correlation of the respective SIC total standard error (Figure 3-154, bottom right) is less similar to the correlation of the SIC error than observed for SICCI-VLF. Except in the Hudson and Baffin Bays, the highest correlations (~0.4) can be observed where leads and polynyas open most frequently. This seems plausible because these are regions with elevated local SIC variability and hence a notable SIC smearing standard error which in turn drives elevated SIC total standard error values. We note, however,

that the area of elevated SIC error correlation north of Fram Strait is only faintly visible (actually even less than for SICCI-VLF) in the SIC total standard error correlation (compare Figure 3-154 bottom left and right). One could hypothesize that this could be a sign of weather-effect induced snow and ice-snow interface metamorphism causing artificial SIC changes at scales larger than leads and polynyas and hence no notable contribution to the SIC smearing standard error.

We chose a correlation threshold of 0.7 (compare Figure 3-38) and derived the correlation lengths. For the SIC error (Figure 3-155, middle and bottom left), we mostly find correlation lengths < 100 km; exceptions are parts of the Hudson and Baffin Bays, of the Chukchi Sea, and those areas of elevated SIC error correlation extending northward from the Fram Strait. Here correlation lengths get close to 300 km or even more. For the SIC total standard error (Figure 3-155, middle and bottom right), we find even smaller correlation lengths of < 50 km over most of the Arctic Ocean. Exceptions are – again – parts of the Hudson and Baffin Bays, the Chukchi Sea and the already mentioned regions subject to elevated lead and polynya frequency. Here correlation lengths get close to 300 km (SICCI-LF) or 400 km (SICCI-VLF).

Southern Hemisphere

Like for the Northern Hemisphere we start showing examples of the correlation of the SIC for six different search areas using i) the correlation with the multi-annual mean daily seasonal cycle (Figure 3-156) and ii) the correlation with the 12-seasons long time series of the daily SIC (Figure 3-157) (compare Figure 3-142 and Figure 3-143).

The search area in image a) is located between South America and the Antarctic Peninsula in a region of open water. Consequently, high correlations are limited to the immediate surrounding of the search area center in both cases (Figure 3-156 and Figure 3-157, image a)). This example is similar to Figure 3-142 a).

The search area in image b) is located northeast of the Antarctic Peninsula in a region with a considerable seasonal sea-ice cover – in a marginal ice zone. Consequently, at least for the correlation with the multi-annual mean daily seasonal cycle (Figure 3-156 b), correlation values are quite high (> 0.9) and spread over a large area along the marginal ice zone. Correlations are zero or below zero or not retrievable towards the north where open water dominates. In contrast, using the correlation to the entire time series (Figure 3-157 b)), high correlation values are much more isolated and the correlation drops of quite fast. This applies more in direction south-north than in direction west-east. This example is similar to Figure 3-142 b) and also d).

The search area in image c) is located in the central Weddell Sea. We find high correlations (~0.9 or higher) for a substantial part of the search area. Correlations decrease towards the sea-ice edge (compare with Figure 3-156 b) but correlations decrease much more towards the Antarctic Peninsula and even become < 0; a similar trend can be found in the example of image b) as well. The likely explanation for this is that the region hugging the Antarctic Peninsula is an area of multiyear ice with sea-ice present year round while at the search area center the sea ice potentially has melted off completely within the 12 seasonal cycles considered, giving that place a completely different seasonal SIC variability. We find that the gradient between the area of high correlation around the search area center and the Antarctic Peninsula region is steeper when using the multi-annual mean daily seasonal cycle than using the time series (compare Figure 3-156 c) and Figure 3-157 c)). The correlation in Figure 3-157 c) drops off much quicker than in Figure 3-156 c).

If we move further south we end up at image d). This search area exhibits quite small regions with high correlations in both, Figure 3-156 and Figure 3-157. While the area with elevated correlations is more irregularly shaped in Figure 3-156 d) it looks quite concentric in Figure 3-157 d). Albeit this the search area center is possibly located in an area of near 100% SIC year-round its correlation with the seasonal sea ice towards the northeast and the multiyear ice towards the Antarctic Peninsula is quite low, i.e. < 0.5 for most of the search area. One possible reason for this could be that this search area is actually located right at the transition zone between the two ice regimes.
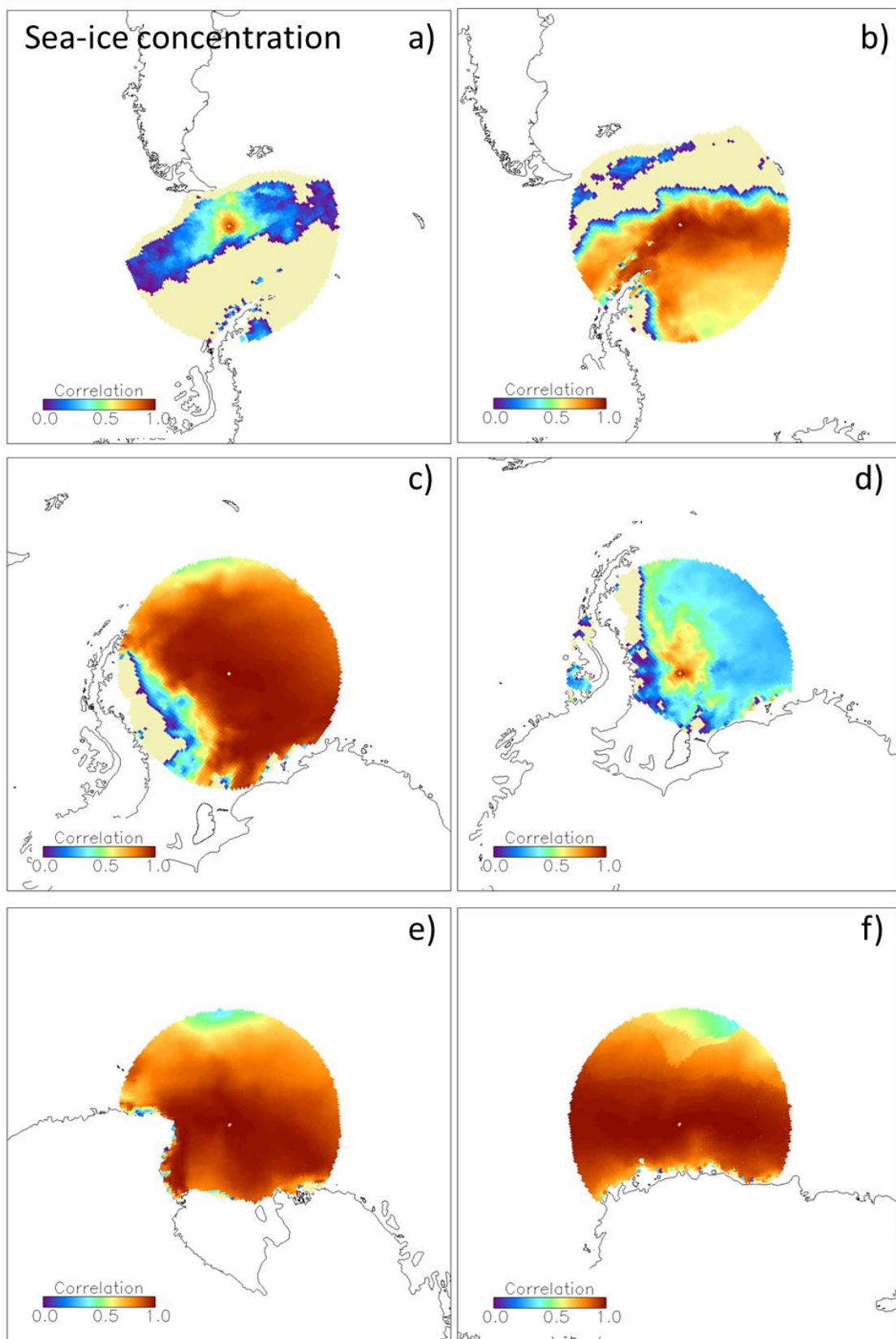
Figure 3-156: Correlation of multi-annual mean daily SICCI-LF (25 km) SIC of one seasonal cycle for six different locations in the Southern Hemisphere. Pale yellow grid cells off the dark blue indicate either that no correlation could be computed or negative correlation values.
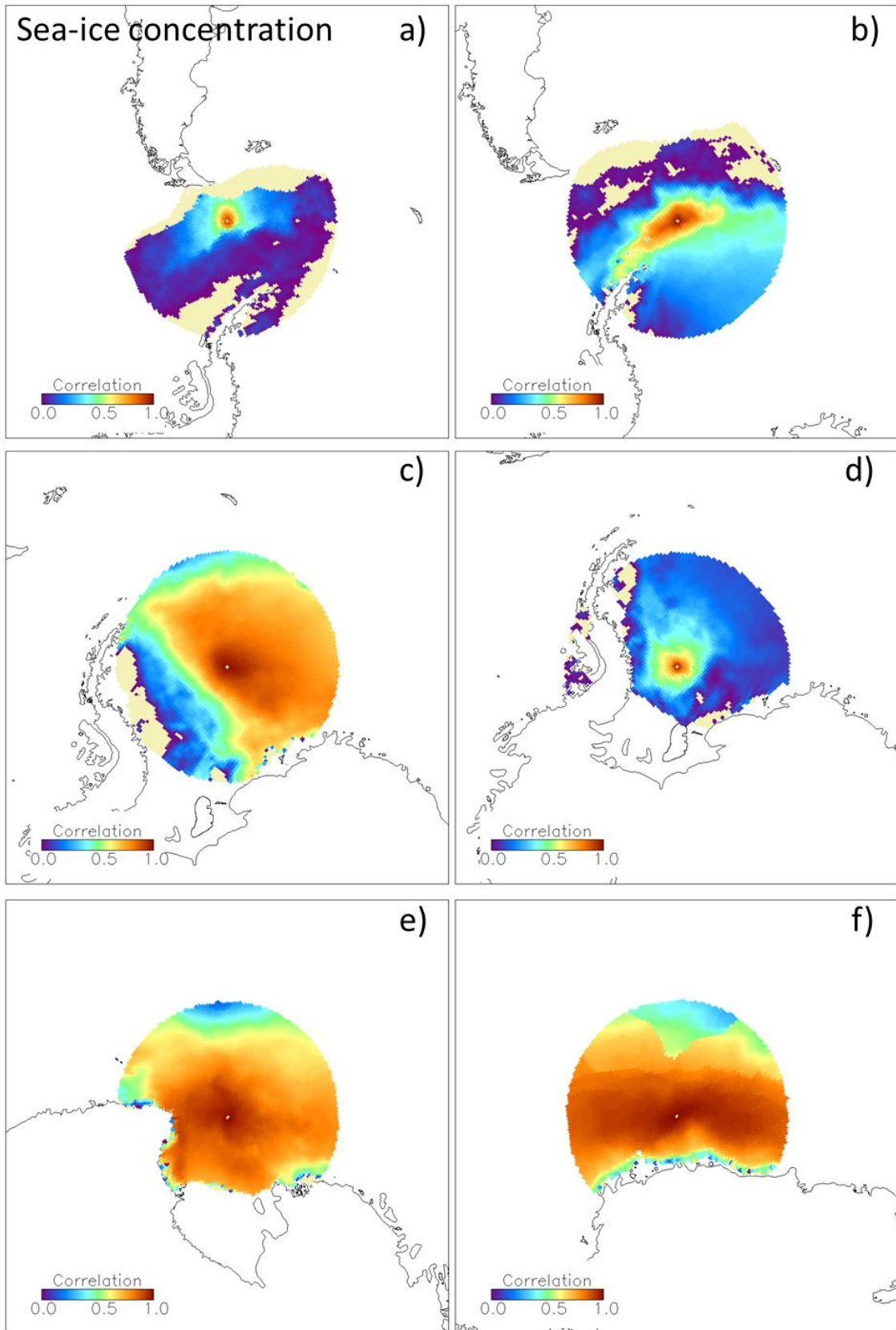
Figure 3-157: As Figure 3-156 but using the time series of daily SIC data of all 13 seasonal cycles.

This last statement is supported by the correlation found for the search area shown in Figure 3-156 f) and Figure 3-157 f) located in the Eastern Weddel Sea north of Neumayer Station. In this purely seasonal sea ice area the correlations are large (> 0.9 or above) for a large area; this area tends to extend west-east in both these figures. Correlations drop towards the coast and towards the marginal ice zone.

A search area of similar characteristics is the one shown in image e) of Figure 3-156 and Figure 3-157 located in the Ross Sea. The only difference to image f) can be seen in Figure 3-157 where the correlation is not only more localized around the search area center but where correlations drop below 0.5 for a relatively large region close the coast to the West – an area also known to host multiyear ice.

We are not going to repeat discussions as related to Figure 3-144 through Figure 3-149 also for the Southern Hemisphere. Instead we move rightaway to the figures showing to decrease of the correlation with distance to the search area center (compare Figure 3-150 and Figure 3-151) in Figure 3-158 and Figure 3-159.

On average, correlations drop off faster, i.e. within a shorter distance to the search area center for SICCI-LF (25 km) than for SICCI-VLF (50 km) – similarly to the Northern Hemisphere. This applies to both the SIC error (top two images in Figure 3-158 and Figure 3-159) and the SIC total standard error (bottom two images in Figure 3-158 and Figure 3-159). The SIC error is correlated over larger distances over sea ice than over open water for SICCI-VLF: correlations fall below 0.5 at ~180 km distance from the search area center over water and over sea ice at ~220 km. For SICCI-LF, the opposite is the case: correlations fall below 0.5 at ~170 km distance from the search area center over open water and over sea ice at ~150 km. This is different from the Northern Hemisphere. The SIC total standard error is correlated over larger distances over open water than over sea ice. Over water, correlations fall below 0.5 at ~300 km and ~110 km distance from the search area center for SICCI-VLF and SICCI-LF, respectively. Over sea ice, corresponding correlations fall below 0.5 at ~150 km and ~90 km distance from the search area center. This is similar to the Northern Hemisphere.

Also similarly to the Northern Hemisphere, the correlation of the average SICCI-VLF SIC total standard error values stays quite high at around 0.4 over the entire remaining search area while in all other cases the correlations drop below or at least reach 0.2 towards the margin of the search area, i.e. in ~ 1000 km distance to the search area center.

We note that not constraining this analysis to the winter-time does not change the results shown in Figure 3-158 and Figure 3-159 notably.
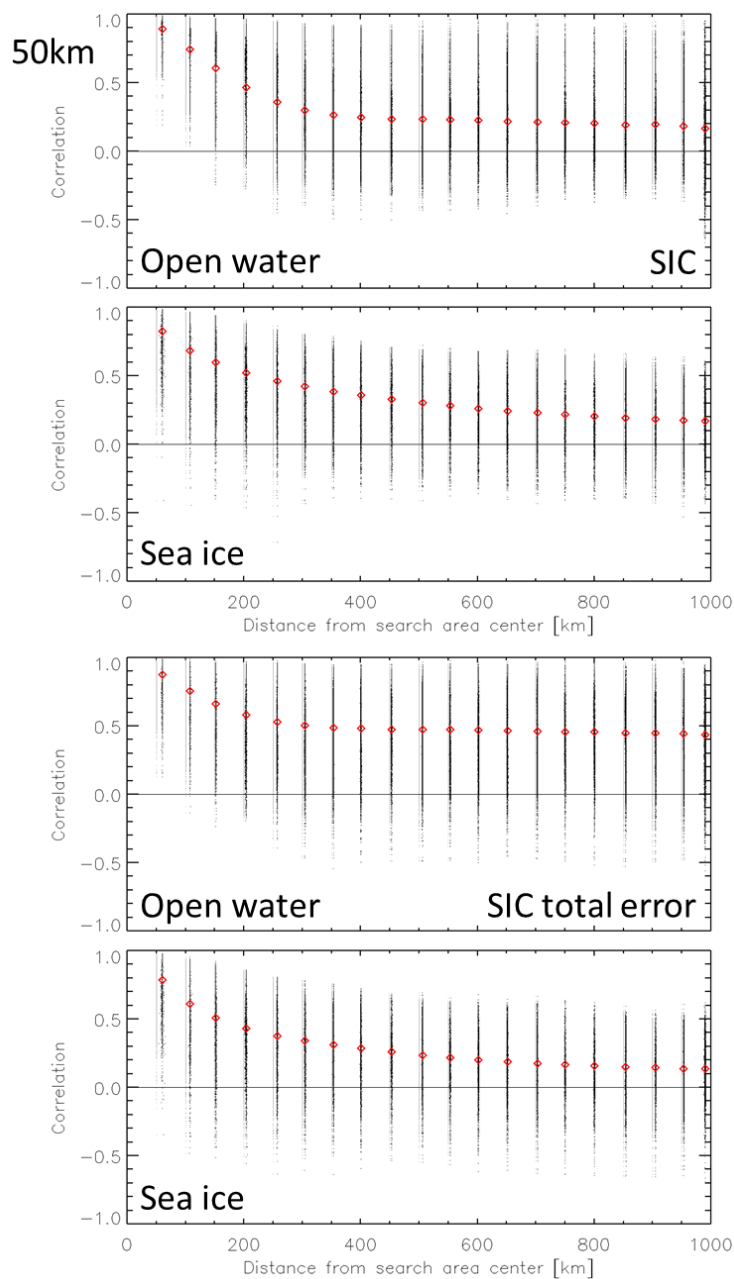
Figure 3-158: Mean correlation values computed for each distance ring around the search area center for all valid multi-annual mean daily seasonal cycle winter-time SIC error and SIC total standard error correlation values obtained using the SICCI-VLF (50.0 km) product of the Southern Hemisphere. Black dots denote individual mean correlation values while red diamonds give the average correlation of all search areas.
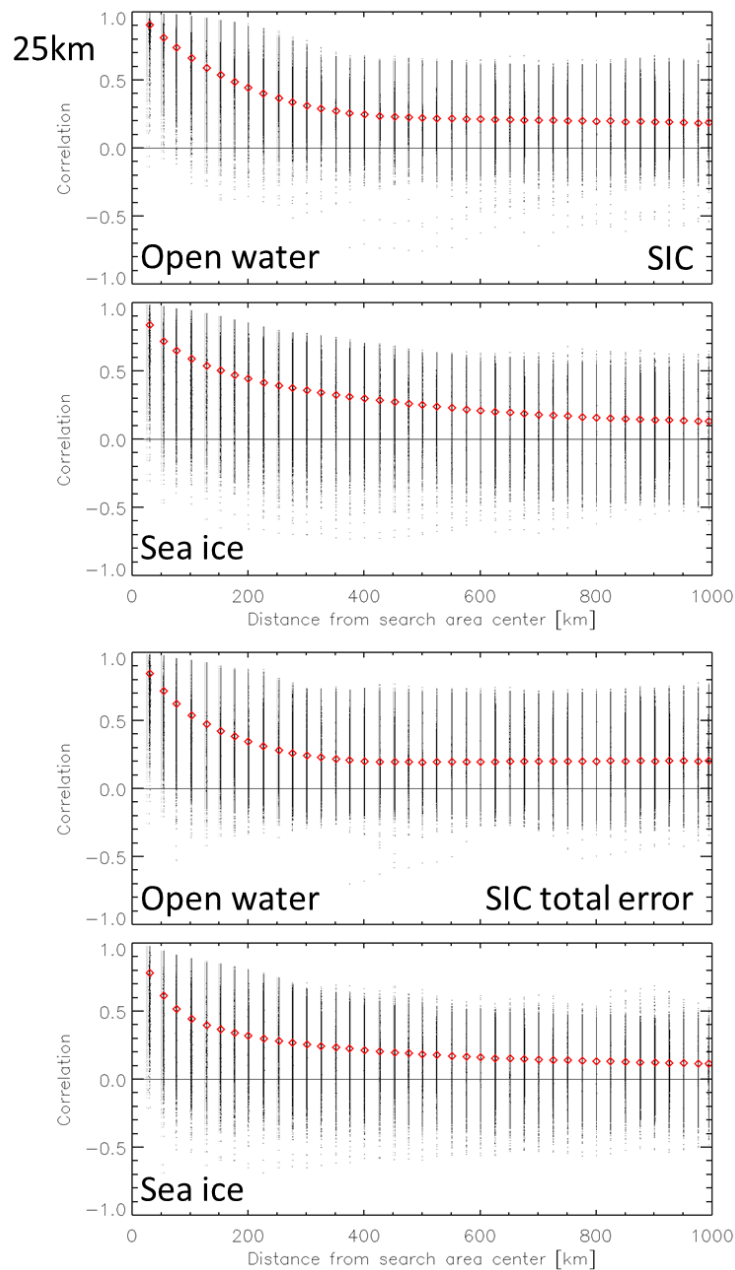
Figure 3-159: As Figure 3-158 but using the SICCI-LF (25 km) product.

In Figure 3-160 and Figure 3-161 we show the spatial distribution of the correlation of the SIC error over open water and of the respective SIC total standard error and the distribution of the correlation length scale – here the distance from the search area center beyond which the correlation is below 0.7 – using all and only the winter-time multi-annual mean daily seasonal cycle SICCI-LF product. The distributions of the correlation of particularly the SIC total standard error are dominated by the seasonal advance and retreat of the sea-ice cover (Figure 3-160, r.h.s.). In these regions the correlations often exceed 0.7 and also show artifacts. For the correlation of the SIC error we find an area of particularly low or even negative correlation directly adjacent to the sea-ice edge (Figure 3-160, l.h.s.); this finding is less pronounced when limiting the analysis to winter. At some distance to

the sea-ice edge, however, the correlation of the SIC error increases again to values up to 0.45, e.g. in the Weddell Sea. We do not find such a gradient in the correlation for the SIC total standard error. Here the correlation is lowest at the northern edge of the shown area, determined by the climatological sea-ice extent mask, while directly adjacent to the ice edge correlations are still ~0.4. An exception to this is an East Antarctic sector between ~120°E and ~160°E where correlations of the SIC total standard error are ~0.5 or even higher also over open water (Figure 3-160, r.h.s.).
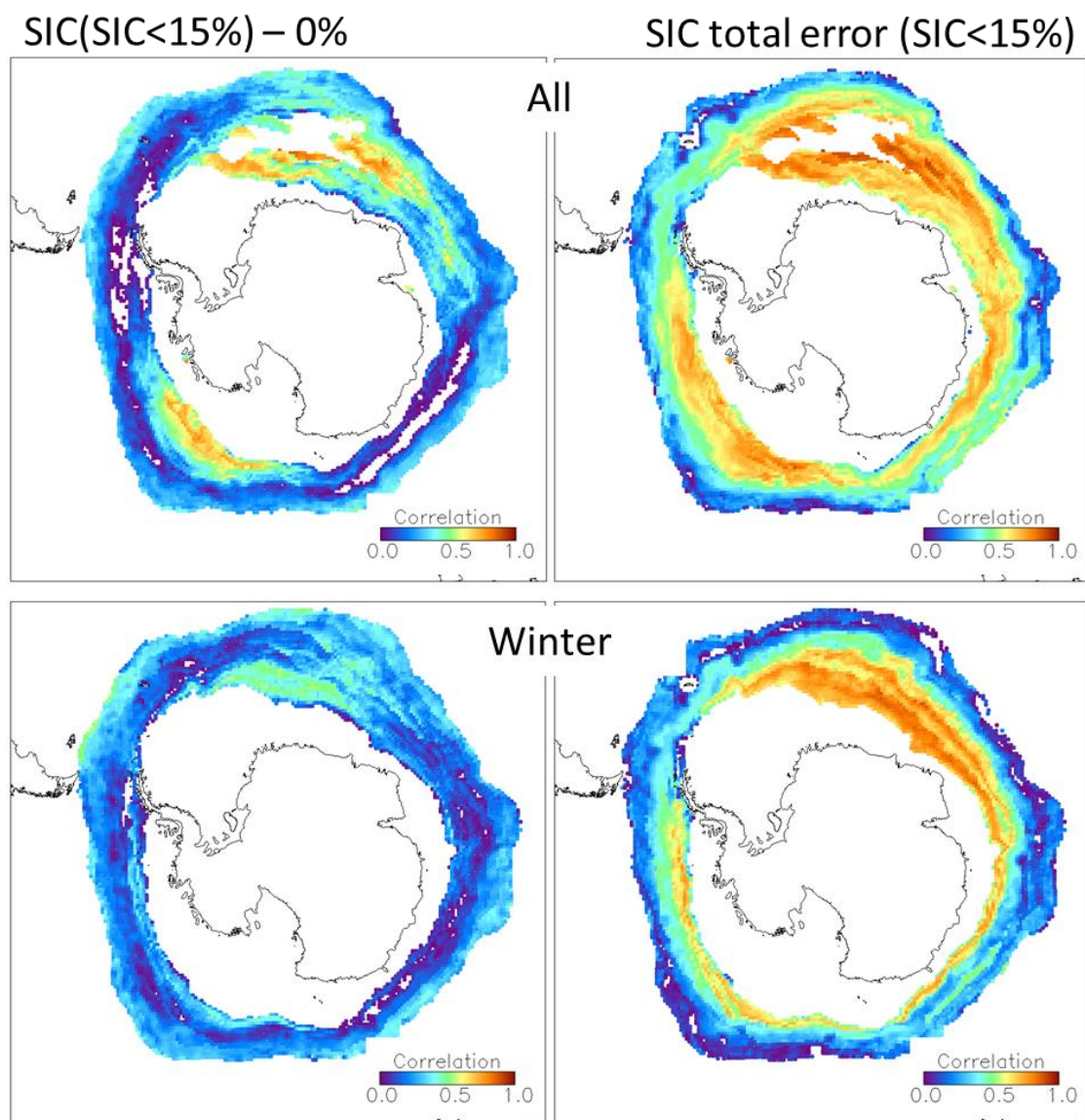
Figure 3-160: Correlation of the SIC error over open water, i.e. SIC – 0% computed for the range -15% … SIC … 15%, for all (top) and winter-time (bottom) valid multi-annual mean daily seasonal cycle values obtained using the SICCI-LF (25.0 km) product of the Southern Hemisphere.

The correlation lengths obtained from Figure 3-160 using a correlation threshold of 0.7 reveal a minimum in the correlation length of around the grid cell size (25 km) for the SIC error along the sea-ice edge; north of it,

i.e. over year-round or winter-round open water, correlation lengths are ~150 km (Figure 3-161, l.h.s.) which together confirms the average distances shown in Figure 3-158 and Figure 3-159. For the correlation length of the SIC total standard error (Figure 3-161, r.h.s.) we find also a ring of close to zero correlation lengths close to the sea-ice edge and larger ones north of it; however, the correlation lengths are on average smaller here, i.e. north of the correlation minimum, than for the SIC error.
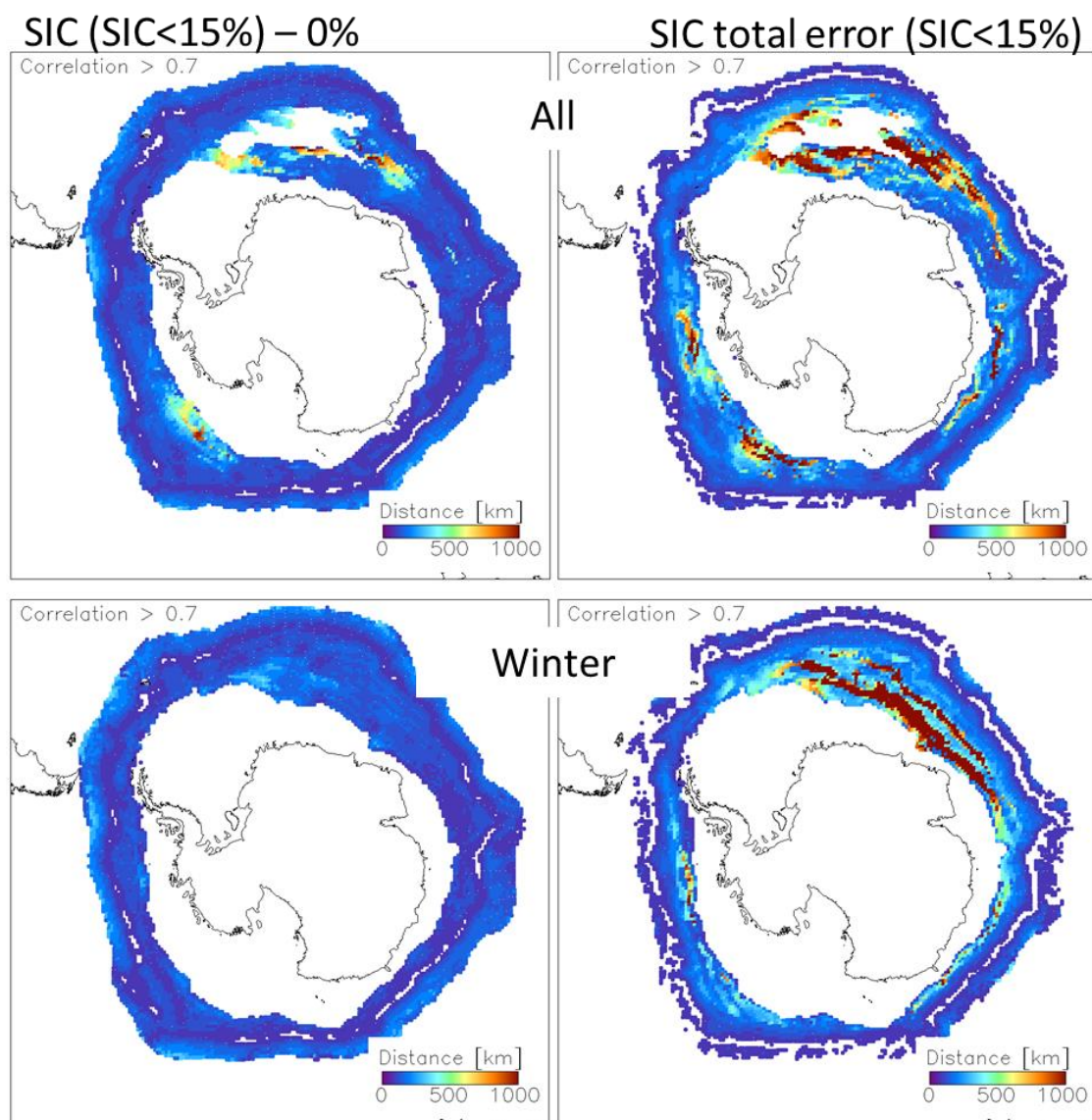
Figure 3-161: Correlation length = Distance from the search area center at which the correlations shown in Figure 3-160 fall below 0.7.

The correlations of the unconstrained SIC and the respective SIC total standard error (Figure 3-162, top) suggest similar conclusions as found for the Northern Hemisphere (compare Figure 3-154, top). The highest correlations of ~0.9 or higher are found in regions subject to a particularly stable seasonal sea-ice cover evolution which is the southern Weddell Sea between about 30°W and 10°E and parts of the Ross Sea. Low correlations, i.e. below 0.5, are observed in the marginal ice zone, in the East Antarctic

between ~100°E and ~160°E and also at the western side of the Antarctic Peninsula. In all these regions the low correlation can be attributed to a seasonal SIC cycle with high interannual variation in the open water fraction - similar to the peripheral seas in the Northern Hemisphere.
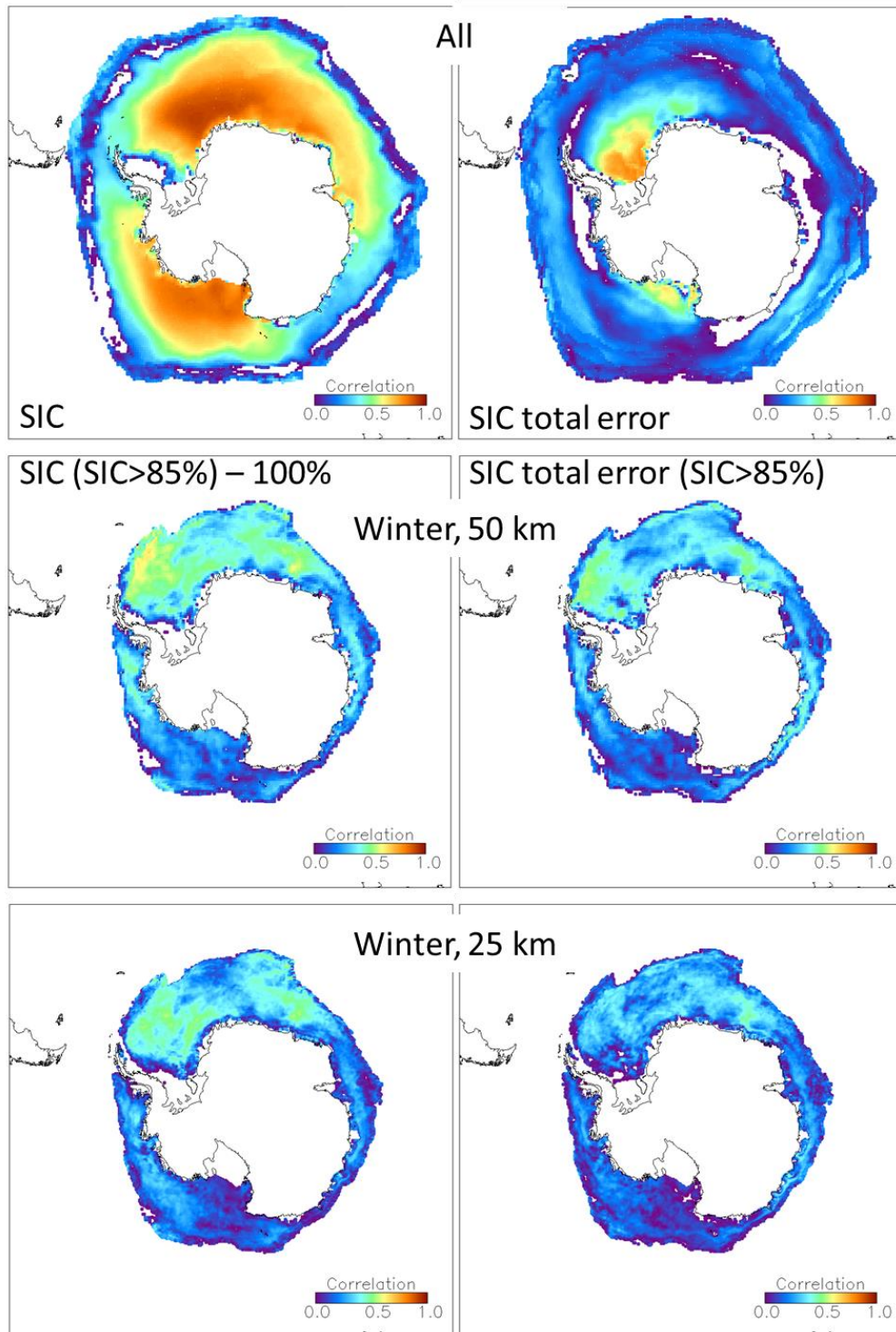
Figure 3-162: Correlation of SIC and SIC total standard error without any constraints (top), and of the SIC error over sea ice, i.e. SIC – 100% computed for the range 85% … SIC … 115%, for winter-time valid multi-annual mean daily seasonal cycle values obtained using SICCI-VLF (50 km, middle) and SICCI-LF (25 km, bottom) SIC of the Southern Hemisphere.
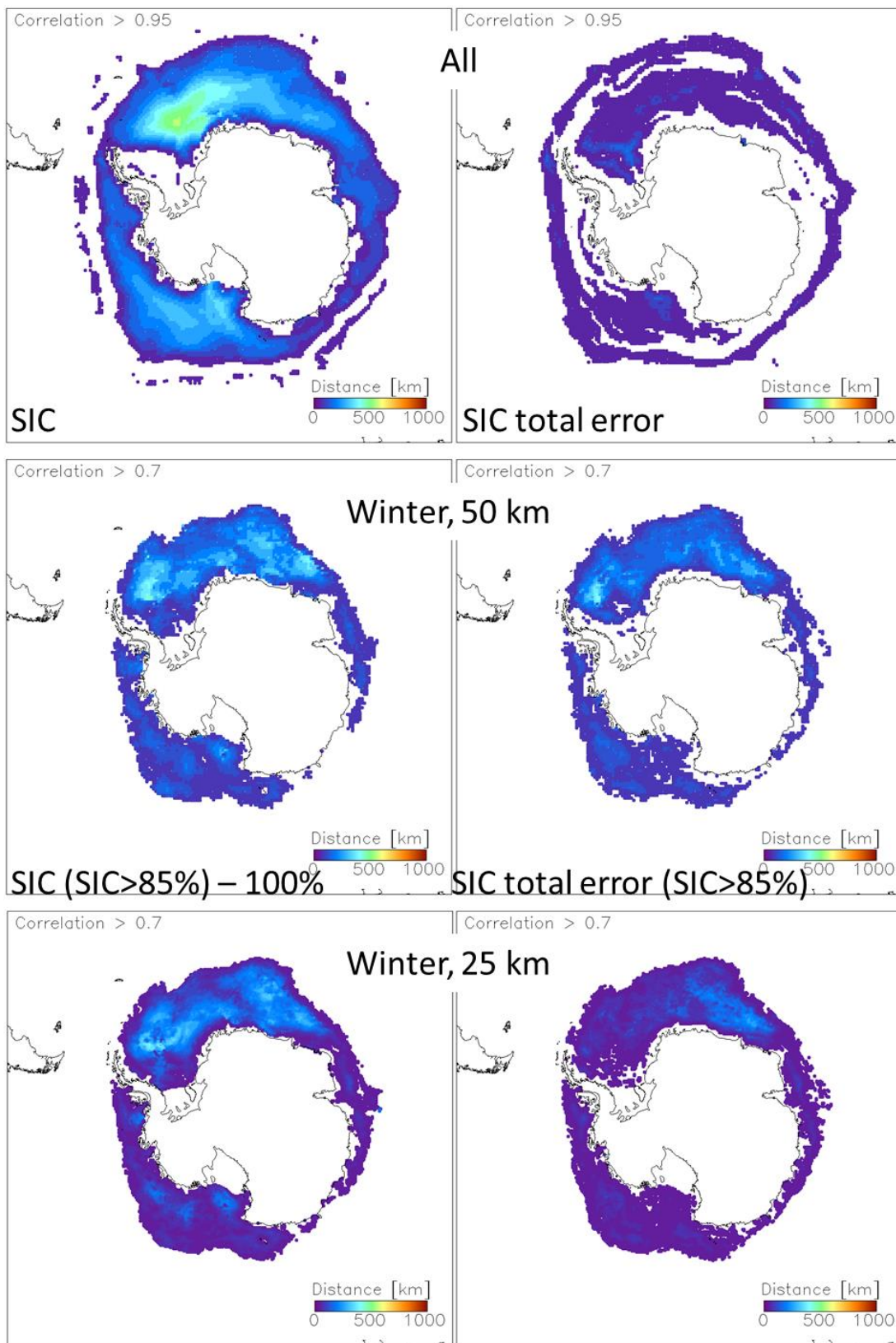
Figure 3-163: Correlation length = Distance from the search area center at which the correlations shown in Figure 3.8.22 fall below 0.95 (top) or below 0.7 (middle and bottom).

The drop in correlation to zero or even negative values at the Weddell Sea side of the Antarctic Peninsula can possibly be attributed to the same effect as mentioned already in the context of the area north of Greenland and the Canadian Arctic Archipelago (compare Figure 3-154): snow and ice-snow interface metamorphism induced changes in surface emissivity and hence retrieved SIC. Or, in other words, the retrieved SIC in these multiyear ice areas varies more than the actual SIC.

The correlation of the SIC total standard error (Figure 3-160, top right) is high, here: > 0.5, in regions where climatologically sea ice is most abundant. Correlations are smallest or even negative in most of the seasonally sea-ice covered regions such as the East Antarctic before they again peak up to values of 0.3 to 0.4 in a belt marking the marginal ice zone and sea-ice edge. This underpins the large role of the SIC smearing standard error to the SIC total standard error in these regions.

When choosing a similarly high correlation threshold of 0.95 to estimate the correlation length for SIC and SIC total standard error like we used in the Northern Hemisphere (Figure 3-155) then we end up with considerably smaller values for the SIC correlation length (Figure 3-163, top). For the SIC, correlation lengths are < 250 km for most of the sea ice cover; values reach 300 km and exceed 400 km in parts of the Ross Sea and of the Weddell Sea, respectively. No correlation length can be computed using this threshold for the multiyear ice covered area of the Weddell Sea. For the SIC total error, correlation lengths stay below 100 km for almost the entire sea-ice cover and are even zero / cannot be estimated for about one third of it.

The correlation of the SIC error over sea ice, i.e. SIC – 100% computed for the range 85% … SIC … 115% for the winter months and the respective SIC total standard error is shown in Figure 3.8.22, middle and bottom, for SICCI-VLF (50 km) and SICCI-LF (25 km), respectively.

Like for the Northern Hemisphere (compare to Figure 3-154) we find a similar pattern in the spatial distribution of the correlation for the SIC error and the SIC total standard error (Figure 3-163, middle and bottom). This applies more to SICCI-VLF than SICCI-LF – again in agreement with our results for the Northern Hemisphere. Overall, we find slightly larger correlations for SICCI-VLF than SICCI-LF. Regionally, largest correlations of ~0.5 or even larger are observed for the SIC error in the several areas of the Weddell Sea; also parts of the East Antarctic sea-ice cover and the Bellingshausen Sea see SIC error correlations reaching ~0.4. Respective correlations for the SIC total standard error are about 0.1 smaller. Correlations near zero are obtained near the Antarctic Peninsula, in the southernmost Ross Sea off the Ross Ice Shelf polynya and in some smaller areas hugging the coast line. In contrast to the Northern Hemisphere, where a patch of elevated SIC error correlation was observed north of Fram Strait which did not have a counterpart in the SIC total standard error correlation (Figure 3-154, bottom), basically all patches with elevated SIC error correlation in Figure 3-162, middle and bottom left) have elevated (though less pronounced) SIC total standard error correlations in Figure 3-162, middle and bottom right.

For the correlation length of the SIC error correlation and the SIC total standard error correlation, both over sea ice (Figure 3-163 middle and bottom) we again chose a correlation threshold of 0.7 (compare Figure 3-155). We find similar correlation lengths for the SIC error for SICCI-VLF and SICCI-LF; most regions see correlation lengths below 100 km, except the Weddell Sea where correlation lengths may reach 300 km and some smaller

patches in the Ross and Amundsen Seas where we find values up to 150 km. While the range of correlation lengths is similar for the SIC total standard error correlation we find a considerable difference for the Weddell Sea: While all patches of the correlation length agree between SIC error and SIC total standard error using SICCI-VLF, only the easternmost patch in the Lazarev / Cosmonaut Seas is found in both maps using SICCI-LF; the region of elevated correlation lengths for the SIC error correlation found in the central / western Weddell Sea (Figure 3-163, bottom left) is not present in the respective map for the SIC total standard error correlation length (Figure 3-163, bottom right). We hypothesize – in accordance with our results of the Northern Hemisphere – that this difference in correlation length could be caused by larger-scale patches of weather-influence induced (snow and ice-snow interface metamorphism) errors in the SIC.

Summary

- The correlation analysis opens a wide field of interpretations and seems to be a key to better understand the limitations of the SICCI-2 SIC products.

- We find a quick decay of the correlation within the 1000 km search area used for the SIC error over both open water and sea ice. The same applies to the correlation of the SIC total standard error.

- We find that SICCI-VLF (50.0 km) and SICCI-LF (25.0km) provide quite similar results in terms of the correlation values, their spatial decay, and their spatial patterns.

- Correlation length scales have been defined based on certain correlation thresholds. When using a threshold of 0.7 then correlation lengths rarely exceed 300 km.

- We find that the spatial distribution of the correlation of the SIC error over sea ice agrees better with the one of the SIC total standard error for SICCI-VLF than for SICCI-LF. In particular we find patches of elevated correlations and larger correlation lengths for the SICCI-LF SIC error which are not observed in the respective SIC total standard error; this applies to both hemispheres.

- THESE RESULTS HAVE TO BE TAKEN AS PRELIMINARY ONES!!! In the mean-time more progress has been made. What has been done in particular is to NOT depend on a fixed threshold to compute the correlation length scale but to approximate a suite of artificial decaying exponential functions and pick the one with the lowest RMSD to the actual correlations (see e.g. Figure 3-158 and Figure 3-159) to compute the correlation length scale from the function:

$R = \exp(-x/L)$

with the correlation R, the distance from the search area center x and the correlation length L. Figure 3-164 shows an arbitrarily chosen example of the suite of articifial functions for one grid cell and Figure 3.8.25 show examples of the resulting correlation length scales for the SIC error (SIC – 100% for SIC > 85%) and the SIC total standard error (for grid cells with SIC > 85%). This investigation follows the ideas of Bellprat et al. [RD-47].
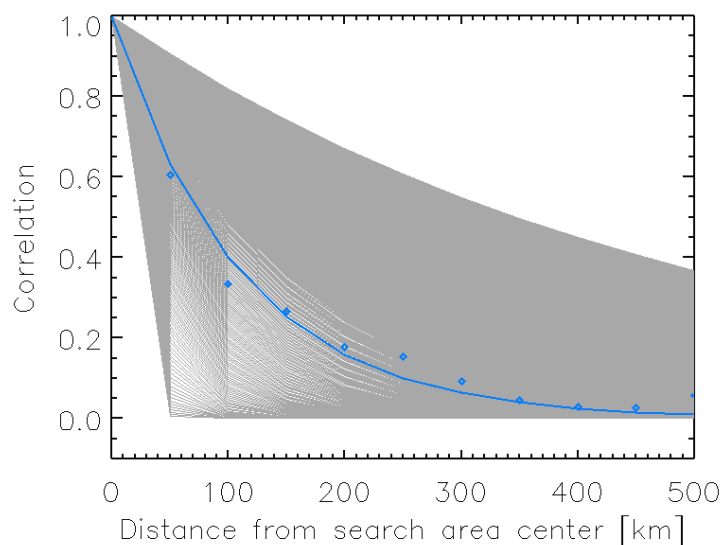
Figure 3-164: Suite of articial decaying exponential function according the the equation given in the text above (grey) together with the actual correlations (blue) for an arbitrarily chosen grid cell of the SICCI-50km product in the Northern Hemisphere for winter.
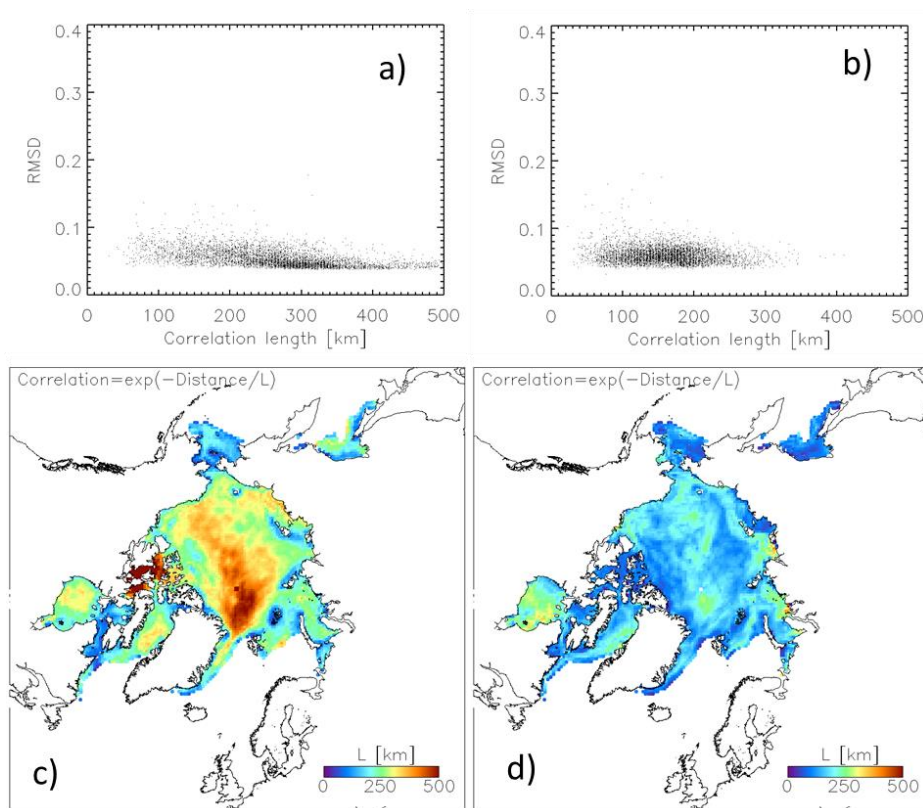
Figure 3-165: Maps of the correlation length for c) SIC error (SIC-100%) and d) SIC total standard error, both for SIC > 85%, for the SICCI-50km product in the Northern Hemisphere for winter. Images a) and b) give the respective distribution of the RMSD of the best exponential fit.

The example shown in Figure 3-165 is based on an investigation taking into account the entire time series of winters (January through March) for the entire period, i.e. 2002 through 2016. In a next step – results are not shown here but available as netCDF files from https://icdc.cen.uni-hamburg.de – the correlation analysis has been computed for the entire time series but for 30-day long, moving by one day, time segments with the aim to have correlation scale information at the same temporal sampling as the SIC data have and using almost the same time period as is used for the computation of the tie points.

4   Summary

In the Northern Hemisphere (Table 4-1), over open water, the SIC error is < 1% and the standard deviation of the SIC error is smaller than the retrieval standard error for all three algorithms. Over pack ice, the SIC error is ~ 2% and ~0.5% (both under-estimation) for SICCI-LF and SICCI-VLF; this error is smaller than the retrieval standard error. The standard deviation of the error is larger than the retrieval standard error for all three algorithms. Overall, SICCI-VLF provides the smallest errors and is the most precise (smallest error SDEV) product.

Table 4-1: Error (= SICCI-2 SIC minus reference SIC (RSIC)), error standard deviation (Error SDEV), retrieval standard error (RSE) and total standard error (TSE) for open water cases (RSIC = 0) and pack ice cases (RSIC = 1) for the Northern Hemisphere; "Wi" and "Su" denotes winter (Nov.-April) and summer (June-Aug.), respectively. Highlighted in *bold italic* are the cases with RSE > |Error| and RSE > Error SDEV. Highlighted in bold only are the cases with RSE > |Error| but RSE < Error SDEV.

Northern Hemisphere	SICCIHF (12.5km)				SICCILF (25km)				SICCIVLF (50km)			
	Error	Error SDEV	RSE	TSE	Error	Error SDEV	RSE	TSE	Error	Error SDEV	RSE	TSE
RSIC=0 Wi	*-0.4*	*2.5*	*3.5*	8.0	*-0.3*	*1.8*	*2.5*	10.5	*-0.5*	*1.5*	*1.8*	16.0
Su	*+0.2*	*2.8*	*4.2*	10.5	*+0.1*	*1.6*	*2.5*	13.0	*+0.5*	*1.1*	*1.4*	18.0
RSIC=1 Wi	-4.2	5.9	4.1	5.8	**-2.2**	3.7	**2.5**	5.0	**-0.5**	2.1	**1.7**	4.5

Table 4-2: Error (= SICCI-2 SIC minus reference SIC (RSIC)), error standard deviation (Error SDEV), retrieval standard error (RSE) and total standard error (TSE) for open water cases (RSIC = 0) and pack ice cases (RSIC = 1) for the Southern Hemisphere; "Wi" and "Su" denotes winter (May-Oct.) and summer (Dec.-Feb.), respectively. Highlighted in *bold italic* are the cases with RSE > |Error| and RSE > Error SDEV. Highlighted in bold only are the cases with RSE > |Error| but RSE < Error SDEV.

Northern Hemisphere	SICCIHF (12.5km)				SICCILF (25km)				SICCIVLF (50km)			
	Error	Error SDEV	RSE	TSE	Error	Error SDEV	RSE	TSE	Error	Error SDEV	RSE	TSE
RSIC=0 Wi	*-0.1*	*1.8*	*3.1*	4.2	*-0.1*	*1.4*	*2.3*	4.5	*-0.1*	*1.3*	*1.7*	5.7
Su	*+0.0*	*2.0*	*3.2*	4.7	*+0.1*	*1.2*	*1.9*	4.8	*+0.4*	*0.9*	*1.4*	6.7
RSIC=1 Wi	**-0.7**	4.0	**4.0**	6.0	**-1.4**	4.0	**2.8**	6.2	**-0.7**	2.4	**2.1**	6.5

In the Southern Hemisphere (Table 4-2), over open water, the SIC error is ~ 0% and the standard deviation of the SIC error is smaller than the retrieval standard error for all three algorithms. The SIC error is a bit smaller than in the Northern Hemisphere. Over pack ice, the SIC error is < 2% and 0.7% (both under-estimation) for SICCI-LF and SICCI-VLF / SICCI-HF, respectively; this error is smaller than the retrieval standard error. The standard deviation of the error is larger than / equal to the retrieval standard error for all three algorithms. Overall, SICCI-HF provides the smallest errors but SICCI-VLF is the most precise (smallest error SDEV) product.

Table 4-3: Error (= SICCI-2 SIC minus reference SIC), error standard deviation (Error SDEV), retrieval standard error (RSE) and total standard error (TSE) for the comparison with Landsat-5 and Landsat-8 SIC, with ship-based observations from ASSIST/IceWatch, with MODIS SIC, and with MODIS ice surface fraction (ISF) for the Northern Hemisphere; "Wi" and "Su" denotes winter (Nov.-April) and summer (June-Aug.), respectively. For Landsat cases RSE and TSE are for winter pack ice conditions. For ASSIST Wi and ASSIST Su RSE and TSE are the average of the open water and pack ice values of the respective season. For MODIS RSE and TSE are the average summer open water and pack ice values. Highlighted in *bold italic* are those "Error" and "Error SDEV" values where RSE > |Error| and RSE > Error SDEV. Highlighted in bold only are those "Error" values where RSE < |Error| but TSE > |Error|. "Error SDEV" values in *italic* are < TSE.

Northern Hemisphere	SICCIHF (12.5km)				SICCILF (25km)				SICCIVLF (50km)			
	Error	Error SDEV	RSE	TSE	Error	Error SDEV	RSE	TSE	Error	Error SDEV	RSE	TSE
Landsat-5	**-4.3**	6.3	4.1	5.8	**-4.6**	5.7	2.5	5.0	**-2.4**	*4.3*	1.7	4.5
Landsat-8	**-4.9**	9.3			**-3.7**	*4.9*			**-2.3**	*3.2*		
ASSIST Wi	-8.4	14.0	3.8	6.9	-9.0	13.5	2.5	7.7	**-7.9**	14.2	1.7	10.2
ASSIST Su	**-6.5**	14.0	4.3	8.4	**-7.5**	14.4	3.1	9.9	**-7.5**	15.1	2.5	12.9
MODIS SIC	***-1.3***	***1.2***	4.3	8.4	***-1.7***	***1.1***	3.1	9.9	***-0.7***	***1.4***	2.5	12.9
MODIS ISF	+18.0	4.6			+18.1	4.7			+17.1	4.9		

For the Northern Hemisphere (Table 4-3), when SICCI-2 SIC is compared to Landsat SIC during winter, SICCI-VLF provides the smallest error: ~2.5% under-estimation, while SICCI-HF provides the largest error: ~4.5% to 5.0%. These errors are within the total standard error but not within the retrieval standard error. When compared to ship-based SIC observations, errors are between 5% and 10% under-estimation for all algorithms and are slightly smaller in summer than winter. During summer these errors are within the total standard error.

For all algorithms, the overall SICCI-2 SIC error with respect to MODIS SIC is < 2% under-estimation, which is within the retrieval standard error. The overall SICCI-2 SIC error with respect to the true sea-ice surface fraction, e.g. MODIS ISF, is ~17% for SICCI-VLF and ~18% for the other two algorithms (Table 4-3). Comparison with Table 3-20 and Table 3-21 reveals: the SICCI-2 SIC error is a function of melt-pond fraction (MPF). Overall, we find an over-estimation of MODIS SIC by ~2% at a MPF of ~5% and an under-estimation of MODIS SIC by ~5% at a MPF of ~35%. For ISF, we find an over-estimation by ~7%, ~15%, ~22%, and 26% for MPF values of ~5%, ~15%, 25%, and 35%, respectively. Note that MPF and ISF are – on average – as accurate as 3-5%.

The passive microwave sensors used cannot discriminate between open water between ice floes (leads and openings) and open water on top of the sea ice (melt ponds). Why do the obtained SIC values agree, when averaged over the entire period (2003-2011) and the entire Arctic Ocean, within their retrieval standard error with MODIS SIC? Locally and regionally, SICCI-2 SIC and MODIS SIC differ regularly by between -20% to +15%. The small overall SIC difference is the result of positive and negative differences compensating each other.

Table 4-4: Error (= SICCI-2 SIC minus reference SIC), error standard deviation (Error SDEV), retrieval standard error (RSE) and total standard error (TSE) for the comparison with Landsat-8 SIC, and with ship-based observations from ASPeCt for the Southern Hemisphere; "Wi" and "Su" denotes winter (May-Oct.) and summer (Dec.-Feb.), respectively. For Landsat, RSE and TSE are the average of pack ice conditions during summer and winter (in contrast to Table 4-3 Landsat-8 images are partly from summer and winter). For ASPeCt Wi and ASPeCT Su RSE and TSE are the average of the open water and pack ice values of the respective season. Highlighted in *bold italic* are those "Error" and "Error SDEV" values where RSE > |Error| and RSE > Error SDEV. Highlighted in bold only are those "Error" values where RSE < |Error| but TSE > |Error|. "Error SDEV" values in *italic* are < TSE.

Southern Hemisphere	SICCIHF (12.5km)				SICCILF (25km)				SICCIVLF (50km)			
	Error	Error SDEV	RSE	TSE	Error	Error SDEV	RSE	TSE	Error	Error SDEV	RSE	TSE
Landsat-8	*-2.8*	*8.5*	5.7	9.0	**-3.4**	*6.4*	3.8	9.1	*-2.4*	*4.4*	3.7	10.3
ASPECT Wi	*-0.1*	9.8	3.5	5.1	*-1.7*	9.2	2.5	5.3	*-1.3*	10.4	1.8	6.1
ASPECT Su	*-1.3*	15.4	5.5	8.3	**-3.1**	16.0	3.5	8.4	*-0.9*	16.6	3.5	10.4

For the Southern Hemisphere (Table 4-4), when SICCI-2 SIC is compared to Landsat SIC during winter, SICCI-VLF provides the smallest error: ~2.5% under-estimation, while SICCI-LF provides the largest error: ~3.5%. These errors are within the retrieval standard error – in contrast to the Northern Hemisphere (Table 4-3). When compared to ASPeCt ship-based SIC observations, errors are < 2% for winter and < ~3% for summer under-estimation for all algorithms; SICCI-LF performs worse compared to the other two algorithms. These errors are considerably smaller than those for the Northern Hemisphere (compare Table 4-3) and are in addition also within the retrieval standard error.

We can conclude: of the three algorithms SICCI-VLF (50.0 km) provides SIC with the highest precision and the lowest error in both hemisphere.

5   Open issues / Outlook

- We refined the analysis of the Landsat data during weeks before finalization of this PVIR-SIC. This improved analysis will possibly lead to more useful SIC data pairs to be compared. Also, instead of using only image-average SIC values for the comparison, grid-cell wise SIC values can now be inter-compared. Results have been presented at the POLAR2018 conference in DAVOS, June 19-23, 2018, and will be matter of one separate publication.

- In the same context, it might be useful to specifically look into special cases where the difference between SICCI-2 SIC and Landsat SIC is either abnormally large or where an especially large fraction of thin ice exits.

- The RRDP2 has only exploited as far as it concerns the information about 100% SIC. Its full potential, i.e. the combination with the many additional co-located meteorological data, has not yet been exploited.

- The inter-comparison with MODIS data, ship-based observations, and Landsat data should be extended to include other SIC products in order to carry out an across-algorithm evaluation. This has been started within the frame-work of the project for MODIS data and has also been presented at the POLAR2018 conference in DAVOS, June 19-23, 2018, and will be matter of one separate publication.

- The correlation analysis results shown so far need more interpretation on the one hand. On the other hand most of what is shown is based on the correlation of the local SIC (error) time series over the entire period with the multi-annual mean SIC (error) time series within the search radius. As stated at the end of the respective section, a more innovative correlation analysis has been carried out in the meantime and will be continued in the near future.

< End of Document >

ESA UNCLASSIFIED - For Official Use